Experimental and Data Modeling Methods for Targeted Water Chemistry Studies related with Nuclear Power Reactors

By

Vaidehi Sharan Tripathi

CHEM 01200604011

BHABHA ATOMIC RESEARCH CENTRE

A thesis submitted to the
Board of Studies in Chemical Sciences
In partial fulfillment of requirements
For the Degree of

DOCTOR OF PHILOSOPHY

of

HOMI BHABHA NATIONAL INSTITUTE

February, 2014

Homi Bhabha National Institute

Recommendations of the Viva Voce Committee

As members of the Viva Voce Committee, we certify that we have read the dissertation prepared by **Mr. Vaidehi Sharan Tripathi** entitled "**Experimental and Data Modeling Methods for Targeted Water Chemistry Studies Related with Nuclear Power Reactors**" and recommend that it may be accepted as fulfilling the thesis requirement for the award of Degree of Doctor of Philosophy.

Chairman - Prof. K. L. Ramakumar	**Date:**	31.7.2014
Guide / Convener - Prof. D. B. Naik	**Date:**	31.7.2014
External Examiner - Dr. S. Muralidharan	**Date:**	31.7.2014
Member 1 - Prof. S. K. Mukerjee	**Date:**	31-07-2014,
Member 2- Prof. A. K. Tyagi	**Date:**	31-07-2014

Final approval and acceptance of this thesis is contingent upon the candidate's submission of the final copies of the thesis to HBNI.

I hereby certify that I have read this thesis prepared under my direction and recommend that it may be accepted as fulfilling the thesis requirement.

Date: 31-07-2014

Place: Mumbai

Guide: Prof. D. B. Naik

STATEMENT BY AUTHOR

This dissertation has been submitted in partial fulfillment of requirements for an advanced degree at Homi Bhabha National Institute (HBNI) and is deposited in the Library to be made available to borrowers under rules of the HBNI.

Brief quotations from this dissertation are allowable without special permission, provided that accurate acknowledgement of source is made. Requests for permission for extended quotation from or reproduction of this manuscript in whole or in part may be granted by the Competent Authority of HBNI when in his or her judgment the proposed use of the material is in the interests of scholarship. In all other instances, however, permission must be obtained from the author.

Vaidehi Sharan Tripathi

DECLARATION

I, hereby declare that the investigation presented in the thesis has been carried out by me. The work is original and has not been submitted earlier as a whole or in part for a degree / diploma at this or any other Institution / University.

Vaidehi Sharan Tripathi

List of publications arising from the thesis

Journals:

1) "Study of nitric acid leachout characteristics from weak base anion exchanger to maintain a specified pH regime during $Gd(NO_3)_3$ removal from moderator system of 540 MWe PHWRs" **V. S. Tripathi**, V. Balaji, G. Venkateswaran and S. C. Dash, *Canadian Journal of Chemical Engineering*, **2009**, *Vol. 87*, 887-895.

2) "Effect of gamma irradiation on chromate sorption over magnetite surface". **V.S. Tripathi**, S.J. Keny, S. Bera and G. Venkateswaran, *Radiation Effects & Defects in Solids*, **2012**, *Vol. 167*, 676–683.

3) "Novel V(III) compound: Electrochemical synthesis of $V(OH)(HCOO)_2$, characterization and evaluation of electroreduction on suitable electrodes" **V. S. Tripathi**, K. K. Bairwa, D. Mal and D. B. Naik, *Journal of The Electrochemical Society*, **2014**, *Vol. 161*, E34 – E39.

Symposia:

1) "Gadolinium removal from the moderator system of TAPP #3 using the three layer bed" **V. S. Tripathi**, V. Balaji, G. Venkateswaran and S. C. Dash, Proc. of Symposium on Operational and Environmental Issues Concerning use of Water as a Coolant in Power Plants and Industries (OPENWAC 2008), 15-16 Dec., 2008, Kalpakkam, pp 189-192.

2) "Electrochemical Investigation of Vanadium Reduction on Graphite Electrode" **V. S. Tripathi**, K. K. Bairwa and S. V. Narasimhan, International Symposium on Materials Chemistry (ISMC-2010), 7-12 Dec., 2010, Mumbai, Poster paper No. A-23.

3) "Electrochemical Synthesis and Characterization of $V(OH)(HCOO)_2$ for Easing the Decontamination Formulation Preparation Methodology for Light Water Reactors" **V. S. Tripathi**, K. K. Bairwa and S. Velmurugan, Proc. of Fifth ISEAC Triennial International Conference on Advances and Recent Trends in Electrochemistry (ELAC-2013), 16-20 Jan., 2013, Hyderabad, pp 485-489.

Vaidehi Sharan Tripathi

Dedicated

to

My Beloved

Late Mother

Acknowledgements

Foremost, I would like to express my sincere gratitude towards my present guide Prof. D. B. Naik, Head, Applied Radiation Chemistry Section, Radiation & Photochemistry Division (RPCD), BARC for his continuous support during my Ph.D study and research, for his patience, motivation, enthusiasm, and immense knowledge. I also thank him for his guidance and for critically reviewing my thesis. I would also like to express my deep sense of gratitude and sincere thanks to my former research guide Prof. G. Venkateswaran, former Head, Analytical Chemistry Division (ACD), BARC who introduced me to the area of reactor water chemistry, for his generous inspiration, guidance, encouragement and useful suggestions.

I would like express my gratitude towards the doctoral committee members for this study, Prof. T. Mukherjee (former Director, Chemistry Group), Prof. K. L. Ramakumar (Director, Radiochemistry & Isotope Group), Prof. S. V. Narasimhan (Former Associate Director, Chemistry Group), Prof. S. K. Mukerjee (Head, Process Development Division) and Prof. A. K. Tyagi (Head, Solid State Chemistry Section, Chemistry Division) for their encouragement, insightful comments, and critical periodic review of the work.

I would like to specially thank to Prof. S. Velmurugan, Head, Water & Steam Chemistry Division (WSCD), BARC-Facilities, Kalpakkam for his keen interest and encouragement for completion of this work. My sincere thanks also go towards

Dr. Shantanu Bera, Dr. S. Nagabhushan Achary, Dr. (Ms.) Naina H. Raje and Dr. Rakesh Kumar for providing immediate and timely attention to my analytical requirements.

I would like to place on record, the co-operation and constant support received from my group colleagues Dr. A. G. Kumbhar, Dr. (Ms.) S. J. Keny, Mr. B. K. Gokhale and Mr. K. K. Bairwa. This work could only be completed with the close co-operation from my group colleagues.

It is my pleasure to acknowledge my fellow colleagues and friends who were always available for any technical discussion, which include Dr. S. Nigam, Dr. S. Varma, Dr. B. P. Mandal, Dr. K. Bhattacharyya and many others for their continuous moral support. I wish to express my gratitude to all staff members of RPCD, ChD and WSCD for their timely administrative assistance.

Last but not the least, I would like to thank my kids, Dishita and Aarav for sparing me from paying attention to them during this work, my wife, Deepti for her immense support and almost single handedly managing the family and my father for his constant encouragement and for providing the spiritual support throughout my life.

Vaidehi Sharan Tripathi

Contents

Synopsis of the thesis titled: Experimental and data modeling methods for targeted water chemistry studies related with nuclear power reactors

Introduction

Water chemistry plays an important role in the smooth functioning of the nuclear power plants (NPPs). Role of water chemistry in an operational NPP ranges from chemistry control for minimizing the corrosion of structural materials to remedial measures of removing the deposited radionuclides from the outer layers of structural material by dissolution using various chemical formulations [1]. It also involves reactivity control in NPPs where soluble burnable poison is added for the purpose. The primary role of water chemistry is minimizing corrosion through control of the water chemistry parameters. The purpose of chemistry control for a NPP is to ensure good fuel clad integrity, minimize radiation field build-up on out-of-core surfaces, prevent tube failures of Heat exchangers and Steam generators and to maintain good integrity of structural materials [2]. This is primarily achieved by maintaining the specified water chemistry regime through addition of the required chemicals or by removal of ionic impurities using ion exchange purification.

Use of water as the heat transport medium has its own merits and demerits. It invariably leads to corrosion and thus formation of corrosion products. For water cooled nuclear power reactors, viz. Boiling Water Reactors (BWR), Pressurized light Water Reactors (PWR) and Pressurized Heavy Water Reactors (PHWR), corrosion products are generated due to the interaction of high temperature coolant with the different structural materials which constitute the primary heat transport system [3-5]. There is always a certain minimum amount of corrosion of structural materials in spite of maintaining optimum water chemistry parameters of the coolant / moderator. Though this minimum corrosion is well within the design allowance, the transport of corrosion products through the core of the nuclear reactor results in their neutron activation and when these activated corrosion products deposit on out-of-core surfaces, the radiation fields start building-up [6]. Thus over the years of reactor operation, radiation field around the primary coolant / moderator circuit tends to go up. Dilute chemical decontamination, wherein the corrosion product oxide on system surfaces bearing radioactive isotopes like Co-60, Mn-54, Cr-51 etc. is dissolved using optimized chemical formulations, is one of the methods to control the buildup of radiation fields around the primary system of nuclear power plants [7]. The key concerns for selection of the chemical formulation are the material compatibility with all the structural materials and the amount of radioactive waste generated as a result of decontamination [8]. The chemical formulation should exhibit high decontamination factor (DF) after its application on the reactor system. This depends on the dissolution kinetics for the surface grown oxide in the given formulation as well as the stability of the oxide layer which varies with the type of reactor systems.

The nature of the surface grown oxide depends upon the water chemistry and hydrothermal conditions. In some cases, this may lead to a requirement of altogether different formulation composition for dissolving the oxide on same structural material. A typical case is the role of dissolved chromate in changing the nature of the surface grown oxide over stainless steel under irradiation. The oxide formed in such a chemistry condition is rich in chromium and hence requires a prior oxidative dissolution pretreatment before applying the conventional reductive formulation for dissolving the iron oxides [9]. Thus, sorption of specific ions from the solution depending upon the operational chemistry parameters may alter the nature of oxide formed on the surface.

Another important water chemistry related aspect is the ion exchange treatment which is the most suitable method for removing dissolved ionic species from the reactor recirculation systems. In a recirculating system purification using an ion exchange column, rate of reduction in concentration of dissolved aqueous ionic species depends upon the flow rate and the volume of inventory to be purified. Ion exchange bed can also act as a source for maintaining the concentration of a specific dissolved ionic species within a specified range. This can be achieved by selecting a proper ion exchanger based on the required selectivity coefficient for the specified ionic species. Such an ion exchanger would remove the dissolved ionic species from solution as long as the sorption equilibrium favours the process. Once the resin phase concentration reaches the saturation as per the selectivity coefficient of the resin, there will be no further removal of the ionic species from the aqueous phase. If the aqueous phase concentration of the ionic species is less than the allowed concentration as per the selectivity coefficient, the ionic species will leach out from the resin phase to the aqueous phase [10]. This can be an ideal way of maintaining specified chemistry regime which can avoid repeated addition of fresh chemical and removal of the same during purification.

Scope and objectives of the study

The water chemistry studies undertaken in the present work are related to the decontamination of stainless steel based NPPs viz. BWRs and PWRs along with the application of ion exchange resins for maintaining the specified water chemistry regime. The chemical decontamination formulation is usually a mixture of a reducing agent, a chelating ligand and a pH maintaining reagent. The action of chemical decontamination formulation can be broadly described in two steps. The strong reducing agents such as V(II)-NTA (nitrilotriacetic acid) or Fe(II)-NTA adsorb on the surface of the oxide and reduce the Fe(III) on surface by the heterogeneous electron transfer mechanism. The oxide lattice is destabilized by the Fe(III) to Fe(II) reduction owing to the ionic size variation and associated increased electrostatic repulsion between the Fe(II) and oxide ions, the Fe(II) ion dissolved in the solution is subsequently stabilized by the complexing agent at the favourable pH conditions [11]. Iron oxides are the major constituent of the surface grown oxides in all types of NPPs operating under different water chemistry regimes. The percentage metal ion composition of iron in the surface oxide ranges from 70 to more than 95. Direct reductive dissolution is effective for low Cr containing oxides. However, if the Cr content is higher, typically > 10 metal atom% chromium in the oxide lattice, an oxidative pretreatment is a required prior to the conventional reductive dissolution to obtain good decontamination factor (DF) [12]. While simple iron oxides like Fe_3O_4, γ-Fe_2O_3, FeOOH and α-Fe_2O_3 etc., can be efficiently dissolved using organic acid reductant based formulations like a mixture of citric acid, ethylenediamine tetra acetic acid (EDTA) and ascorbic acid (CEA) where ascorbic acid acts as the reducing agent, the chromium, nickel substituted iron oxides like $Fe_{2-x}Cr_xO_3$, $Fe_xCr_yNi_zO_4$ $(x+y+z = 3)$ etc., require formulation based on stronger reducing agents like V(II) EDTA,V(II) $(pic)_3$ etc. These Ni and Cr substituted oxides are primarily formed on stainless steel based light water cooled nuclear power reactors like Boiling Water Reactor (BWR) and Pressurised Water Reactor (PWR) [13].

Thus, a methodology to synthesize the strong reducing agent namely V(II) at large scale is imperative for undertaking decontamination of stainless steel based NPPs. Major part of the present work is related with the studies on optimization of the synthesis of V(II) based formulation. The strongly reducing nature of V(II) requires careful handling under inert condition. Otherwise it will react with atmospheric oxygen and will instantaneously get oxidized to V(III). The stringent requirement of inert condition poses immense handling related issues for the large scale application. These can be addressed in two ways.

The first and the preferred one is to prepare a material compatible V(II) solid compound which can be directly added to the reactor system during the decontamination campaign. The second option is to optimize the preparation of a high concentration V(II) solution in a material compatible formulation which will reduce the volume to be handled during the decontamination campaign. The stringent condition of material compatible formulation limits the choice of synthesis routes. Electrochemical route is the one which provides the flexibility of selective synthesis. Electrolytic route allows us to select the exact medium required for synthesis without any addition of spare reagent or formation of any byproduct. The prevalent oxidation states of vanadium compounds are 5+ and 4+. The methodology used for the synthesis was based on electroreduction of saturated aqueous V(V) or V(IV) precursor solutions in the material compatible formulation. The maximum concentration has been evaluated for V(V) in formic acid medium at different molar ratio and also for V(IV) in formic acid media. The solid compounds obtained by precipitation during the process were also characterized for their chemical composition. Electrochemical studies using aqueous vanadium solution were performed to select the suitable electrode. A two compartment electrolysis cell was designed and fabricated in-house which was used for electroreduction of various vanadium formate solutions. A V(III)-formate solid compound obtained by electroreduction was also characterized for the chemical composition and solubility in aqueous solution. Complexation of the V(III) compound to obtain highly stable aqueous solution is also studied.

The electrolysis requires an efficient methodology for monitoring as the product is highly reactive and air sensitive. On-line continuous solution potential monitoring with a redox electrode impressed with a high frequency of 1.13 kHz, 10 mV alternating voltage to overcome polarization of the electrode has been evolved for evaluating the progress of electrolysis. A redox speciation method for periodic batch samples has also been evolved which is based on simple, rapid and sensitive indirect spectrophotometric measurement.

Dissolution of oxide from the surface also entails understanding the nature of oxide formed on the structural surfaces. Presence of chromate in medium has been studied for its role in modifying the representative iron oxide. Effect of gamma irradiation on the oxide modification has been compared with isothermal interaction.

Weak base anion exchange resin has been evaluated for maintaining the specified pH during Gd^{3+} removal. The use of nitric acid loaded weak base anion exchange resin has been studied for the purpose.

Organization of the thesis:

The thesis contains seven chapters. The first chapter gives the details of the water chemistry controls practiced in the various NPPs and related issues. The second chapter contains the discussion of the experimental and instrumental techniques used in the study. Third to sixth chapter contain the description of the research work carried out in details. Seventh chapter contains the overall summary of conclusions of the study. The brief overview of the chapters is given below:

Chapter 1: Introduction

This chapter outlines the overall general introduction to the issues related with the water chemistry of NPPs. The basis for evolution of water chemistry specifications for the various types of NPPs is discussed. The issue of oxide growth mechanism on the structural material surfaces and related activity transport and radioactivity field buildup is discussed. A broad outline of the topic is presented on the basis of literature survey. The general perspective of decontamination and related practices is also discussed. A summary of the methodologies of oxide dissolution based on the literature reports is presented. The varying mechanisms of chemical dissolutions for different kind of oxides have been also been enlisted. The requirement of a strong reducing agent for dissolution of oxides grown over the stainless steel surfaces is discussed. Criteria for selection of a suitable decontamination formulation on the basis of fulfillment of additional preconditions imposed by the specific requirements of NPPs are discussed. A brief account of evolution of various decontamination formulation to meet the above mentioned requirements is also given. The specific role of chromate in modification of the representative oxides, its enhanced sorption in presence of gamma irradiation is discussed. The water chemistry control by application of nitric acid loaded weak base anion exchange resin is also discussed in this chapter.

Chapter 2: Experimental methods

This chapter outlines the experimental setup details used in the study including the description of cell used for electrolysis, the arrangement made for monitoring redox potential and the recirculation loop with an ion exchange column used for water chemistry control using ion exchange bed. Synthesis of representative oxides for chromate sorption studies is also described. Brief principle of instrumental techniques used for characterization and analysis in the study is described in the chapter. These include electrochemical techniques like cyclic voltammetry and potentiodynamic polarization using PGSTAT 302N from Ecochemie which can operate within ± 15 V, 2 A working range, atomic absorption spectroscopy (AAS) using Avanta from GBC with 8 lamp holder, ion chromatography (IC) using DX-120 from Dionex, Fourier transform Infrared spectroscopy (FTIR) using MB 102 FTIR from Bomem having a scan range of 4000 - 400 cm^{-1} with a resolution of 2 cm^{-1}, Ultraviolet-visible spectroscopy (UV-vis) using Jasco-700 spectrophotometer having a scan range of 900 to 190 nm, thermogravimetry (TG) using SETSYS by SETARAM , X-ray diffraction (XRD) using Philips powder x-ray diffractometer based on PW1710 processing unit with vertical goniometer (model PW1820) coupled to PW1729 x-ray generator having Cu K_α x-ray source (30 KV and 20 mA) and X-ray photoelectron spectroscopy (XPS) using VG model - ESCALAB MK 200X spectrometer equipped with Al kα x-ray energy of 1486.6 eV and FWHM of 0.85 eV along with Mg kα x-ray energy of 1253.6 eV and FWHM of 0.75eV.

Chapter 3: Studies on Optimization of Parameters for Vanadium Synthesis in Low Oxidation State

This chapter describes the studies undertaken to optimize the vanadous, V(II) formulation preparation methodology for large scale preparation. Vanadous formulation in a material compatible media is required for decontamination of stainless steel based NPPs namely BWRs and PWRs. The prevalent oxidation states of vanadium are vanadate (VO_2^+) and vandyl (VO^{2+}) in the aqueous medium. The solubility of sodium metavanadate in the formic acid medium is compared with its vanadyl counterpart which is obtained by chemical reduction using hydrazine. V(V) as vanadate and V(IV) as vanadyl ions have been in-situ generated and sequentially concentrated to evaluate the saturation solubilities. Instantaneous solubility was evaluated by turbidimetric and conductivity measurements. Vanadyl ion has shown almost two times higher solubility than the vanadate ion in similar concentration of formic acid. The residual vanadium solubility in the aged solutions was determined by elemental analysis separately. The lower solubility of vanadate in aqueous media is attributed to its deprotonation and associated hydrolysis behavior [14]. The tendency to undergo deprotonation decreases with decreasing oxidation state and hence vanadyl is expected to have higher solubility than that of the vanadate ion in a given aqueous media. A stable solution of 450 mM of vanadyl formate could be prepared by reduction of sodium metavanadate with 225 mM hydrazine in 2.7 M formic acid medium. These solubility studies have been described in the chapter.

Electrochemical route is selective and free of byproducts and hence is the method of choice for synthesizing vanadous formulation in material compatible state. The selection of suitable cathode material is a key factor for electrolytic reduction process. The ease of fabrication of cathode in the required geometry for its subsequent use in the electrolysis cell, safe and easy handling during operation are issues to be addressed while selecting a cathode material. The primary requirement for a good cathode material is to provide high current efficiency for the desired reduction process. The synthesis of V(II) in acidic medium will be affected by the competing proton reduction process as the formal redox potential for hydrogen evolution is more positive than that for V(III)/V(II) redox potential. Thus, a high current efficiency for V(III)/V(II) redox process can only be obtained at electrodes which have high overpotential for hydrogen evolution. Stainless steel and carbon based cathodes (glassy carbon and graphite rod) have been evaluated for the vanadium reduction using potentiodynamic polarization and cyclic voltammetry. Tafel parameters for these electrodes were compared to evaluate the electrochemical kinetics of vanadium reduction. The exchange current density is around five times higher for V(III) on stainless steel (1.268×10^{-6} A cm^{-2}) as compared to that on glassy carbon (2.403×10^{-7} A cm^{-2}). The exchange current density for HCOOH itself is much higher (~23 times) for stainless steel electrode (4.667×10^{-7} A cm^{-2}) as compared to that for glassy carbon (2.039×10^{-8} A cm^{-2}). The increase in exchange current density for V(III) as compared to that for HCOOH is much more on glassy carbon electrode, 11.8 times as compared to 2.7 times for stainless steel electrode. Exchange current density for V(III) has shown two fold increase upon addition of equimolar concentration of HCOOH on stainless steel electrode (2.882×10^{-6} A cm^{-2}) whereas it reduced to less than half on glassy carbon (1.065×10^{-7} A cm^{-2}) for similar acid addition. Thus, carbon based electrodes will give better current efficiency for V(III) reduction in formic acid media. Cyclic voltammetry studies have further elucidated the mechanism of interaction of these electrodes with V(III) in presence of formic acid. The part consumption of current for acid reduction on stainless steel electrodes and blocking of active sites by H^+ adsorption on carbon surfaces was observed in cyclic voltammetric studies. Although electrochemical parameters evaluated for glassy carbon and graphite electrodes were similar, the electrochemical characteristics of graphite electrode were complicated owing to the porous nature of its surface. The electrochemical studies have established that carbon based electrodes will be suited for electrolytic reduction of vanadium in formic acid medium as compared to stainless steel electrode.

Controlled current electrolysis of vanadium in formic acid medium has been evaluated in a two compartment cell. The electrolysis was evaluated for saturation concentrations of V(V) as well as V(IV) solutions. A V(III) precipitate was obtained for both V(V) and V(IV) solutions with saturated concentrations. As the saturation concentration for vanadyl solution (~450 mM) is higher than that of vanadate solution (~250 mM), the product yield is higher for the vanadyl solution. Also it takes lesser time as compared to that for obtaining the product from vanadyl as only single step reduction is involved for vanadyl reduction. The redox potential variation analysis in conjunction with coulometric calculations shows that the precipitation of V(III) compound is governed by both pH and concentration factors. The chemical formula of the product as established by compositional analysis using AAS and IC, TG and FTIR is $V(OH)(HCOO)_2$. The compound dissolves instantaneously in water but a polymeric vanadium compound is subsequently formed which is insoluble in water. The polymerization of dissolved compound depends upon the concentration as well as the aging duration. High concentration solutions undergo polymerization instantaneously while the low concentration solutions undergo polymerization over a period of time. The stoichiometric ratio of the compound and nitrilotriacetic acid (NTA) resulted in a stable aqueous solution upto a concentration of 250 mM. The compound was also dissolved with citric acid in equimolar concentration ratio to evaluate the solubility of V(III)-citrate complex. The complex is highly soluble and a stable concentration of 1 M V(III)-citrate complex could be prepared under inert atmosphere. Solutions with two times citric acid and three times citric acid (molar ratio) have shown exactly the same UV-visible spectral pattern as that of solution of equimolar concentration ratio. This indicates formation of only equimolar V(III)-citrate complex with the present compound. These high concentration V(III) formulations in material compatible composition without any spare/additional chemicals will be highly suited for preparation of the required V(II) formulation for NPP decontamination applications. An electrolytic cell designed for high current can be used for V(II) preparation with a small volume to be handled at the above mentioned concentration levels. Direct electrolysis of vanadate or vanadyl solutions at a maximum concentration of 125 mM also gives V(II) as final product, but with higher volume to be handled and also with the presence of equimolar concentration of Na which will add to the total ionic load of the spent decontamination formulation.

Vanadyl formate has also been reduced with Zn amalgam at high concentration (350 mM). The brown precipitate obtained by the chemical reduction has been found to be a V(II) compound with partial solubility in water. However this compound could be dissolved in a complexing medium of NTA with heating. The proper separation of the solid from the zinc amalgam medium and purification to remove traces of zinc is difficult in this case.

Chapter 4: Redox speciation studies for aqueous vanadium solutions

This chapter describes the methodology developed for redox speciation of aqueous vanadium. A methodology for in-situ monitoring of the electrolytic synthesis of vanadous formate with minimum intervention has been developed. This is based on continuous solution potential monitoring with a redox electrode impressed with a high frequency alternating voltage to overcome polarization of the electrode. The redox potential measurement by the conventional setup has been unsuccessful as the polarization of the platinum redox electrode led to a non responsive readout after some time. The application of high frequency alternating voltage on the electrode by the conductivity meter during the measurement could effectively overcome the polarization. The two pole conductivity meter applies frequency as per the conductivity of solution to avoid polarization. Redox potential measurement using one of the two poles of the conductivity meter against a Ag/AgCl, sat. KCl reference electrode gives a proper response for the entire range of electrolysis.

The redox speciation method for periodic batch samples has also been evolved which is based on simple, rapid and sensitive indirect spectrophotometric measurement. V(V) in solution is evaluated by adding Fe(II) and estimating the Fe(III) formed by the spectrophotometric determination of the sulfosalicylic acid complex. The usual Fe(II) o-phenanthroline method could not be used owing to severe interference of the V(V)/V(IV) redox couple with the iron o-phenanthroline complex. The Fe(III) sulfosalicylic acid complex shows a linear dynamic range for 2 to 10 ppm Fe(III) and the absorption maxima is observed at 510 nm. Vanadium may exist in solution in (II), (III), (IV), or (V) valence state, or as a mixture of any two contiguous valence states during the progress of electrolysis. The redox speciation involves evaluating the V(V) reducing strength of the sample. This is done by converting the sample to V(V)/V(IV) mixture by adding known excess V(V) aliquot to the sample. The residual V(V) is then analysed as described above. Total vanadium concentration in the sample is separately evaluated by completely oxidizing it to V(V) with acidic permanganate and then by repeating the above mentioned analysis. Neither V(IV) nor Mn(II) has shown any interference over a wide range of concentration in the analysis of Fe(III) sulfosalicylic acid complex. The composition of the redox mixture in the sample is then calculated by correlating the V(V) reducing strength of the redox mixture with the total vanadium concentration of the sample.

Direct spectrophotometric determination of V(III) and V(II) solutions has also been evaluated. This is explored to further simplify the analysis of these solutions owing to the highly air sensitive nature of these solutions. V(II) formate has shown two peaks, one at 562 nm and other at 843 nm while V(III) formate has shown a peak at 591 nm and a hump at around 420 nm. The peak positions for the two species are severely interfering at the peak of 562 nm for V(II) and the absorbance for the peak at 843 nm is too low for V(II). Thus, the direct spectrophotometric determination of V(II) and V(III) as formate is not feasible. The V(III)/V(II) solution formed during electrolysis was added to a solution of 0.5 M KSCN in 1 M HCl and the UV-visible spectra was recorded. The complexed V(II) SCN shows a blue shift in the peaks and thus the peak positions for V(II) and V(III) are well resolved in the thiocyanate media. Thus, direct determination of aqueous V(II) and V(III) is feasible in the thiocyanate media in the concentration range of 2-10 mM.

Chapter 5: Chromate sorption over magnetite in presence of gamma irradiation

This chapter describes the effect of gamma irradiation on chromate sorption process over one of the NPP representative oxide, magnetite. Aqueous chromate sorption on suspended magnetite in presence of gamma irradiation has been evaluated. Kinetics of chromate removal was evaluated using Lagergren’s absorption model [15]. Chromate removal with respect to the accumulated dose followed a Lagergren’s pseudo first order kinetic model. A comparison of kinetics of chromate removal with respect to total accumulated dose for gamma irradiation experiment vis-à-vis with respect to time of treatment for different isothermal interactions has been undertaken. Rate constants indicate that the chromate removed per minute in isothermal equilibration at 80 ^{o}C is comparable to the chromate removed per kiloGray of gamma radiation absorbed. The rate constant for isothermal interaction increased from 0.0016 min^{-1} for 40 ^{o}C to 0.0026 min^{-1} for 60 ^{o}C and then to 0.0041 min^{-1} for 80 ^{o}C. The increase in rate constants followed Arrhenius behaviour with temperature. The chromate sorption rate for gamma irradiation varied from 0.0029 kGy^{-1} for the gamma source of 0.2 kGy/h to 0.0042 kGy^{-1} for the gamma source of 3.4 kGy/h and to 0.0047 kGy^{-1} for the gamma source of 4.0 kGy/h. There is a redox interaction between the chromate and the ferrous of the suspended magnetite which was confirmed by XPS analysis. This process reaches a saturation much before the consumption of entire ferrous ions of magnetite indicating a passivating nature of the product. The complete sorption of chromate could not be obtained in these studies although the Fe(II) to chromate mole ratio was kept at 28:1. This is attributed to the formation of passive maghemite (γ-Fe_2O_3) layer on the surface of magnetite. The effect of radiation on both chromate solution and dispersed magnetite to alter the redox process could be ascertained. For varying amount of magnetite, the amount of chromate reduced normalised to the amount of magnetite taken has shown a decreasing trend with the increasing amount of magnetite. This suggests that the chromate reduction on magnetite is a surface phenomenon in the presence of irradiation. Gaussian-Lorenzian peak fittings to the XPS data has been done to evaluate the chemical composition of the deposited chromium and the resultant change in the chemical composition of the iron in the oxide lattice. This indicated that the magnetite equilibrated with chromate under γ irradiation resulted in a different surface composition as compared to the one obtained in absence of γ irradiation. The binding energy of Cr $2p_{3/2}$ showed the presence of Cr^{3+}. However, Cr $2p_{3/2}$ peak-binding energy and peak width was higher than that for the non-irradiated case. It appears that Cr in the irradiated sample is present as different Cr^{3+}-bearing species. Fe 2p peak also showed higher binding energy and broader peak unlike that of the samples of isothermal equilibration with chromate. Cr^{3+} on the surface of magnetite was present in two different compounds, CrOOH and Cr_2O_3. Similarly the presence of FeOOH was also found after fitting the Fe $2p_{3/2}$ spectrum. XPS data indicated the presence of hydroxyl group and oxide group attached to both iron and chromium moieties in case of irradiation whereas only oxide group were seen in only temperature treatment. The O1s peak in case of non irradiated sample is sharp and comparable with peak shape of O1s showed by standard magnetite. But in the irradiated case the O1s peak is broader and indicated the presence of some –OH group in the sample (peak at around 531.5 eV).

Thus, it was found that the redox interaction in presence of γ-irradiation proceed through several different pathways. Prominent presence of hydroxyl group indicates the important role of reducing radicals on the heterogeneous redox interaction.

Chapter 6: Water chemistry control by weak base anion exchanger

This chapter describes the study undertaken to maintain the pH within the specified limits by nitric acid leach out from the nitric acid loaded weak base anion (NLWBA) exchanger. Nitric acid sorption-desorption on weak base ion exchange resin was studied for the removal of $Gd(NO_3)_3$ from solution while maintaining the pH in the range of

5.0 – 5.5. This pH range is required to keep the Gd in aqueous phase without causing any significant corrosion damage of the structural material by the acidic water chemistry. A simple model based on first order dependence for both sorption and desorption has been developed and the experimental data was fitted to the model to deduce the required parameter values. Eluting of nanopure water through various nitric acid loaded weak base resins has shown the leaching of nitric acid from the weak base resin with the leaching of nitric acid following a first order decrease for upto 20% loading of the weak base resin. Elution of nitric acids with varying concentrations through the nitric acid loaded weak base resins has shown that the leach out of nitric acid from weak base resin is a combined effect of mass action and electrostatic repulsion. The equilibrium constants for the 5%, 10%, 20%, 50% and 100% NLWBA mixtures with fresh weak base anion (WBA) exchanger were determined to be 5.8, 7.2, 10.5, 9.2 and 8.7 dm^3 mol^{-1} respectively. The equilibrium constants evaluated for the experiments where nitric acid concentration equivalent to 5%, 10%, 20%, 50% and 100% loading were recirculated through fresh resin were 9.1, 13.5, 20.3, 6.5 and 6.2 dm^3 mol^{-1} respectively. Thus, recirculation experiments with nitric acid have shown that the leaching is governed by the equilibrium effects and the optimum efficiency of weak base resin is obtained when the loading is around 20 %.

A strong acid cation exchanger topped mixed bed of strong acid cation exchanger and weak base anion exchanger column was used to remove $Gd(NO_3)_3$ at 4 and 15 $mgKg^{-1}$ concentrations under a given flow velocity and a given available ion exchange capacity in a recirculation mode. The initial column outlet pH went above the specified limit during the initial period of Gd removal. A mixed bed configuration of same amount of resins has given a wider range of outlet pH as compared to the layered bed. A 5% nitric acid loaded weak base anion exchanger as a bottom layer of the ion exchange column was used to overcome the initial pH rise of the layered bed column outlet by the leach out of nitric acid. This three layer column was effectively removing Gd while maintaining the technical specifications of pH and conductivity.

Chapter 7: Conclusions

This chapter summarizes the important conclusions drawn from the studies discussed in the preceding chapters. The scope of future work in this area of research is also mentioned briefly.

The salient findings and conclusions of the study are given below:

1) Aqueous vanadyl ions have higher solubility than that of vanadate ions in formic acid media.
2) Electrochemical evaluation of carbon based electrode and stainless steel electrodes for selection of better cathode material for aqueous vanadium reduction has suggested that carbon based electrodes are more suited for the application. The evaluation of Tafel plots indicate that a significant part of current is lost in hydrogen evolution by formic acid reduction on stainless steel electrodes while the acid blocks the active sites on carbon electrode resulting in reduction of current density. Thus, a higher current efficiency is obtained for vanadium reduction on carbon based cathode.
3) Controlled current electrolysis of 350 mM aqueous vandyl formate has resulted in precipitation of an ionic V(III) compound. The compound readily dissolves in pure water but subsequently precipitates out as polymer depending upon concentration and ageing duration. However a stable aqueous solution with high V(III) concentration could be prepared from it by adding a suitable complexing agent like nitrilotriacetic acid which results in formation of 250 mM V(III) solution and citric acid which results in formation of more than 1 M V(III) solution.
4) Controlled current electrolysis of vanadate and vanadyl formate solutions with concentrations below 125 mM results in formation of aqueous solution of vanadous formate.
5) Chemical reduction of 350 mM vanadyl formate using Zn amalgam has resulted in precipitation of a vanadous compound.
6) In-situ monitoring of the electrolytic synthesis of vanadous formate based on continuous solution potential monitoring with a redox electrode impressed with a high frequency alternating voltage to overcome polarization of the electrode has been developed.
7) A simple, rapid and sensitive indirect spectrophotometric method has been developed for redox speciation of aqueous vanadium formate solution. Addition of known excess vanadate could convert all contiguous redox couples of vanadium formate into V(V)/V(IV) mixture. V(V) in solution is evaluated by adding Fe(II) and estimating the Fe(III) formed by the spectrophotometric determination of its sulfosalicylic acid complex.
8) Direct spectrophotometric determination of aqueous V(III)/V(II) formate solution could be achieved by adding thiocyanate as complexing agent. V(II) absorption peaks

undergo a blue shift in the thiocyanate media and thereby giving well resolved peaks for the two aqueous vanadium redox species.

9) Chromate reduction on magnetite in presence of γ irradiation follows a Lagergren's pseudo first order kinetic model with respect to the applied dose. The extent of chromate reduction with increasing magnetite amount indicates that the process is a surface phenomenon.
10) XPS data has shown a difference in the surface composition of magnetite equilibrated with chromate due to the effect of irradiation as compared to that of isothermal equilibration.
11) Elution of nano pure water through various NLWBAs has shown that there is a leachout of nitric acid from the NLWBA. The fitting of the experimental data to the first order decrease of the leaching rate has shown a good agreement upto 20% initial loading of the WBA. At higher loadings the leaching follows multiple mode behavior.
12) Recirculation of nitric acid solution through WBA and nano pure water through NLWBAs has shown that the leaching of nitric acid is governed by the equilibrium effect.
13) $Gd(NO_3)_3$ removal using a SAC topped mixed bed of SAC and WBA column led to high column outlet pHs during initial stages of the run.
14) SAC topped mixed bed of SAC and WBA has given better result for Gd removal as compared to a similar composition mixed bed under identical conditions in terms of the pH profile.
15) Use of a 5% NLWBA under the given flow velocity and the given available resin capacity has led to efficient removal of Gd while adhering to the technical specification of pH to remain between 5.0-5.5.

References:

[1] J. A. Ayres, *Decontamination of Nuclear Reactors and Equipments*, Ronald Press, New York, (1970).

[2] K. S.Venkateswarulu, *Water Chemistry - Industrial and Power Station Water Treatment*, New Age International (P) Limited, Publishers, New Delhi (1998).

[3] J. A. Sawicki, *Journal of Nuclear Materials*, 419 (2011) 85.

[4] I. ul Haq, N. Cinosi, M. Bluck, G. Hewitt and S. Walker, *Nuclear Engineering and Design*, 241 (2011) 155.

[5] R. L. Tapping, *Journal of Nuclear Materials*, 383 (2008) 1.

[6] *Coolant Technology of Water Cooled Reactors*, Vol. 3, IAEA, Vienna, October 1992, IAEA-TECDOC-667.

[7] *Decontamination Handbook*, EPRI, Palo Alto, CA: July 1999. TR-112352.

[8] C. J. Wood, *Progress in Nuclear Energy*, 23 (1990) 35.

[9] J. Manjanna, and G. Venkateswaran, *Ind. Eng. Chem. Res.*, 41 (2002) 3053.

[10] V. M. Bhandari, V. A. Juvekar, S. R. Patwardhan, *Ind. Eng. Chem. Res.*, 31 (1992) 1060.

[11] M. G. Segal and R. M. Sellers, *J. Chem. Soc., Faraday Trans.*, 78 (1982) 1149.

[12] K. Kim, H. J. Lee, M. Choi, D. W. Kang and S. Inoue, *Nuclear Engineering and Design*, 229 (2004) 91.

[13] K. Asahi, M. Kitamura, E. Ibe, Y. Asakura, and S. Uchida, *Nuclear Science and Engineering*, 95 (1987) 257.

[14] M. Vijayakumar, L. Li, G. Graff, J. Liu, H. Zhang, Z. Yang and J. Z. Hu, *J Power Sources*, 196 (2011) 3669.

[15] E. Demirbas, M. Kobya, E. Senturk, and T. Ozkan, *Water SA*, 30 (2004**)** 533.

List of Figures

List of Tables

CHAPTER-1

Introduction

Nuclear energy is a clean source of electrical power. Water cooled reactors constitute more than 95% of the total nuclear power plants (NPPs) in the world. The favourable properties of water to be used as the coolant medium varies with temperature and pressure [1]. The natural pH of water decreases with increasing temperature and this makes it a more corrosive medium at higher temperatures. Corrosive coolant in NPPs can lead to several specific issues [2] namely:

- damaging the integrity of the boundaries restricting radioactivity such as fuel clad and primary circuit materials;
- increasing the out-of-core radiation fields, and thus influencing man rem budgeting;
- increasing the formation of deposits, which may reduce the heat transfer and enhance localized corrosion processes.

Thus, the water chemistry control is imperative for achieving a considerable operational life for a NPP. Water chemistry is controlled to minimize contaminant concentration and to mitigate loss of material due to general, crevice, pitting, and flow-accelerated corrosion and cracking caused by stress corrosion cracking (SCC). Water chemistry controls have been specified for the existing water cooled reactors for the different stages like normal operations, startups, shutdown and abnormal operation [3]. For Boiling Water Reactors (BWRs), maintaining high purity of water reduces susceptibility to SCC. For Pressurized Water Reactors (PWRs) and Pressurized Heavy water Reactors (PHWRs), additives are used for reactivity control and to control the pH conditions to inhibit corrosion.

There is always a certain minimum amount of corrosion of structural materials in spite of maintaining optimum water chemistry parameters of the coolant/moderator [4]. The solubilized/suspended corrosion products get activated as they pass through the reactor core and deposit at various locations based on their solubility at a particular temperature and water chemistry regime.

Modified and newer water chemistry regimes have been applied in operating plants to reduce radioactivity buildup, to be able to use extended fuel cycles (higher burnup), and to apply effective remedies for existing corrosion problems (plant life extension). Zinc dosage in PWR and BWR plants, noble metal addition in BWRs, hydrazine dosage to primary coolant in Vado-Vodyannoy Energeticheskiyr Reactor (VVER) plants, optimization of pH and boron/lithium or potassium ions ratio in primary coolant with regard to high fuel enrichment and extended fuel cycles are examples of these modifications. Thus, water chemistry of NPPs is an active field of research which immensely contributes towards their better performance.

This chapter discusses structural materials and water chemistry of water cooled reactors, oxide growth and activity transport issues of NPPs along with general methods of decontamination and the scope of work undertaken in this desertation.

1.1 Structural materials and water chemistry controls of water cooled reactors

The heat transport circuits for water cooled reactors consist of several different structural materials constituting the various components of the circuit. Each component is made up of the best suited material for its functional requirement which includes considerations for requirements of neutron economy, material strength, heat transfer efficiency and corrosion resistance. The selection of material for the components of heat transport circuit has undergone continuous revision based on the experience of operation and development of better materials. The major component changes are the steam generator tubes (from Monel-400 to Incoloy-800), condenser tubes (from admiralty brass to stainless steel 316-L for in land water cooling and aluminum brass and cupronickel to titanium for sea water cooling), Moderator heat exchanger (from cupro-nickel to stainless steel 316-L) and coolant tube material (from zircalloy-2 to zirconium-2.5% niobium) [5]. A brief summary of the components and their structural material for the different types of water cooled reactors is enlisted in **Table 1.1**.

Table 1.1: Major construction material used in coolant circuits

Components	**PWR**	**VVER**	**BWR**	**PHWR**
Reactor Vessel	Low alloy steel pressure vessel clad with austenitic stainless steel	Low alloy steel pressure vessel clad with austenitic stainless steel	Low alloy steel pressure vessel clad with austenitic stainless steel	austenitic stainless steel (calendria)
Coolant Channel (Pressure tubes)	--	--	--	Zircaloy-2 / Zr-2.5% Nb alloy
Fuel cladding	Zircaloy-4	Zr-1% Nb	Zircaloy-2	Zircaloy-2 / 4
Out-of-core piping	Austenitic SS	Ti stabilized SS	Austenitic SS	Carbon steel
Steam Generator tubing	Inconel alloy-600 / Incoloy-800	Austenitic stainless steel	--	Monel-400, Alloy-600 & 800
Pressure tube end fittings	--	--	--	400 series stainless steel

The nature of corrosion product formed in the heat transport circuits of NPPs depend upon the surface area of the structural materials exposed to the medium under the existing dynamic hydrothermal conditions. The major share of surface area in the primary heat transport circuit comes from the steam generator tubes in case of PWRs and PHWRs whereas stainless steel and zircaloy constitute the major share of surface area in case of BWRs [6]. The nature of the corrosion products formed by the interaction of coolant depends upon the composition of the structural materials. The elemental composition of the relevant metal alloys used in water-cooled nuclear reactors is shown in **Table 1.2**.

The different coolant chemistry parameters such as pH, dissolved oxygen, conductivity etc., are maintained based on the compatibility of coolant with the structural material in terms of corrosion and heat transfer efficiency and the type of reactor. Chemistry control for NPPs varies with the designed hydrothermal conditions. While in BWRs the reactor vessel itself acts as a steam generator, in PWRs and PHWRs the primary coolant transfers the acquired fission heat through a set of separate steam generators (SG) to the secondary coolant (light water). Thus, in BWR recirculation system, the coolant exists in two phases (liquid and steam) while in PWRs and PHWRs, the coolant exists in single phase in the primary heat transport system.

A brief design overview of these NPPs and the resulting water chemistry controls is discussed hereunder:

Boiling Water Reactor (BWR): It is a vessel type reactor where light water is used as the coolant medium which concurrently acts as the moderator as well. Water is allowed

Table 1.2: Elemental composition (in wt. %) of relevant alloys

Alloys	SS -304	SS -316	CS	Inconel -600	Incoloy -800	Monel -400	Zircaloy -2	Zircaloy -4	Stellite
Fe	Balance	Balance	Balance	6-10	Balance	1.4	0.07-0.20	0.18-0.24	-
Cr	18-20	16-18	0.012	14-17	19-23	-	0.05-0.15	0.07-0.13	20-33
Ni	8-11	10-14	0.008	Balance	30-35	Balance	0.03-0.08	0.007-0.008	0-13
Sn	-		-	-	-	-	1.2-1.7	1.2-1.17	-
Zr	-		-	-	-	-	Balance	Balance	-
Mo	-	2-3	-	-	-	-	-	-	0-6
Co	-		<0.1	-	-	-	-	-	Balance
Cu	-		-	0.50	0.75	31.5	-	-	-
Zn	-		-	-	-	-	-	-	-
Al	-		-	-	-	-	-	-	-
Mn	2	2	0.03	0.2	1.5	1.0	-	-	-
Ti	-		-	-	0.15	-	-	-	-
C	0.08	0.08	0.08	-	-	-	-	-	-
Si	0.03	1	0.02	0.50	-	-	-	-	-
S	0.75	0.030	0.02	0.015	-	-	-	-	-
P	0.04	0.045	0.01	-	-	-	-	-	-

to boil in core and fission heat is removed from the reactor core by conversion of water to steam. The reactivity is controlled by control rod movement. The principal construction materials employed in the BWR coolant circuit are zircaloy-2 fuel cladding (48% of total coolant circuit area), stainless steel (SS) piping and reactor vessel cladding (44%) and carbon steel (CS) in feed water system (8%) and stellite in pumps and valve shafts. The BWR coolant operates at 270 -285 ^{0}C at near neutral pH (5.5 -7.5). As the coolant undergoes in core boiling, there is very little scope of adding chemicals for chemistry control. However, hydrogen addition, zinc injection and noble metal chemical addition have been introduced in advanced BWRs [7]. In BWRs operating under normal water chemistry conditions, radiolysis of water generates oxygen in concentrations of about 0.2 ppm (DO) in the liquid phase. Thus, in BWRs the oxide deposits are formed under conditions, which are substantially oxidizing. **Fig 1.1** shows the simplified schematic diagram of a single cycle BWR heat transport circuit.

Fig 1.1: Simplified schematic diagram of a BWR

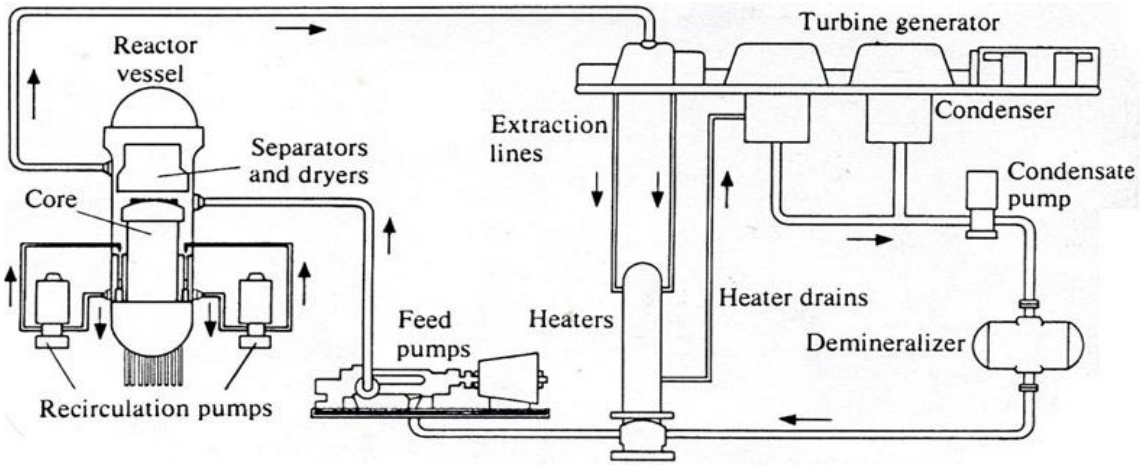

Pressurized Water Reactor (PWR): This is the most popular design among the existing NPPs. This is also a vessel type reactor with same light water being used as coolant and moderator simultaneously. As compared to BWRs, an additional component, steam generator (SG) is introduced in PWRs. This serves as a boundary for maintaining pressure along with containing radioactivity within the primary heat transport circuit.

Here, the coolant is used as a single phase liquid by maintaining a pressure above the saturation vapor pressure for the temperature of operation. This provides the flexibility of better chemistry control in the circuit by addition of required chemicals as compared to BWRs. The reactivity control is also by soluble burnable poison injection like H_3BO_3 or $Gd(NO_3)_3$ (it is also called chemical shim) which results in better fuel clad integrity owing to uniform flux profile as compared to control rods based control which results in a non-uniform flux profile in the reactor core. **Fig 1.2** shows the simplified schematic diagram of a PWR heat transport circuits.

Fig 1.2: Simplified schematic diagram of a PWR

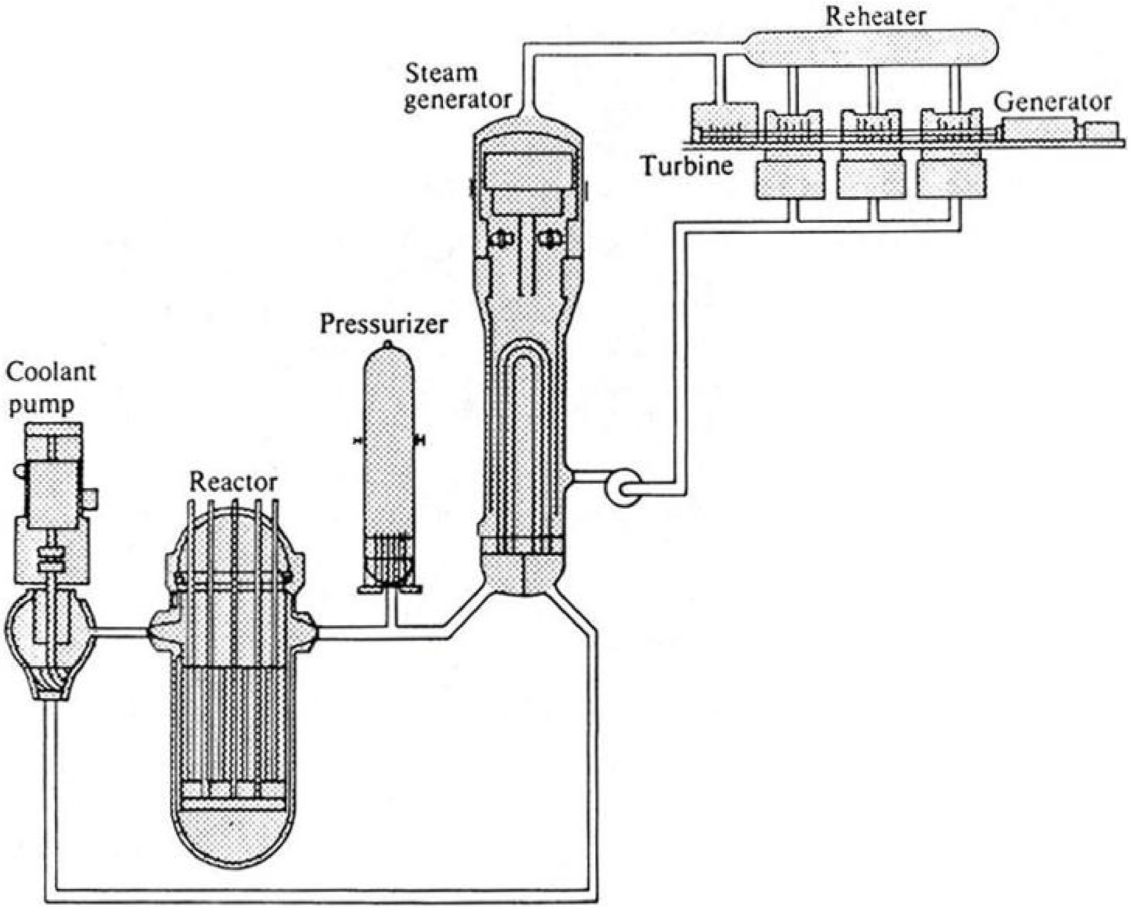

The principal materials in PWR primary circuit are Zircaloy-4 fuel cladding (20%), Inconel-600/800 steam generator tube (75%), SS piping, reactor vessel cladding (5%) and cobalt base alloy as valve seats and hard facing materials. The primary coolant circulating system contains boric acid (~1200 ppm at starting and in operation during the end of the cycle) and lithium hydroxide (0.2 - 2.0 ppm) to maintain pH ~10.5. Hydrogen is added and maintained in the coolant to control oxygen concentration at <0.01 ppm during reactor operation [8]. This creates a reducing atmosphere and thus the oxides on PWR surfaces are formed under predominantly reducing conditions. The system operates at a temperature of 270 - 315 ^{0}C and there is no in-core boiling of the coolant. In PWRs, a large fraction of the primary loop is Inconel-600 / Incoloy-800 and a significant portion consists of SS. Therefore a different kind of film is formed on PWR primary loop surfaces. The film is relatively thin (1-2.5 μm), dense, uniform and is quickly formed initially but later the rate of growth decreases substantially.

Pressurized Heavy Water Reactor (PHWR): The PHWR is among the safest designs of the commercial NPPs. It is a channel type reactor with separate coolant and moderator circuits. Heavy water is used in the primary heat transport circuit as well as moderator circuit. The primary heat transport circuit is the high temperature circuit and hence the chemistry control for minimizing corrosion is practiced in this circuit. The moderator circuit is a low temperature circuit and hence a high isotopic purity heavy water is maintained in this circuit. The neutron poisons for chemical shim is added in moderator as per the operational requirement. The PHWR primary circuit uses several materials such as zirconium alloys for fuel cladding and pressure tubes comprising about 13% of the total surface area of the primary coolant circuit. A large fraction (77%) of primary

Fig 1.3: simplified schematic diagram of a PHWR

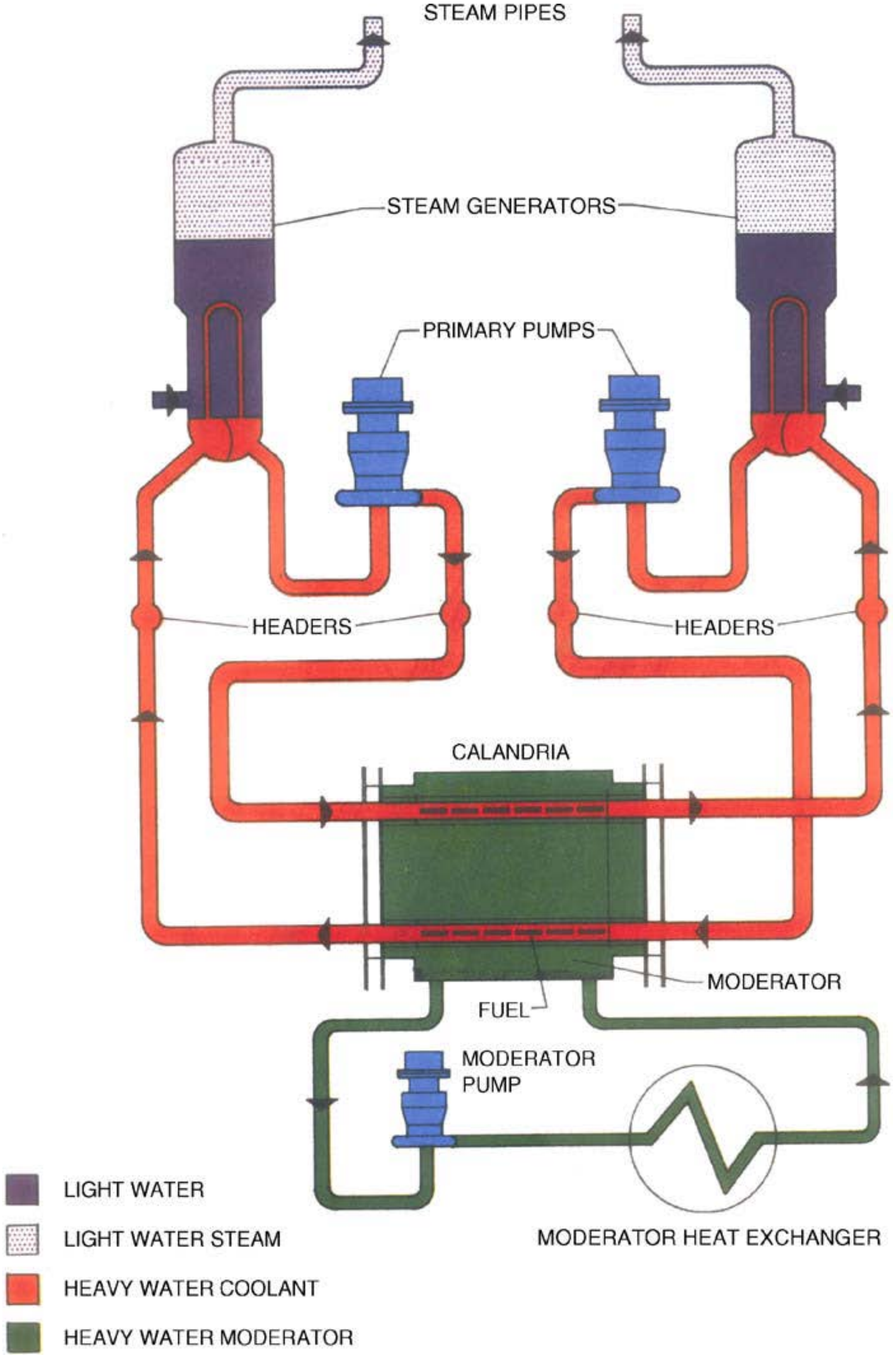

coolant loop is made up of Monel/Incoloy-800 SG tubes, which are used in the SG and other heat exchangers. The use of carbon steel (~10%) for piping and vessel-shells is an inherent feature of the design. The chemistry of the primary coolant in PHWR resembles that of PWR in the sense that in both alkaline and deoxygenated conditions are maintained. The major difference is that in PHWRs the chemical shim control of reactivity is confined in a separate moderator circuit by addition of soluble neutron poisons like boron or gadolinium. The coolant does not contain any neutron poison and its pH is ~ 10.5, as measured at room temperature [9]. **Fig 1.3** shows the moderator and coolant circuit of primary system of a typical PHWR.

1.2 Oxide growth and activity transport in nuclear power plants

1.2.1 Corrosion products of iron in aqueous medium

Iron is the major constituent of the coolant circuit and thus its corrosion products play an important role in deposit formation. Ferrous hydroxide is the initial product resulting from the interaction of water with iron at low temperatures [2]:

$$\mathrm{Fe} \longrightarrow \mathrm{Fe}^{2+} + 2\mathrm{e}^{-} \qquad (1.1)$$

(Anodic reaction)

$$2\mathrm{e}^{-} + 2\mathrm{H_2O} \longrightarrow 2\mathrm{OH}^{-} + \mathrm{H_2} \qquad (1.2)$$

(Cathodic reaction in absence of oxygen)

$$2e^{-} + 1/2O_2 + H_2O \longrightarrow 2OH^{-} \quad (1.3)$$

(Cathodic reaction in presence of oxygen)

The ferrous hydroxide initially formed decomposes into hematite and magnetite at high temperatures:

$$2Fe(OH)_2 \longrightarrow Fe_2O_3 + H_2 + H_2O \quad (1.4)$$

$$3Fe(OH)_2 \longrightarrow Fe_3O_4 + H_2 + 2H_2O \quad (1.5)$$

At lower temperatures ferrous hydroxide disproportionates into magnetite and iron (eq. 1.6) which is formed as an intermediate unstable species, reacts with water to give magnetite (equation 1.8).

$$4Fe(OH)_2 \longrightarrow Fe_3O_4 + Fe + 4H_2O \quad (1.6)$$

The iron formed reacts with water to generate H_2. Also, in the presence of oxygen, magnetite is directly formed by ferrous hydroxide:

$$Fe(OH)_2 + ½\, O_2 \longrightarrow Fe_3O_4 + 3H_2O \quad (1.7)$$

It has also been reported that magnetite may be formed directly from iron in an aqueous environment under deaerated conditions at temperatures above 60 ^{0}C.

$$3Fe + 4OH^{-} \longrightarrow Fe_3O_4 + 2H_2O + 4e^{-} \quad (1.8)$$

$$4H_2O + 4e^{-} \longrightarrow 4OH^{-} + 2H_2 \quad (1.9)$$

The rate of formation of magnetite by Schikorr reaction (1.5) becomes significant at a temperature of ~ 185 ^{0}C and almost instantaneous at 215 ^{0}C and above [10]. The protective quality and the overall rate of growth of the magnetite coat depends mainly on the temperature, dissolved oxygen content and pH of the water. The possible species of iron in aqueous environment are summarized in **Scheme 1.1**.

Scheme 1.1 Possible oxidized species of iron under aqueous environment

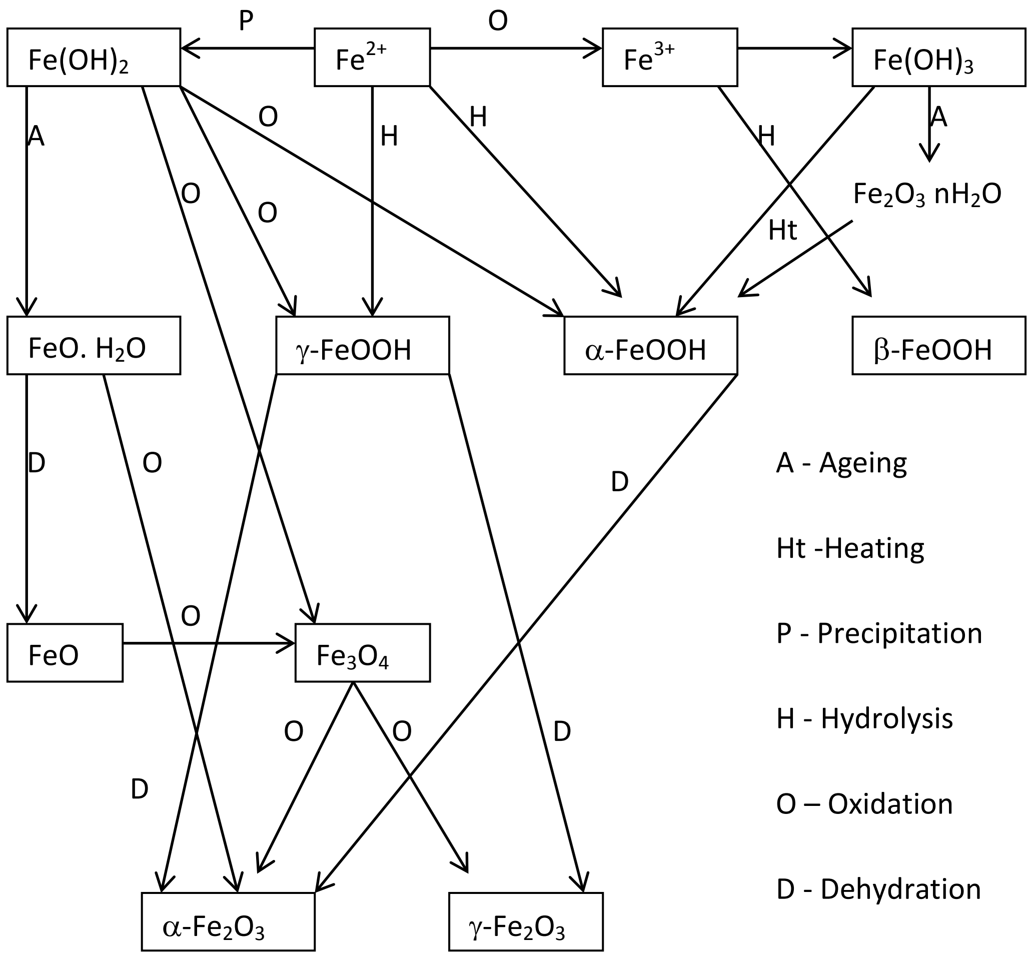

Thus the factors that most strongly influence the types of corrosion film are the structural materials and the coolant chemistry environment. The corrosion film is also affected by the presence of other structural materials [11].

1.2.2 Process of deposition of corrosion products

The interaction of high temperature coolant with structural materials results in the formation of corrosion products with incorporation of varying degree of substitutional elements released from the different alloys. The thickness, composition, protective nature, porosity and elemental depth variation of deposits also depend on water chemistry condition during reactor operation. Consolidation model has been used to explain the process of deposition. Turner and Klimas derived a consolidation model based on a two-layer deposit with a labile portion and a consolidated portion [12]. It assumed that the portions interacted with each other, leading to the model expression. Lister and Cussac have shown that transients behave differently from steady accumulations in case of bulk boiling [13]. They have proposed a comprehensive model which included microlayer evaporation, particle filtering through rings of deposit, particle trapping at the surface of growing bubbles, and an increase in concentration at bubble nucleation sites by a pumping action as bubbles deposit are considered.

In general, the oxide film formed on the inner surfaces of primary system can be considered to be of two types: the ‘grown-on’ protective oxides which are usually thick but strongly adherent to the base metal (inner layer) and the loose ‘deposited’ oxides which overlay the grown oxide (outer layer). Generally grown-on oxide constitutes the thin inner layer of the oxide deposit. In the case of PWR/ BWRs, grown-on oxides are chromium rich (due to SS) having spinel structure like $FeCr_2O_4$ and $NiFe_2O_4$ [14]. Typical layers of corrosion products found on the BWR/ PWR/ PHWR primary circuits and SG (PWR/PHWR) is pictorially described in **Fig 1.4**.

Fig 1.4: Nature of oxides formed on the BWR, PWR and PHWR primary circuits and steam generators

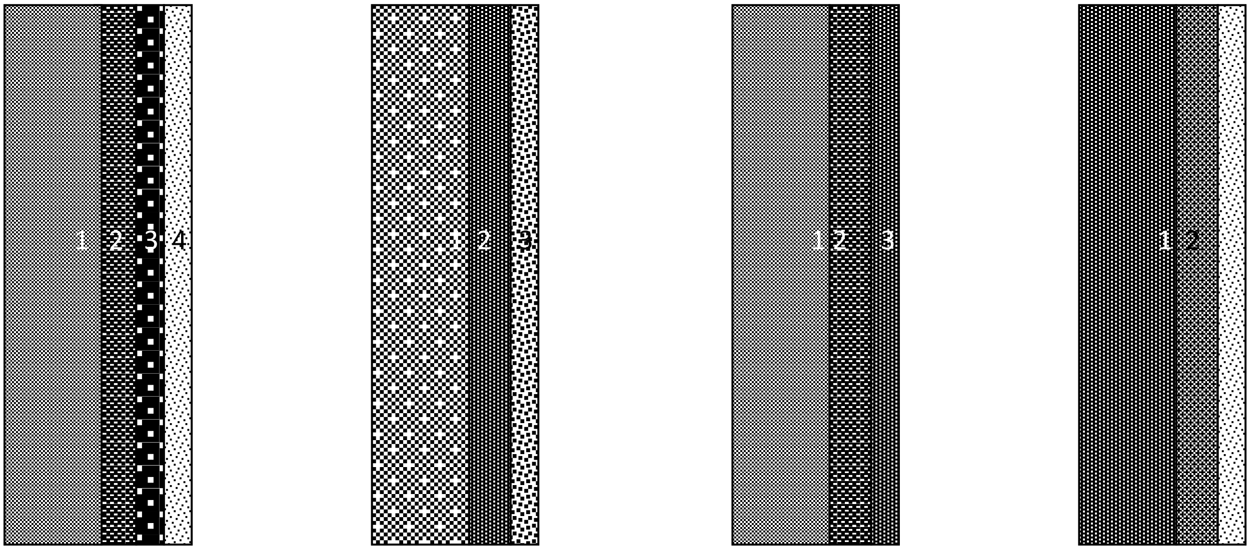

(**1**=> Base Metal **2**=> Inner layer **3**=> Outer layer **4**=> Outermost layer)

(BWR Primary circuit)	(PHWR Primary circuit)	(PWR Primary circuit)	(Steam Generator)
1. Stainless steel (SS)	1. Carbon steel (CS)	1. Stainless steel (SS)	1. Monel-400, Inconel-600, and Incoloy-800
2. $FeCr_2O_4$, Cr_2O_3	2. Fe_3O_4	2. $FeCr_2O_4$, Cr_2O_3	2. $FeCr_2O_4$, Cr_2O_3
3. $NiFe_2O_4$, Fe_3O_4, $Fe_{2-x}Cr_xO_3$ $(2<x<0)$, $Ni_xFe_{3-x-y}Cr_yO_4$ $(x \leq 1, y \leq 1)$	3. Mainly Fe_3O_4 and to some extent $NiFe_2O_4$	3. Fe_3O_4, $NiFe_2O_4$, $Fe_{2-x}Cr_xO_3$ $(2<x<0)$, $Ni_xFe_{3-x-y}Cr_yO_4$ $(x \leq 1, y \leq 1)$	3. $NiFe_2O_4$, $Ni_xFe_{1-x}Cr_2O_4$ $(x \leq 1)$, Fe_3O_4, Cu_2O, CuO.

Although the exact chemical composition of the oxide can vary from system to system and within the same system from one location to another, some generalizations are possible. In the case of PHWRs, the deposits on the CS surfaces are largely made-up of Fe_3O_4 and very minor amount of nickel ferrite. An oxide (mostly magnetite) film of 40-50 μm thickness had been observed on the CS surfaces that have seen about 10 years of operation. On the other hand, in the case of BWRs and PWRs, the reactor vessel and the piping surfaces in the primary circuit are made-up of SS-304, cladded carbon steel and the oxide deposits on these surfaces are a mixture of Fe, Cr and Ni containing spinels / inverse spinels oxides.

1.2.3 Radiation field build-up

The soluble as well as particulate matter (crud) released from the base metal pass through the reactor core along with the coolant. During their passage through the core, the nuclides of the corrosion products undergo neutron activation (thermal and fast neutron) due to the presence of high neutron flux in the core, resulting in the generation of activated corrosion products (ACPs). These ACP can get redeposited on the out-of-core surfaces; thereby causing radiation exposure to the personnel involved in the maintenance tasks in the primary heat transport system areas [15]. The fission products (FPs), most of which are radioactive and are formed during the operation of nuclear power plant, are commonly contained within the fuel clad and are released only if the clad develops a defect.

Table 1.3 shows some of the major contributing ACPs and FPs. Although, a big list of radionuclide is identified as contaminants, in most of the reactors ^{60}Co ($t_{1/2}$ 5.27 y, γ 1.17 and 1.33 MeV) and ^{58}Co ($t_{1/2}$ 71.3 d, γ 0.811 MeV) with their long life and high gamma energies are dominant among all the activated corrosion products and are of potential concern [16].

Table 1.3: Prevalent radionuclides found in primary heat transport circuits of NPPs

Radio-nuclides	$t_{1/2}$ (days)	Source (generation)
Corrosion products		
^{60}Co	1900	^{59}Co(n,γ)
^{58}Co	72	^{58}Ni(n,p)
^{51}Cr	273	^{50}Cr(n, γ)
^{59}Fe	45	^{58}Fe(n,γ)
^{54}Mn	310	^{54}Fe(n,γ)
^{65}Zn	244	^{64}Zn(n,γ)
^{124}Sb	60	^{123}Sb(n,γ)
Fission Products		
^{144}Ce	290	U(n,f)
^{95}Zr	63.3	U(n,f) & ^{94}Zr(n,γ)
^{140}La	-	U(n,f)
^{95}Nb	35	^{95}Zr$\rightarrow$ (β^- decay)
^{137}Cs	11000	U(n,f)
^{106}Ru	365	U(n,f)

Based on a study made from the data collected from different nuclear power plants, the contribution to the personnel exposure from various isotopes are

^{60}Co, ^{58}Co	80-85 %
^{59}Fe, ^{54}Mn, ^{51}Cr	5-10 %
Fission products	10 %

1.2.4 Mechanism of Radioactivity build-up

Radionuclides are incorporated in the surface oxide layer by several mechanisms. The major routes of radionuclide incorporation in oxide layer are [17]:

Direct corrosion reaction: Oxide formation by the direct corrosion reaction of the base metal with the aqueous medium can be represented as:

$$3\,Fe + 4\,H_2O \rightarrow Fe_3O_4 + 4\,H_2 \qquad (1.10)$$

$$2\,Fe + Co + 4H_2O \rightarrow CoFe_2O_4 + 4\,H_2 \qquad (1.11)$$

Ion-exchange Mechanism: These are decided by the site preference energies and the lattice stabilization brought out by ion exchange.

$$[Fe^{3+}]_t\ [Fe^{2+}Fe^{3+}]_o\, O_4 + Co^{2+} \rightarrow [Fe^{3+}]_t\ [Co^{2+}Fe^{3+}]_o\, O_4 + Fe^{2+} \qquad (1.12)$$

Adsorption: The charge acquired by the oxide surface is responsible for electrostatically attracting an oppositely charged species in solution causing its adsorption onto the oxide surface. This can be represented as $\zeta = k\,(pzc - pH)$ where ζ is the zeta potential on the oxide surface which is a measure of the surface charge, ‘pzc’ is the pH at which the oxide surface shows zero charge and pH defines the experimental H^+ concentration in solution. A typical adsorption can be represented as

$$-M-H + Co(OH)^+ \rightarrow -M-O-Co(OH) + H^+ \qquad (1.13)$$

The adsorbed species can subsequently undergo an ion-exchange process with the rest of the oxide, thereby resulting in bulk incorporation of exchanged metal-ion. This of course depends on the lattice stabilization brought about by the exchange process.

Co-precipitation: The corrosion product existing in coolant can get deposited onto the base metal as a result of solubility/super solubility consideration. The subsequent interaction of the deposited species with the oxide surface depends on the thermodynamic stabilization brought as a result of such interaction. Otherwise the surface will contain a mixture of different metal ions.

Isotopic exchange: An inactive metal ion in the oxide surface can undergo isotopic exchange with its active isotope in solution. For e.g.

$$[Fe^{3+}]_t\ [Co^{2+}Fe^{3+}]_o\, O_4 + {}^{*}Co^{2+} \leftrightarrow [Fe^{3+}]_t\ [{}^{*}Co^{2+}Fe^{3+}]_o\, O_4 + Co^{2+} \qquad (1.14)$$

Particulate Deposition: The settling of suspended particles due to gravity in no or low flow areas such as surge tank and dead legs causes localized build-up of hotspots of radioactivity.

Among the above processes, the direct corrosion reaction contributes in a major way to corrosion product build-up especially on new surfaces while particulate deposition is the least dominant mechanism.

1.3 Minimizing and control of radiation field in primary heat transport systems

Radiation exposure to operating staff directly depends on the radiation dose level of the coolant systems. The nuclear regulatory agencies such as International Commission on Radiation Protection (ICRP) and in India, Atomic Energy Regulatory Board (AERB) have prescribed the limits to which personnel manning nuclear facilities can be exposed to radiation. Currently, the prescribed limits are 100 mSv for 5 years individual exposure and should not exceed 30 mSv in any calendar year during the 5-year block [18].

Steps to control the buildup of radiation fields are taken right from the design and commissioning stages of the plant apart from those at regular operational stages. The methods being considered/followed during design, operation and maintenance of water-cooled nuclear reactors for man-sievert reduction and plant life extension are enlisted hereunder [19].

- Adopting stringent measures in selection and specification of construction materials resulting in reduction of cobalt inventory in the primary coolant system. Culmonoy, is being considered as substitutes for stellite.

- Stringent coolant chemistry conditions to minimize the corrosion product formation, deposition on the fuel and their subsequent release into out of core surfaces.

- Designing a purification system with a very short clean-up half-life.

- *Electro-polishing*: Electro-polishing of some of the components leaves a very smooth microstructure on the surface, resulting in significant reduction in radiation field build-up. Electro-polishing of channel heads in steam generators has been developed for PWR and PHWRs applications.

- *Hot conditioning*: At the commissioning stage, pre-filming of structural material by controlled corrosion process before achieving nuclear heat helps in minimizing the activity transport.

At the operational level, following are the important procedures being practiced.

- Replacing the defective fuel as soon as the defect is detected in the case of PHWRs, where there is on-line refueling facility.

- *Controlling Coolant chemistry*: Controlling chemistry parameters at different stages such as operation, during power ramping (increasing or decreasing reactivity of the core) and during reactor shut down is important to reduce the corrosion damage and subsequent release and redeposition of radioactivity on the out-of-core surfaces.

- The control of [Ni]/ [Fe] concentration in the feed water to ≤ 0.2 is helpful in controlling the radiation fields in the initial stages of newly commissioned BWRs. The concentrations of Ni and Co species diminish in reactor water with such control. This ratio [Ni]/ [Fe] ≤ 0.2 is achieved by iron injection at the condensate extraction pump discharge.

- Use of high quality purification circuit to remove soluble (ionic) and particulate (0.1-10 μm) form of ACPs through ion exchange and filtration unit.

- *Metal ion passivation (Zn/ Mg addition to coolant)*: Metal – ion passivation is a relatively nascent field of research with the aim to control the rate of radiation field buildup. The beneficial action of Zn and / or Mg is that, these ions can effectively incorporate into protective oxides (Fe_3O_4, $NiFe_2O_4$ and $FeCr_2O_4$) and make them even more compact and adherent while inhibiting the incorporation of unwanted radionuclide such as ^{60}Co.

- *Hydrogen injection and Noble-metal addition (Pt/Rh):* Hydrogen injection with and without noble metal passivation has been developed to mitigate the Inter-Granular Stress Corrosion Cracking (IGSCC) of BWR components. The method is based on the catalytic recombination of the radiolytically produced O_2 and H_2O_2 with H_2 to form H_2O on metal surface, thereby achieving electrochemical potential of (-300 mV vs. SHE) on the surface of stainless steel. Noble metal passivation lowers the hydrogen injection levels achieving the same benefits of concentration, but achieved with much lower H_2 addition. Noble metal passivation is a palliative to the reactor fence ^{16}N problem faced with regular Hydrogen Water Chemistry (HWC).

- *Chemical Decontamination*, which is a curative step, involves the quantitative dissolution of oxide matrix containing radionuclide using suitable formulations/ reagents without affecting the base metal. This method has been proved to be an efficient and advantageous among the various methods mentioned above. In BWRs, a reasonable decontamination (> 80% radioactivity removal) is achieved if the outer layers are removed, and the same trend is observed in PHWRs too.

1.4 Decontamination

In the case of water-cooled nuclear reactors, contamination on out of core surfaces, viz. the inside surfaces of pipes and equipment through which the coolant/moderator water (or heavy water) flows dominate the person-sievert problem. Periodic decontamination procedure by means of chemical dissolution of the outer oxide layer of the structural surfaces is practiced to address this issue in operational NPPs [20]. Experience has shown that in a typical PHWR, in a single decontamination campaign about 150 to 300 Kg of iron has been removed to completely decontaminate the full system (the entire PHT system, volume, ~ 70,000 liters).

The decontamination procedures may be broadly divided into two main groups:

[1] Physical or Non-chemical Decontamination procedures and

[2] Chemical Decontamination procedures.

1.4.1 Physical/ Non-chemical decontamination procedures

Depending on the end-purpose and the system to be decontaminated, one has a choice of several methodologies developed over the past 2-3 decades. These can be broadly classified as

⇒ Mechanical cleaning methods like brushing, wiping, ultrasonic cleaning etc

⇒ Steam blasting

⇒ Cleaning using abrasives such as use of water jet, or dry ice pellets (propelled by jet of CO_2) with or without admixtures like glass beads, quartz beads, B_2O_3 or other abrasive materials.

The usefulness of physical methods is restricted since a pre-condition for these is the accessibility of the surface to be treated. Besides, these processes tend to abrade not only the protective oxide film but also the base metal, thereby roughening the surface and aiding the subsequent penetration of radioactive nuclides into the base metal. Apart from the disadvantages of inaccessibility of area of intricate geometry, application of physical methods is generally limited to external surfaces.

1.4.2 Chemical decontamination procedures

Chemical decontamination, involves the dissolution of the radioactive deposits on the surfaces of alloys using specially developed chemical formulations. It aims at reducing the radiation field by dissolving the oxide film on the system surfaces without any appreciable attack on base metal. Since, selective removal of radionuclide from the oxide film is not possible, complete removal of the protective host film is the only way by which radionuclides can be removed from the system [21]. Chemical decontamination has the unique advantage of cleaning surfaces of different sizes, geometry and at various locations both accessible and inaccessible. Chemical decontamination methods can be classified into two types namely

(a) Hard-chemical decontamination and

(b) Soft-chemical decontamination

Hard-chemical Decontamination:

Hard chemical decontamination is the chemical procedure for removing oxide layers completely using strong chemical formulations. These methods are based on the use of concentrated reagents (6 - 10% w/v) such as redox reagents (Ce^{3+}/Ce^{4+}) in the presence of mineral acids (e.g. nitric/sulphuric acid), and can accomplish complete removal of oxide layers. The major drawback of hard chemical decontamination is its excessive corrosive nature besides generation of large quantities of radioactive wastes. This kind of decontamination is normally carried out during the decommissioning of certain component or in those cases where the corrosion is not the serious concern.

Soft-chemical decontamination:

Soft decontamination procedures are based on the use of dilute chemical reagents (typically 0.1% w/v of dissolved chemicals) such as reducing/oxidizing agents, chelating agent and organic acids to bring about only partial dissolution of the oxide layers. Hence, the treatment period required has to be longer. These methods are generally less corrosive in nature and generate lesser volume of radioactive wastes.

Conventionally, the end result of a decontamination process is expressed in terms of the Decontamination Factor (DF) achieved by the campaign.

DF = dose rate before decontamination/ dose rate after decontamination

i.e. the ratio of radiation field at a particular location before and after the decontamination. DF is normally calculated for the selected points in a system/pipe-work, excluding the background radiation level. A plot of DF vs. activity removed will yield an exponential plot suggesting the high DF values do not mean high activity removal. Achieving a DF of 2-10 is often acceptable as DF = 10 correspond to removal of 90% radioactivity.

1.5 Oxide Dissolution

Oxide dissolution in a solution can be interpreted in terms of extent of under-saturation of solution with respect to the oxide. The factors that influence the rate of dissolution are temperature, composition of solution phase (pH, redox potential, concentration of acids, reductants and complexing agents etc.) and the properties of the oxide (specific surface area, stoichiometry, crystal symmetry, presence of defects etc.) [22]. Additives in solution adsorb on the oxide and affect the energy of attachment between the surface ions and those of the interior. Iron oxide dissolution can proceed through several pathways:

(1) Acid dissolution ⇒ attack the sub lattice oxide ions (O^{2-}) with protons

(2) Reductive / Oxidative dissolution ⇒ attack the cations of the sub lattice with reductants/oxidants.

1.5.1 Acid Dissolution

The strong affinity of protons with the structural oxide ions assist in the release of iron from the oxide lattice. Acids dissolution is described through adsorption of proton by the surface OH group, resulting in weakening the Fe-O bond which finally leads to labilizing the iron from the oxide lattice [23].

In the case of hematite or magnetite, the formal stoichiometry for the acid/ non-reductive dissolution reaction can be shown as:

$$Fe_2O_3 + 6H^+ \longrightarrow 2Fe^{3+} + 3H_2O \quad (1.18)$$

$$Fe_3O_4 + 8H^+ \longrightarrow 2Fe^{3+} + Fe^{2+} + 4H_2O \quad (1.19)$$

Studies have shown that in the case of many oxides the acid attack is rather slow. Even at very high concentrations (6-10%), the dissolution was significantly slow on oxides containing few at. % of chromium/nickel and no dissolution was obtained with nickel ferrite [24]. Also, use of mineral acid is not desirable in the system as it can lead to corrosion problem as well as disposal problem. Hence, in operating nuclear reactors, no such dissolution is being carried out.

1.5.2 Reductive / Oxidative Dissolution

Since most of the corrosion products found in primary system of water-cooled reactors are iron/nickel/chromium-containing oxides which exhibit variable valency states, they are amenable for reductive/oxidative dissolution. The redox dissolution was found to be advantageous (faster kinetics) over conventional acid based slow dissolution.

Reductive Dissolution:

Reducible metal oxides can undergo dissolution by four general pathways in acidic aqueous solution: proton-assisted (acid), ligand-promoted, reductive, and ligand-promoted reductive dissolution [25]. Reductive dissolution of iron oxides involves adsorption of the reducing agent on the surface of oxide. This is followed by the fast inner or outer sphere electron transfer resulting in formation of Fe^{2+} at the interface. The processes subsequent to the reduction of the surface Fe^{3+} ions, i.e. the actual dissolution reactions involve terrace-ledge-kink mechanism. The driving force for the disruption of the oxide surface and the ejection of Fe^{2+} ions into the bulk solution is the increase in size of iron ions on reduction (crystallographic radii for the high-spin ions are 0.75 Å for Fe^{2+} and 0.65 Å for Fe^{3+}), and the increased electrostatic repulsion between the electron clouds of the iron ions and the adjacent O^{2-} ions [26]. There are many reducing agents with redox potential sufficiently negative to bring about reduction of Fe^{3+} in the oxide lattice. The standard reduction potential for a number of reducing agents is given in **Table 1.4**. These can be broadly classified into four categories:

- reducing agents based on organic acids such as formic, citric, oxalic, ascorbic acids etc.
- inorganic reducing agents such as hydrazine, sodium dithionite etc.

- reduced metal ions (Low Oxidation state Metal Ion LOMI) such as Fe^{2+}, V^{2+}, Cr^{2+}, etc. Further, the redox potentials of these metal ions can be modified by complexation with chelating agents.
- reducing radicals generated radiolytically such as hydrated electron (e^-_{aq}), hydroxy isopropyl radicals, [$(CH_3)_2COH$] etc.

Table 1.4: Standard Redox potentials (written using reduction potential convention) of some of the reagents suitable for use in decontamination formulations

Reducing agents	E^0 in V (*v/s*. SHE)	Reducing agents	E^0 in V (*v/s*. SHE)
Hydrazine	-0.23	e^-_{aq}	-2.7
Formic acid	-0.40	Cr^{2+}_{aq}	-0.41
Thioglycolic acid	-0.23	Cr(II)-EDTA	-0.99
Gallic acid	-0.44	Cr(II)-bipyridil	-0.12
Oxalic acid	-0.23	V^{2+}-formate	-0.26
Ascorbic acid	0.27	V(II)-picolinate	-0.41
Sodium dithionate	-0.40	Fe^{2+}_{aq}	+0.77
Propane-2-radicals	-1.25	Fe(II)-EDTA	+0.12
		Fe(II)-oxalate	+0.21

The formulation employed for reductive dissolution also contains suitable chelating agent to keep the reduced metal ion in solution by complexation [27]. The stability constant values of complexes from various chelating agents, which are common ingredients of decontamination formulations, with some of the metal ions present in the corrosion product, are shown in **Table 1.5**.

Table 1.5: Stability constant values of different metal ions with the some of the ligands

Metal ion species	Log K at 25 ^{0}C			
	Picolinic acid (ML_3/ $M.L^3$)	EDTA (ML/ M.L)	NTA (ML/ M.L)	Citric acid (ML/ M.L)
Fe^{2+}	11.3	14.3	8.84	3.1
Fe^{3+}	12.8	25.1	15.8	12.5
Ni^{2+}	17.22	18.5	11.3	5.1
Cr^{3+}	14.0	23.4	>10	-
Cu^{2+}	7.4	18.7	12.7	13.2
Co^{2+}	14.1	16.3	10.6	5.0
Ce^{3+}	-	15.9	10.9	3.2
La^{3+}	-	15.5	10.4	6.2
Zr^{4+}	-	29.9	20.8	-

Oxide dissolution of austenitic stainless steel structural materials:

The austenitic stainless steel pipework in BWRs and PWRs result in formation of substituted ferrites like $Fe_{2-x}Cr_xO_3$, $Fe_xCr_yNi_zO_4$ ($x+y+z = 3$) etc. on the surface. The outermost oxide layers on these pipeworks are mainly Ni and Cr substituted ferrites. These oxides show poor dissolution behaviour in concentrated acids or in the presence of strong complexing agents [28]. Such oxides have shown better dissolution efficiency in the V(II) formulations as compared to organic acid based complexing-dissolution formulations. Vanadous formulations create a stronger reducing condition as compared to the organic acid based reducing agents. These formulations are used directly or in combination of oxidizing pretreatment step of alkaline permanganate/acidic permanganate depending upon the concentration of Cr in the oxide layer. Dissolution of representative oxides such as $NiFe_2O_4$ in vanadous formulation has indicated that the reaction at the particle surface is the rate determining step and the species reacting at the surface is the vanadous complex. The dissolution is triggered by the rapid outer sphere electron transfer from vanadous ion to the ferric ion in the surface. Vanadous based formulations are qualified for application of decontaminating entire reactor system owing to the superior material compatibility characteristics of these formulations [29].

Oxidative dissolution:

Normally oxidative dissolution is employed for chromium oxides and chromium-rich iron oxides such as MCr_2O_4 ($M=Fe^{2+}$, Ni^{2+}, Co^{2+} etc) [30]. It involves the oxidation of Cr^{3+} in the oxide lattice to Cr^{6+}, which is generally done using acid/alkaline permanganate reagents, hydrogen peroxide, ozone etc. In the case of chromium containing oxides, the oxidative dissolution / treatment result in chromium depletion in the residual oxides, thereby facilitating the subsequent reductive dissolution. Permanganate based oxidative dissolution is most commonly practiced. Most of the time the effectiveness of permanganate depends on the nature of metal surface (e.g. CS, SS, Incaloy etc) being treated, since MnO_2 can deposit on these surfaces based on the surface charges and prevent further action of reagent by forming a barrier. Thus, during the decontamination of reactor components, once the oxidative dissolution step is over, the system has to be cleaned up before applying the reductive dissolution step.

1.6 Decontamination chemical/ reagent requirements

1.6.1. Ion-exchange behavior / regenerative mode of dissolution

In nuclear industry the removal of spent decontamination formulation i.e. metal ions as well as the constituents of the formulations is predominantly practiced using ion exchange resin. In regenerative dilute chemical decontamination process, the ion exchange resins do the additional job of regenerating the formulation by continuously removing the metal ions and activities from their complexes and releasing the complexants and the H^+ ions back to the system for further decontamination / dissolution of oxide deposits [31]. Strong acid cation exchange resins are used for regeneration and mixed beds are used for finally removing constituents of formulation at the end of decontamination.

Major constituent of the formulation used for decontamination are carboxylic acids or amino carboxylic acids that exist mostly in anionic form. However, a fraction of the amino carboxylic acid can be protonated by the organic acids present in the formulation and hence can exist in cationic form. This results in the removal of these species by the cation exchange resin in regenerative decontamination process. Though the loss of ion exchange capacity due to the pick – up of formulation constituents is not significant, the decrease in the chemical concentration of the constituents that is removed leads to decreased dissolution. Detailed studies carried out on this phenomenon showed that DTPA, EDTA, PA and HEDTA are removed in large quantities. The extent of adsorption is minimum for NTA and PDCA.

The order of selectivity of metal ions (by ion exchange resin) observed in non-complexing medium is reversed in complexing medium. For instance, the trivalent metal ions (e.g. Fe^{3+}, Cr^{3+} etc) have poor selectivity and lower apparent capacity than divalent metal ions in complexing medium. Chromium (III) and iron (III) ions are not at all removed by the cation exchange resin in EDTA and in most other complexant media. For divalent ions the capacity value decreases with increase in stability constant of the complex formed. Cu^{2+} and Ni^{2+} have low apparent capacity because of the high stability of the complexes (with EDTA, see Table 1.5) and Co^{2+} ion has relatively high capacity.

In the case of conventional LOMI formulations (non-regenerative), attempts are being made to make the LOMI process a regenerative process by an ingenious method. The spent LOMI is allowed to pass through an electrolytic cell consisting of three-electrode compartments [32]. The central compartment is separated from the other two by cation exchange membrane and is filled with IX resins. The metal ions dissolved by LOMI reagent pass to the cathode compartment through the cation membrane and are reduced to its metallic form and the regenerated LOMI goes back to the system. This way the active waste is reduced to an ultimate low volume solid waste.

1.6.2 Consideration of radiolytic degradation

During the full system decontamination (including reactor core), the formulation chemicals get exposed to radiation. This leads to a loss of formulations and at times results in the generation of various degradation products including reactive transient species [30]. The extent of decomposition depends on the duration of exposure and also the time elapsed between the reactor shut down and the decontamination. It has been observed in the laboratory experiments that citric acid resists decomposition when it is present along with EDTA and ascorbic acid. Also, the presence of aromatic ring in the constituents of formulations (for instance picolinic acid, pyridine dicarboxylic acid etc) increases their stability. Irradiation also results in in-situ generation of low oxidation state metal ions in the presence of stable complexing agents and thus aiding the decontamination process when such reagents are used for the purpose [33].

1.6.3 Material compatibility considerations

Structural material integrity is a primary concern for any chemical addition in the nuclear power plants (NPPs). Decontamination formulations too have to fulfill this criterion. The composition of decontamination formulation has undergone continuous modification to address this issue. The shift from oxalic acid based CITROX process to

LOMI based formulations is based on the material compatibility concerns [34]. This was based on the laboratory observations of inter granular attack (IGA) of oxalic acid on sensitized stainless steel.

Certain inhibitors (e.g. Rodine 92B) and some times surfactants (e.g. Triton X-100) are being added to the formulation to protect any base metal loss (wall thinning). However, this depends on the nature of formulations / systems being treated. Conventionally filming amine based inhibitors are found very effective (even at 50 ppm level), and are easy to remove both on cation / anion exchange resin during regeneration step. It is reported that even sulfur-based inhibitors can be employed safely since the removal process has been proved to be effective.

1.7 Present scenario of operational decontamination processes

The decontamination processes practiced for chemical decontamination can be classified into three categories depending upon their mode of action

1. Strong single electron transfer based reducing agents e.g. Low Oxidation state Metal Ions (LOMI) containing formulations.
2. Formulations based on the mixture of chelating agents (e.g. EDTA, NTA etc.) and organic acid (e.g. oxalic acid, citric acid, ascorbic acid etc), which may also be reducing in nature. Processes such as CORD, CAN-DEREM, CAN-DECON, DOW NS-1, EDF-EMMA, are some of such processes.

3. Oxidant based formulations which contain alkaline/ acid permanganate e.g. APAC, APOX, MOPAC processes. These are generally used for removing Cr from the oxide and are usually used in combination with 1 or 2.

1.8 Scope and objectives of the present work

The water chemistry studies undertaken in the present work are related to the decontamination of stainless steel based NPPs viz. BWRs and PWRs along with the application of ion exchange resins for maintaining the specified water chemistry regime.

A methodology to synthesize the strong reducing agent namely V(II) on large scale is imperative for undertaking decontamination of stainless steel based NPPs. Major part of the present work is related with the studies on optimization of the synthesis of V(II) based formulation. This included evaluating maximum solubility of the suitable precursor solutions, studies for optimization of electrolytic route of V(II) preparation, synthesis and characterization of different oxidation state vanadium solids, development of redox speciation methodology for quantification of different redox mixtures of aqueous vanadium redox mixtures along with studies related with chromate sorption over magnetite in the presence of gamma irradiation and chemistry control methodology development by nitric acid leaching from weak base anion exchange resin column. These are briefly mentioned below.

1.8.1 Maximum solubility studies for aqueous V(V) and V(IV) formate solutions

V(V) or V(IV) solutions are the stable precursors available for synthesis of V(II) formulations. V(V) formate could be obtained by direct addition of formic acid to sodium metavanadate solution while V(IV) formate was obtained by chemically reducing the V(V) formate by hydrazine addition. Maximum solubility of aqueous V(V) and V(IV) formate solution has been evaluated by gradually increasing the concentration with conductivity and turbidity monitoring. This is the primary step for optimizing the process of V(II) synthesis as ideally the synthesis should begin with the maximum concentration of precursor.

1.8.2 Optimization of electrolytic synthesis route for V(II) preparation

Electroreduction of aqueous V(V) or V(IV) precursor solutions in the material compatible formulation is the most suitable route for preparation of V(II). Electrolysis provides flexibility of selecting the reaction media along with avoiding any by-products addition during the synthesis process. Controlled current electrolysis using two compartment cell has been used for V(II) preparation. The primary objective of the study has been to optimize the time of electrolysis. The selection of suitable cathode material for achieving high current efficiency for the process, evaluation of maximum concentration of precursor solution feasible for electroreduction to V(II) and evolving better precursors as per the results has been studied.

1.8.3 Synthesis and characterization of different oxidation state vanadium solids

Different solids of vanadium have been prepared by aqueous route in the formic acid medium. The vanadium compounds were obtained for all known aqueous vanadium oxidation states viz. V(V), V(IV), V(III) and V(II). The compounds were obtained by preparing aqueous saturated solutions of the different oxidation states of vanadium through various routes. The compounds were characterized for the chemical composition, oxidation states, thermal stability, structural information and formation of aqueous complexes with suitable ligands namely nitrilotriacetic acid (NTA) and citric acid.

1.8.4 Redox speciation method development for quantification of aqueous vanadium redox mixtures

Vanadium exists in aqueous solution as V(II), V(III), **V**(IV), or V(V), or as a mixture of any two contiguous valence states. As mentioned earlier, the lower oxidation states are air sensitive and hence the synthesis of lower oxidation state aqueous vanadium compounds require continuous monitoring to ensure inert atmosphere in the experimental setup. Thus redox speciation of aqueous vanadium is an essential prerequisite for efficient synthesis of lower oxidation state aqueous vanadium compounds.

Spectrophotometric determination of aqueous vanadium is the method of choice when rapid redox speciation is required [35]. However, direct spectrophotometric determination of vanadium suffers from poor sensitivity and selectivity. Extraction to organic phase followed by spectrophotometric determination using suitable chromophores is normally practiced to improve sensitivity and selectivity [36, 37]. Catalytic spectrophotometric methods are also used for sensitive spectrophotometric determination of V(V) [38]. However, these methods require extensive processing of the sample, maintaining specific concentration ratio of reagents and providing specific reaction conditions for good result. A modified method used by King and Garner [39] has been used for spectrophotometric redox speciation. The vanadium samples are initially analysed for total V(V) reducing strength. This is done by converting the sample to

V(V)/V(IV) mixture by adding known excess V(V) solution. Also, another aliquot of the sample is completely oxidized to V(V) by acidic $KMnO_4$ [40]. Redox interaction of V(V) with Fe(II) is known to be instantaneous in acidic aqueous medium and has been used to evaluate the V(V) concentration [41]. The same route but with the estimation of Fe(III) by the established spectrophotometric Fe(III)-sulfosalicylate complex method [42] has been followed. The figures of merit has already been evaluated for the method [43]. The interference of V(IV) and Mn(II) on the method has been evaluated as these ions will be a part of the sample matrix. Direct spectrophotometric method for V(III)/(II) speciation based on thiocyanate complex formation is also explored.

Redox potential monitoring has been explored for on-line measurement during electrolytic preparation of lower oxidation state aqueous vanadium compounds. Solution potential monitoring with a redox electrode impressed with a high frequency of 1.13 kHz, 10 mV alternating voltage to overcome polarization of the electrode has been evolved for evaluating the progress of electrolysis.

1.8.5 Chromate sorption over magnetite in presence of gamma irradiation

Chromate reduction on various iron oxides has been evaluated in several studies [44]. Chromate has been used as a corrosion inhibitor for various applications where iron based alloys are the structural materials [45]. In the shutdown cooling heat exchanger (closed system) in reactor systems such as BWRs, chromate is still in use as the corrosion inhibitor. Under certain operational conditions this chromate can come into primary coolant recirculation circuit and can interact with the iron oxide bearing surface of the structural materials. Here, the presence of ionizing radiation will be an important parameter to be accounted for the interaction of chromate with the iron oxides. Structural modification of the oxide surface of the recirculation system due to concomitant presence of chromate and irradiation is of immense importance. One of the important implications of the chromium bearing oxide surface is modification in the chemical formulation to be employed for decontamination of the recirculation system.

Magnetite is one of the representative oxides formed on the structural material surfaces. Effect of gamma irradiation on the heterogeneous chemical interaction of chromate with the magnetite has been studied and it has been compared with the isothermal interactions at various temperatures.

1.8.6 Water chemistry control by weak base anion exchanger

Soluble burnable poison in the moderator has been selected for reactivity control during startup and shutdown (secondary shutdown system) of the 540 MWe pressurized heavy water reactors (PHWRs) in India. Gadolinium nitrate in heavy water moderator is used for the purpose. As a secondary shutdown tool Gd is used at 15 mg kg^{-1} concentration in the moderator system. The pH range of operation for this system is specified to be 5.0 - 5.5. The upper limit for pH is restricted to avoid any precipitation of Gd in the system [46] and the lower limit is fixed to maintain the material compatibility of the different structural materials of the composite moderator system [47]. Colloidal hydroxide/hydrous oxide/oxide formation has been reported for rare earths in the pH range of 4.5 to 6.0 at relatively much higher concentrations by forced hydrolysis [48]. The concentration of Gd in moderator system is maintained by direct addition from the secondary shutdown system as $Gd(NO_3)_3$ for increasing the concentration or by removal through ion exchange columns. Removal of Gd involves a mixed bed of strong acid cation exchanger (SAC) and weak base anion exchanger (WBA). WBA is used to avoid any precipitation of Gd as $Gd(OH)_3$ due to removal of nitrate prior to Gd^{3+} removal on SAC. During the removal of Gd through such a column, in the initial stages the pH at the outlet of the column goes above 5.5 and remains above 5.5 for about one half life of recirculation through the column. However, the bulk moderator system pH remains within the specified limit throughout the run. Feasibility of maintaining the pH of the ion exchange column outlet within the specified limits of the bulk moderator system by the leach out of nitric acid from the weak base resin of the column has been studied. The leachout characteristics of nitric acid from weak base resin as a function of nitric acid loading and initial inlet concentration at a particular flow rate is evaluated. Based on the evaluation of leaching from the nitric acid loaded WBA, a column configuration is suggested for maintaining the column outlet pH within the specified limits during the Gd^{3+} removal from the moderator system.

1.9 References

[1] S. V. Lishchuka, N. P. Malomuzh, P. V. Makhlaichuk, *Phys. Lett. A*, 375 (2011) 2656.

[2] W. E. Berry, R. B. Diggle, *EPRI NP-522* (1979).

[3] *Coolant Technology of Water Cooled Reactors*, Vol. 1, IAEA, Vienna, September 1992, IAEA-TECDOC-667.

[4] *Corrosion in Nuclear Engineering*, W.E. Berry John Wiley & sons, 1971.

[5] Y. S. R. Prasad, Proc. of *The National Symposium of Water and Steam Chemistry in Power Plants and Industrial Units* (SWACH-2000), Mumbai, Feb 23-25, 2000, pp 1-9.

[6] D. Ferrett, G. C. W. Comley, *IAEA-TECDOC-356*, 67 (1985).

[7] S. E. Garcia and C. J. Wood, *International Conference on Water Chemistry of Nuclear Reactor Systems*, (NPC 08), Berlin, 2008, Paper L4-1.

[8] *Optimization of Water Chemistry to Ensure Reliable Water Reactor Fuel Performance at High Burnup and in Ageing Plant* (FUWAC), IAEA, Vienna, October 2011, IAEA-TECDOC-1666.

[9] S. S. Bajaj and A. R. Gore, *Nucl. Eng. and Design*, 236 (2006) 701,

[10] G. Schikorr, *Z. Elektrochem*., 35 (1929) 65.

[11] Y. L. Sandler, *Corrosion*, 35 (1979) 205.

[12] C. W. Turner and S. J. Klimas, *Proc. Engineering Foundation Conference on Heat Exchanger Fouling, Davos*, 2001, pp. 19–26.

[13] D. Lister and F. Cussac, *Heat Transfer Engineering*, 30 (2009) 840.

[14] R. Riess and K. Lundgren, *Crud in PWR/VVER and BWR Primary Circuits*, LCC-2 Special Topic Report, ANT International, 2006.

[15] *Modelling of Transport of Radioactive Substances in the Primary Circuit of Water-Cooled Reactors*, IAEA, Vienna, March 2012, IAEA-TECDOC-1672.

[16] R. A. Shaw, *Nucl. Technol.*, 44 (1979) 97.

[17] G. Venkateswaran, Proc. of *The National Symposium of Water and Steam Chemistry in Power Plants and Industrial Units* (SWACH-2000), Mumbai, Feb 23-25, 2000, pp 20-33.

[18] *International Basic Safety Standards for Protection against Ionizing Radiation and for the Safety of Radiation Sources*, Safety Series No. 115, IAEA, Vienna, 1996.

[19] *Coolant Technology of Water-cooled Reactors: An Overview*, Technical Report Series No. 347, IAEA, Vienna, 1993.

[20] *Decontamination Handbook*, EPRI, TR-112352, Palo Alto, CA: July 1999.

[21] J. A. Ayres, *Decontamination of Nuclear Reactors and Equipments*, Ronald Press, New York, 1970.

[22] J. L. Smee, '*Dissolution Characteristics of Metal oxide in Water cooled Reactors in Decontamination and Decommissioning of Nuclear Facilities*' (Ed. Marilyn, M) Osterhout, Plennum Press, NY. 1980.

[23] R. M. Cornell and R. Giovanoli, *Clay Minerals*, 28 (1993) 223.

[24] M. G. Segal, T. Swan, *Water Chemistry of Nuclear Reactor Systems 3*. BNES, London, (1983) 187.

[25] M. D. S. Afonso, P. J. Morando, M. A. Blesa, S. Banwart and W. Stumm, *J. Colloid and Interface Sc.*, 138 (1990) 74.

[26] M. G. Segal and R. M. Sellers, *J. Chem. Soc., Faraday Trans.*, 78 (1982) 1149.

[27] A. B. O'Brien, M. G. Segal, *J. Chem. Soc. Faraday Trans I*. 83 (1987) 371.

[28] D. G. Wickham, *Inorg. Synth.*, 9 (1967) 152.

[29] D. Bradbury, M. G. Segal, T. Swan, G. C. W. Comley, D. J. Ferrett, *Nucl. Energy*, 20 (1981) 403.

[30] T. Swan, M. G. Segal, W. J. Williams, M. E. Pick, *EPRI-NP 5522M*, USA, 1987.

[31] A. L. Rufus, S. Velmurugan, S. K. Padma, V. S Sathyaseelan, S. V Narasimhan, P. K. Mathur, *Nucl. Technol.*, 122 (1998), 228.

[32] P. M. Tucker, *Nuclear Engineering International*, 38 (1993) 18.

[33] R. M. Sellers, *Radiat. Phys. Chem.*, 21 (1983) 295.

[34] C. J. Wood, *Progress in Nuclear Energy*, 23 (1990) 35.

[35] M. J. C. Taylor and J. F. van Staden, *Analyst*, 119 (1994) 1263.

[36] C. Agarwal, M. K. Deb, R. K. Mishra, *Analytical Letters*, 23 (1990) 2063.

[37] S. A. Abbasi, *Analytical Letters*, 9 (1976) 113.

[38] M. R. Shishehbore and R. Jokar, *Anal. Methods*, 3 (2011) 2815.

[39] W. R. King, and C. S. Garner, *J. Phys. Chem.*, 58 (1954) 29.

[40] C. L. Rulfs, J. J. Lagowski, and R. E. Bahor, *Anal. Chem.*, 28 (1956) 84.

[41] H. Willard and P. Young, *Ind. Eng. Chem.*, 6 (1934) 48.

[42] K. Ogawa and N. Tobe, *Bull. Chem. Soc. Japan*, 39 (1996) 223.

[43] D. G. Karamanev, L. N. Nikolov, V. Mamatarkova, *Minerals Engineering*, 15 (2002) 341.

[44] M. L. Peterson, A. F. White, G. E. Brown, G. A. Parks, *Environ. Sci. and Technol.*, 31 (1997) 1573.

[45] E. McCafferty, M. K. Bernett, J. S. Murday, *Corr. Sci.*, 28 (1988) 559.

[46] P. Sasikumar, K. Shivakamy, A. L. Rufus, V. K. Mittal, S. Bera, S. Velmurugan, S. V. Narasimhan, *Power plant chemistry*, 9 (2007) 34.

[47] G. T. Chandler and M.H. Anderson, *WSRC-MS-91-502* (1991).

[48] E. Matijevic, *United States Patent 5015452* (1991).

CHAPTER-2

Experimental Methods

2.1 Introduction

The description of the synthesis routes, experimental setups used for water chemistry studies, equipment and techniques used in these studies is provided in this chapter. The water chemistry studies undertaken in the present work involved designing and fabricating a two compartment electrochemical cell for preparation of V(II) formate, setting up a recirculation loop with an ion exchange column for studying water chemistry control using ion exchange bed, synthesizing different vanadium formate solids. Solution studies to evaluate maximum solubility of V(V) and V(IV) precursor aqueous solutions involved periodic conductivity and turbidimetric measurements along with gravimetric measurements for V(IV) solutions. Instrumental techniques used in this work involve the analytical characterization instruments such as UV-visible spectrophotometry, atomic absorption spectrophotometry (AAS), ion chromatography (IC) along with other solid characterization instruments such as x-ray diffractometer (XRD), Fourier Transform Infrared Spectroscopy (FTIR), thermogravimetry (TG) and X-ray photoelectron spectroscopy (XPS). Electrochemical characterization of electrodes was done using the potentiostat / galvanostat having FRA (frequency response analyser) module. The brief description of these setups and the instrumental methods used in this work is presented below.

2.2 Description of the electrolytic cell

Controlled potential electrolysis was carried out in a specially designed and in house fabricated cell of borosilicate glass. This cell is having two compartments separated by an anion exchange membrane. Approximately one liter capacity cell with 750 ml cathode compartment solution (catholyte) and ~60 ml anode compartment solution (anolyte) was used. The cell is designed in a vertical cylindrical fashion. The outer cylinder is the cathode compartment in which the anode compartment goes from the top lid in a concentric arrangement. An anion exchange membrane was placed at bottom of the anode compartment to separate the catholyte and the anolyte. The cathode rested at the bottom of anode compartment below the anion exchange membrane. Graphite felt is used as cathode material and stainless steel mesh is used as anode material. They face each other and distance between the cathode and anode was kept at minimum to achieve maximum current efficiency for the process. Cathode and anode were connected to dc power supply unit using insulated wires. The design of the two compartment electrolytic cell is shown in **Fig 2.1**. IOLAR nitrogen was purged through both cathode and anode compartment during the electrolysis to maintain inert atmosphere in cathode compartment and to provide a sweeping effect to remove the carbon dioxide from the anode which is produced during electrolysis and gets deposited on the anode thereby polarizing the anode. Oxygen at 2 ppm level is present in the nitrogen gas used for deaeration as impurity. Oxygen trap arrangement was used to remove this oxygen. The V (II) formate was used in oxygen trap because it is a strong reducing agent that can reduce dissolved oxygen to water thereby resulting in highly pure N_2 entering the electrolysis cell. Zinc amalgam in acidic medium was used in oxygen trap to reduce the V(III) to V (II). In the designed cell, there is a problem of locked air in between the membrane and

Fig 2.1: Design of the two compartment electrolysis cell separated by an anion exchange membrane

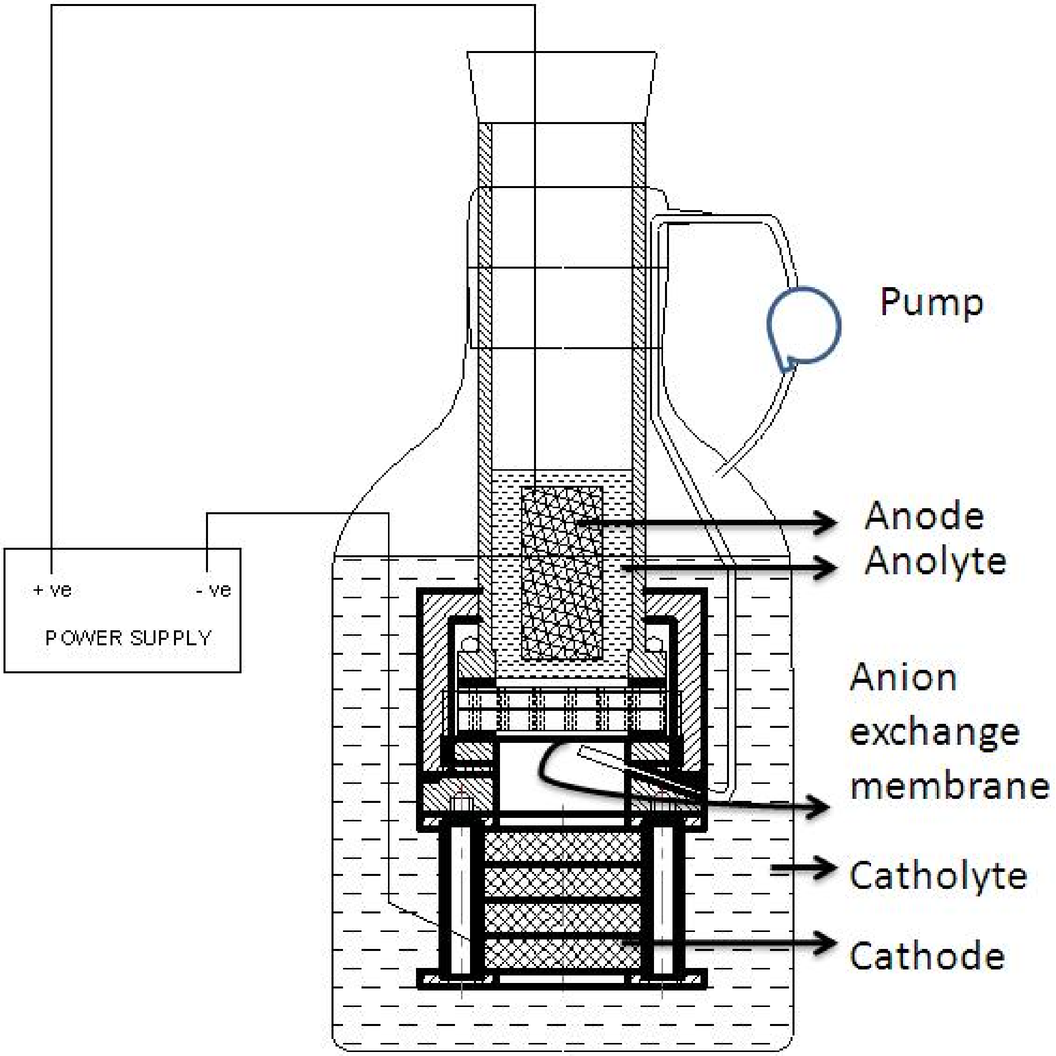

the nut tightening it from the cathode compartment side to avoid any leakage of the anode compartment solution in the cathode compartment or vice versa. This locked air results in electrical isolation of anolyte and catholyte and thereby disturbing the current flow path. A provision for pumping out this locked air is made by providing a circulation arrangement which additionally provides hydrodynamic convection and hence improved current efficiency. The cathode potential was measured between cathode terminal and reference electrode placed in a luggin probe filled with a conducting solution of sodium formate. The luggin probe goes close to the surface of the cathode in the cathode compartment solution. Cooling arrangements were provided in both cathode and anode compartment to remove the heat from the solution since the membrane is having a maximum operable temperature limit of 50 ^{o}C. Copper tube was used for cooling the cathode compartment by wrapping it around the cathode compartment because of its high thermal conductivity. Stainless steel was used for the cooling in anode compartment. This tube was electrically insulated from the anode.

2.3 Simulated moderator purification system setup for gadolinium removal studies

An experimental set up has been designed and fabricated to simulate the moderator purification system of the Indian 540 MWe PHWRs, Tarapur Atomic Power Station (TAPS 3&4). The flow velocity of the system was simulated in the laboratory setup along with the lower bed volume (BV) and empty bed contact time (EBCT) as compared to the actual system. Empty bed contact time (EBCT) and bed volumes (BV) are usually employed in the evaluation of fixed-bed column’s performance [1]. BV is defined as:

BV =Volume of treated solution/Volume of resin (2.1)

EBCT is defined as:

EBCT = L/u (2.2)

Where, L is the column length and u is the solution velocity. Simulated laboratory setup of the moderator purification system of TAPS 3 & 4 is shown in **Fig 2.2**.

Fig 2.2: Simulated setup of the moderator purification system of TAPS 3 & 4

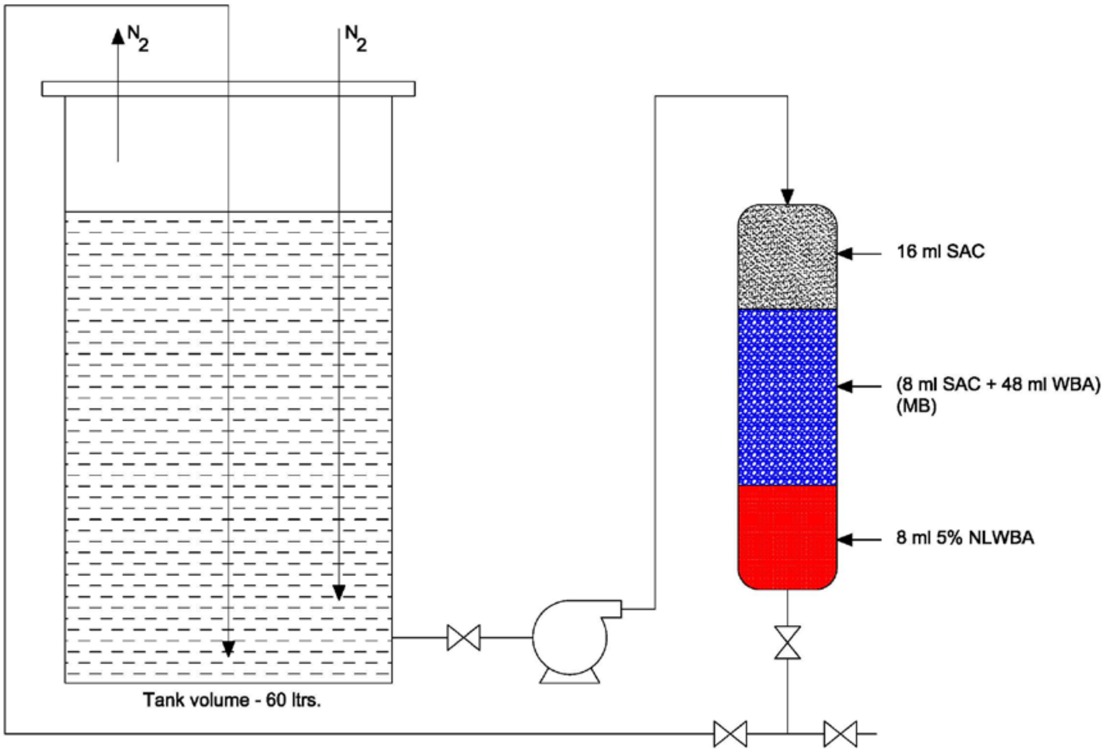

The moderator inventory is 2,66,363 l of heavy water while the ion exchange columns have a volume of 200 l. In the laboratory studies, 60 l of 4 and 15 mg kg^{-1} solution of $Gd(NO_3)_3$ at pH 5 was circulated through 80 ml resin column. The column consisted of 16 ml strong acid cation exchanger (SAC) (Auchtel duolite ARC 9351 in H^+ form with macroporous polystyrene matrix, sulfonic acid functional group, and exchange capacity of 1.8 meq ml^{-1}) topped mixed bed of 8 ml SAC and 48 ml weak base anion exchanger (WBA) (Auchtel duolite ARA 9369 WBA with macroporous polystyrene matrix, tertiary amine functional group, and total exchange capacity of 1.4 meq ml^{-1}) as such and in another experiment, a similar column with a bottom packing of 8 ml of 5% nitric acid loaded weak base anion exchanger (NLWBA) mixture with fresh WBA. Thus, the bed volume of the experimental setup was almost half of that in the reactor. This system has been used to study the water chemistry control using ion exchange resins.

2.4 Synthesis of different oxidation state vanadium formate solids from aqueous solution

Sodium metavanadate (AR grade, from S D Fine Chem. Ltd.) and formic acid (ca. 90 %, AR grade from S D Fine Chem. Ltd.) have been used to obtain various vanadium compounds. Sodium metavanadate has been selected for the study owing to its good solubility in water. It is also stable compound as compared to its ammonium analogue [2]. Formic acid is selected to satisfy the criteria of a material compatible product which can be used in nuclear power plants without having any adverse effect on structural materials. The solids for each known stable oxidation state of vanadium have been obtained from the above mentioned precursor from the aqueous solution. A saturated solution of vanadium in the required oxidation state has been prepared through the feasible route and the precipitate obtained subsequently was filtered and taken for characterization.

Saturated solution of V(V) could be directly obtained by mixing $NaVO_3$ and formic acid solutions in a molar ratio of 1:2 or higher. Metavanadate converts to vanadate by protonation as shown below:

$$NaVO_3 \rightarrow Na^+ + VO_3^- \quad (2.3)$$

$$VO_3^- + 2H^+ \rightarrow VO_2^+ + H_2O \quad (2.4)$$

Vanadate is known to undergo precipitation at higher concentrations [3] as per the following equation:

$$V_2O_5\,(s) + 2H^+\,(aq.) \leftrightarrow 2VO_2^+\,(aq.) + H_20\,(l) \quad (2.5)$$

Thus, at higher concentrations, V_2O_5 could be precipitated out through the aqueous route. The yield of V_2O_5 has been found to depend upon the concentration of formic acid in the solution.

V(IV) solution was obtained by chemical reduction using hydrazine in acidic medium. This reduction is feasible only at a high temperature of almost 80 ^oC and at almost twice the required concentration of hydrazine as per the following reaction.

$$VO_2^+ + 2H^+ + e^- \rightarrow VO^{2+} + H_2O \qquad E^o = 1.00V \text{ vs. NHE} \quad (2.6)$$

$$VO_3^- + 4H^+ + e^- \rightarrow VO^{2+} + 2H_2O \qquad \text{(overall reduction process)} \quad (2.7)$$

$$N_2H_4 \rightarrow N_2 + 4H^+ + 4e^- \qquad E^o = 0.23 \text{ V vs. NHE} \qquad (2.8)$$

The stoichiometry of the above process was established experimentally. Hydrazine can provide one H^+ out of four required by sodium metavanadate for reducing to VO^{2+}. When the formic acid was stoichiometrically three times the sodium metavanadate concentration, the chemical reduction of V(V) could not be completed even after a period of more than 24 hours whereas when the formic acid added was four times the sodium metavanadate concentration, the V(V) reduction was instantaneous as indicated by the change in the color of the solution and the corresponding change in the solution potential.

Hence, the total process during this reduction can be expressed as:

$$4NaVO_3 + 12HCOOH + N_2H_4 \rightarrow 4HCOONa + 4VO(HCOO)_2 + N_2 + 8H_2O \qquad (2.9)$$

Executing the above reaction at sufficiently high concentration of vanadium resulted in precipitation of blue colored vanadyl formate which was filtered, washed and taken for subsequent characterization.

V(III) solution could be obtained by electroreduction of either V(V) or V(IV) formate solutions. Electrolysis of solutions of higher concentrations (above 150 mM) has resulted in precipitation of a V(III) formate solid. This green colored solid was filtered and washed before characterization.

V(II) solution could be obtained by electroreduction of either V(V) or V(IV) formate solutions below 125 mM concentration. It can also be obtained by reduction of either V(V) or V(IV) formate solutions by zinc amalgam. Reduction of high concentration of V(IV) formate solution (ca. 350 mM) using zinc amalgam has resulted in precipitation of a brown colored V(II) formate solid which was also characterized after filtering, washing and drying.

2.5 Instrumental techniques

2.5.1 Ultraviolet - Visible Spectrophotometry

UV - visible Spectroscopy is used in the quantitative determination of solution of transition metal ions and highly conjugated organic compounds. Molecules absorb UV-visible light to undergo an electronic transition from the ground state to excited electronic state. The electronic transition follows certain selection rules. UV absorptions are generally broad because vibrational and rotational levels are associated with the electronic levels. A beam of light from a visible and/or UV light source is separated into its component wavelength by a prism or diffraction grating. Monochromatic beam in turn is split into two equal intensity beams by a beam splitter. One beam, the sample beam (colored), passes through a transparent cuvette containing a solution of the compound being studied in transparent solvent. The other beam, the reference (coloured), passes through an identical cuvette containing only the solvent. The intensities of these light beams are then measured by electronic detectors and compared. The intensity of the reference beam, which should have suffered little or no light absorption, is defined as I_0. The intensity of the sample beam is defined as I. The Beer-Lambert law states that the absorbance of a solution is directly proportional to the solution path length b and the concentration c of the absorbing species.

$$A = -\log_{10} (I / I_0) = \varepsilon \cdot c \cdot l \qquad (2.10)$$

Where A is the measured absorbance, I_0 is the intensity of the incident light at a given wavelength, I is the transmitted intensity, l the path length of the beam through the sample and c the concentration of the absorbing species. For each species and wavelength, ε is a constant known as the molar absorptivity or extinction coefficient.

Application in present work: UV-visible spectra was acquired for the aqueous solutions in a 10 mm path length quartz cuvette with a scanning speed of 200 nm/min using Jasco-V 700 UV-visible spectrophotometer. UV-visible spectrophotometry has been extensively used in the present work in analysing the solution composition of the transition metal ions. It has also used been used to evaluate the oxidation states of various redissolved vanadium formate solids. The analysis methods used in this study were ferric analysis as ferric sulfosalicylic acid complex, direct vanadium analysis as V(III)/V(II) thiocyanate complex, chromate analysis as Cr(VI) s-diphenyl carbazide complex and gadolinium analysis as Gd arsenazo(III) complex.

Ferric forms a red colored complex with sulfosalicylic acid and its wavelength of maximum absorbance (λ_{max}) is 465 nm. The pH of the analysed solution was maintained at 4.5 using acetic acid-sodium acetate buffer. This complex shows a linear dynamic range for 2 to 10 ppm Fe(III) [4].

Direct spectrophotometric method for V(III)/V(II) speciation based on thiocyanate complex formation has been developed. Well separated peaks for V(II) and

V(III) are obtained with $K_4[V(II)(SCN)_6]$ having a maxima at 724 nm while $K_3[V(III)(SCN)_6]$ having a maxima at 595 nm in highly acidic solution (ca. 0.5 M HCl). The thiocyanate complex shows a linear dynamic range for 2 to 10 mM V(III)/V(II) solution.

Chromate forms a reddish violet complex with s-diphenyl carbazide in acidic media with absorption maximum (λ_{max}) at 540 nm. The analysis is done in 1M H_2SO_4 media. This complex shows a linear dynamic range for 0.2 to 1 ppm Cr(VI) [5].

Gadolinium forms a violet colored complex with arsenazo (III) in acidic media having absorption maximum (λ_{max}) at 650 nm. The complex shows a linear dynamic range of 0.05-to 0.3 ppm Gd solution [6].

2.5.2 Flame Atomic Absorption Spectrometry (FAAS)

The soluble metal ions are atomized under flame which subsequently absorb the characteristic wavelength photons emitted by the same metal lamp source. The extent of absorption is proportional to concentration and it follows the Beer-Lambert law. Sample solutions are usually aspirated with the gas flow into a nebulizing/mixing chamber to form small droplets before entering the flame. Flame burner is subsequently used for desolvation, vaporization and atomization of liquid sample at higher temperature (2100 – 2800 ^{o}C) [7]. Depending upon the nature of sample to be aspirated, the flame is obtained by using acetylene / N_2O as fuels and air / O_2 as oxidants.

Application in present work: AAS has been used for vanadium and zinc analysis in the redissolved vanadium formate solids. Avanta AAS from GBC has been used for analysis. Vanadium has been analysed by N_2O – acetylene fuel mixture and the absorbance was measured at 318.5 nm. Zinc was analysed with air – acetylene fuel mixture and the absorbance was measured at 213.9 nm. Sodium has also been analysed with the same system in the emission mode. The sample has been prepared by dissolving 15 mg of solid in ultrapure nitric acid and then diluting the resulting solution to the desired volume for analysis. Triplicate analysis have been used to report the results.

2.5.3 Inductively Coupled Plasma – Atomic Emission Spectroscopy (ICP-AES)

It is an emission based technique and hence is more sensitive than the absorbance based techniques like AAS. The plasma torch excites all the sample elements to their thermally excited state. These excited elements subsequently emit light at their characteristic wavelengths as they return to ground state. This light is collected by the spectrometer and passes through a diffraction grating that serves to resolve the light into a spectrum of its constituent wavelengths. Within the spectrometer, this diffracted light is then collected by photomultiplier tubes as detector and amplified to yield an intensity measurement that can be converted to an elemental concentration by comparison with calibration standards. This technique is also known as inductively coupled optical emission spectrometer (ICP-OES), is a very sensitive technique for identification and quantification of elements in a sample [8]. Detection limits typically range from parts per million (ppm) to sub parts per billion (ppb), depending on the element and instrument capability. The ICP-AES from HORIBA JOBIN YVON Model ULTIMA 2 was used for elemental analysis. The instrument has sequential scanning facility based on Czerny Turner monochromator with 1 meter focal length and a high frequency 40.68 MHz RF generator. The instrument gives resolution of <10 pm up to 430 mm and < 18 pm up to 430 -800nm. The relative standard deviation was less than 1.5 % for elements analyzed by the technique.

Application in present work: The metal ion concentrations as analysed by FAAS has been verified by the ICP-AES analysis. The samples were prepared by dissolving around 7 mg of solid in ultrapure nitric acid and then making up the resulting solution to 50 ml for analysis. Emissions from Na, V and Zn were measure at 309.311, 330.237 and 202.551 nm respectively. Triplicate analysis were done and the mean value are reported.

2.5.4 Ion Chromatography

Ion chromatography is the reversible adsorption of charged molecules to immobilized ion groups on a matrix of opposite charge. The ions are separated from one another over a column using a suitable mobile phase. The separation is due to the differential migration of the ions on an ion exchange column [9]. Ion exchange process is characterized by a corresponding ion exchange equilibrium, which determines the distribution between the mobile and stationary phase:

$$E^-_{stat} + A^-_{mob} \leftrightarrow A^-_{stat} + E^-_{mob} \qquad (2.11)$$

A: sample ion, E: eluent ion

The equilibrium coefficient is given by the expression:

$$K_A = [A^-_{stat}][E^-_{mob}]/[A^-_{mob}][E^-_{stat}] \tag{2.12}$$

K_A differs for different ions and hence their affinity for the stationary phase also differs. Affinity and hence separation of ions is governed by the charge on the ion and the hydrated radius of the ion. In the third stage, substances are removed from the column by increasing the ionic strength of the eluting buffer. After separation the ions are quantitatively analyzed by suitable detector. The detector employed is usually a conductivity detector but for transition metal ions UV-visible absorption detector is used. For conductivity detection the solvent is neutralized or suppressed. Thereafter the conductivity obtained is purely due to the ions of the sample.

Application in present work: Dionex DX-120 ion chromatograph with Dionex IonPac®AS14 (4×250 mm) analytical column and ASRS Ultra II 4mm suppressor column was used for analysis. A solution of 3.5 mM Na_2CO_3 and 1 mM $NaHCO_3$ has been used as eluent. Analysis was carried out at the eluent flow rate of 1 ml/min using the sample injection loop volume of 100 µl. Peaks were analysed by using the PeakNet-SE 5.21 software. The samples were prepared by dissolving the vanadium formate solids in nitrilotriacetic acid (NTA) and citric acid (CA) media. The amount of NTA and CA were taken so as to form their equimolar solution with respect to vanadium. The concentration of formate ions in these solution were analysed by the IC.

2.5.5 Powder X-ray diffraction (XRD)

XRD is a nondestructive method for the structure analysis of crystals. The sample is irradiated with monochromatic X-rays and the intensity of the diffracted radiation is recorded. An important field of application is the identification of crystalline fractions in powders. Every crystal lattice scatters the X-rays in its own unique diffraction pattern producing a fingerprint of its atomic and molecular structure. Bragg's law governs the conditions for diffraction and diffracted beams are often referred to as reflections [10]. Constructive interference of the reflected beams emerging from different planes will take place if the difference in the path lengths of two rays is equal to whole number i.e.

$$n\lambda = 2d_{hkl} \sin\theta \qquad (2.13)$$

Where θ is the glancing angle and d_{hkl} is the spacing between the set of crystal plane of Miller's indices hkl and n is an integer (1, 2, etc., corresponding to first order, second order, etc respectively).

Application in present work: XRD patterns of the samples (vanadium formate solids) were recorded with Philips powder X-ray diffractometer based on PW1710 processing unit with vertical goniometer (Model PW1820) coupled to PW1729 x-ray generator. The Cu $K_{\propto}$ X-ray was produced from Philips sealed X-ray tube (30 KV and 20 mA). The produced X-ray was filtered using a Ni-filter. The diffracted beam was further monochromatized using curved graphite monochromator with (002) face. The diffracted X-ray photons were counted using a sealed gas proportional counter. Interfacing the processing unit to a computer collected the data in the two-theta range of 10-70° at a scanning speed of 2^0/min. Peak calculation was done with Cu $K_{\alpha 1}$ wavelength (1.5406

Å). Comparing the standard JCPDS files, the phases present in the samples were identified.

2.5.6 Fourier-Transformed Infrared (FT-IR) spectrometer

The technique is based on the fact that a chemical substance shows marked selective absorption (at resonance frequency) in the infrared region. The absorption of IR radiation, gives rise to close-packed absorption bands, called an IR absorption spectrum, and the IR absorption band extends over a wide wavelength range. The mid-infrared region which ranges approximately from 4000–400 cm^{-1} (2.5 – 25 μm) is used to study the fundamental vibrations and associated rotational-vibrational structure. The vibrational mode in a molecule will be "IR active," if it is associated with changes in the dipole [11]. Various bands present in IR spectrum correspond to the characteristic functional group and bonds present in a chemical substance. Thus, an IR spectrum of a chemical substance is a fingerprint for its identification. The compound absorbs IR radiation only when the natural frequency of vibration of some part of a molecule (i.e. atoms or group of atoms comprising it) is the same as that of the incident radiation. Also, the absorption of IR-radiation should cause a change in its electric dipole moment as an additional criterion.

Application in present work: IR spectra of the samples were recorded using a Fourier-transform infrared spectrometer (BOMEM, MB 102) over the range of 400-4000 cm^{-1}. The samples disks for IR were prepared by adding ~1mg sample to ~300 mg KBr. The mixture was ground thoroughly and pressed (~160 bars) to obtain pellets, and was mounted in the IR-sample mounting slot to record the spectra.

2.5.7 Thermogravimetry

Thermo Gravimetric Analysis (TGA) is an analytical technique used to determine a material‘s thermal stability and the fraction of volatile components by monitoring the weight change that occurs as specimen is heated. The measurement is normally carried out in air or in an inert atmosphere, like helium or argon, and the weight is recorded as a function of temperature. The TGA can give information such as composition of multi-component systems, thermal stability of materials, oxidative stability of materials, estimated lifetime of a product, decomposition kinetics of materials, the effect of reactive or corrosive atmosphere on materials, moisture and the volatile content of materials [11]. These essential components include a container in the form of a crucible to hold the sample, a furnace that can heat the sample to a high temperature, and an appropriate balance that continuously monitors the sample weight. The test material is placed in an alumina cup that is supported on an analytical balance located outside the furnace chamber. The balance is zeroed, and the sample cup is heated according to a predetermined thermal cycle. The balance sends the weight signal to the computer for storage, along with the sample temperature and the elapsed time.

Application in present work: Experiments have been carried out using Netzsch Thermobalance (Model No.: STA 409 PC Luxx). In this work Pt vs. Pt-10% Rh thermocouples were used as temperature and differential temperature sensors. Recrystallised alumina sample holders were used as sample and reference holders. TG–DTA data analysis was done using Proteus software from Netzsch. Simultaneous TG–DTA–EGA measurements were carried out individually on accurately weighed vanadium samples (about 10 mg) in air and inert atmosphere by heating from room temperature to 700 ^{0}C at a heating rate of 10 ^{0}C min^{-1}. The flow rate of high purity nitrogen was maintained at 100 ml min^{-1}to transport the volatile products. Nitrogen was also used as protective gas to the thermobalance at a flow rate of 20 ml min^{-1}.

2.5.8 X-Ray Photoelectron Spectroscopy (XPS)

Photoelectron spectroscopy is a surface-sensitive (0.5 – 2 nm), nondestructive method for the investigation of the elements and chemical bonds of conducting, semiconducting and insulating solids and powders.

In X-Ray Photoelectron Spectroscopy monoenergetic soft X-Rays bombard a sample material, causing electrons to be ejected. Identification of the elements present in the sample can be made directly from the kinetic energies of these ejected photoelectrons. If the energy of monochromatic X rays is known (hν) and the kinetic energy of the emitted photoelectrons K_e is measured with an electron spectrometer then the binding energy (B_e) of the atomic orbital from which the electron originates can be calculated by means of the equation [12]

$$B_e = h\nu - K_e - \phi,\ \phi \text{ is the work function of the spectrometer} \qquad (2.14)$$

On a finer scale it is also possible to identify the chemical state of the elements present from small variations in the determined kinetic energies. The relative concentrations of elements can be determined from the measured photoelectron intensities. For a solid, XPS probes 2-20 atomic layers deep, depending on the material and the energy of electron. The particular strengths of XPS are, semi quantitative elemental analysis of surfaces without standards, and chemical state analysis, for materials as diverse as biological to metallurgical. XPS also is known as Electron Spectroscopy for Chemical Analysis (ESCA).

Application in present work: The XPS study of substituted samples in the present study were carried out on VG model - ESCALAB MK 200X spectrometer equipped with an Al K_{∞} source (1486.6 eV) and calibrated with Au $4f^{7/2}$ line at 84.0 eV from a specimen of Au film on Si substrate. A few milligram of well-ground sample powder was spread uniformly over indium foil and pressed. The foil was attached to a stainless steel stub for mounting to the X-Y-Z translator of the XPS system. The appropriate corrections for charging effect were made with the help of a weak carbon 1s signal appearing at 285.1 eV.

2.5.9 Electrochemical techniques

Tafel Plot

One of the elementary relations in electrochemistry, Butler- Volmer equation which is the relationship between current and overpotential is used to study the heterogeneous kinetics and is expressed as follows [13]

$$i = FAK^0[C_O(0,t)e^{-\alpha f\left(E-E^{0'}\right)} - C_R(0,t)e^{(1-\alpha)f\left(E-E^{0'}\right)}] \qquad (2.15)$$

where k_0 is the standard rate constant, A is the electrode surface area, $E^{0'}$ is the potential where forward and reverse rate constants have same value, α is the transfer coefficient, f = (F/RT), other terms have their usual meaning in electrochemistry. If the solution is well stirred or the current is kept very low so that the surface concentration do not differ appreciably from the bulk values, the Butler- Volmer equation can then be rewritten as

$$i = i_0[e^{-\alpha f\eta} - e^{(1-\alpha)f\eta}] \qquad (2.16)$$

Where, i_0 is the exchange current density and η=(E-$E^{0'}$) is called overpotential. For very large values of η (either negative or positive), equation (2.16) can be written as

$$i = i_0 e^{-\alpha f\eta}$$

or, $$\eta = \frac{2.303RT}{\alpha f} log i_0 - \frac{2.303RT}{\alpha f} log i \qquad (2.17)$$

Equation (2.17) follows the Tafel form which is, η = a+b log i

Where, a = (2.303RT/αf)log i_0 and b = - (2.303RT/αf)

A plot of η verses log i is called the Tafel plot. Analysing the slope of this plot, kinetic information about an electrochemical reaction can be extracted. The overpotential for a given current is indicative of the activation energy required to drive the redox reaction. Higher exchange current density indicates faster kinetics and hence lower activation barrier and vice versa. Tafel slopes are related with the symmetry of the barrier to the reaction. If the barrier is perfectly symmetric, the Tafel slope for a single electron transfer process will be 118 mV/dec. A higher Tafel slope indicates steeper slope of the potential energy surface with respect to the reaction coordinate and hence slow rise in rate of reaction with increasing overpotential. If the Tafel slope is less than 118 mV/dec, the reaction rate will increase significantly upon applying higher overpotential. A much lower Tafel slope indicates multielectron transfer.

Cyclic Voltammetry

In cyclic voltammetry, the current response of a small stationary electrode in an unstirred solution is measured after exciting it by a triangular voltage waveform. The measurement is carried out under a diffusion controlled conditions. The potential is first varied linearly from one end to the other, after reaching the extreme value the scan direction is reversed, and the potential is returned to its initial value. The excitation cycle can be repeated several times. The voltage extremes at which reversal takes place are called switching potentials [14]. The range of switching potentials chosen for a given experiment is that within which a diffusion-controlled oxidation or reduction of the analyte takes place.

Important variables in a cyclic voltammogram are the cathodic peak potential (E_{pc}), anodic peak potential (E_{pa}), cathodic peak current (i_{pc}), and anodic peak current (i_{pa}). For a reversible electrode reaction, anodic and cathodic peak currents are approximately equal in value but opposite in sign. For a reversible electrode reaction at 298 K, the difference in peak potentials, ΔE_p, is

$$\Delta E_p = |E_{pa} - E_{pc}| = 0.0592/n \text{ V} \qquad (2.18)$$

where n is the number of electrons involved in the half reaction. When the electron transfer kinetics is very slow, irreversibility comes into play and the value of ΔE_p exceeds the expected value. For irreversible reactions, the value of ΔE_p increases with increasing the scan rate. Quantitative relation between scan rate and peak current is given by Randles-Sevcik equation which is (at 298K)

$$i_p = 2.686\times10^5 n^{3/2} AcD\upsilon^{1/2} \tag{2.19}$$

where i_p is the peak current (A), A is the electrode area (cm^2), D is the diffusion coefficient (cm^2/sec), c is the concentration (mol/cm^3), and υ is the scan rate (V/s).

Thus, scan rate affects the peak current and accordingly the variation could be applied to ascertain the reversibility of the redox process.

Cyclic voltammetry is also used to study the coupled chemical reactions. Variation in peak current with varying scan rates gives fair idea about the coupled chemical reactions. Thus, the mechanism of complex heterogeneous redox reactions could be understood by cyclic voltammetry.

Application in present work: Electrochemical evaluations were carried out in a glass cell with a solution volume of 25 ml under inert conditions. Planar disk electrodes of stainless steel, graphite and glassy carbon were used with the geometric surface area of 0.18, 0.18 and 0.13 cm^2 respectively. All potentials were measured against the Ag/AgCl, sat. KCl reference electrode and platinized platinum was used as the counter electrode. Tafel plot, cyclic voltammetry and AC impedance data were obtained for 0.5 mM HCOOH, 1 mM $V(OH)(HCOO)_2$, solution of 0.5 mM HCOOH and 1 mM $V(OH)(HCOO)_2$ and solution of 1 mM HCOOH and 1 mM $V(OH)(HCOO)_2$ for all of the above mentioned electrodes. 0.5 M KNO_3 was used as supporting electrolyte in all these experiments. The electrodes were polished initially by coarse polishing paper and finally with 0.05 µm size alumina suspension over a nylon cloth, and washed with distilled water before each experiment.

Tafel plot was evaluated for each system after a stable open circuit potential (OCP) value was obtained. The potential was scanned from 400 mV negative potential to 400 mV positive potential with respect to OCP at a scan rate of 1mV/s.

Cyclic voltammograms were obtained at the scan rates of 10 mV/s, 20 mV/s, 50 mV/s, 100 mV/s, 500 mV/s and 1000 mV/s for all systems with the scan range of -650 mV to + 1200 mV vs. Ag/AgCl, sat. KCl.

2.6 References

[1] J. P. Chen, M-L. Chua, B. Zhang, *Waste Management*, 22 (2002) 711.

[2] J. Trau, *J. Thermal Anal.*, 6 (1974) 355.

[3] M. Skyllas Kazacos, C. Menictas, and M. Kazacos, *J. Electrochem. Soc.*, 143 (1996) L86.

[4] K. Ogawa and N. Tobe, *Bull. Chem. Soc. Japan*, 39 (1996) 223.

[5] Jens E.T. Andersen, *Anal. Chim. Acta*, 361 (1998) 125.

[6] K. Macgibbon, R. Culligan And G.H. Brown, Point Lepreau Generating Station Chemistry Laboratory Analytical Procedure :Gadolinium Arsenazo III, 78200-AP-GA1, 2014.

[7] J.A. Dean and T.C. Rains, “Flame Emission and Atomic Absorption Spectrometry”, New York: Marcel Dekker Inc., Vol. 1 (1971).

[8] E. S. Dipietro, M. M. Bashor, P. E. Stroud, B. J. Smarr, B. J. Burgess, W. E. Turner and J. W. Neese, *Sc. Total Environ.*, 74 (1988) 249.

[9] J. S. Fritz and D. T. Gjerde, *Ion Chromatography, Third Ed.*, Weinheim: Wiley-VCH, (2000).

[10] C. Kittel, *Introduction to Solid State Physics*, New York John Wiley & sons, 1953.

[11] D. A. Skoog, F. J. Holler and T. A. Nieman, *Principles of Instrumental Analysis*, Harcourt Asia Pvt. Ltd., 2001.

[12] D. Briggs and M. P. Seah, *Practical Surface Analysis by Auger and X-ray Photoelectron Spectroscopy*, John Wiley & Sons, 1987.

[13] A. J. Bard and L. R. Faulkner, *Electrochemical Methods Fundamentals and Applications: Second Edition*, John Wiley & Sons, Inc. 2001.

[14] P. T. Kissinger and W. R. Heineman, *J. Chem. Edu.*, 60 (1983) 702.

CHAPTER-3

Studies on Optimization of Parameters for Vanadium Synthesis in Low Oxidation State

3.1 Introduction

Decontamination of light water reactors wherein stainless steel is used as major structural material such as BWRs and PWRs involves removal of various substituted ferrites with high lattice energies. Strong reducing agents such as ones based on vanadium (II) and chromium (II) are very effective in reductive dissolution of such oxides [1-5].

Although vanadous formulations can be easily obtained by chemical reduction using stronger reducing agents like zinc amalgam, but the subsequent use in nuclear power reactor limits the option of synthesis owing to the material compatibility and the active waste volume generation issues [6]. Synthesis of vanadous formulation through electrolytic reduction is a viable option for the purpose as any other chemical route will inevitably introduce spare reagents/byproducts in the formulation [7]. These spare reagents/byproducts will finally increase the ionic load of the spent decontamination formulation and thereby lead to higher active waste volume generation. Concerns about material compatibility for stainless steel structural materials rule out use of any strong acid or its conjugate anion in the formulation [8, 9]. Electrolytic route provides the flexibility to select the exact required medium for synthesis without any addition of spare reagent/byproduct [10]. The prevalent oxidation states of vanadium compounds are 5+ and 4+. The conversion from the prevalent 5+ or 4+ state to 2+ requires considerable time due to the ensuing three or two step electrolysis. The stringent requirement of inert condition poses immense handling related issues for the large scale application. These can be addressed in two ways. The first and the preferred one is to prepare a material compatible V(II) solid compound which can be directly added to the reactor system during the decontamination campaign. The second option is to optimize the preparation of a high concentration V(II) solution in a material compatible formulation which will reduce the volume to be handled during the decontamination campaign.

V(V) or V(IV) solutions are the stable precursors available for synthesis of V(II) formulations. V(V) formate could be obtained by direct addition of formic acid to sodium metavanadate solution while V(IV) formate was obtained by chemically reducing the V(V) formate by hydrazine addition. Maximum solubility of aqueous V(V) and V(IV) formate solution has been evaluated by gradually increasing the concentration with conductivity and turbidity monitoring.

Electroreduction of aqueous V(V) or V(IV) precursor solutions in the material compatible formulation is the most suitable route for preparation of V(II). Controlled current electrolysis using two compartment cell has been studied for V(II) preparation. Suitable cathode materials have been evaluated for the purpose. The synthesis of V(II) in acidic medium will be affected by the competing proton reduction process as the formal redox potential for hydrogen evolution is more positive than that for V(III)/V(II) redox potential. Thus, a high current efficiency for V(III)/V(II) redox process can only be obtained at electrodes which have high overpotential for hydrogen evolution. Heavy metals like Hg, Cd and Pb are known to have high overpotential for hydrogen evolution [11] but these are avoided in large scale application owing to their high toxicity. Stainless steel and carbon based cathodes could be among the viable options. On the other hand, accelerated hydrogen evolution in the presence of V(III)/V(II) redox couple will indicate a cathode which can be used for electrocatalytic hydrogen generation from weak organic acids. The electrochemical characteristics of glassy carbon and stainless steel electrodes have been evaluated for the electroreduction of synthesized vanadic hydroxyl formate. Tafel plot evaluation and cyclic voltammetric studies of these materials have been carried out for the purpose.

Different solids of vanadium have been prepared by aqueous route in the formic acid medium. The vanadium compounds were obtained for all known aqueous vanadium oxidation states viz. V(V), V(IV), V(III) and V(II). The compounds were obtained by preparing aqueous saturated solutions of the different oxidation states of vanadium through various routes. The compounds were characterized for the chemical composition, oxidation states, thermal stability, structural information and formation of aqueous complexes with suitable ligands namely nitrilotriacetic acid and citric acid.

3.2 Experimental

3.2.1 Evaluation of maximum solubility of V(V) and V(IV) aqueous solutions

The maximum solubility of V(V) formate was evaluated by its in situ generation by mixing the stock solutions of $NaVO_3$ and HCOOH in the 1:2 and 1:6 molar ratio. The conductivity was measured using CON 1500 conductivity meter from Eutech Instruments with four probe electrode and resolution of 0.001 µS cm^{-1} and turbidity was measured using Systronics µC turbiditymeter 135 with a 25 mm diameter flat bottom test tube. The concentration of the solution was progressively increased to evaluate the saturation solubility behaviour of V(V). V(IV) formate solution was in situ generated by mixing the stocks of $NaVO_3$, HCOOH and $N_2H_4{\cdot}H_2O$ in required molar ratio at 80 ^{o}C under inert atmosphere. The concentration of the solution was progressively increased with periodic measurement of conductivity and turbidity.

3.2.2 Constant current electrolysis and electrochemical evaluation of electrodes

Sodium metavanadate was electrolyzed in formic acid medium using a two compartment electrolysis cell. The constant current electrolysis was carried out with V(V) precursor at 125 mM concentration and V(IV) precursor at 350 mM concentration. Similar concentration of formic acid was used as anolyte. The electrochemical cell used is an in-house designed and fabricated glass cell with two compartments separated by an anion exchange membrane. The cell consists of two concentric cylindrical compartments, the inner being anode compartment and outer one being cathode compartment. An anion exchange membrane was placed at bottom of the anode compartment to separate the catholyte and the anolyte. Graphite felt was used as the cathode while stainless steel AISI 304 was used as the anode and the compartments were separated by a commercial anion exchange membrane. Constant current electrolysis was carried out using Aplab regulated DC power supply type: CBPS/10 with a current density of around 55 mA/cm^2 across the anion exchange membrane. Catholyte volume was 550 ml while the anolyte volume was 50 ml. Applied cell voltage, cathode potential, solution potential and the current obtained during the process were monitored to assess the reduction.

Electrochemical evaluations were carried out in a glass cell with a solution volume of 25 ml under inert conditions. Planar disk electrodes of stainless steel, graphite and glassy carbon were used with the geometric surface area of 0.18, 0.18 and 0.13 cm^2 respectively. All the potentials were measured against the Ag/AgCl, sat. KCl reference electrode and platinized platinum was used as the counter electrode. Tafel plot, cyclic voltammetry and AC impedance data were obtained for 0.5 mM HCOOH, 1 mM $V(OH)(HCOO)_2$, mixture of 0.5 mM HCOOH and 1 mM $V(OH)(HCOO)_2$ and mixture of 1 mM HCOOH and 1 mM $V(OH)(HCOO)_2$ for all of the above mentioned electrodes. 0.5 M KNO_3 was used as supporting electrolyte in all these experiments. The electrodes were polished initially by coarse polishing paper and finally with 0.05 µm size alumina suspension over a nylon cloth, and washed with distilled water before each experiment.

Tafel plot was evaluated for each system after a stable open circuit potential (OCP) value was obtained. The potential was scanned from 400 mV negative potential to 400 mV positive potential with respect to OCP at a scan rate of 1mV/s.

Cyclic voltammograms were obtained at the scan rates of 10 mV/s, 20 mV/s, 50 mV/s, 100 mV/s, 500 mV/s and 1000 mV/s for all the systems with the scan range of -650 mV to + 1200 mV vs. Ag/AgCl, sat. KCl.

3.2.3 Synthesis and characterization of different oxidation state vanadium solids

The vanadium solids in various oxidation states viz. V(V), V(IV), V(III) and V(II) were obtained from the respective vanadium formate solutions by exceeding the solubility limit. V(V) formate saturated solution was directly obtained by mixing $NaVO_3$ with HCOOH in the required molar ratio. V(IV) formate saturated solution was prepared by the chemical reduction of V(V) formate solution using hydrazine at 80 ^{o}C under inert atmosphere. V(III) formate saturated solution was prepared by electrolytic reduction of high concentration (350 mM) V(IV) solution while V(II) formate saturated solution was obtained by electrochemical reduction of 350 mM V(IV) formate solution using zinc amalgam. The precipitates obtained were filtered, washed, and dried in a vacuum desiccator. The dried precipitates were grinded using mortar and pestle before washing and drying again. The process was repeated several times. These precipitates were used for characterization. Compositional analysis was done by Atomic Absorption Spectrometry (AAS), Inductively Coupled Plasma – Atomic Emission Spectroscopy (ICP-AES) and Ion Chromatography (IC). For AAS and ICP-AES, the samples were prepared by dissolving the known weight of precipitate in ultrapure nitric acid and then diluting the resulting solution to the desired volume for analysis. Based on the analysed vanadium content in the precipitate, the solids were dissolved in equimolar concentration of nitrilotriacetic acid (NTA) and citric acid and these solutions were used for IC analysis. A solution of 3.5 mM Na_2CO_3 and 1 mM $NaHCO_3$ has been used as eluent. Analysis was carried out at the eluent flow rate of 1 ml/min using the sample injection loop volume of 100 µl. Further characterization with thermogravimetry (TG) using Netzsch Thermobalance (Model No.: STA 409 PC Luxx), infra-red spectroscopy (IR) in KBr matrix (Bomem MB 102 FTIR) and UV –visible spectroscopy (Jasco-700) were also carried out. XRD using Philips powder X-ray diffractometer based on PW1710 processing unit and XPS using VG model - ESCALAB MK 200X were carried out for the structural characterization of the samples.

3.3 Results and discussion

3.3.1 Maximum solubility of V(V) and V(IV) in formate medium

Conductivity and turbidity variation of V(V) in a 1:2 molar ratio formic acid aqueous solution is shown in **Fig 3.1**. A clear intense yellow colored solution was obtained upon progressively increasing the concentration of the solution. There is a steady rise in conductivity upto 250 mM V(V). Turbidity remained almost stable upto this concentration. Conductivity increased suddenly when the concentration was raised beyond 250 mM. Turbidity too started increasing gradually beyond this concentration of vanadium. Aqueous vanadium species is known to have the tendency to undergo deprotonation [12]. In the electrolyte medium the vanadium cations are solvated by water molecules forming hydrated cations $[V(H_2O)_n]^{y+}$ where the electron density from molecular orbital of the water molecules is transferred to the empty orbitals of the metal cation. This charge transfer weakens the O–H bond in the coordinated water molecules and makes it more acidic leading to deprotonation of the hydrated vanadium cations as follows [13]:

$$[V^{z+}(H_2O)_n]^{y+} + hH_2O \rightarrow [V^{z+}(OH)_h(H_2O)_{n-h}]^{(y-h)+} + hH_3O^+ \qquad (3.1)$$

In this deprotonation reaction, the hydrolysis ratio (h), i.e. the number of hydroxyl groups created, is directly proportional to the charge of the vanadium cation (z+) and inversely proportional to the pH of the solution, which is explained in the charge–pH diagram reported by Jørgensen [13]. Thus, the deprotonation results in the precipitation of vanadium while the acid stays in solution. This results in sudden increase in the conductivity as is seen in **Fig 3.1**.

Fig 3.1: Conductivity and turbidity variation of V(V) formate solution (two times acid)

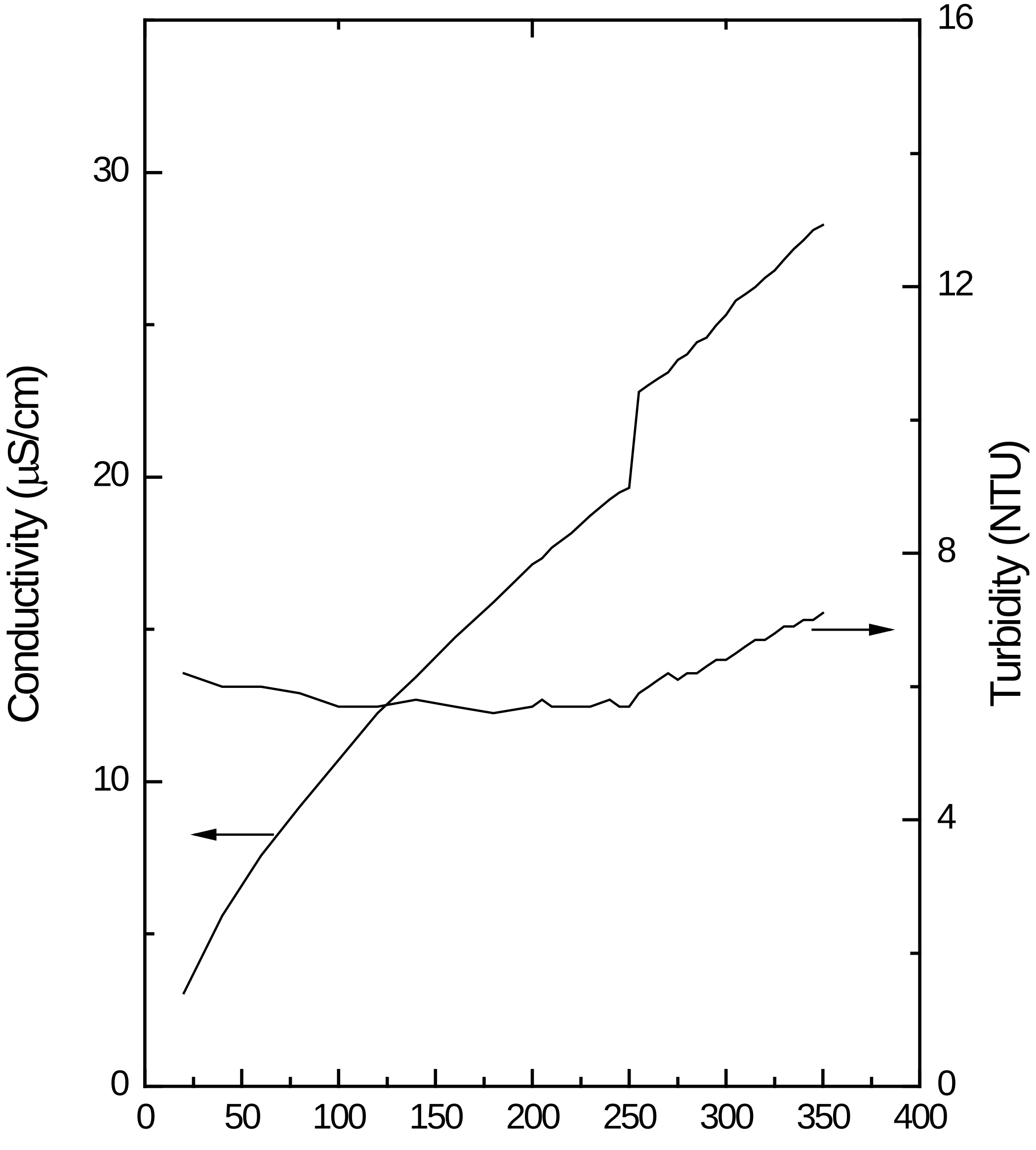

Fig 3.2: Molar conductivity variation with concentration for (A) V(V) in 2 times formic acid; (B) V(V) in 6 times formic acid and (C) V(IV) in 6 times formic acid

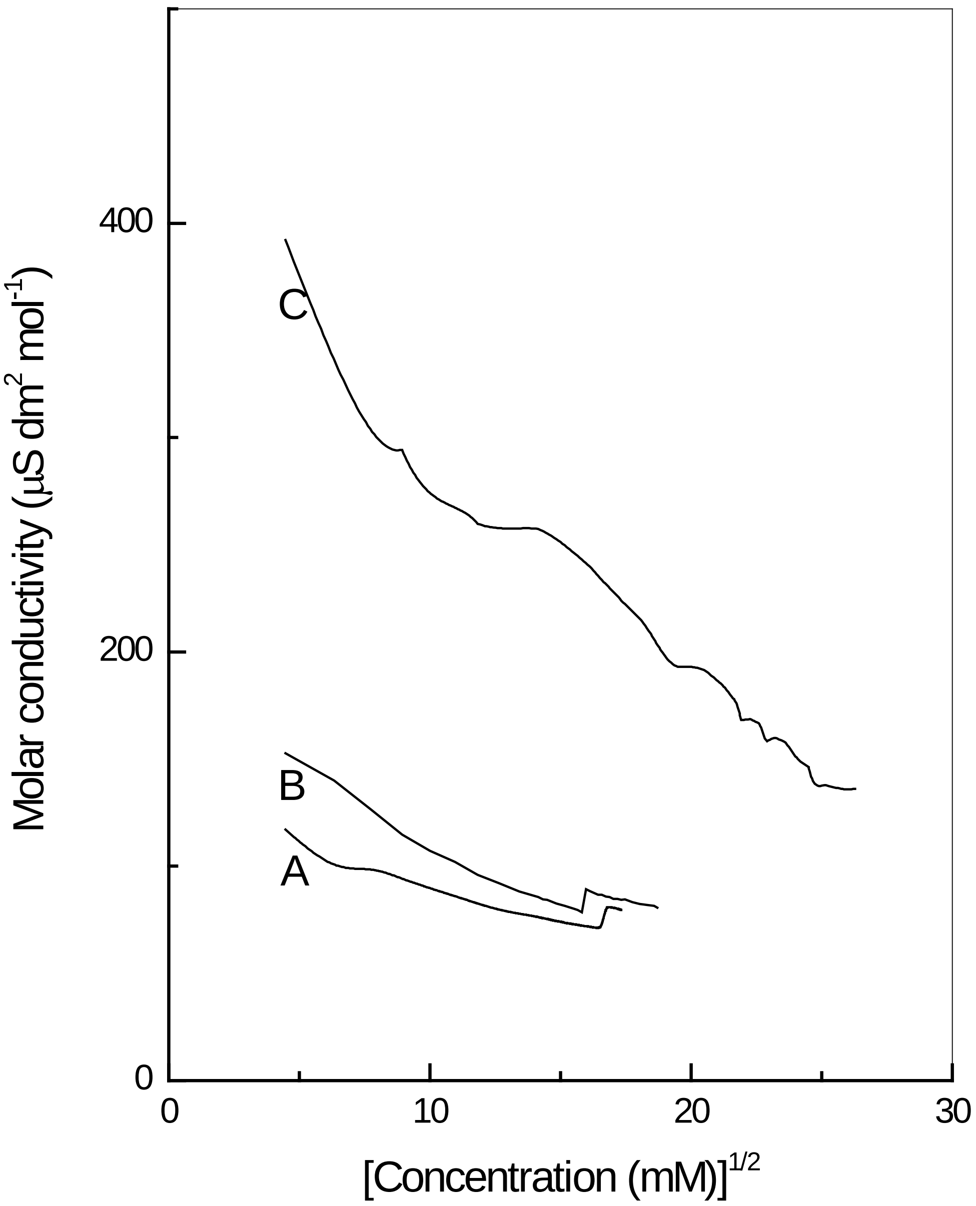

Fig 3.3: Conductivity and turbidity variation of V(V) formate solution (six times acid)

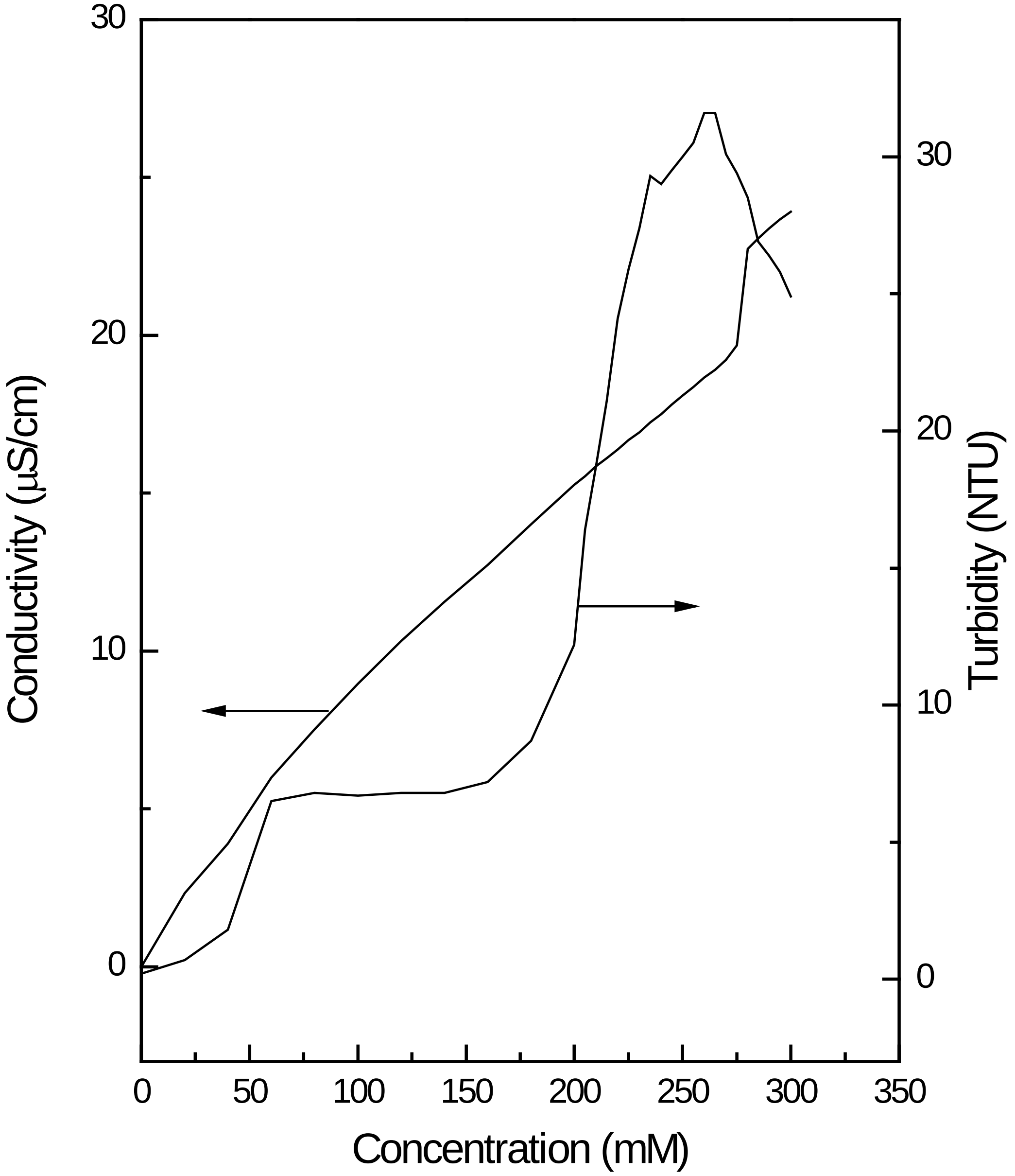

The molar conductivity variation with concentration has shown the nature of intermediate electrolyte as per the Debye-Huckel-Onsagar expression for solution conductivity:

$$\Lambda_m = \Lambda_m^o - (A + B \cdot \Lambda_m^o) \cdot \sqrt{c} \qquad (3.2)$$

Where, Λ_m is the molar conductivity, Λ_m^o is the limiting molar conductivity, c is the electrolyte concentration and A and B are constants that depend quantities such as temperature, the charges on the ions and the dielectric constant and viscosity of the solvent. This is shown by the plot A in **Fig 3.2**.

Conductivity and turbidity variation of V(V) solution in a 1:6 molar ratio formic acid solution is shown in **Fig 3.3**. Conductivity of the solution has increased gradually upto a concentration of 275 mM. Formation of higher vanadium concentration solution with increasing acidity can be explained by the equilibrium [14]:

$$V_2O_5\ (S) + 2H^+ \rightleftharpoons 2VO_2^+\ (aq) + H_2O \qquad (3.3)$$

There is a sharp rise in conductivity upon further increase in the concentration of vanadium. Variation in turbidity has shown that the solution is less stable at even lesser concentration. The turbidity of solution started rising beyond concentration of 150 mM vanadium in solution. This can be attributed to the tendency of V(V) to form oligomeric species which seems to remain suspended in solution and not significantly affect the conductivity of the solution. Turbidity has started decreasing once the deprotonation initiated indicating that the suspended oligomeric vanadium species undergoes deprotonation at a faster rate than the soluble vanadate species. The intermediate electrolyte behavior of the vanadate remained unchanged with increasing acidity as shown in plot B, **Fig 3.2**.

V(IV) solubility has been evaluated in the formate media by its in-situ formation by hydrazine addition (as described in Chapter 2). The variation in conductivity, turbidity and density of the solution with increasing concentration is shown in **Fig 3.4**. The conductivity has increased gradually with increasing concentration upto 350 mM. Beyond 350 mM concentration, there is periodic dip in the conductivity before further rise. This indicates that the solution is unstable beyond this concentration and there may be nucleation and redissolution with progressive in situ reaction upon hydrazine addition. The Turbidity has shown no change upto 465 mM concentration. There is a drop in turbidity from ~ 4.0 to ~3.0 which again went up to initial value upon increasing the concentration above 600 mM. The variation in density with concentration was fitted to the polynomial equation:

$$y = a_0 + a_1x + a_2x^2 + a_3x^3 + a_4x^4 + a_5x^5 \tag{3.4}$$

where y is the conductivity of solution and x is the concentration of V(IV) and a_i, i=0-5 are the constants. A good fitting to this equation has been obtained indicating that the density variation can be represented with reasonable accuracy by the variable degree polynomial expression [15]. Fitted density plot indicates that the instantaneous solubility of the solution is much higher and the concentration upto 680 mM could be achieved before the saturation behaviour is seen for the density indicating precipitation. Fitting the conductivity data to the Debye-Huckel-Onsagar expression indicates that the V(IV) formate is a strong electrolyte in aqueous media as shown by plot C, **Fig 3.2**.

Fig 3.4: Conductivity, turbidity and density variation of V(IV) formate solution

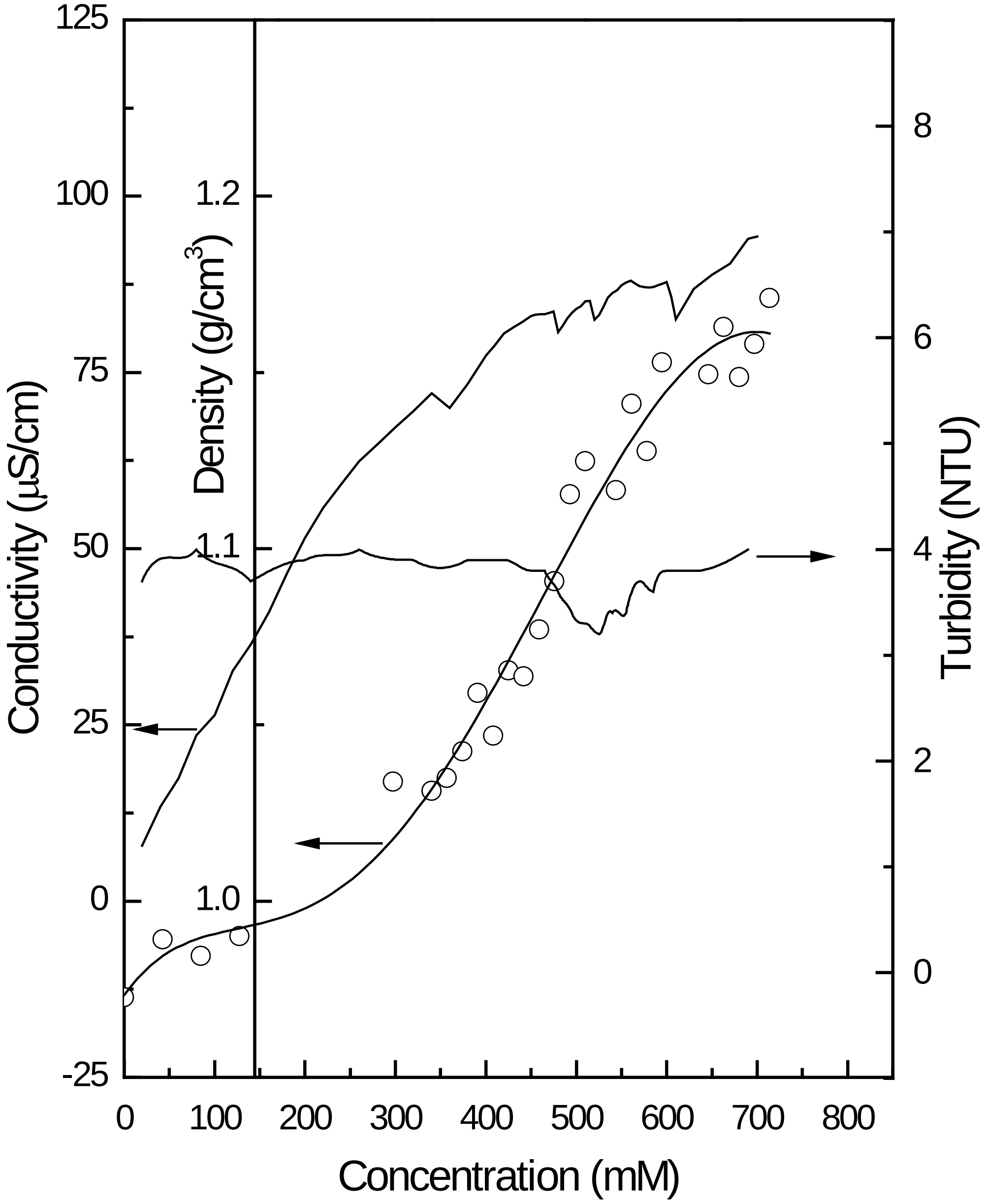

The equilibrium concentration of these solutions were determined after two weeks of the solution preparation. Polymeric film had formed on the surface of the glass vessel used to stored V(V) solution while a blue precipitate layer could be seen at the bottom of the vessel in which V(IV) solution was kept. The equilibrium concentrations were found to be 50 mM for V(V) with two times formic acid, 150 mM for V(V) with six times formic acid and 450 mM for V(IV) with six times formic acid.

3.3.2 Constant current electrolysis for vanadium reduction

V(V) formate and V(IV) formate at a concentration of 125 mM were separately reduced by the constant current electrolysis. These reduction processes in cathode compartment can be shown as:

$$VO_2^+ + 2H^+ + e^- \rightarrow VO^{2+} + H_2O \qquad E° = 1.00\text{ V vs SHE} \qquad (3.5)$$

$$VO^{2+} + 2H^+ + e^- \rightarrow V^{3+} + H_2O \qquad E° = 0.337\text{ V vs SHE} \qquad (3.6)$$

$$V^{3+} + e^- \rightarrow V^{2+} \qquad E^o = -0.255\text{ V vs. SHE} \qquad (3.7)$$

Formate ion migrates to anode compartment from the cathode compartment through the anion exchange membrane continuously during the progress of electrolysis. In the anode compartment, two formate ions form one carbon dioxide and one formic acid molecule. This reaction can be expressed as

$$2HCOO^- \rightarrow CO_2 + 2e^- + HCOOH \qquad (3.8)$$

In this way the concentration of formic acid continuously increases in anode compartment during the process. This also leads to a rise in the solution volume of the anode compartment by migration of water molecule to anode compartment owing to the osmotic effect.

A clear V(II) formate solution has been finally obtained by electrolysis of either V(IV) or V(V) precursors. V(IV) formate takes 2/3rd time to form V(II) as compared to V(V) formate. Based on the total charge passed for the reduction, the current efficiency for the process was calculated to be more than 85%. Rest of the current can be attributed to the hydrogen evolution by acid reduction which is a competitive process and for the reduction of the oxygen which might have diffused in the cathode compartment during electrolysis.

3.3.3 Electrochemical evaluation of suitable cathode material

Potentiodynamic polarization studies: The Tafel plots evaluated for the stainless steel, glassy carbon and graphite electrodes are shown in **Fig 3.5**. The plots were evaluated for the rising part of the current and the electrochemical parameters determined by the evaluation are enlisted in **Tables 3.1, 3.2** and **3.3**. Corrosion potential of $V(OH)(HCOO)_2$ system is more negative than that of HCOOH for both stainless steel and glassy carbon electrodes. Corrosion potential of V^{3+} has shifted towards positive direction with addition of acid in case of glassy carbon electrode whereas it has shifted to more negative values upon addition of acid for stainless steel electrode. The behaviour of glassy carbon is as anticipated for mixing the solutions of different corrosion potential values as per the mixed potential theory.

Fig 3.5: Tafel plots for various solutions on (A) stainless steel and (B) glassy carbon and (C) graphite electrodes for (i) 0.5 mM HCOOH; (ii) 1mM $V(OH)(HCOO)_2$; (iii) 1mM $V(OH)(HCOO)_2$ with 0.5 mM HCOOH and (iv) 1 mM $V(OH)(HCOO)_2$ with 1 mM HCOOH

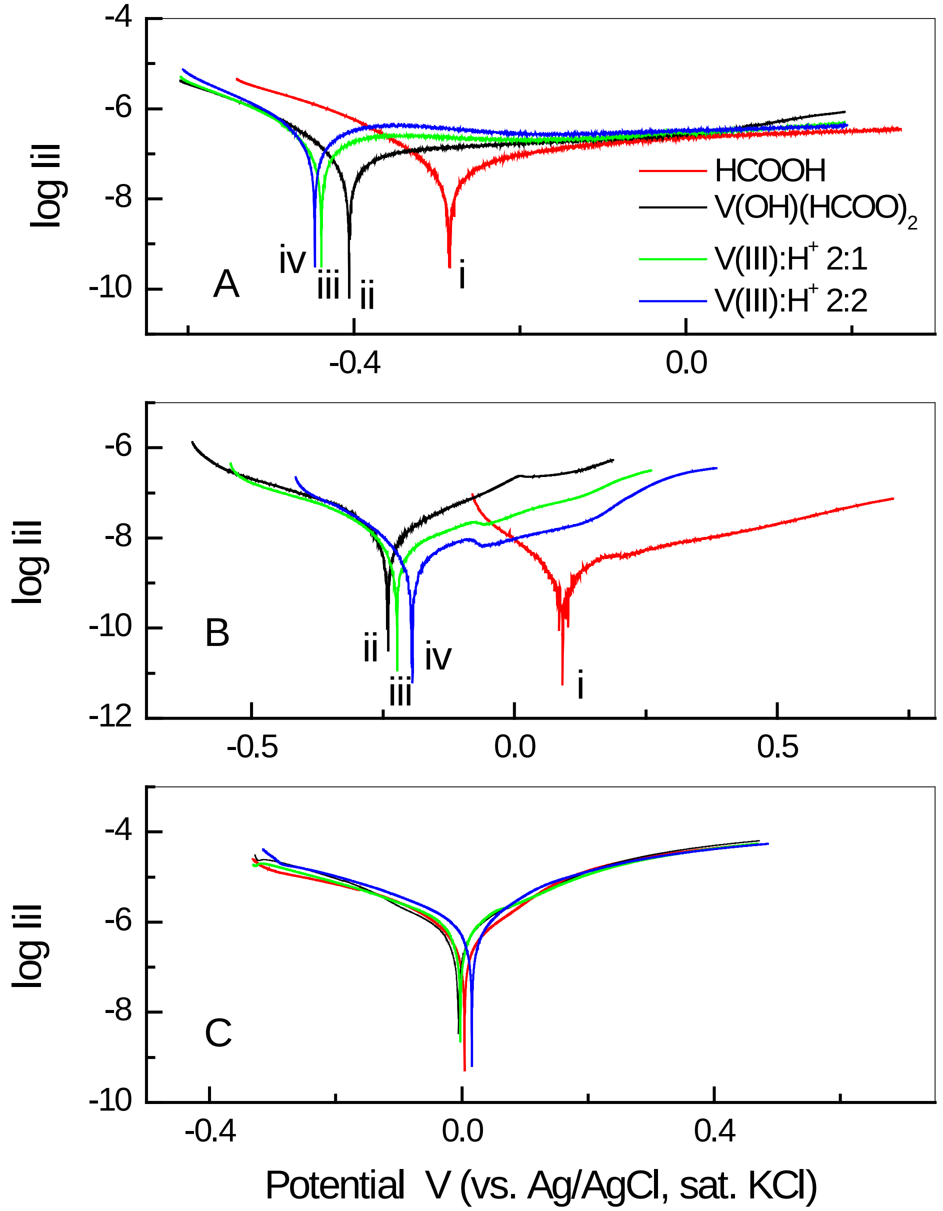

Table 3.1: Electrochemical parameters evaluated by analysis of Tafel plots on Stainless steel (SS304L) electrode

Analyte	E_{corr} (V)	i_o (A/cm^2)	b_c (V/dec)	b_a (V/dec)
Only 1mM $V(OH)(HCOO)_2$	-0.406	1.268E-6	0.1558	-4.5947
Only 0.5 mM HCOOH	-0.285	4.667E-7	0.1336	0.6246
1mM $V(OH)(HCOO)_2$ + 0.5 mM HCOOH	-0.439	2.882E-6	0.1656	-0.805
1 mM $V(OH)(HCOO)_2$ + 1 mM HCOOH	-0.445	3.247E-6	0.1502	-1.2192

Table 3.2: Electrochemical parameters evaluated by analysis of Tafel plots on glassy carbon electrode

Analyte	E_{corr} (V)	i_o (A/cm^2)	b_c (V/dec)	b_a (V/dec)
Only 1mM $V(OH)(HCOO)_2$	-0.237	2.403E-7	0.3194	0.3571
Only 0.5 mM HCOOH	0.092	2.039E-8	0.1511	0.4777
1mM $V(OH)(HCOO)_2$ + 0.5 mM HCOOH	-0.221	1.065E-7	0.2123	0.6027
1 mM $V(OH)(HCOO)_2$ + 1 mM HCOOH	-0.191	5.934E-8	0.1719	0.6877

Table 3.3: Electrochemical parameters evaluated by analysis of Tafel plots on graphite electrode

Analyte	E_{corr} (V)	i_o (A/cm^2)	b_c (V/dec)	b_a (V/dec)
Only 1mM $V(OH)(HCOO)_2$	-0.006	7.517E-6	0.2328	0.2154
Only 0.5 mM HCOOH	0.004	8.397E-6	0.3067	0.2085
1mM $V(OH)(HCOO)_2$ + 0.5 mM HCOOH	-0.002	1.058E-5	0.3154	0.263
1 mM $V(OH)(HCOO)_2$ + 1 mM HCOOH	0.016	1.089E-5	0.2988	0.2177

However, the behaviour of stainless steel electrode indicates deviation from normal redox process on the electrode. The exchange current density is higher for V(III) on stainless steel as compared to that on glassy carbon (~ 5 times). The exchange current density for HCOOH itself is much higher for stainless steel electrode as compared to that for glassy carbon (~23 times). The increase in exchange current density for V(III) as compared to that for HCOOH is much more on glassy carbon electrode, 11.8 times as compared to 2.7 times for stainless steel electrode. Exchange current density for V(III) has shown two fold increase upon addition of equimolar concentration of HCOOH on stainless steel electrode whereas it reduced to less than half on glassy carbon for similar acid addition. Further addition of acid has changed the current densities on these two electrodes in similar fashion though to different extents. There is a minor rise in the current density in case of stainless steel while the current density reduced again to about half in case of glassy carbon. This indicates that there is a reduction in active surface availability for V(III) reduction on carbon surface with addition of acid. This was further verified by similar addition of HNO_3. The cathodic Tafel slopes for stainless steel electrode remained similar for V(III) even after addition of HCOOH while on glassy carbon, the addition of acid lead to significant decrease in the cathodic Tafel slope. This indicates that addition of acid makes V(III) reduction kinetically more favourable on carbon surfaces. The anodic side of the potentiodynamic graph has shown a non linearity to Tafel behviour at high overpotentials on glassy carbon electrode. Non linearity to Tafel behaviour on anodic polarization is more prominent and sets in at lower overpotentials on stainless steel electrode. The shift in corrosion potential in variation with the mixed potential theory and high increase of exchange current density on addition of acid in case of stainless steel electrode indicates that there could be an electrocatalytic reduction of HCOOH by V(III). The electrochemical behaviour of graphite electrode has been erratic. This is attributed to the porous nature of the graphite surface leading to intercalation of redox active ions inside the electrode [16]. This will lead to higher exchange current density as is observed. Also, the Tafel slopes are too high indicating non ideal behaviour of the electrode. However, the variation of corrosion potential has followed almost similar trend as that of glassy carbon. Thus, a similar electrochemical behaviour is anticipated for graphite for vanadium reduction in the presence of HCOOH. This study shows that using carbon based electrodes will give better current efficiency for V(III) reduction in formate media.

Cyclic voltammetric studies: Cyclic voltammograms of the above mentioned systems on stainless steel, glassy carbon and graphite electrodes are shown in **Figures 3.6, 3.7** and **3.8** respectively. As is evident from the voltammograms, both the carbon based electrodes have a very sluggish redox interaction with formic acid as no clear peak is obtained for only acid voltammograms on these electrodes for either forward scan or reverse scan. However HCOOH has shown a strong redox interaction with stainless steel electrode for both forward and reverse scans. There is one strong peak at the high positive potential (0.8 to 1.1 V vs. Ag/AgCl, sat. KCl) which shows good linearity to square root of the scan rate. This indicates it corresponds to oxidation of $HCOO^-$ leading to CO_2 evolution. The reverse scan has shown multiple peaks. The peak heights for these peaks have been analysed with respect to scan rate variation. The peak positions for the peak around 200 mV vs. Ag/AgCl, sat. KCl has shifted continuously to more positive potential

Fig 3.6: Cyclic Voltammograms of (A) 0.5 mM HCOOH, (B) 1 mM V(OH)(HCOO)$_2$, (C) solution of 0.5 mM HCOOH and 1 mM V(OH)(HCOO)$_2$, (D) solution of 1 mM HCOOH and 1 mM V(OH)(HCOO)$_2$ and (E) cyclic voltammograms of all these solution at 10 mV/s scan rate on stainless steel electrode.

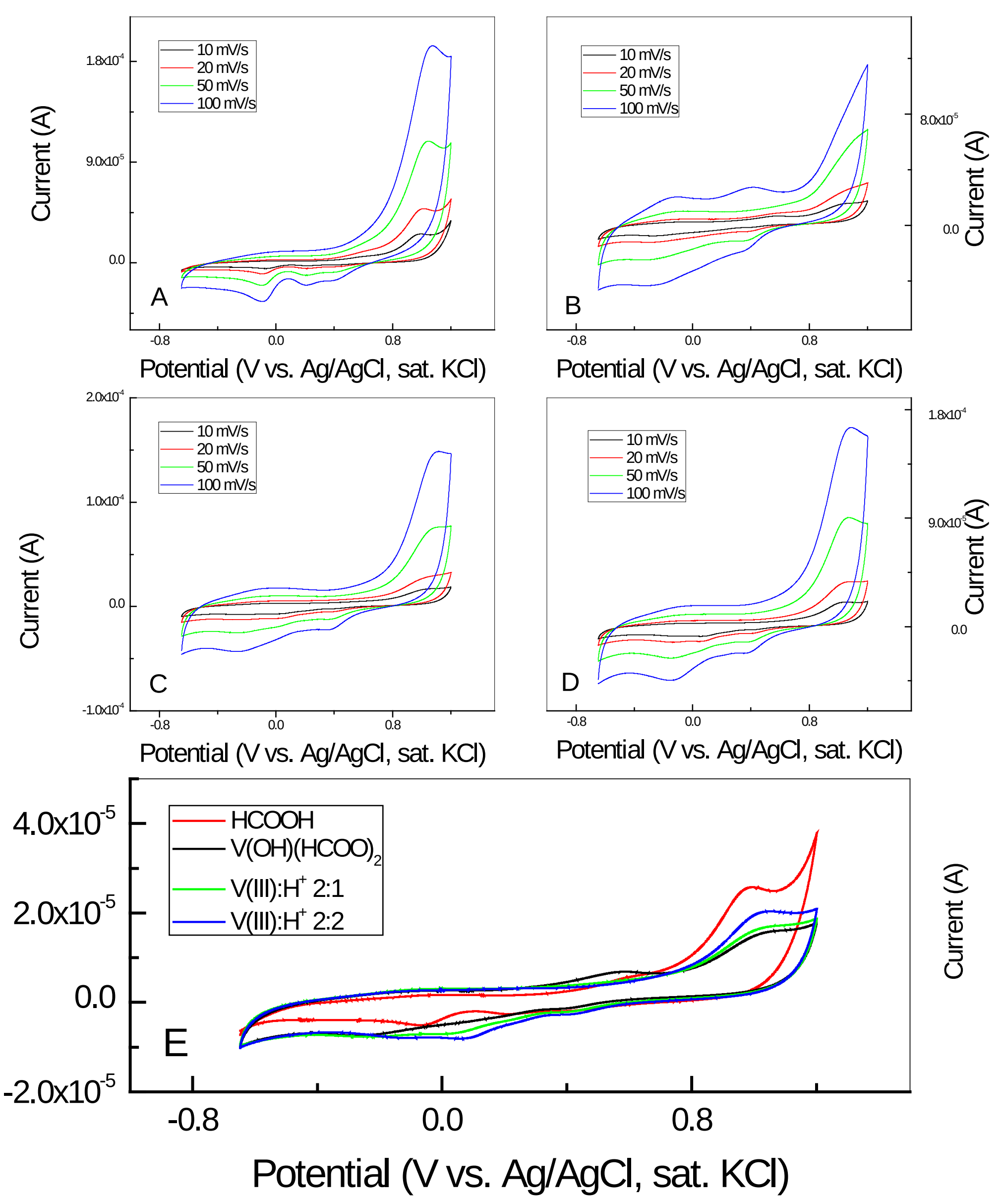

Fig 3.7: Cyclic Voltammograms of (A) 0.5 mM HCOOH, (B) 1 mM V(OH)(HCOO)$_2$, (C) solution of 0.5 mM HCOOH and 1 mM V(OH)(HCOO)$_2$, (D) solution of 1 mM HCOOH and 1 mM V(OH)(HCOO)$_2$ and (E) cyclic voltammograms of all these solution at 10 mV/s scan rate on glassy carbon electrode.

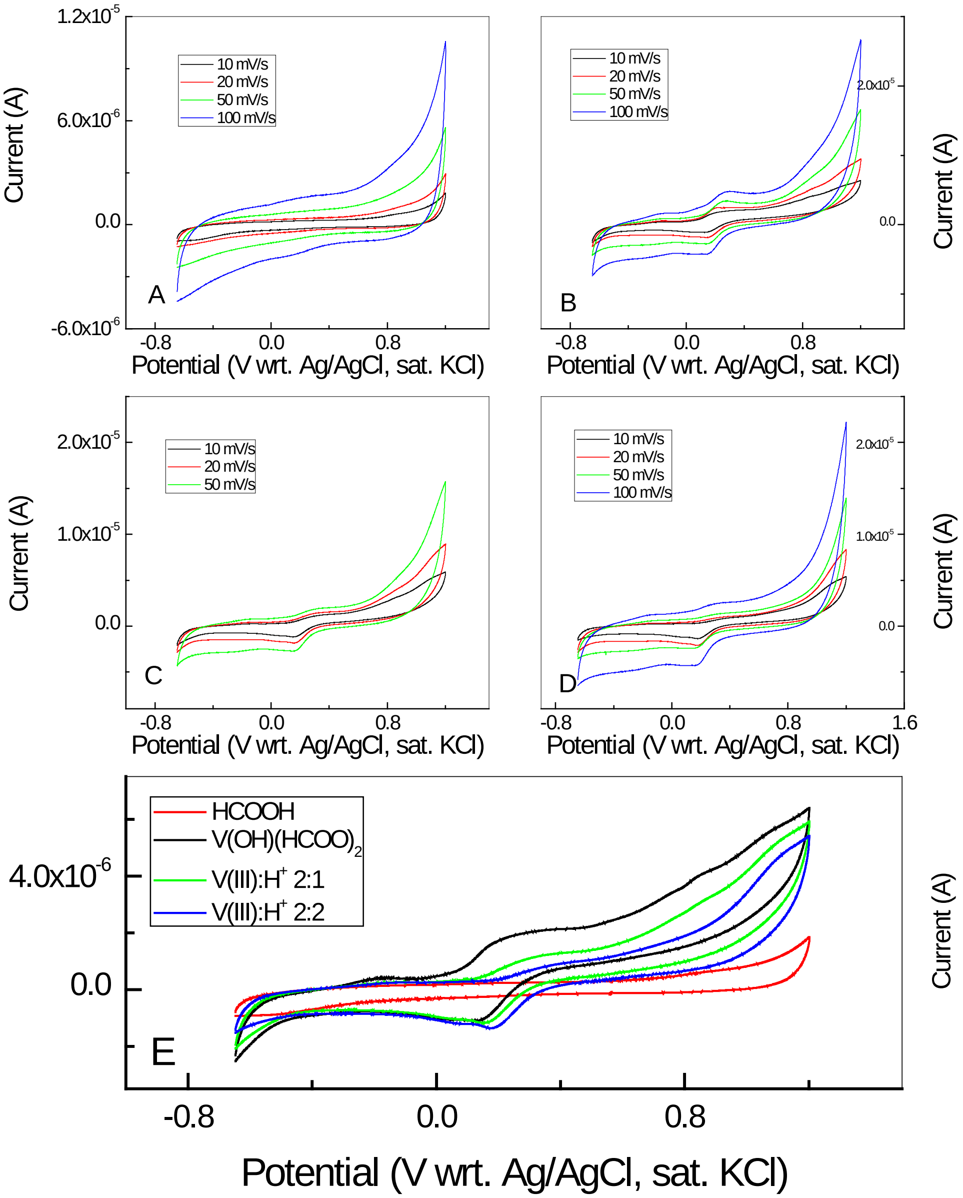

Fig 3.8: Cyclic Voltammograms of (A) 0.5 mM HCOOH, (B) 1 mM V(OH)(HCOO)$_2$, (C) solution of 0.5 mM HCOOH and 1 mM V(OH)(HCOO)$_2$, (D) solution of 1 mM HCOOH and 1 mM V(OH)(HCOO)$_2$ and (E) cyclic voltammograms of all these solution at 10 mV/s scan rate on graphite electrode.

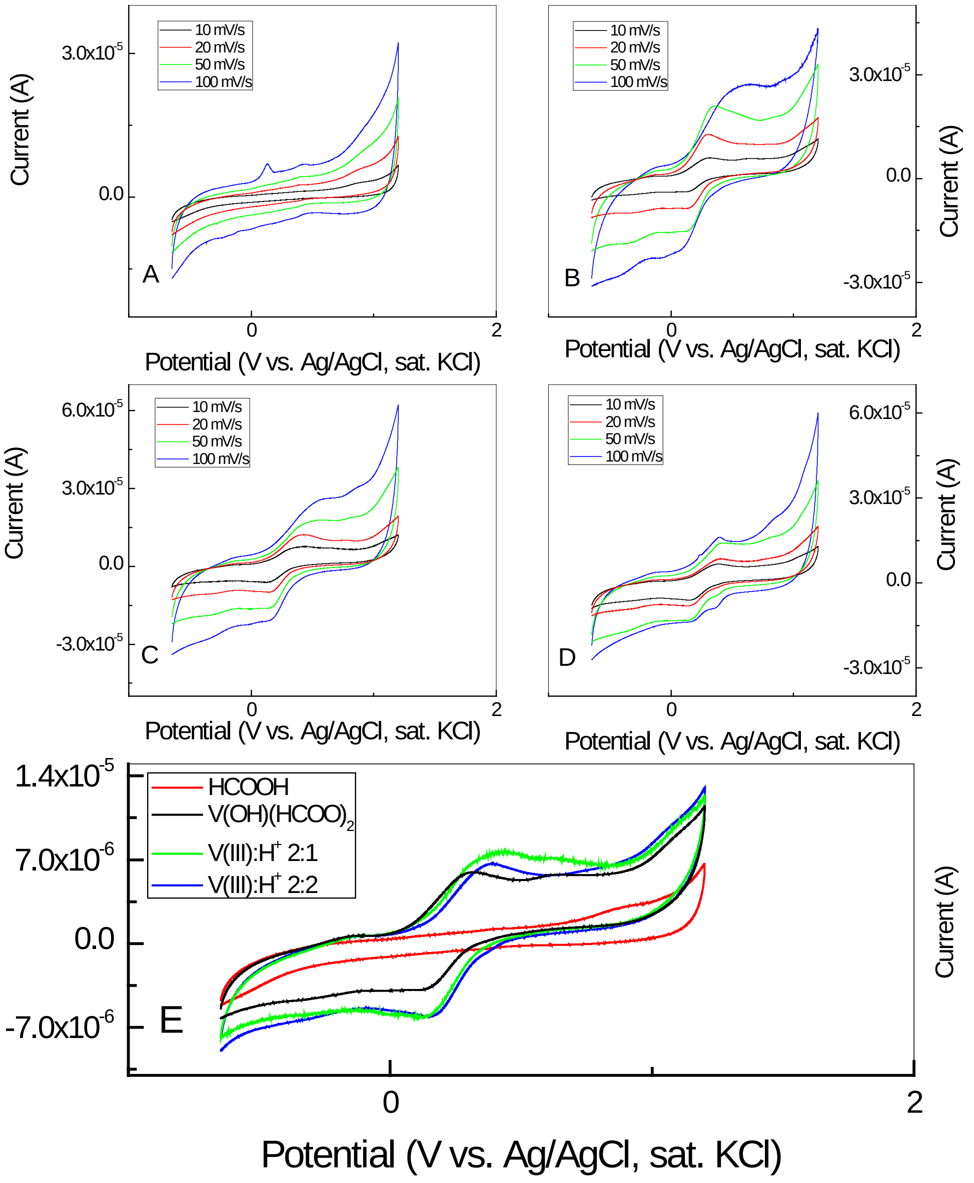

with increasing scan rate indicating irreversibility while the other peak at around -90 mV has remained fixed at the same potential. The peak height variation of the first peak with respect to square root of scan rate has shown a better fitting while the peak height variation with respect to the scan rate has shown a better fitting for the second peak. This indicates that the first peak is due to the faradic process while the second peak is due to adsorption of some species on the electrode.

Cyclic voltammograms for only $V(OH)(HCOO)_2$ on all electrodes has shown a good redox interaction. Stainless steel has shown irreversible peaks corresponding to V(III)/V(II) redox couple and also for V(IV)/V(III) redox couple. The peak positions have shifted with increasing scan rates but the peak height variation has followed a linear trend with the square root of scan rate indicating diffusion controlled faradic process. The irreversibility indicates that the process has sluggish kinetics on stainless steel electrode. The peak height of the peak observed at high positive potential (~1.0 V) during forward scan has decreased with increasing scan rate indicating that this peak corresponds to the V(IV)/V(V) oxidation process which depends on the concentration of in-situ generated V(IV). Addition of HCOOH to $V(OH)(HCOO)_2$ (**Fig 3.6 C** and **3.6 D**) has increased the irreversibility of V(III)/V(II) and V(IV)/V(III) redox couples. The forward peaks for both processes have vanished while the reverse peak for V(IV)/V(III) redox couple has shown a rise due to interfering acid reduction process. The forward scan also shows formate oxidation peak at high positive potentials. However this peak is lesser than that for only formic acid system. This is due to the consumption of acid by the formation of higher oxidation state vanadium species in the same potential region. The comparative variation of these voltammograms is shown in **Fig 3.6 E**. The sequential increase in the current with increasing acid in $V(OH)(HCOO)_2$ solution during the reverse scan in the potential region corresponding to acid reduction indicates that significant amount of current is consumed for acid reduction on the stainless steel electrode during the application of higher negative potential.

The cyclic voltammogram for only $V(OH)(HCOO)_2$ on glassy carbon electrode is shown in **Fig 3.7 B**. There is a redox peak corresponding to V(IV)/V(III) redox couple. The forward peak is irreversible while the reverse peak is at the fixed potential and hence reversible. Peak height variation with scan rate has shown that the process is diffusion controlled in both the directions. Rising part of the voltammogram at higher positive potentials (~1.0 V) during forward scan is for V(IV)/V(V) oxidation process which is dependent on the in-situ generated V(IV). Again the rising part in the reverse scan at extreme negative potential (> -0.5 V) is due to V(III)/V(II) reduction process. Addition of HCOOH to $V(OH)(HCOO)_2$ solution has changed the shape of voltammogram as shown in **Fig 3.7 E**. The V(IV)/V(III) redox couple has become increasingly irreversible with the continuous vanishing of V(III)/V(IV) oxidation peak. While the V(IV)/V(III) reduction peak has continuously increased with acid addition. Again the current in the region of V(IV)/V(V) oxidation process has also decreased with increasing acid concentration. This indicates formation of a different V(IV) species with increasing acid concentration which has a different redox behaviour on glassy carbon surface. The decrease in current at extreme negative potentials during reverse scan is conforming to the Tafel investigations wherein reduction in current was seen with increasing acid concentration. This confirms the blocking of active sites by H^+ adsorption on carbon surfaces. However, there is no loss of current due to hydrogen evolution from acid

Fig 3.9: Variation of peak current height with respect to the square root of scan rate

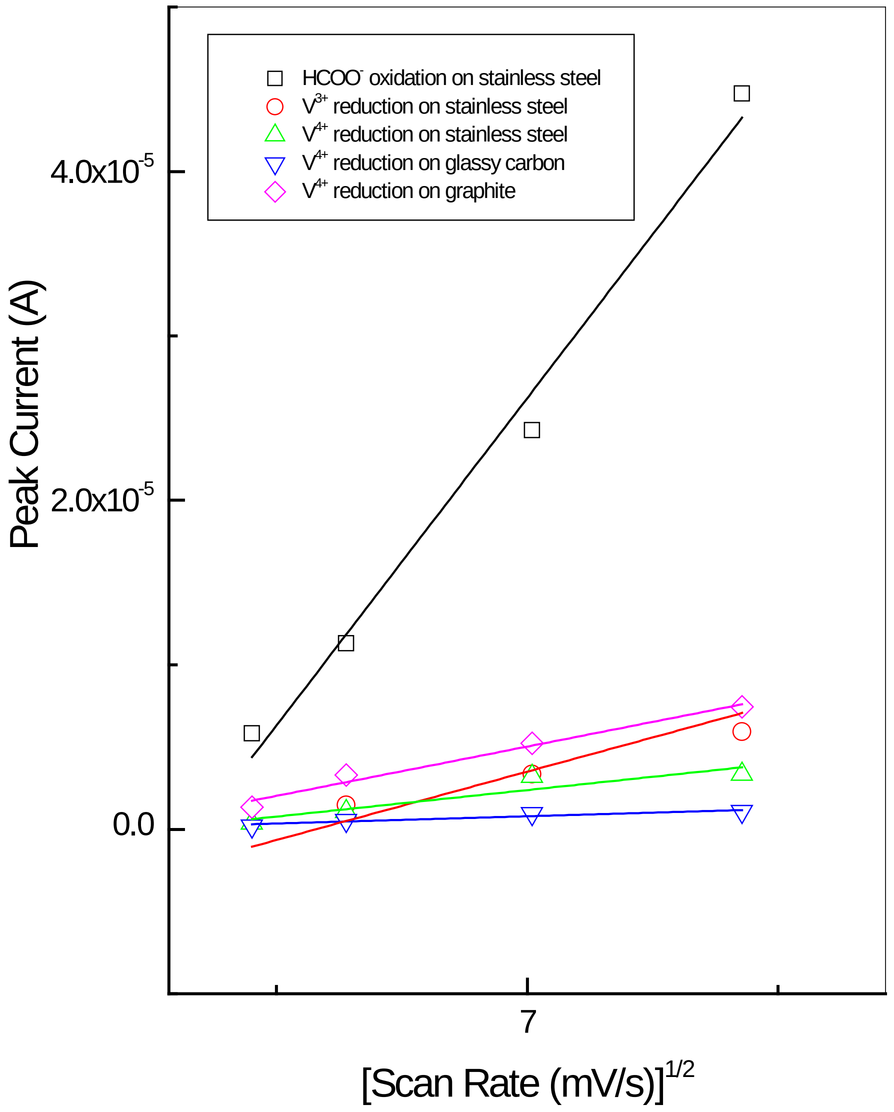

reduction when excess acid is added to $V(OH)(HCOO)_2$ solution on glassy carbon electrode.

The cyclic voltammogram for only $V(OH)(HCOO)_2$ on graphite electrode is shown in **Fig 3.8 B**. The irreversible V(IV)/V(III) redox couple with a diffusion controlled current behaviour is seen in the central region of the voltammogram. Here again the forward peak is irreversible while the backward peak was obtained at same potential indicating reversibility. Some typical plots of peak current variation with square root of scan rate are shown in **Fig 3.9**. V(IV)/V(V) oxidation process and V(III)/V(II) reduction process are seen in the similar region as that of glassy carbon electrode. Thus, voltammogram on graphite resembles with that on glassy carbon electrode for $V(OH)(HCOO)_2$. However, the addition of HCOOH to $V(OH)(HCOO)_2$ solutions has shown irregular behaviour on graphite electrode but with some similarity to those on glassy carbon electrode. This irregularity can again be attributed to the highly porous surface of graphite which will lead to intercalation of ions inside the pores and hence complications in the voltammogram.

3.3.4 Synthesis and characterization of different oxidation state vanadium solids

Constant current electrolytic reduction of 350 mM $VO(HCOO)_2$ resulted in precipitation of a V(III) formate in the cathode compartment. **Fig 3.10** shows the solution potential variation during the electrolysis. Initial sharp change in the solution potential is due to the conversion of residual V(V) to V(IV) which amounts to around 7 % of the total

Fig 3.10: Solution potential and current variations during the progress of electrolysis

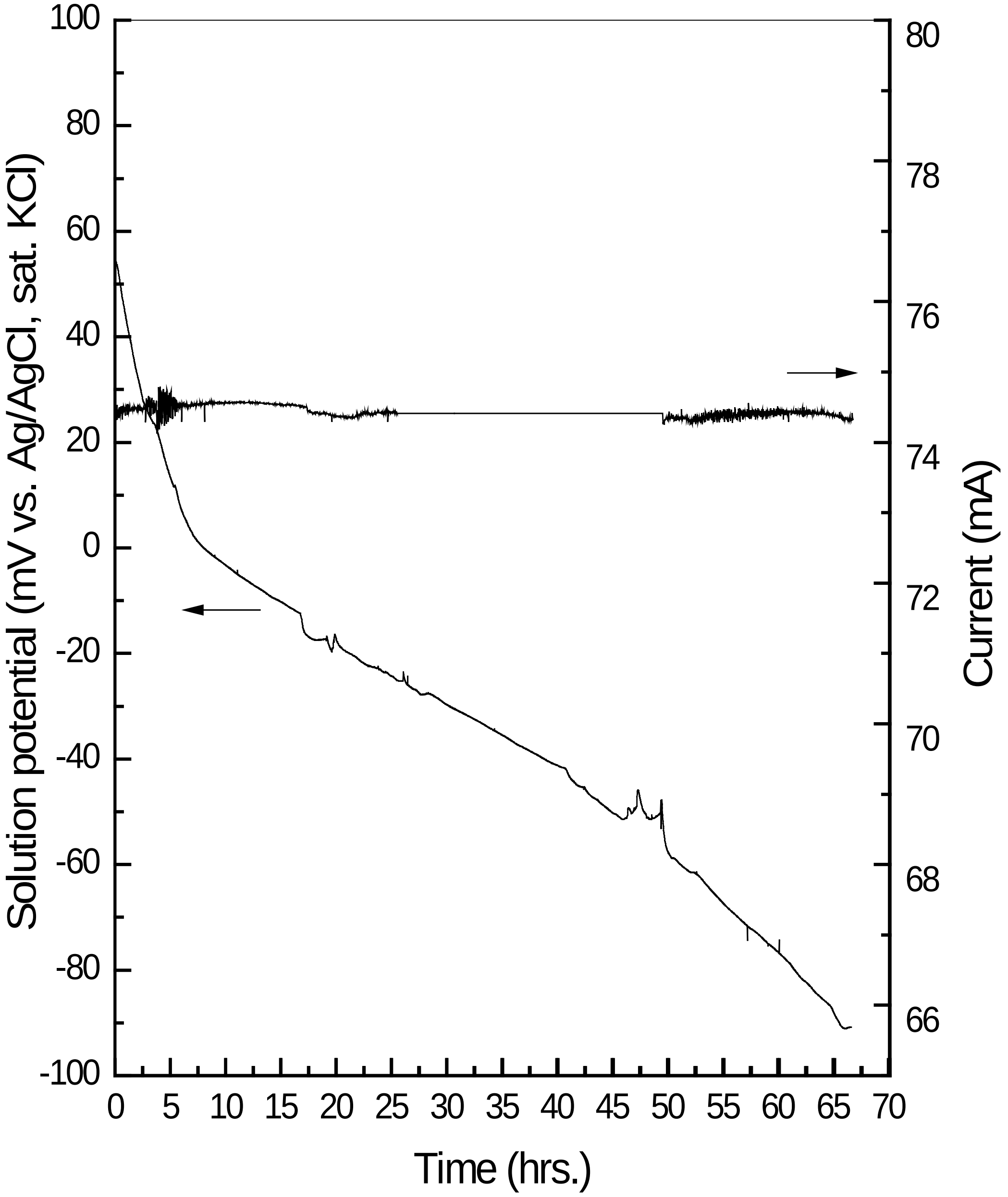

concentration as per the coulometric calculation. The subsequent shift in the slope corresponds to V(IV) → V(III) reduction. There is a continuous consumption of acid in cathode compartment as per equation (3.6) and a continuous rise in concentration of acid in anode compartment as per equation (3.8) with the progress of electrolysis. This leads to a gradual rise in pH in cathode compartment with progress of electrolysis.

There are two sharp peaks in solution potential variation graph in the region corresponding to around 38 % conversion of V(IV). The sudden rise in solution potential at this instance indicates that there is an instantaneous variation in V(IV) to V(III) ratio in favour of V(IV). This indicated V(III) precipitation. The combination of coulometric calculation and potential shift due to concentration as indicated by Nernst equation has been used to evaluate the amount of V(III) precipitated out. The first peak corresponds to precipitation of 25.2 mmols of V(III) and the second peak corresponds to 11.1 mmols of V(III). While solution concentration of V(III) just before the rise of potentials were 133 mM and 105 mM respectively. This indicates that the precipitation of V(III) during the electrolysis is dependent on both concentration of V(III) and pH. At higher pHs precipitation occurs at lower V(III) concentration. Thus, the yield of the precipitate can be further increased by increasing the pH. It may be noted here that at much lower initial concentration of vanadium with similar solution composition, V(II)-formate solution is obtained as the final product of electrolysis.

Compositional characterization of synthesized vanadium compounds: The synthesis of other vanadium formate solids has been described in chapter 2. The solids were analyzed for the chemical composition using atomic absorption spectrophotometer (AAS) and inductively coupled plasma atomic emission spectrophotometer (ICP-AES) for the metal ions and using ion chromatography (IC) for the formate ions. The details of experimental procedure are given in Chapter 2. The optimum working conditions for the FAAS were wavelength of 318.5 nm, hollow cathode lamp current of 20 mA, N_2O flow rate of 13 l/min and acetylene flow rate of 6.8 l/min. The standards were prepared from the same stock of $NaVO_3$. The summary of results obtained from the chemical analysis is given in **Table 3.4**.

Table 3.4: AAS elemental analysis of solids dissolved in ultrapure nitric acid

S. No.	**Sample description**	**Wt. taken in 50ml (mg)**	**Sodium (ppm)**	**V (ppm) (20 times diluted)**	**ZInc (ppm)**
1	V^{5+} : HCOOH = 1 : 2 solution precipitate	10.21	8.68 ± 0.52	4.63 ± 0.32	BDL
2	V^{5+} : HCOOH = 1 : 6 solution precipitate	10.42	6.81 ± 0.42	4.97 ± 0.36	BDL 0
3	V^{4+} precipitated by exceeding solubility limit	9.87	0.24 ± 0.32	2.84 ± 0.23	BDL 0
4	V^{3+} precipitated by electrolysis	10.24	0.13 ± 0.42	2.79 ± 0.23	BDL 0
5	Air oxidized V^{3+} precipitate	10.05	1.36 ± 0.38	3.17 ± 0.24	BDL 0
6	V^{2+} formate precipitated from zinc amalgam	10.16	BDL	2.97 ± 0.21	2.47 ± 0.18

BDL: Below detection limit

The AAS analysis of vanadium suffered from severe deposition on the burner which affected the flame characteristics and hence the vanadium analysis from AAS required verification form alternate method. ICP AES has been used to verify the results of AAS. Emissions from Na, V and Zn were measured at 309.311, 330.237 and 202.551 nm respectively. Triplicate analysis were done and the mean value is reported. The results of ICP AES analysis is summarized in **Table 3.5**.

The solids were dissolved in equimolar concentration of nitrilotriacetic acid (NTA) and citric acid (CA) as per the ICP-AES results. 15 mg of solid was dissolved in the required amount of NTA and CA in sealed test tubes by heating 80 ^{o}C in a water bath and ultrasonicating it till a clear solution was obtained. The UV – visible spectra was acquired for these solutions. UV – visible spectra of these samples in NTA solution is shown in **Fig 3.11** and that in the citric acid solution is shown in **Fig 3.12**. These solutions were also analysed for total vanadium and the redox compostion of vanadium by the spectrophotometric methodology which is discussed in the next chapter.

Table 3.5: ICP-AES elemental analysis of solids dissolved in ultrapure nitric acid

S. No.	Sample description	Wt. taken in 50ml (mg)	Na (ppm)	V (ppm)	Zn (ppm)
1	V^{5+} : HCOOH = 1 : 2 solution precipitate	6.89	5.92 ± 0.09	65.85 ± 0.38	BDL
2	V^{5+} : HCOOH = 1 : 6 solution precipitate	7.10	4.59 ± 0.08	71.80 ± 0.65	BDL
3	V^{4+} precipitated by exceeding solubility limit	6.90	0.20 ± 0.05	42.28 ± 0.34	BDL
4	V^{3+} precipitated by electrolysis	7.10	0.12 ± 0.08	42.13 ± 0.45	BDL
5	Air oxidized V^{3+} precipitate	6.86	0.91 ± 0.21	47.66 ± 0.37	BDL
6	V^{2+} formate precipitated from zinc amalgam	7.20	BDL	46.32 ± 0.14	1.76 ± 0.04

BDL: Below detection limit

The UV-visible spectra of V(V) solids dissolved in both NTA and CA medium indicate the presence of V(IV) in the solution. The absorbance seen in the high wavelength region can only be ascribed to V(IV) species as V(V) can not show any absorption in higher wavelength regions. Pentavalent vanadium has no d electron and

Fig 3.11: UV-visible spectra of vanadium samples dissolved in nitrilotriacetic acid. 1) solid obtained by exceeding the solubility of V^{5+} : HCOOH = 1 : 2 solution; 2) solid obtained by exceeding the solubility of V^{5+} : HCOOH = 1 : 6 solution; 3) solid obtained by exceeding the solubility of V^{4+} : HCOOH = 1 : 6 solution; 4) V^{3+} solid obtained by electrolysis of V^{4+} formate; 5) Air oxidized V^{3+} precipitate and 6) V^{2+} formate precipitated from zinc amalgam

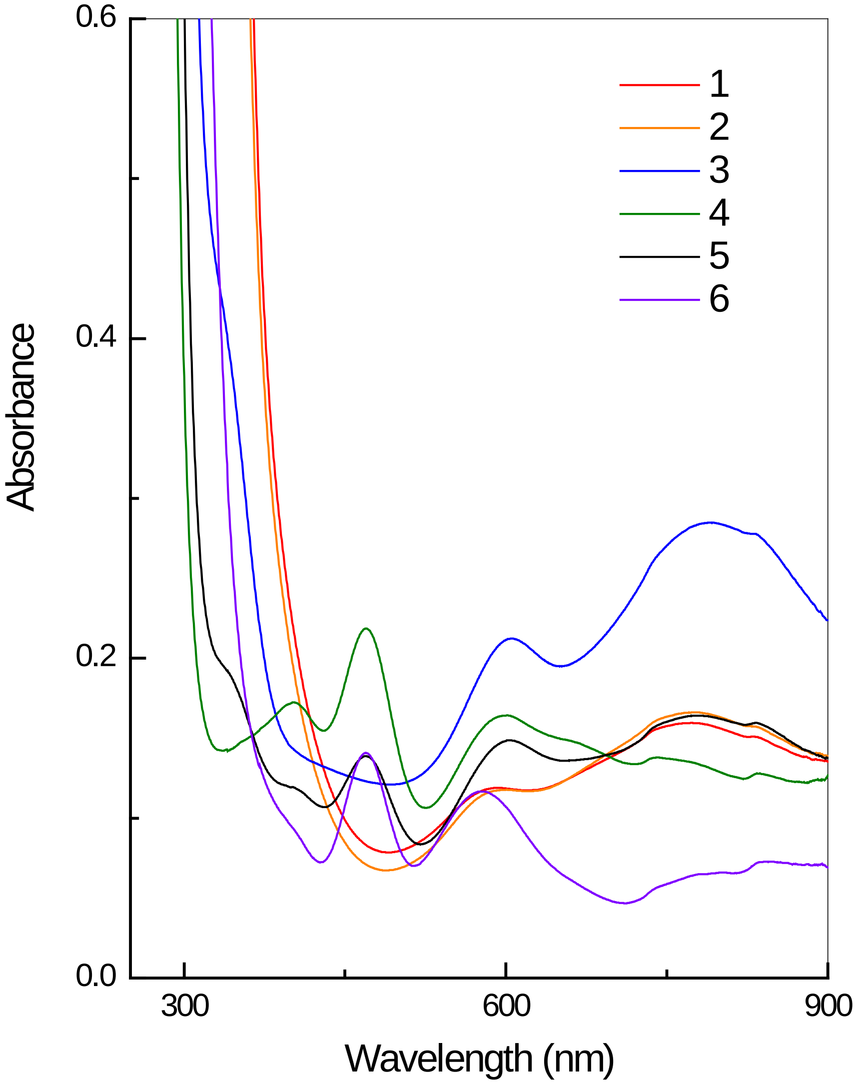

Fig 3.12: UV-visible spectra of vanadium samples dissolved in citric acid. 1) solid obtained by exceeding the solubility of V^{5+} : HCOOH = 1 : 2 solution; 2) solid obtained by exceeding the solubility of V^{5+} : HCOOH = 1 : 6 solution; 3) solid obtained by exceeding the solubility of V^{4+} : HCOOH = 1 : 6 solution; 4) V^{3+} solid obtained by electrolysis of V^{4+} formate; 5) Air oxidized V^{3+} precipitate and 6) V^{2+} formate precipitated from zinc amalgam

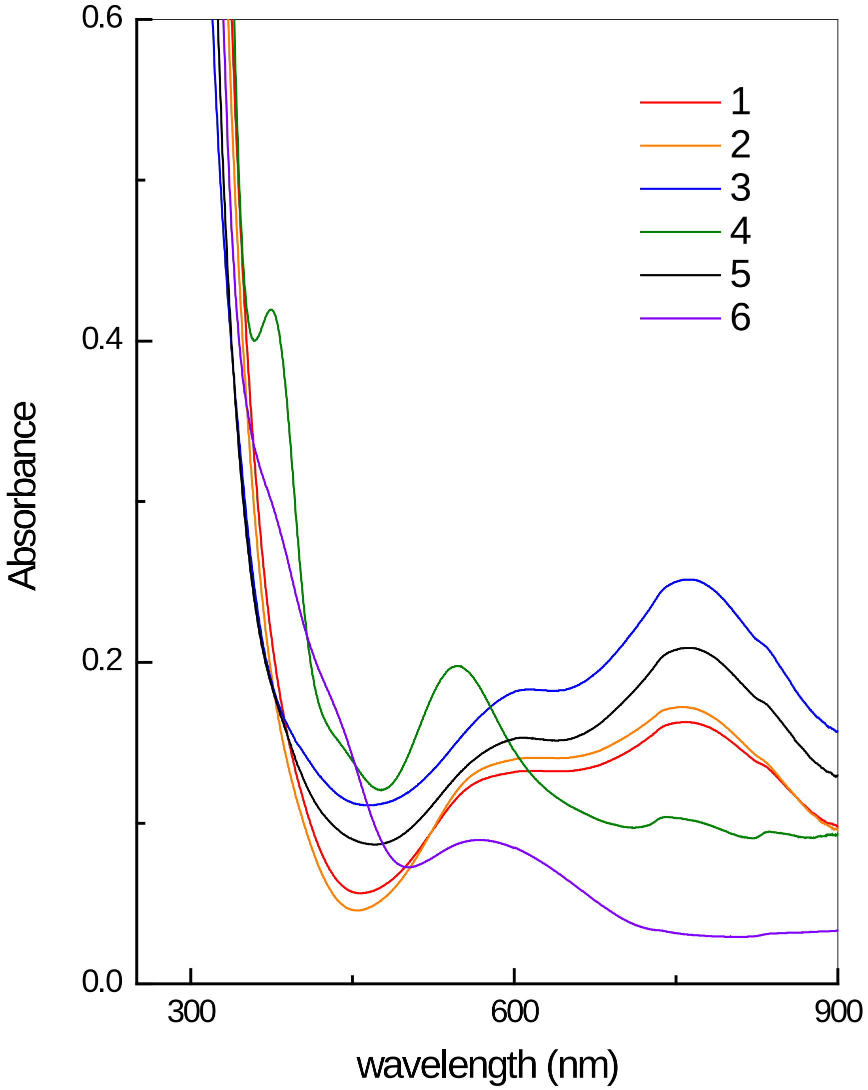

hence d-d transitions are not possible. The electronic absorption spectrum for V(V) are ascribed to charge transfer bands which appear in the wavelength region of around 220 - 270 nm [17]. The dissolution was carried out under inert condition with the organic acid ligands which have lower standard reduction potential values than that for V(V)/V(IV) redox couple. This could have resulted in the formation of V(IV) during the dissolution [18]. As per the spectrophotometric redox speciation analysis, 41.2 % V(V) was converted into V(IV) in nitrilotriacetic acid medium while 63.7 % V(V) was converted into V(IV) in citric acid medium.

The V(IV) electronic transition exhibits two bands characteristic of VO^{2+} ions in tetragonal symmetry (not the octagonal symmetry because the distance between the V atom and the axial ligand molecule is longer than that of the corresponding planar ligand molecules). In the tetragonal C_{4V} symmetry the electronic transitions are described by $^2B_{2g} \rightarrow E_{2g}$ and $^2B_{2g} \rightarrow {}^2B_{1g}$ respectively [19]. The intense band in the region of 780 nm ($^2B_{2g} \rightarrow E_{2g}$) and a weak shoulder in the region of 600 nm ($^2B_{2g} \rightarrow {}^2B_{1g}$) are the characteristic d-d transitions of aqueous vanadyl ion. The spectra of vanadyl in different media is shown separately in plot A, **Fig 3.13**. The $^2B_{2g} \rightarrow E_{2g}$ transition remains unaltered for NTA (789 nm) and formic acid medium but it has slightly shifted to lower wavelength in citric acid medium (760 nm). The $^2B_{2g} \rightarrow {}^2B_{1g}$ transition has been more intense in both NTA (605 nm) and citric acid (609 nm) medium as compared to formic acid (635 nm) medium and also it is slightly shifted to lower wavelength in these complexing media.

The UV-visible spectra of the compound precipitated by electrolysis indicates that vanadium is present in only V(III) oxidation state. The aqueous solution of the compound has no peak beyond 750 nm which clearly indicates absence of V(IV) in solution. The broad band with a peak at around 584 nm corresponds to the d-d transition $^3T_{1g}(F) \rightarrow {}^3T_{2g}(F)$ and the high absorbance shoulder with a peak at 418 nm is due to the charge transfer transition to $^3A_{2g}(F)$ state of the hydroxylated V(III) in solution. The red shift in the d-d transition for V(III)-NTA complex (467 nm) corresponding to $^3T_{1g}(F) \rightarrow {}^3T_{2g}(F)$ indicates the heptadentate nature of the complex. NTA is known to form mononuclear heptadentate complex with V(III) in aqueous medium. Two less intensity peaks are also seen on either side of this transition at 399 and 594 nm respectively. The compound was also dissolved with citric acid in equimolar concentration ratio to evaluate the solubility of V(III)-citrate complex. V(III)-citrate spectra is similar in nature to the spectra of the original compound but with blue shifted peaks viz. 547 nm for $^3T_{1g}(F) \rightarrow {}^3T_{2g}(F)$ and 373 nm for the charge transfer transition indicating chelating effect of citrate. The V(III) spectra in various complexing media is shown in plot B, **Fig 3.13**.

Divalent vanadium (V^{2+}) of d^3 configuration in aqueous solutions can give three electronic transitions, i.e., $^4A_{2g} \rightarrow {}^4T_{2g}$, $^4A_{2g} \rightarrow {}^4T_{1g}(F)$ and $^4A_{2g} \rightarrow {}^4T_{1g}(P)$ in an octahedral geometry. In $[V(H_2O)_6]$, the three bands are observed at 416, 571 and 847 nm [20]. The inherent instability of the V(II) solutions makes it difficult to interpret its UV-visible spectra. The vanadium formate UV-visible spectra has shown two peaks at 826 and 562 nm which can be assigned to $^4A_{2g} \rightarrow {}^4T_{2g}$ and $^4A_{2g} \rightarrow {}^4T_{1g}(F)$ transitions. The UV-visible spectra in NTA medium has shown one intense peak at 471 nm and a broad weak peak at 590 nm. Both these peaks are located at very similar wavelengths as compared to that of the corresponding V(III) species but the broad peak around 373 nm is not seen in the case of V(II) NTA. The V(II) spectra in citric acid solution has shown a

Fig 3.13: UV – visible spectra of (A) V(IV); (B) V(III) and (C) V(II) solids redissolved in nitrilotriacetic acid (NTA); Citric acid (CA) and formic acid.

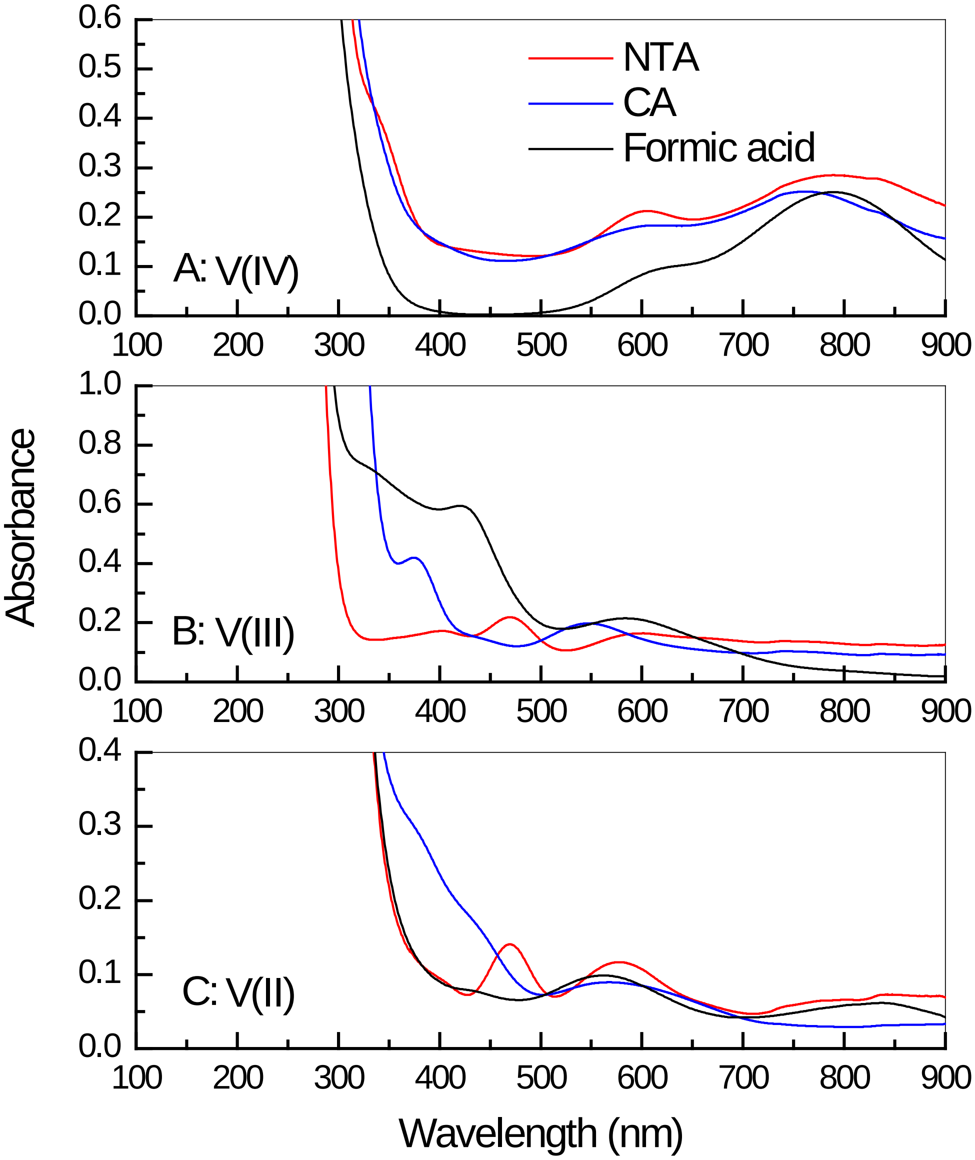

single broad peak with $\lambda_{max.}$ at 568 nm. These spectra are shown in plot C, **Fig 3.13**. As per the spectrophotometric redox speciation analysis, 2.74 % V(II) was converted into V(III) in NTA medium while 7.2 % V(II) was converted into V(III) in citric acid medium.

Fig 3.14 shows the typical ion chromatograms of the vanadium formate solids dissolved in citric acid (Plot B, **Fig 3.14**) and NTA (Plot C, **Fig 3.14**). The ion chromatogram for the standard formate ion is also shown in Plot A, **Fig 3.14**. The retention time for formate ion on the column has been found to be 2.94 minutes which remained unchanged for either NTA medium or the citric acid medium. An additional broad peak is seen for NTA dissolved samples which could be due to the negatively charged complex formed in this medium that remains unaffected upon passing through the column.

The formate amount determined in the samples were corrected for the sodium and zinc concentrations present in the solid as per the ICP-AES analysis. The weights of solids were corrected for sodium formate and zinc formate and the remaining weights were taken as that of the actual vanadium compound. The calculated weight ratio and the molar ratio of vanadium to formate for these solid is enlisted in **Table 3.6.**

Thermogravimetric analysis of vanadium compounds: Thermogravimetric analysis of the samples were also done to evaluate the thermal stability and also to further elucidate the empirical formulae for the synthesized compounds.TG and DTA plots of V(IV) formate are shown in **Fig 3.15.** There is a single step of weight loss in both air and nitrogen atmosphere and the sample has shown very good stability upto 190 ^{o}C in both

Fig 3.14: Typical chromatograms of (A) formate standard; (B) citric acid dissolved vanadium formate solid and (C) nitrilotriacetic acid dissolved vanadium formate solid

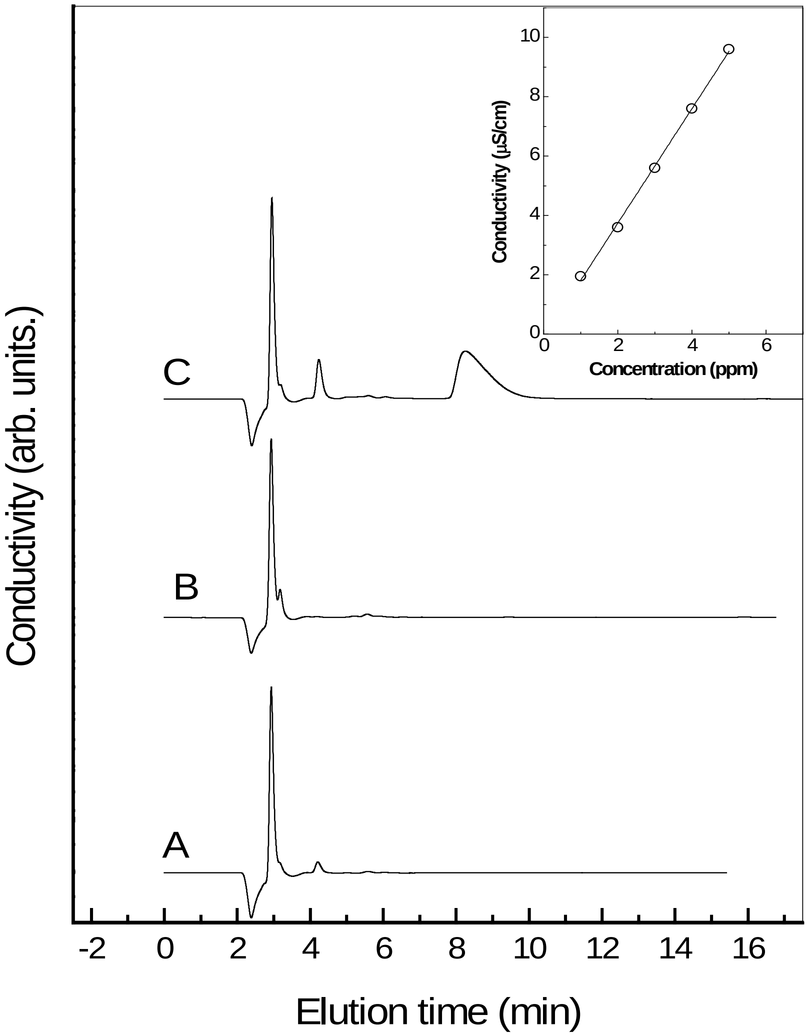

Table 3.6: Calculated weight ratio of vanadium and formate and mole ratio of formate with respect to vanadium in the sodium and zinc formate corrected vanadium compound

S. No.	Sample description	V (g/g)	Formate (g/g)	Formate (g/g)	Moles of formate per mole of V	
			(NTA dissolved sample)	(CA dissolved sample)	(NTA dissolved sample)	(CA dissolved sample)
1	V^{5+} : HCOOH = 1 : 2 solution precipitate	0.547	--	--	--	--
2	V^{5+} : HCOOH = 1 : 6 solution precipitate	0.559	--	--	--	--
3	V^{4+} precipitated by exceeding solubility limit	0.297	0.517	0.521	1.97	1.99
4	V^{3+} precipitated by electrolysis	0.324	0.572	0.565	2.00	1.98
5	Air oxidized V^{3+} precipitated by electrolysis	0.354	0.633	0.684	2.02	2.19
6	V^{2+} formate precipitated from zinc amalgam	0.292	0.512	0.523	1.99	2.03

environments. The weight loss is 51.8 % in air and 45.8 % in nitrogen atmosphere. The empirical formula for this compound based on charge and mass balance as per the values of **Table 3.6** and the TG data is proposed to be $VO(HCOO)_2 \cdot H_2O$. The weight loss for this compound in air would result in a residual weight of V_2O_5 which will be 52 % while in nitrogen atmosphere it will result in formation of VO_2 with the residual weight of 47.4 %. These values are in good agreement with the experimental values.

Fig 3.16 shows the TG plots of the V(III) compound obtained by electrosynthesis in air and nitrogen environments. The weight loss analysis indicated a presence of 8.84 % water in the sample. The subsequent overall percent weight loss amounts to 46.9 % in nitrogen atmosphere. This matches well with the $V(OH)(HCOO)_2$ to V_2O_3 conversion which will undergo 47.5 % weight loss. In oxygen atmosphere, the weight loss

Fig 3.15: Thermogravimetric and differential thermal analysis plots for V(IV) formate in air and nitrogen atmosphere

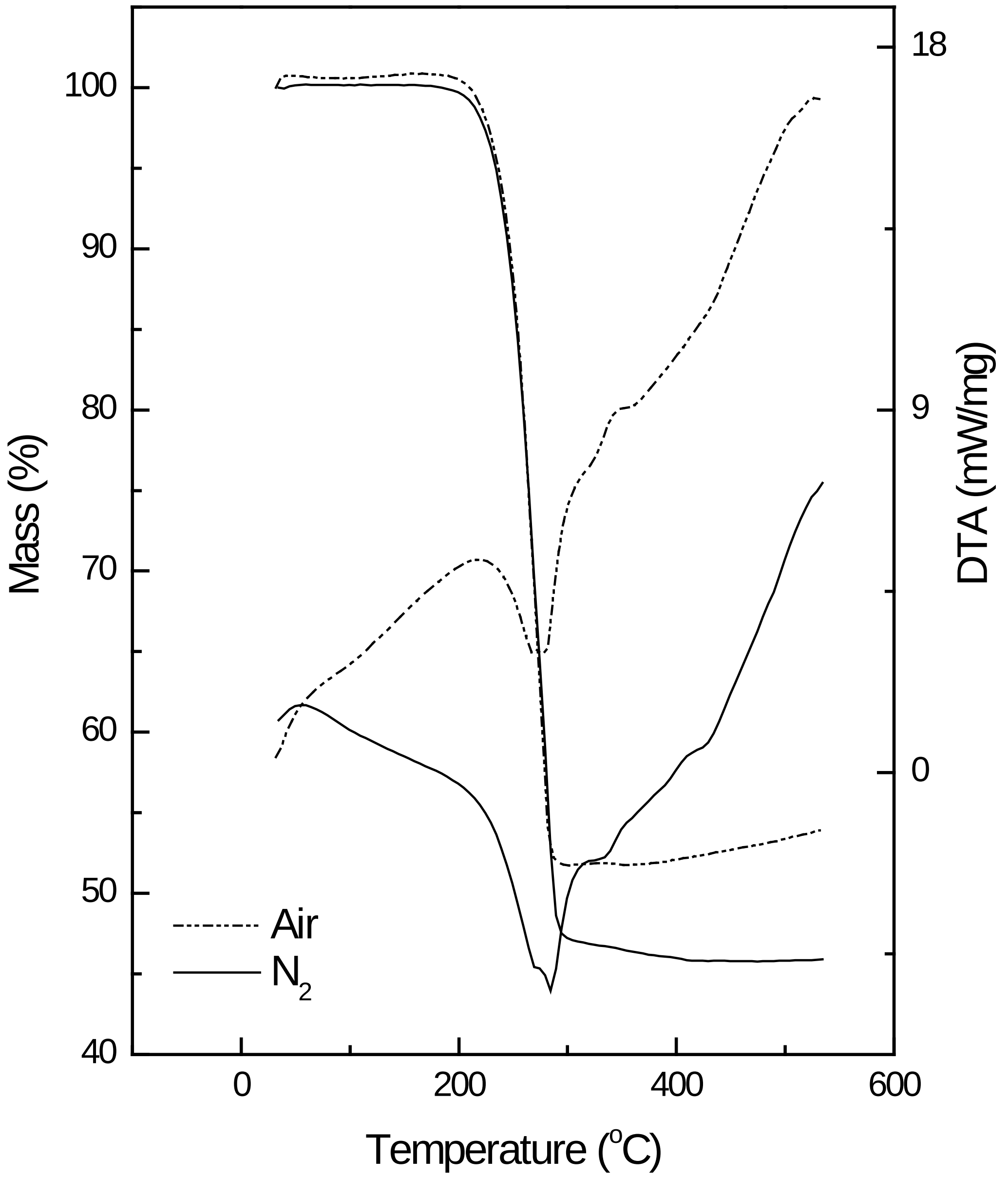

Fig 3.16: Thermogravimetric and differential thermal analysis plots for V(III) formate in air and nitrogen atmosphere

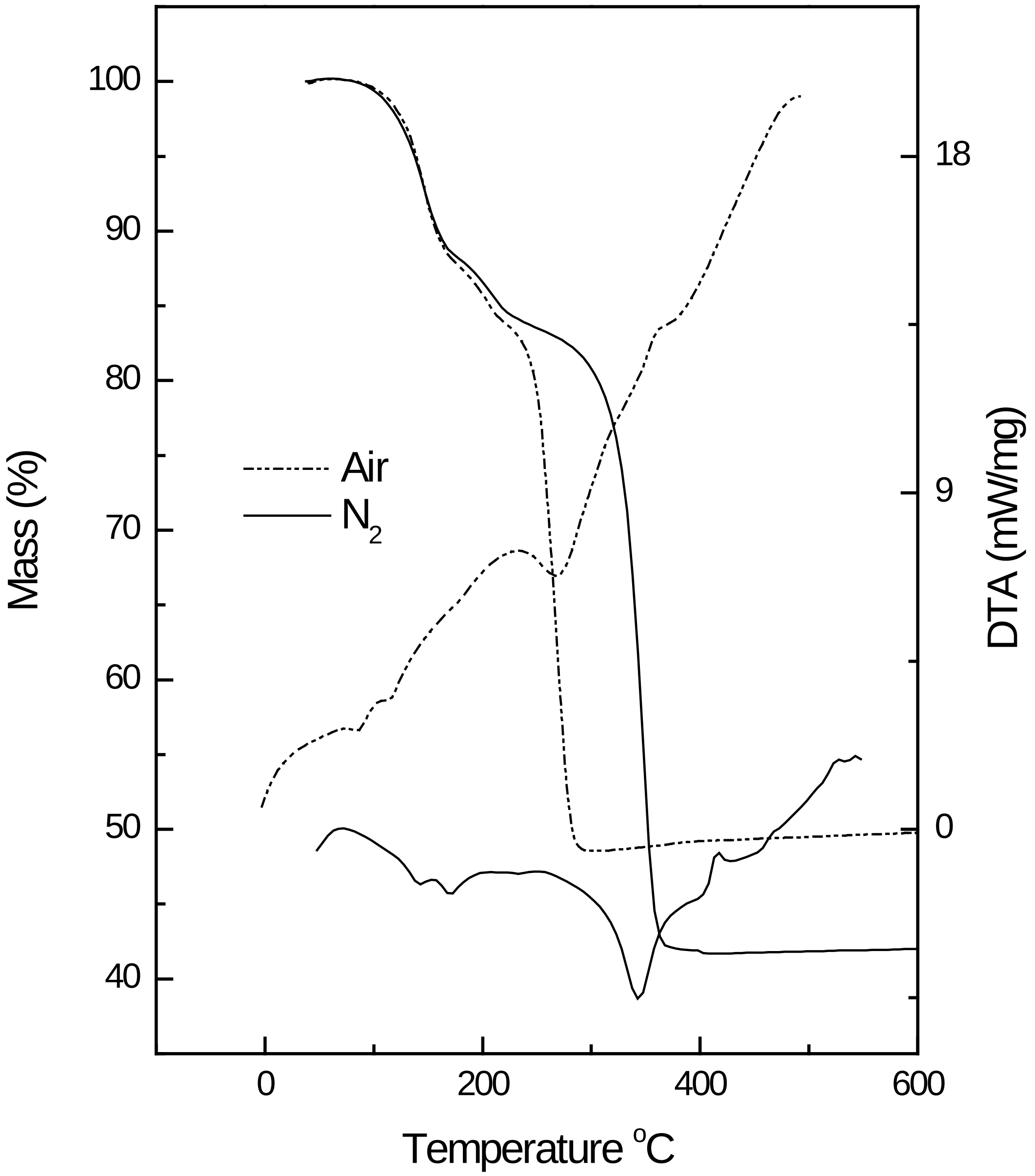

Fig 3.17: Thermogravimetric and differential thermal analysis plots for V(II) formate in air and nitrogen atmosphere

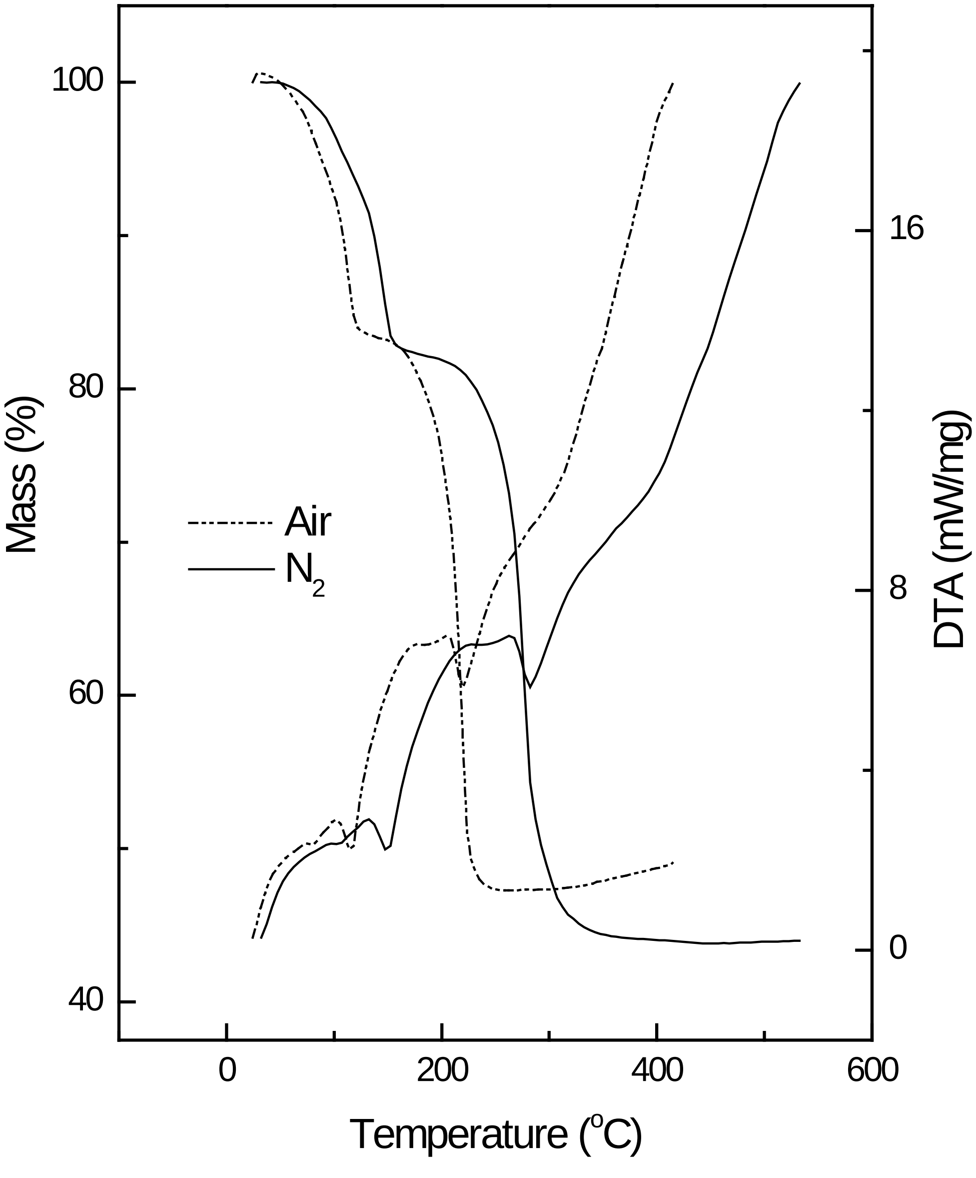

calculation after residual water correction comes to 54.5 % which matches well with the $V(OH)(HCOO)_2$ conversion to V_2O_5 amounting to a weight loss of 57.6 %. Thus, TG analysis has also indicated the same chemical composition of the precipitate as the one estimated by the chemical analysis. The TG pattern shows that the compound is stable upto 160 ^oC in air atmosphere although the overall stability is more in nitrogen atmosphere. There is a small hump in both atmospheres which correspond to a weight loss of around 5.2 %. This can be attributed to dehydration of $V(OH)(HCOO)_2$ resulting in $V_2O(HCOO)_4$. The second step corresponds to V_2O_3 formation in case of nitrogen atmosphere and V_2O_5 formation in air atmosphere.

Thermogravimetric and differential thermal analysis plots of V(II) formate in nitrogen and air atmosphere are shown in **Fig 3.17**. There are two step decomposition processes seen in both environments which are accompanied by endothermic peaks in differential thermogram plots. The decomposition process starts from the initial stage of heating itself in both the atmospheres, but the rate of decomposition is faster in air. The overall residual weight in air remains to 48.9 % while it comes down to 43.8 % in nitrogen atmosphere. These mass losses could be well explained if the formula weight of the V(II) compound is taken as $V(HCOO)_2{\cdot}2H_2O$. The overall decomposition processes can be represented as

$$4V(HCOO)_2{\cdot}2H_2O + 7O_2 \rightarrow 2V_2O_5 + 8CO_2 + 12H_2O \text{ (in air)} \qquad (3.9)$$

$$2V(HCOO)_2{\cdot}2H_2O \rightarrow V_2O_3 + 4CO_2 + H_2O + 5H_2 \text{ (in nitrogen)} \qquad (3.10)$$

These decompositions would result in a residual weight of 51.4 % and 42.4 % in air and nitrogen atmosphere respectively. The intermediate decomposition step results in the residual weight of 83.17 % in air and 82.12 % in nitrogen indicating similar product formation. The intermediate product can be formed by the oxidative dehydration of the parent compound which can be represented by as

$$4V(HCOO)_2\cdot 2H_2O + O_2 \rightarrow 2V_2O(HCOO)_4 + 8H_2O \text{ (in air)} \qquad (3.11)$$

$$2V(HCOO)_2\cdot 2H_2O \rightarrow V_2O(HCOO)_4 + 3H_2O + H_2 \text{ (in nitrogen)} \qquad (3.12)$$

These decompositions would result in the residual weight of 84.2 % which is in reasonable agreement with the experimental values. Thus the thermogravimetric analysis has further elucidated the empirical chemical formula of the vanadium compounds.

Infrared spectral evaluation of the vanadium compounds: Infrared spectrum of the vanadium solids are given in **Fig 3.18**. The infrared spectra of these compounds can be broadly divided into three regions. The one is the broad peak in the region of 3800 to 2500 cm^{-1} which is due to the hydroxide or water molecule in the compound, the next region corresponds to the asymmetric and symmetric vibrational modes of carboxyl groups which are located in the region of 1580 to 1560 cm^{-1} or split in two or more peaks and 1375 to 1350 cm^{-1} or split in two or more peaks respectively [21]. The third region corresponds to the group of peaks below 1100 cm^{-1} which correspond to the various possible V-O vibrational interactions.

Infrared spectrum of the V(V) compound, (plot A, **Fig 3.18**) shows a broad peak in the higher wavenumber region which can be attributed to the absorbed water. The moderate peak pattern in the intermediate region of 1750 to 1300 cm^{-1} can be attributed to the presence of sodium formate impurity in the compound. A single broad peak has been

Fig 3.18: Infrared spectrum of A) solid obtained by exceeding the solubility of V^{5+} : HCOOH = 1 : 6 solution; B) solid obtained by exceeding the solubility of V^{4+} : HCOOH = 1 : 6 solution; C) Air oxidized V^{3+} precipitate D) V^{3+} solid obtained by electrolysis of V^{4+} formate; and E) V^{2+} formate precipitated from zinc amalgam; in KBr matrix

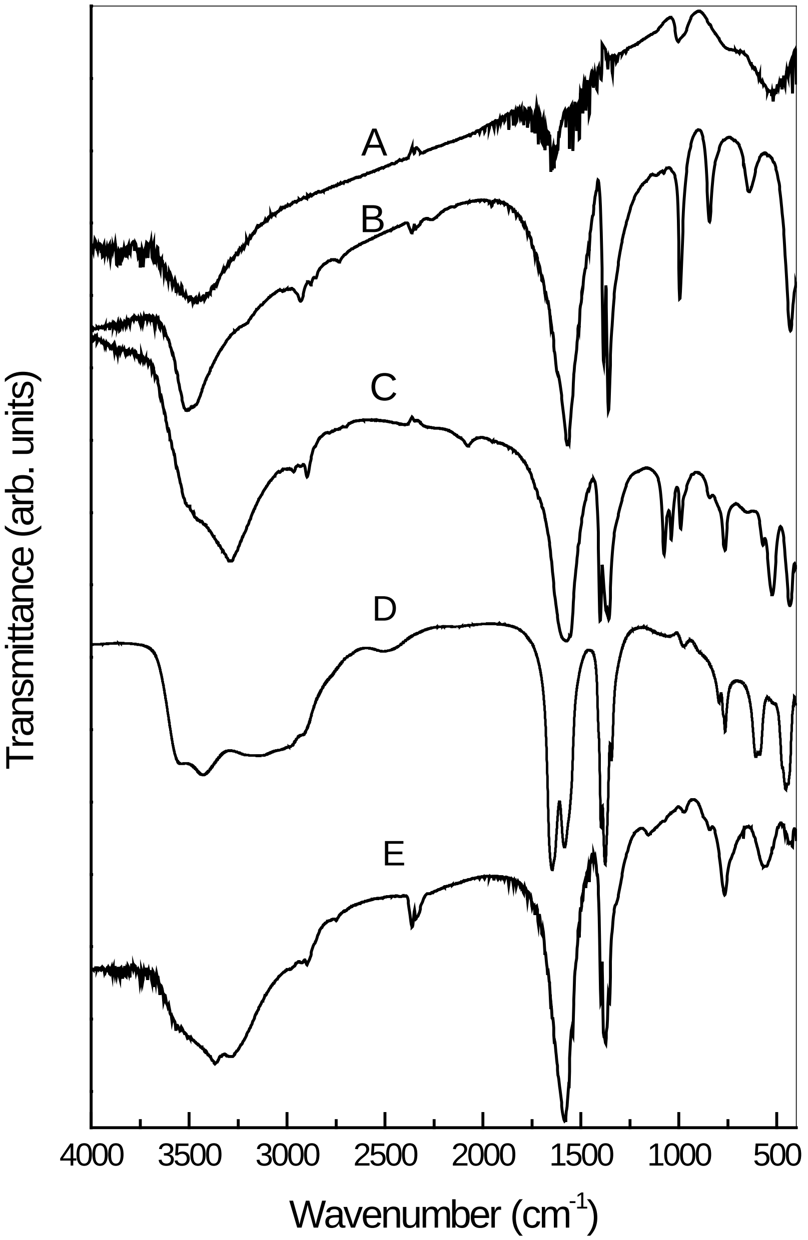

obtained in the region of 997 to 966 cm^{-1} which can be attributed to the V=O vibrational interaction which shows a peak in this region [22].

Infrared spectrum of the V(IV) compound (plot B, **Fig 3.18**) has shown a broad peak in the higher wavenumber region which indicates the presence of water molecule in the compound. The peaks at 1565 and 1361 cm^{-1} correspond to the asymmetric and symmetric vibrational modes of carboxyl groups. Frequency separation between asymmetric and symmetric vibrational modes of carboxyl groups have been used to differentiate the type of bonding between the metal and the ligand. The separation value of more than 200 cm^{-1} indicates the presence of ionic carboxylic species or monodentate coordination, whereas less than 150 cm^{-1} indicates chelating or bridging coordination [23]. The separation for these peaks is around 204 cm^{-1} in the V(IV) compound indicating absence of chelation or bridging coordination of carboxyl group. The sharp peak at 988 cm^{-1} correspond to the V=O vibrational interaction. The lower wavenumber peaks at 843 and 636 cm^{-1} could be due to other V-O vibrational interactions.

Infrared spectrum of the V(III) compound (plot D, **Fig 3.18**) has also shown a wide peak in the 2900 to 3600 cm^{-1} region which is due to the –OH vibrational absorption. The peaks at 1646 and 1375 cm^{-1} correspond to asymmetric and symmetric vibrational modes of carboxyl groups. The separation for these peaks is around 270 cm^{-1} which indicate the absence of chelation or bridging coordination of the carboxyl group in the V(III) compound. Also, the asymmetric stretching peak is split in two indicating strong interaction of V(III) with these vibrational levels. A weak band at around 1000 cm^{-1} which is the signature peak corresponding to V=O stretching mode indicates the presence of mild V(IV) impurity. The group of peaks around 453, 587, 606 and 762 cm^{-1} can be due to V-O vibrations.

Infrared spectrum of the air oxidized V(III) compound (plot C, **Fig 3.18**) has shown a mixed behaviour as compared to that of pure V(III) and V(IV) compounds. The interesting vibrational absorptions are in the lower wavenumber region. Here, the V=O vibrational absorption is split in three peaks located at 1074, 1038 and 991 cm^{-1}. Also, the lower V-O vibrational absorption peaks are shifted to higher wavenumbers as compared to that for the V(III) compound. These peaks are located at 453, 587, 606 and 762 cm^{-1}.

Infrared spectrum of the V(II) compound, (plot E, **Fig 3.18**) shows a broad peak in the higher wavenumber region which can be attributed to the presence of water molecule in the compound. The peaks at 1583 and 1373 cm^{-1} correspond to the asymmetric and symmetric vibrational modes of carboxyl groups. Again the separation of these peaks indicate that there is no chelating or bridging coordination of the carboxyl group in the V(II) compound. Two peaks located at 765 and 557 cm^{-1} could be seen at lower wavenumber regions which can be attributed to V-O vibrational interactions.

X-ray photoelectron (XPS) spectroscopic study of the vanadium compounds: X-ray photoelectron (XPS) spectra of the solids are shown in **Fig 3.19** and **3.20**. Peak analysis of the XPS spectra is given in **Table 3.7**. The V $2p_{3/2}$ peak has shown a variation in binding energy value from 516.8 eV to 517.8 eV. Most of the samples show wide peak width of V $2p_{3/2}$ ranging from 2.2 eV to 2.9 eV but the V(II)-formate precipitated from zinc amalgam has shown exceptionally wide V $2p_{3/2}$ peak with the FWHM of 3.7 eV. This can be due to the presence of multiple valence states of vanadium in the sample.

This indicates that the samples could have undergone some surface oxidation before the acquisition of XPS spectra. However, this trend of increasing FWHM with the decrease in the oxidation state of vanadium has been reported earlier [22]. There is a shift in the binding energy values of both V $2p_{3/2}$ and V $2p_{1/2}$ photoelectron peaks with the change in the oxidation state of vanadium in the sample as per the expected trend. Both these peaks have shifted to higher binding energies with the increasing oxidation state of vanadium in the samples. The O 1s peak for V(V) has been obtained at 530.7 eV with a peak width of 1.7 eV which matches well with that of the V_2O_5. The O 1s photoelectron peak has shown a variation from 532.6 eV to 533 eV with a peak width in the range of 2.2 to 2.4 eV for V(II) to V(IV) based samples. The oxygen is bound to the carboxylate moeity in these samples which can result in this higher binding energy for O 1s peaks [24]. Carbon 1s photo electron peaks for these samples is shown in Fig 3.20. C 1s peak at around 289.4 eV indicates the presence of COO- type carbon. The C 1s peak at around 285 eV indicates the presence of C=C type carbon (contaminant carbon also comes at this binding energy).

Thus, the XPS spectra again confirms that the V(V) sample is V_2O_5. V $2p_{3/2}$ shows a very small difference in binding energy for V(IV) and V(III) compounds namely 515.5 and 515.6 respectively. So these two states are not distinguishable by XPS spectra. V(V) shows significant shift from V(III) (around 1 eV) and hence these compounds are distinguishable by XPS analysis. The oxidation state of vanadium in the compounds of V(IV) to V(II) could only be broadly made out as the peak width has been too large for these compounds. Auger parameter may be a good parameter to evaluate these samples. But this needs standard stable samples for V(IV), V(III) and V(II).

Table 3.7: XPS Peak values of various vanadium solids

S. No	Sample description	V 2p 3/2 (eV) (FWHM)	O 1s (eV) (FWHM)	C1s (eV)	Atom percent
1	V^{5+} : HCOOH = 1 : 2 solution precipitate	517.3 (1.6)	530.1 (1.6)	284.2	O 64, V 25, C 11
2	V^{5+} : HCOOH = 1 : 6 solution precipitate	517.7 (1.8)	530.7 (1.7)	285.1	O 54, V 29, C 17
3	V^{4+} precipitated by exceeding solubility limit	517.8 (2.2)	533.0 (2.3)	285.1 289.4	O 58, V 11, C 31
4	V^{3+} precipitated by electrolysis	516.9 (2.9)	532.6 (2.2)	285.1 289.0	O 61, V 12, C 27
5	Air oxidized V^{3+} precipitated by electrolysis	517.5 (2.5)	532.8 (2.4)	285.1 289.5	O 64, V 14, C 22
6	V^{2+} formate precipitated from zinc amalgam	516.8 (3.7)	532.8 (2.2)	289.4	O 69, V 7, C 24

The elemental composition determined by the relative peak intensities is roughly in agreement with the compositional analysis by ICP-AES and ion chromatography.

X-ray diffraction study of the vanadium compounds: The formation of different phases of the formates of different vanadium ions were further confirmed from their powder XRD patterns. Typical powder XRD patterns recorded for these compounds are shown in **Fig 3.21.** All the XRD patterns were recorded by using well powdered samples mounted on a slide without any additional binder. Copper Kα X-ray was used for XRD studies and the diffraction data were collected in the step scan mode between the two-theta of 5 to 70°. From the **Fig 3.21**, it can be observed that all the samples except that of V(V) were crystalline in nature and have shown distinct sharp peaks. The preliminary analysis of the XRD data was carried out by comparing these with the standard XRD patterns of vanadium oxide, vanadyl oxy formate, and other related hydrate compounds. Except for

Fig 3.19: XPS spectra of vanadium and oxygen for A) solid obtained by exceeding the solubility of V^{5+} : HCOOH = 1 : 6 solution; B) solid obtained by exceeding the solubility of V^{4+} : HCOOH = 1 : 6 solution; C) Air oxidized V^{3+} precipitate D) V^{3+} solid obtained by electrolysis of V^{4+} formate; and E) V^{2+} formate precipitated from zinc amalgam

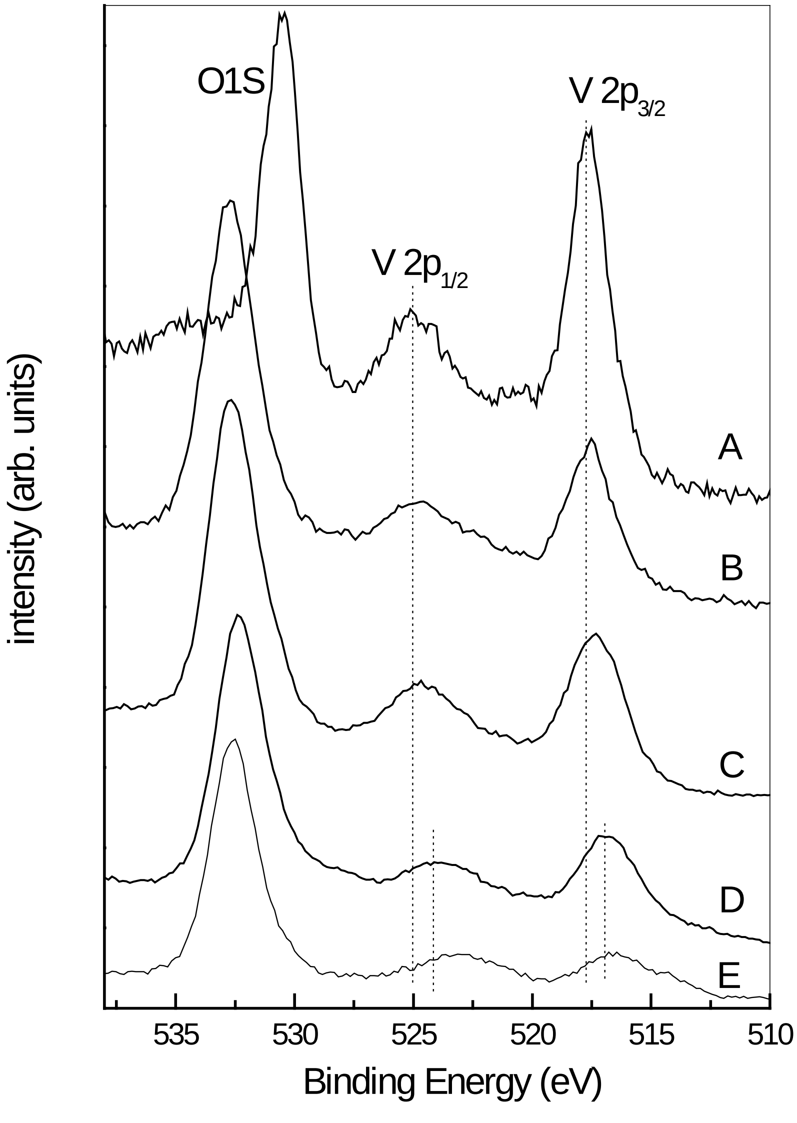

Fig 3.20: XPS spectra of carbon for A) solid obtained by exceeding the solubility of V^{5+} : HCOOH = 1 : 6 solution; B) solid obtained by exceeding the solubility of V^{4+} : HCOOH = 1 : 6 solution; C) Air oxidized V^{3+} precipitate D) V^{3+} solid obtained by electrolysis of V^{4+} formate; and E) V^{2+} formate precipitated from zinc amalgam

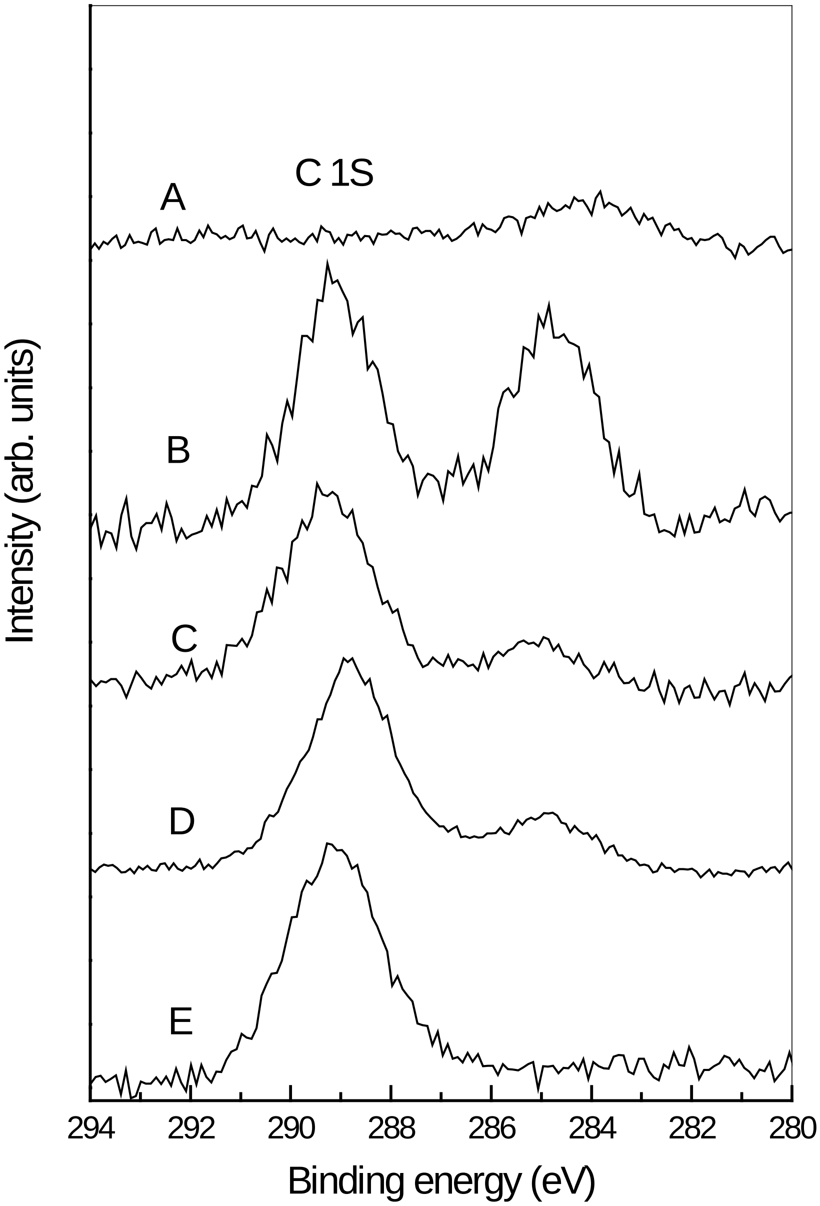

the V(IV) oxy formate, none of the XRD pattern could be assigned due to unavailability of any standard reference patterns. The observed d-values in the powder XRD pattern of V(IV) oxy formate were in close agreement with the reported vanadium oxy formate hydrate, $VO(HCOO)_2 \cdot H_2O$ phase of V(IV) (JCPDS-PCPDF- 01-074-6946). Thus the observed formate of the V(IV) could be assigned to this compound. However, the observed XRD pattern has shown shifts in the positions of some peaks and differences in the intensity distribution from the reported data. This could be due to either presence of preferred orientations or feeble but noticeable differences in the structure. The matched XRD pattern of the V(IV) formate compound with the Vanadium oxy formate Hydrate $VO(HCOO)_2 \cdot H_2O$, reported in the PCPDF database is shown in **Fig 3.22**.

The XRD pattern of V(III) and V(II) formate were subsequently analyzed by comparing the observed d-values and intensities with the JCPDS-PCPDF database. Any isostructural compound or phases in the available database (PDF2, version - 6.2) could not be matched to the observed peaks of the V(III) compound. Thus, the composition could be assumed as new structure type and hence needs more detailed investigation for the structure. Similar analysis for the XRD pattern of the V(II) formate revealed a close similarity to the reported pattern for $Fe(HCOO)_2 \cdot 2H_2O$ (JCPDS-PCPDF-19-0604). This compound is probably isomorphous with several other formate dehydrates of group 3A divalent transition metal ions like Ni^{2+}, Cu^{2+}, Zn^{2+}. The matched XRD pattern of the V(II) formate compound with the cupric formate diydrate $Cu(HCOO)_2 \cdot 2H_2O$, reported in the PCPDF database is shown in **Fig 3.23**.

The phase analysis of the compounds were further done to get some insight into their structures. The observed reflections were indexed to get unit cell parameters. All the

Fig 3.21: XRD pattern of A) solid obtained by exceeding the solubility of V^{5+} : HCOOH = 1 : 6 solution; B) solid obtained by exceeding the solubility of V^{4+} : HCOOH = 1 : 6 solution; C) V^{3+} solid obtained by electrolysis of V^{4+} formate; and D) V^{2+} formate precipitated from zinc amalgam

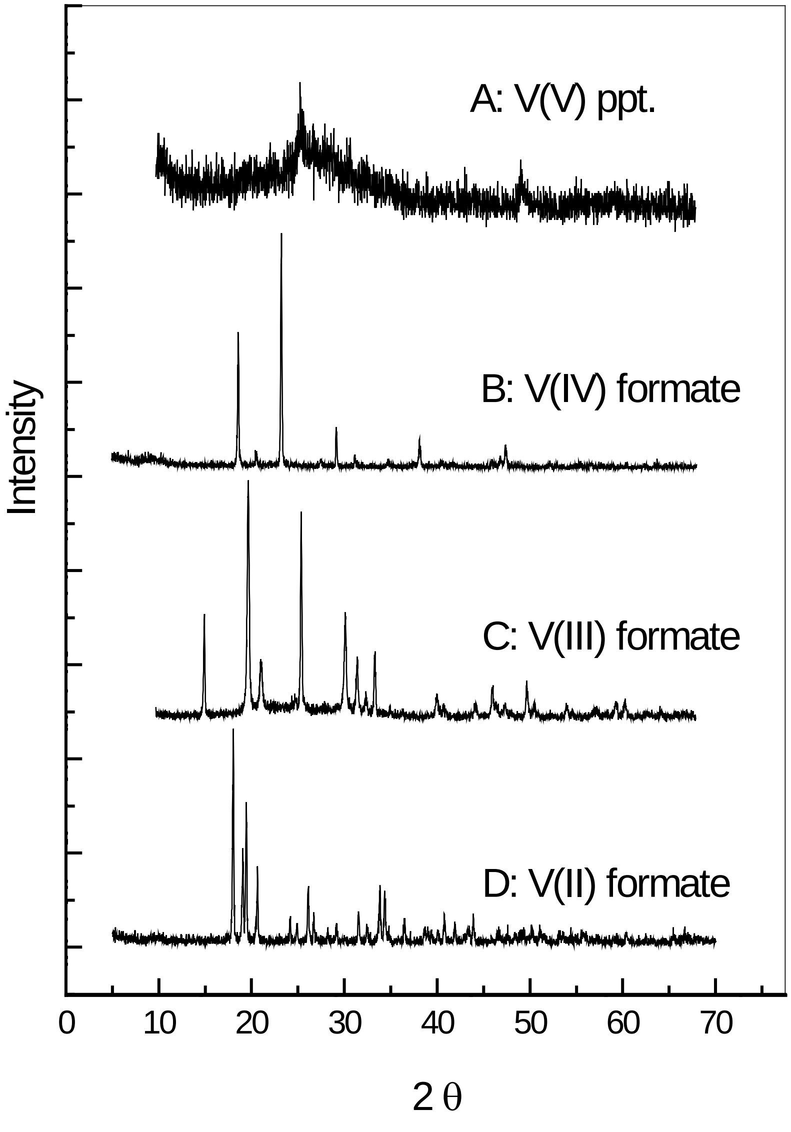

Fig 3.22: Comparison of the XRD pattern of V(IV) formate with the matched reference

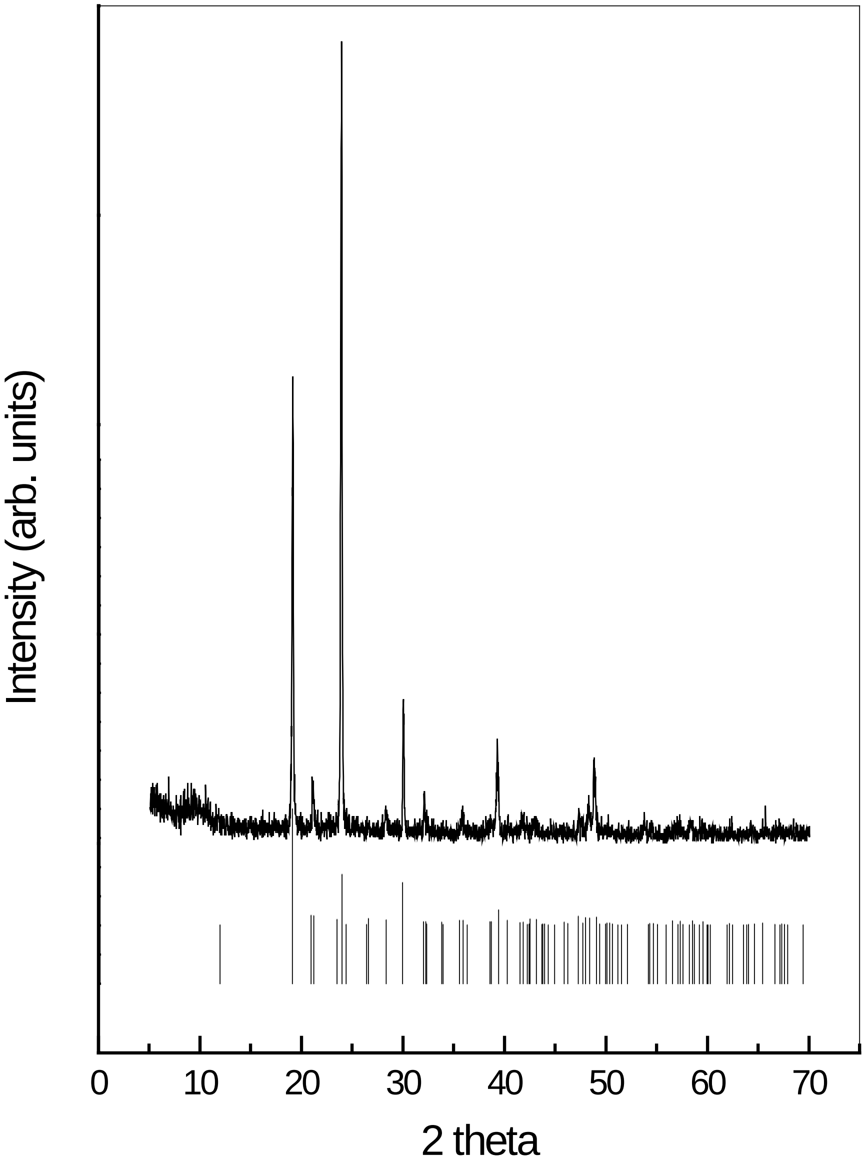

Fig 3.23: Comparison of the XRD pattern of V(II) formate with the matched reference

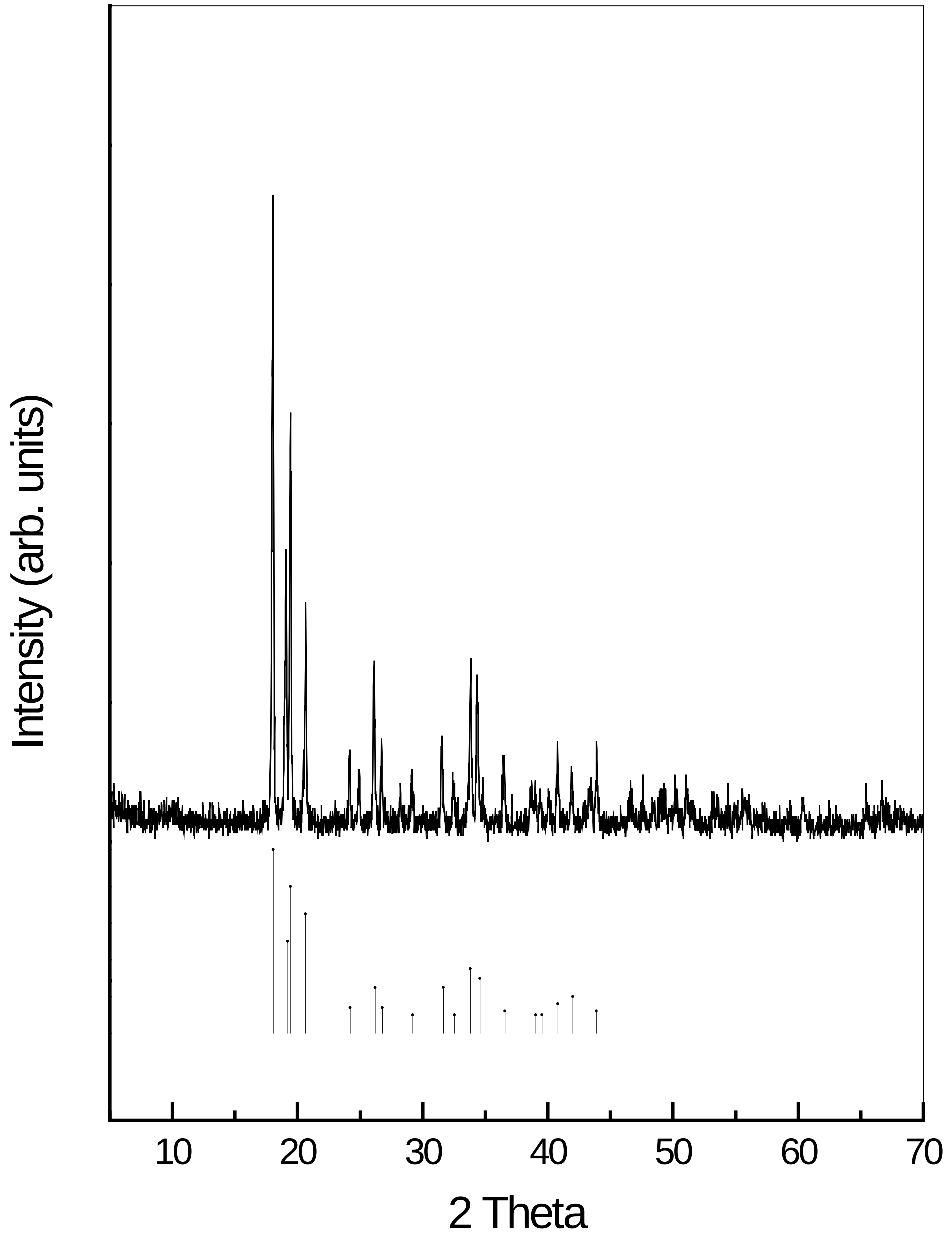

indexing and least square refinements were carried out by the using indexing software. The goodness of the indexing were concluded from the better figure of merits defined as equation mentioned below. The unit cell parameters thus obtained were refined by least square method. A list of the observed and calculated peak positions (d-value/2theta) are given in **Tables 3.8, 3.9 and 3.10**. The refined unit cell parameters of these phases are given below of each table.

The typical figures of merit of indexing are given either by de-Wolff's (M20 or M_N) or Louer's (F_N). These two figures of merit are defined as

$$\boldsymbol{M_N = \frac{Q_N}{2\left|\overline{\Delta Q}\right|}\frac{N_{obs}}{N_{pos}}} \qquad\qquad \boldsymbol{F_N = \frac{1}{\left|\overline{\Delta\theta}\right|}\frac{N_{obs}}{N_{pos}}}$$

Where, $Q_N = \dfrac{1}{{d_N}^2}$, for Nth reflection, $\overline{\Delta Q}$ and $\overline{\Delta\theta}$ are average errors in Qs and 2θs

N_{pos} = No possible lines for the observed unit cell till the last observed reflections

The Louer's figures of merit F_N is written in the form of $F_N = F_N(\overline{\Delta\theta}, N_{pos})$

All the XRD patterns were indexed to get the unit cell parameters. However, at present, the detailed symmetry and structure were not analysed. From the indexing procedure, an orthorhombic lattice has been assigned for the structure of V(IV) formate while two different type of monoclinic lattices were assigned for V(II) and V(III) formate. The observed unit cell parameter for V(IV) formate (a: 8.392 (9) Å; b: 7.443 (5) Å and c: 8.447 (7) Å and unit cell volume = 527.6 (8) Å^3) are in good agreement with the reported values (a: 8.395 Å; b: 8.510 Å and c: 7.433 Å and cell volume: 531.02 Å^3) as mentioned above. The minor variations in the unit cell parameters and intensity distribution might be due to some differences in their structures. Besides, a number of weak reflections reported for this phase could not be observed in the present study, which may be because of poorer diffraction data quality. Hence, no further structural details are not attempted. The monoclinic unit cell parameters observed for the V(II) formate (a: 9.383 (3) Å; b: 7.146 (2) Å and c: 8.678 (3) Å, β = 97.56 (3) and unit cell volume = 576.8 (3) Å^3) have similarity with the various reported M(II) formate di-hydrate (M = Cu, Zn, Fe). The reported unit cell parameters for $Zn(HCOO)_2 \cdot 2H_2O$ are: a = 9.305 Å; b = 7.145 Å and c = 8.690 Å, β = 97.41° and unit cell volume = 572.92 Å^3 (JCPDS-PCPDF-14-0761). The difference in the unit cell parameters compared to these reported formats might be due to the difference in ionic radii of the cations.

Table 3.8: Unit cell parameters of V(IV) formate obtained by indexing the XRD pattern

S. No	**h**	**k**	**l**	**2 Theta (obs)**	**2 Theta (cal)**	**T(obs -cal)**	**I/I_o (%)**	**d(obs)**	**d(cal)**	**d(obs -cal)**
1	1	1	1	19.151	19.074	0.077	62	4.631	4.649	-0.019
2	2	0	0	21.162	21.155	0.006	8	4.195	4.196	-0.001
3	0	2	0	23.943	23.892	0.051	100	3.714	3.721	-0.008
4	1	2	1	28.299	28.257	0.042	5	3.151	3.156	-0.005
5	2	0	2	30.049	29.993	0.055	18	2.972	2.977	-0.005
6	2	2	0	32.102	32.122	-0.021	5	2.786	2.784	0.002
7	3	1	1	35.852	35.874	-0.022	4	2.503	2.501	0.001
8	1	3	1	39.296	39.311	-0.015	14	2.291	2.29	0.001
9	3	1	3	47.351	47.37	-0.019	5	1.918	1.918	0.001
10	2	0	4	48.275	48.201	0.075	6	1.884	1.886	-0.003
11	0	3	3	48.827	48.888	-0.062	10	1.864	1.861	0.002
12	0	4	2	53.795	53.792	0.004	4	1.703	1.703	0.000
13	3	0	5	64.318	64.367	-0.049	3	1.447	1.446	0.001

The calculated unit cell parameters were a: 8.392 (9) Å; b: 7.443 (5) Å and c: 8.447 (7) Å and unit cell volume = 527.6 (8) Å^3. The figures of merit for this indexing were found to be F 13= 2.3 (0.043,130) and M 13= 5.3.

Table 3.9: Unit cell parameters of V(III) formate obtained by indexing the XRD pattern

S No	**h**	**k**	**l**	**2Theta (obs)**	**2Theta (cal)**	**T(obs-cal)**	**I/I_o (%)**	**d(obs)**	**d(cal)**	**d(obs-cal)**
1	-1	0	1	9.013	9.014	0.000	100	9.811	9.811	0.001
2	1	0	1	13.484	13.479	0.004	52	6.567	6.569	-0.002
3	0	0	2	13.618	13.615	0.004	51	6.502	6.504	-0.002
4	0	1	1	15.83	15.822	0.008	36	5.598	5.601	-0.003
5	1	1	0	17.087	17.018	0.07	19	5.189	5.21	-0.021
6	-2	0	2	17.976	18.084	-0.108	10	4.935	4.905	0.029
7	2	0	0	18.442	18.502	-0.061	9	4.811	4.795	0.016
8	-1	0	3	18.979	18.8	0.179	31	4.676	4.72	-0.044
9	0	0	3	20.614	20.483	0.131	10	4.309	4.336	-0.027
10	-2	1	2	23.062	23.112	-0.049	17	3.856	3.848	0.008
11	2	1	0	23.447	23.444	0.003	12	3.794	3.794	0.000
12	-1	1	3	23.637	23.682	-0.045	14	3.764	3.757	0.007
13	1	1	2	24.086	24.088	-0.002	10	3.695	3.694	0.000
14	-1	0	4	25.206	25.166	0.04	3	3.533	3.538	-0.005
15	1	0	3	25.704	25.702	0.002	47	3.466	3.466	0.000
16	-2	0	4	26.127	26.272	-0.146	10	3.411	3.392	0.019
17	2	0	2	27.04	27.15	-0.109	33	3.297	3.284	0.013
18	-1	1	4	28.966	29.048	-0.082	14	3.082	3.074	0.008
19	0	2	1	29.621	29.596	0.025	16	3.016	3.018	-0.002
20	2	1	2	30.8	30.801	0.000	13	2.903	2.903	0.000
21	3	1	0	31.487	31.479	0.009	9	2.841	2.842	-0.001
22	-1	0	5	31.865	31.848	0.017	7	2.808	2.81	-0.001
23	1	0	4	32.417	32.404	0.013	8	2.762	2.763	-0.001
24	2	0	3	32.915	32.913	0.002	16	2.721	2.721	0.000
25	-2	2	1	33.43	33.588	-0.158	11	2.68	2.668	0.012
26	2	2	0	34.447	34.426	0.021	6	2.603	2.605	-0.002
27	-4	0	1	35.366	35.253	0.113	8	2.538	2.546	-0.008
28	-2	2	3	36.296	36.174	0.122	6	2.475	2.483	-0.008
29	-4	1	2	37.27	37.339	-0.068	4	2.412	2.408	0.004
30	-3	1	5	37.726	37.703	0.023	10	2.384	2.386	-0.001
31	-1	0	6	38.748	38.76	-0.011	5	2.324	2.323	0.001
32	1	0	5	39.301	39.334	-0.033	5	2.292	2.291	0.002
33	-4	1	4	39.576	39.506	0.07	6	2.277	2.281	-0.004

Table 3.9: Continued…

S No	h	k	l	2Theta (obs)	2Theta (cal)	T(obs-cal)	I/I$_o$ (%)	d(obs)	d(cal)	d(obs-cal)
34	-3	0	6	39.829	39.863	-0.034	10	2.263	2.261	0.002
35	0	2	4	40.239	40.168	0.071	6	2.241	2.245	-0.004
36	3	2	0	40.667	40.514	0.153	4	2.218	2.227	-0.008
37	-1	1	6	41.501	41.503	-0.002	12	2.176	2.176	0.000
38	1	1	5	42.051	42.046	0.005	5	2.149	2.149	0.000
39	3	2	1	42.856	43.078	-0.221	5	2.11	2.1	0.01
40	-5	0	3	43.341	43.307	0.034	9	2.088	2.089	-0.002
41	-5	0	4	44.219	44.233	-0.014	5	2.048	2.048	0.001
42	4	0	2	45.264	45.223	0.041	3	2.003	2.005	-0.002
43	-4	2	3	45.78	45.753	0.027	2	1.982	1.983	-0.001
44	-4	2	1	46.159	46.119	0.04	5	1.967	1.968	-0.002
45	-5	1	4	46.682	46.713	-0.032	3	1.946	1.944	0.001
46	3	0	4	46.979	47.147	-0.168	4	1.934	1.928	0.007
47	-4	2	4	47.23	47.237	-0.007	6	1.924	1.924	0.000
48	-1	3	3	47.997	48.018	-0.021	3	1.895	1.895	0.001
49	1	3	2	48.227	48.239	-0.012	4	1.887	1.886	0.000
50	-5	1	5	48.661	48.668	-0.007	4	1.871	1.871	0.000
51	0	0	7	49.043	49.02	0.023	3	1.857	1.858	-0.001
52	2	2	4	49.355	49.332	0.023	5	1.846	1.847	-0.001
53	-4	2	5	49.74	49.749	-0.009	4	1.833	1.833	0.000
54	4	0	3	50.422	50.295	0.127	3	1.81	1.814	-0.004

The calculated unit cell parameters were a: 10.457 (8) Å; b: 6.206 (5) Å and c: 14.184 (10) Å, α = 90; β = 113.50 (5) and γ = 90 and unit cell volume = 844.1 (1.1) Å^3. The figures of merit for this indexing were found to be F30 = 6.5(0.054, 85) and M20 = 3.7.

Table 3.10: Unit cell parameters of V(II) formate obtained by indexing the XRD pattern

S No	**h**	**k**	**l**	**2Theta (obs)**	**2Theta (cal)**	**T(obs-cal)**	**I/I_o (%)**	**d(obs)**	**d(cal)**	**d(obs-cal)**
1	-1	1	1	18.03	18.027	0.004	100	4.916	4.917	-0.001
2	2	0	0	19.068	19.067	0.001	39	4.651	4.651	0.000
3	1	1	1	19.433	19.42	0.013	63	4.564	4.567	-0.003
4	0	0	2	20.639	20.633	0.006	36	4.3	4.301	-0.001
5	0	1	2	24.137	24.13	0.007	13	3.684	3.685	-0.001
6	-1	1	2	24.931	24.946	-0.014	11	3.569	3.567	0.002
7	2	1	1	26.105	26.097	0.008	26	3.411	3.412	-0.001
8	1	2	0	26.715	26.706	0.01	16	3.334	3.335	-0.001
9	-1	2	1	28.221	28.213	0.008	9	3.16	3.161	-0.001
10	-2	1	2	29.159	29.148	0.011	9	3.06	3.061	-0.001
11	2	2	0	31.516	31.551	-0.034	14	2.836	2.833	0.003
12	-2	2	1	32.406	32.44	-0.034	7	2.76	2.758	0.003
13	-1	1	3	33.829	33.857	-0.028	25	2.648	2.645	0.002
14	3	1	1	34.341	34.354	-0.013	25	2.609	2.608	0.001
15	1	2	2	34.79	34.777	0.013	8	2.577	2.578	-0.001
16	-2	2	2	36.497	36.52	-0.023	11	2.46	2.458	0.001
17	1	3	1	40.786	40.783	0.003	13	2.211	2.211	0.000
18	-3	1	3	41.928	41.916	0.011	9	2.153	2.154	-0.001
19	-1	3	2	43.896	43.88	0.017	14	2.061	2.062	-0.001
20	-4	2	1	46.606	46.594	0.012	7	1.947	1.948	0.000
21	-3	2	3	47.603	47.592	0.011	10	1.909	1.909	0.000
22	-6	2	2	66.677	66.675	0.003	7	1.402	1.402	0.000

The calculated unit cell parameters were a: 9.383 (3) Å; b: 7.146 (2) Å and c: 8.678 (3) Å, α = 90; β = 97.56 (3) and γ = 90 and unit cell volume = 576.8 (3) $Å^3$. The figures of merit for this indexing were found to be F22 = 6.8(0.013, 251) and M20 = 11.4.

Summary

The maximum aqueous solubility of V(IV) formate has been found to be more than that of V(V) formate. Controlled current electroreduction of these compounds at concentrations around 125 mM has resulted in formation of soluble V(II) formate in the medium while at higher concentrations, V(III) formate precipitated out upon electrolysis. Reduction of V(IV) formate at 350 mM concentration using zing amalgam resulted in precipitation of V(II) formate. The chemical formulae of the vanadium compounds precipitated out by exceeding their solubility limits in the different oxidation states viz. V(V), V(IV), V(III) and V(II) were determined by a combination of chemical analysis, spectroscopic techniques, thermogravimetry and XRD. The formulae of the synthesized compounds were found to be V_2O_5, $VO(HCOO)_2\cdot H_2O$, $V(OH)(HCOO)_2$ and $V(HCOO)_2\cdot 2H_2O$ respectively.

3.4 References

[1] M. G. Segal and R. M. Sellers, *J. Chem. Soc., Faraday Trans.*, 78 (1982) 1149.

[2] T. Swan, M. G. Segal, W. J. Williams, M. E. Pick, *LOMI Decontamination Reagents and Related Preoxidation Process. Electric Power Research Institute: Report EPRI NP-5522M*. CEGB; Berkeley, U.K., (1987).

[3] M. G. Segal and T. Swan, *Water Chemistry of Nuclear Reactor Systems 3*, BNES, London, UK, (1983) p187.

[4] J. Manjanna and G. Venkateswaran, *Hydrometallugry.*, 61 (2001) 45.

[5] D. Bradbury, M. G. Segal, T. Swan, G. C. W. Comley and D. J. Ferrett, *Nucl. Enegry*, 20 (1981) 403.

[6] L. N. Moskvin, V. V. Krivobokov, A. K. Andrianov, and A. A. Efimov, *Radiochemistry*, 52 (2010) 585.

[7] V. S. Tripathi, J. Manjanna, G. Venkateswaran, B. K. Gokhale, and V. Balaji, *Ind. Eng. Chem. Res.*, 43 (2004) 5989.

[8] C. J. Wood, *Progress in Nuclear Energy*, 23 (1990) 35.

[9] *Decontamination Handbook*, EPRI, TR-112352, Palo Alto, CA: July 1999.

[10] A. J. Bard and L. R. Faulkner, *Electrochemical Methods Fundamentals and Applications: Second Edition*, John Wiley & Sons, Inc. 2001.

[11] B. E. Conway and J. O'M. Bockris, *J. Chem. Phys.*, 26 (1957) 532.

[12] M. Vijayakumar, L. Li, G. Graff, J. Liu, H. Zhang, Z. Yang and J. Z. Hu, *J. Power Sources*, 196 (2011) 3669.

[13] Z.L.K.Z.C. Wang, Functional and Smart Materials—Structural Evolution and Structure Analysis, Springer-Verlag, 1998.

[14] M. S. Kazacos, C. Menictas and M. Kazacos, *J. Electrochem. Soc.*, Vol. 143 (1996) L86.

[15] Yi-Chen Kao and Chein-Hsiun Tu, *J. Chem. Eng. Data*, 54 (2009) 1927.

[16] Q. Yin, N.P. Brandon and G.H. Kelsall, *J. App. Electrochem.*, 30 (2000) 1109.

[17] S. Lakshmi Reddy, Tamio Endo and G. Siva Reddy, Electronic (Absorption) Spectra of 3d Transition Metal Complexes, Chapter 1, http://dx.doi.org/10.5772/50128.

[18] R. N. Keller, Coordination Chemistry of group (IV) and (V) metals, *ARL 66-0082*, 1966.

[19] M. Vijayakumar, S. D. Burton, C. Huang, L. Li, Z. Yang, G. L. Graff, J. Liu, J. Hua, M. Skyllas-Kazacos, *J. Power Sources*, 195 (2010) 7709.

[20] O. G. Holmes and D. S. McClure, *J. Chem. Phys.*, 26 (1957) 1686.

[21] I. Asif, S. Ali, S. Shahzadi and S. Mahmood, *J. Chin. Chem. Soc.*, 54 (2007) 23.

[22] I.L. Botto, M.B. Vassallo, E.J. Baran and G. Minelli, *Mater. Chem. Phys.*, 50 (1997) 267.

[23] P. Persson, M. Karlsson, and Lars-Olof Öhman, *Geochimica et Cosmochimica Acta*, 62 (1998) 3657.

[24] C. He, Y. Liu, Z. Xue, M. Zheng, H. Wang, Y. Xiao, H. Dong, H. Zhang, B. Lei, *Int. J. Electrochem. Sci.*, 8 (2013) 7088.

CHAPTER-4

Redox Speciation Studies of Aqueous Vanadium Solutions

4.1 Introduction

Vanadium ions exists in aqueous solution as V(II), V(III), **V**(IV), or V(V), or as a mixture of any two contiguous valence states [1]. The lower oxidation states are air sensitive and hence the synthesis of lower oxidation state vanadium compounds in aqueous solution require continuous monitoring to ensure inert atmosphere in the experimental setup. Thus redox speciation of aqueous vanadium is an essential prerequisite for efficient synthesis of lower oxidation state aqueous vanadium compounds in aqueous solutions.

Synthesis of vanadous formulation through electrolytic reduction is a viable option for the purpose of its use in the decontamination formulation as electrolysis provides the advantage of selecting a non corrosive medium while avoiding any spare ionic species in the final product [2]. These are primary objectives for nuclear power plant application owing to structural integrity and active waste volume generation concerns. The prevalent oxidation states of vanadium compounds are (V) and (IV) and preparation of V(II) from these states require proper monitoring of the process. V(II) and even V(III) formulations are air sensitive and hence a stringent inert atmosphere has to be maintained throughout the preparation process. Thus, a reliable on-line vanadium redox species measurement based on minimum intervention and fast response is required to monitor the progress of electrolysis. Redox potential monitoring has been explored for on-line measurement during electrolytic preparation of lower oxidation state aqueous vanadium compounds. Solution potential monitoring with a redox electrode impressed with a high frequency of 1.13 kHz, 10 mV alternating voltage to overcome polarization of the electrode has been evolved for evaluating the progress of electrolysis.

Spectrophotometric determination of aqueous vanadium is the method of choice when rapid redox speciation is required [3]. However, direct spectrophotometric determination of vanadium suffers from poor sensitivity and selectivity. Extraction to organic phase followed by spectrophotometric determination using suitable chromophores is normally practiced to improve sensitivity and selectivity [4, 5]. Catalytic spectrophotometric methods are also used for sensitive spectrophotometric determination of V(V) [6]. However, these methods require extensive processing of the sample, maintaining specific concentration ratio of reagents and providing specific reaction conditions for good results. A modified method used by King and Garner [7] has been used for spectrophotometric redox speciation. The vanadium samples are initially analysed for total V(V) reducing strength. This is done by converting the sample to V(V)/V(IV) mixture by adding known excess of V(V) solution. Also, another aliquot of the sample is completely oxidized to V(V) by acidic $KMnO_4$ [8]. Redox interaction of V(V) with Fe(II) is known to be instantaneous in acidic aqueous medium and has been used to evaluate the V(V) concentration [9]. The same route but with the estimation of Fe(III) by the established spectrophotometric Fe(III)-sulfosalicylate complex method [10] has been followed. The figures of merit has already been evaluated for the method [11]. The interference of V(IV) and Mn(II) on the method has been evaluated as these ions will be a part of the sample matrix. Direct spectrophotometric method for V(III)/(II) speciation based on thiocyanate complex formation is also explored.

4.2 Experimental

125 mM sodium metavanadate was electrolyzed in 750 mM formic acid medium using a two compartment electrolysis cell. Graphite felt was used as the cathode while stainless steel AISI 304 was used as the anode and the compartments were separated by a commercial anion exchange membrane. Constant current electrolysis with a current density of around 55 mA/cm^2 across the anion exchange membrane was used to electrolyze 550 ml of the solution. One of the two plates of the conductivity probe of the conductivity meter (TH-2300, El-Hamma Instruments) has been used to measure solution potential with respect to a Ag/AgCl, sat. KCl reference electrode with the help of a digital multimeter (81K-TRMS, MECO) connected to PC. The conductivity meter applies a high frequency of 1.13 kHz, 10 mV alternating voltage signal on the redox probe.

0.5 ml of sample was periodically collected at an interval of 30 minutes with a 5 ml liquid syringe and was mixed with an aliquot of stock V(V) solution (125 mM $NaVO_3$ in 750 mM HCOOH). The ratio of the mixture was varied form 1:1 to 1:3 and finally to 1:4 for the sample volume to initial stock volume respectively with the progressing stages of electrolysis. These variations in the composition were done when V(V) concentration in the mixture came down to 62.5 mM for the first two stages of electrolysis (as per the analysis). The mixture was initially diluted to 41.6 times with deaerated water in a 25 ml volumetric flask (0.6 ml of mixture taken) under inert atmosphere and then finally to another 25 times in a 1 cm path length spectrophotometric quartz cuvette of 12.5 ml volume (0.5 ml of diluted mixture taken) again under the inert atmosphere. 1 ml of 3 mM $FeSO_4$ stock solution in 50 mM H_2SO_4 was added to the cuvette. Finally, 5 ml of 2 M CH_3COOH and 1.1 M CH_3COONa buffer solution was added before adding 5 ml of 40 mM sulfosalicylic acid solution to the cuvette and making up the solution to 12.5 ml by adding water. The absorbance was measured at 465 nm.

Total vanadium concentration was separately determined by using 10 ml of 41.6 times diluted V(V)/V(IV) mixture. The mixture was converted to pure V(V) solution by drop wise addition of acidified $KMnO_4$ (5 mM $KMnO_4$ in 40 mM H_2SO_4 solution) at 80 ^{o}C until a stable purple color solution is obtained. The solution was made up to 20 ml after cooling and was analysed by ferric sulfosalicylic acid method as described above.

V(IV) formate was prepared by reducing $NaVO_3$ by hydrazine in formic acid medium [12]. It was mixed with initial stock V(V) solution (125 mM $NaVO_3$ in 750 mM HCOOH) in a molar ratio of 0.1 to 30. The resulting mixture was analysed by the above mentioned procedure to evaluate the V(IV) interference in the analysis. $MnSO_4$ was also mixed with stock V(V) solution in 0.1 to 30 molar ratio and the solution was analysed for the Mn^{2+} interference in the analysis process.

Direct spectrophotometric determination of V(III) and V(II) solutions has also been evaluated. This is explored to further simplify the analysis of these solutions. The V(III)/V(II) solution formed during the electrolysis was added to a solution of 0.5 M KSCN in 1 M HCl and the UV-visible spectra was recorded.

4.3 Results and discussion

4.3.1 Evaluation of progress of electrolysis

The redox potential variation using the platinum electrode impressed with an alternating potential is shown in **Fig 4.1**. Segment I of the curve represents V(V)/V(IV) redox couple, segment II represents the V(IV)/V(III) redox couple while the segment III indicates the V(III)/V(II) redox couple. The redox potential measurement by the conventional setup has been unsuccessful as the polarization of the platinum redox electrode led to a non responsive readout after some time. The polarization of redox electrode could be ascertained by the receipt of proper response from the electrode upon its cleaning using aqua regia solution. Redox potential measurement using one of the two plates of the conductivity meter against a Ag/AgCl, sat. KCl has been explored to overcome the polarization of the redox probe. The application of high frequency alternating voltage on the electrode by the conductivity meter during the measurement could effectively overcome the polarization and hence the response for the entire range of electrolysis has been proper. The two pole conductivity meter applies frequency as per the conductivity of solution to avoid polarization. Combining the expression for concentration variation for flow cell under limiting current condition and Nernst equation, the variation in potential with respect to time can be given as:

$$E_{sol.} = E^{o\prime} - {RT}/{nF} \; ln\,[e^{pt} - 1] \qquad (4.1)$$

Where, E_{sol} is the redox potential of the solution, $E^{o'}$ is the formal potential of the solution; R, T, n and F are the usual constants of the Nernst equation; t is the time of

Fig 4.1: Redox potential variation of vanadium formate solution during electroreduction

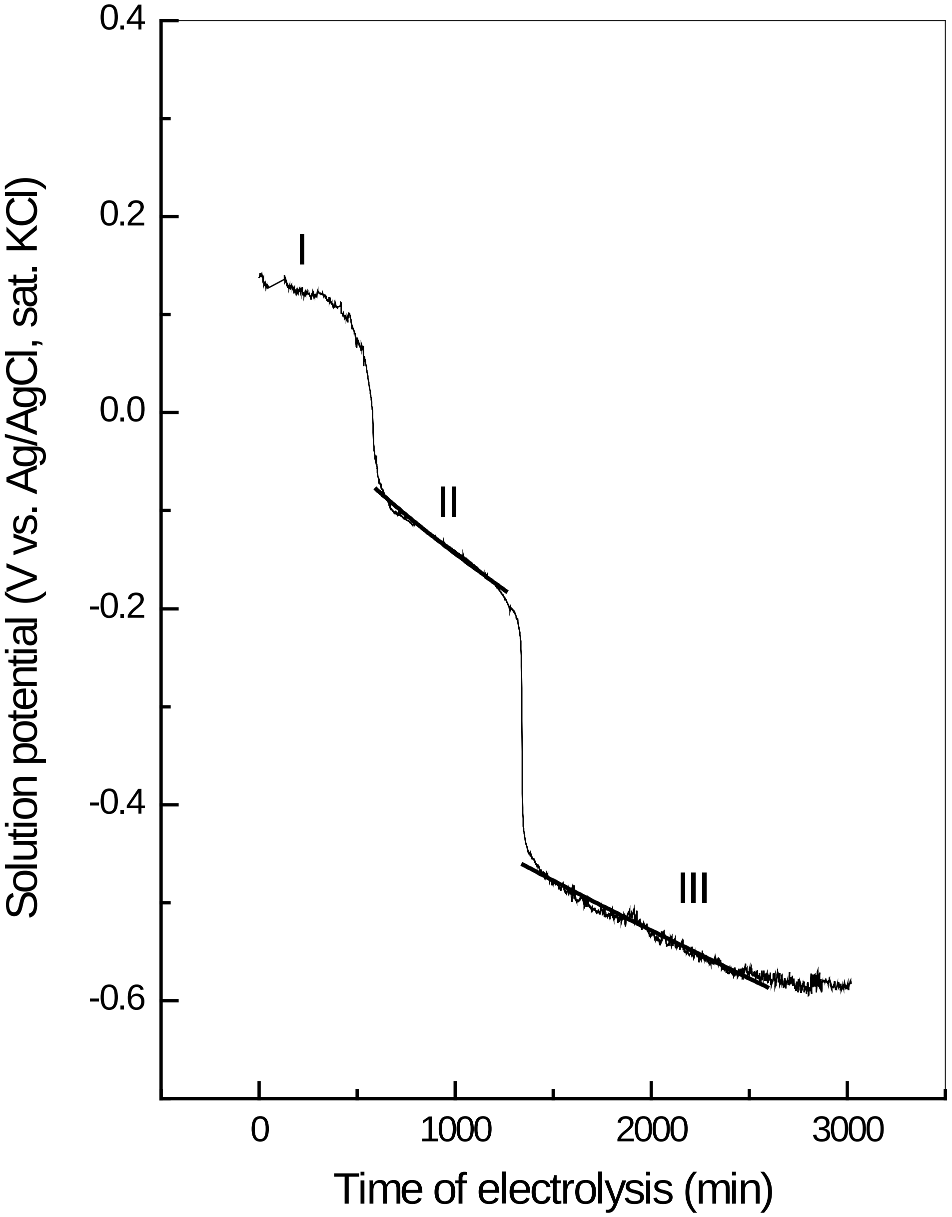

electrolysis and p is the cell factor which depends upon mass transfer rate, specific area and porosity of the electrode [13]. The redox potential variation has been fitted to equation (4.1) in three segments and a good fitting could be observed for all the three segments.

The cell factor value obtained by fitting the solution potential variation to equation (4.1) has been similar for the three segments with the values of 0.00162, 0.00207 and 0.00223 min^{-1} for segment I, II, and III respectively. The similar cell factor values indicate the proper progress of the controlled current electrolysis for the entire run.

4.3.2 Spectrophotometric method for redox speciation of aqueous vanadium ions

The indirect spectrophotometric method for redox speciation of aqueous vanadium ions has been evolved on the basis of rapid redox reaction of V(V) with Fe(II) [9]. The resulting mixture has been analysed by the spectrophotometric determination of the resulting Fe(III) formed by the redox interaction of V(V) with Fe(II). The UV-visible spectrum of the Fe(III) sulfosalicylic acid complex at pH 4.5 is shown in **Fig 4.2**. The absorption maximum ($\lambda_{max.}$) for the complex was observed at 465 nm. The molar extinction coefficient obtained under the experimental conditions was determined to be 3740 dm^3 mol^{-1} cm^{-1}. This method has been selected for determination of iron as the known standard method of analyzing iron by using o-phenanthroline as the chromogenic agent could not be used in the present system. The Fe(III)/Fe(II)-o-phenanthroline complex has the standard reduction potential of +1.06 V vs. SHE which is higher than the redox potential of V(V)/V(IV) (1.0 V vs. SHE) system. Thus if o-phenanthroline is used

Fig 4.2: UV-visible spectrum of the ferric sulfosalicylic acid complex at pH 4.5

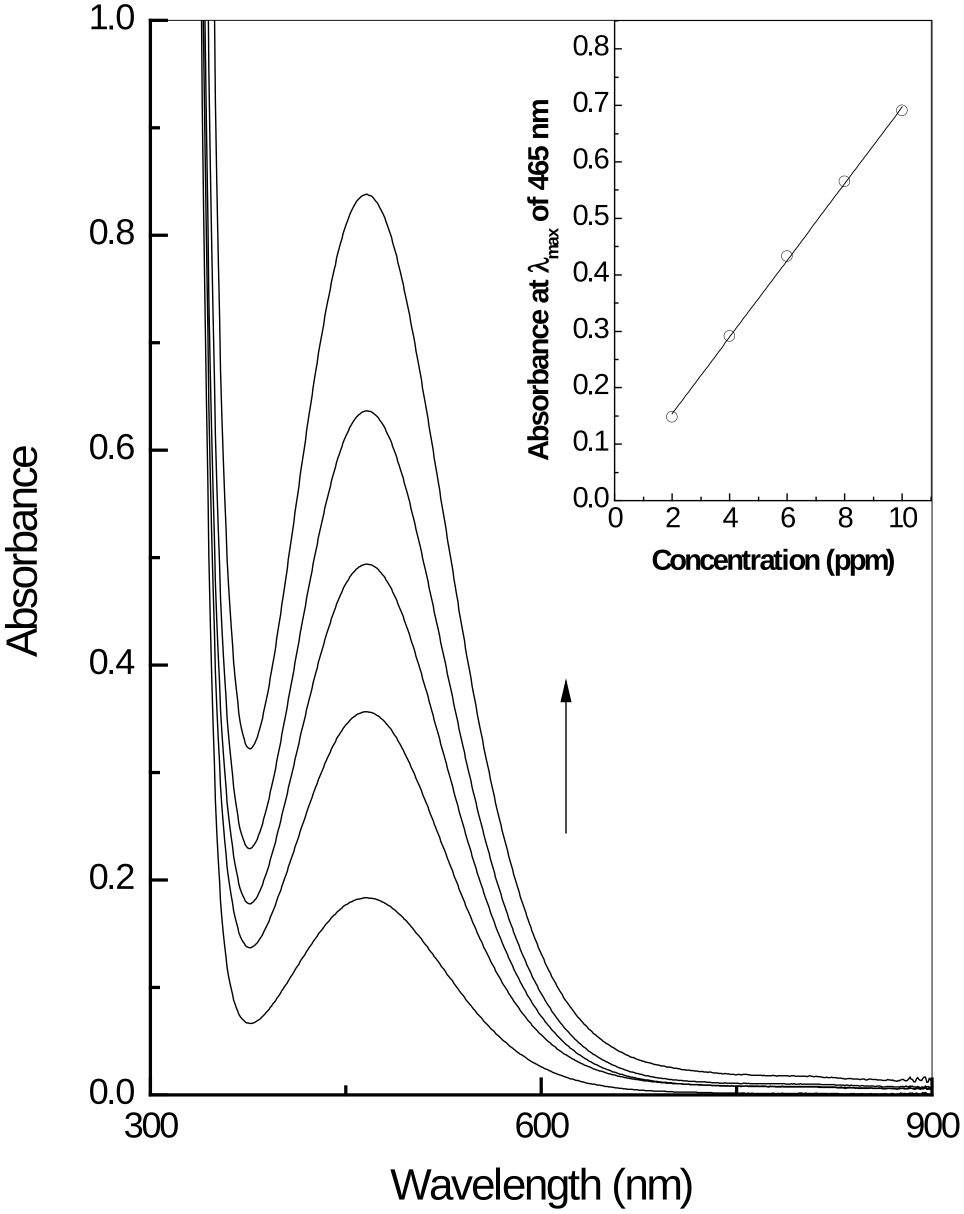

for the analyzing the residual Fe(II), erroneous results will be obtained due to the oxidation of V(IV) by Fe(III)-o-phenanthroline in the solution. Such an interaction between Fe(III)-sulfosalicylic acid complex and V(V)/V(IV) solution is not observed.

The analysis procedure was developed in a way where minimum other chemicals are added to the system to avoid large matrix variations. Hence initial V(V) solution alone was used for oxidation of all vanadium solutions having different oxidation states which were formed during the course of electrolysis. The procedure was verified by the triplicate analysis of the known redox mixtures of vanadium formate which were prepared by mixing V(II) formate and V(V) formate. The results of the analysis are given in **Tables 4.1 and 4.2**.

Table 4.1: Results of analysis of V(III)-V(IV) mixture (triplicate analysis)

Mixture Taken V(III) + V(IV) (mM)	**V(III) analysed (mM)**	**V(IV) analysed (mM)**
5 + 5	4.9 ± 0.13	4.9 ± 0.11
10 + 10	10.01 ± 0.13	9.9 ± 0.06
5 + 10	4.95 ± 0.15	10.1 ±0.05
10 + 5	9.9 ± 0.07	5.1 ± 0.14

Table 4.2: Results of analysis of V(II)-V(III) mixture (triplicate analysis)

Mixture Taken V(II) + V(III) (mM)	**V(II) analysed (mM)**	**V(III) analysed (mM)**
5 + 5	5.52 ± 0.29	5.1 ± 0.18
10 + 10	9.74 ± 0.04	10.2 ± 0.09
5 + 10	4.94 ± 0.38	10.1 ± 0.08
10 + 5	10.3 ± 0.02	5.1 ± 0.11

This method has been found to have no interference from the excess V(IV) in solution. Any change in absorbance values could not be seen even upon adding 10 mM concentration of V(IV) in the analysis solution which is about 50 times the concentration of the V(IV) normally expected in the analysis solution. Also, the interference from manganese (Mn^{2+}) has also been checked. Any interference of Mn^{2+} in the Fe(III) slfosalicylic acid spectrophotometric determination could not be observed.

Thus, this method could be used to assess the progress of electrolysis during the preparation of V(II) formate. The variation in concentration of the various aqueous vanadium redox species during the electrolysis of V(V) formate solution is shown in **Fig 4.3**. The change in concentration could be seen to closely follow the redox potential variation as shown in **Fig 4.1**. Thus, this indirect spectrophotometric method is a useful and rapid method of analyzing various redox mixtures of vanadium species in an aqueous medium.

4.3.2 Direct spectrophotometric determination of aqueous V(III)/V(II) redox couple

Aqueous V(III) and V(II) ions have relatively sharp absorbance peaks as compared to V(IV) or V(V) and hence the direct spectrophotometric determination of these species has been evaluated. The spectral behaviour of V(II) and V(III) formate is shown in **Fig 4.4**. V(II) formate has shown two peaks, one at 562 nm and other at 843 nm while V(III) formate has shown a peak at 591 nm and a hump around 420 nm. The calibration plot for these peak absorbance values is shown in **Fig 4.5**. The absorbance values have shown a good linear fitting with the slope of 0.00727 and 0.0854 for V(II) at 562 and 842 nm respectively while a slope of 0.03225 was obtained for V(III) at 591 nm.

Fig 4.3: Variation in the concentration of various vanadium redox species during controlled current electroreduction of V(V)

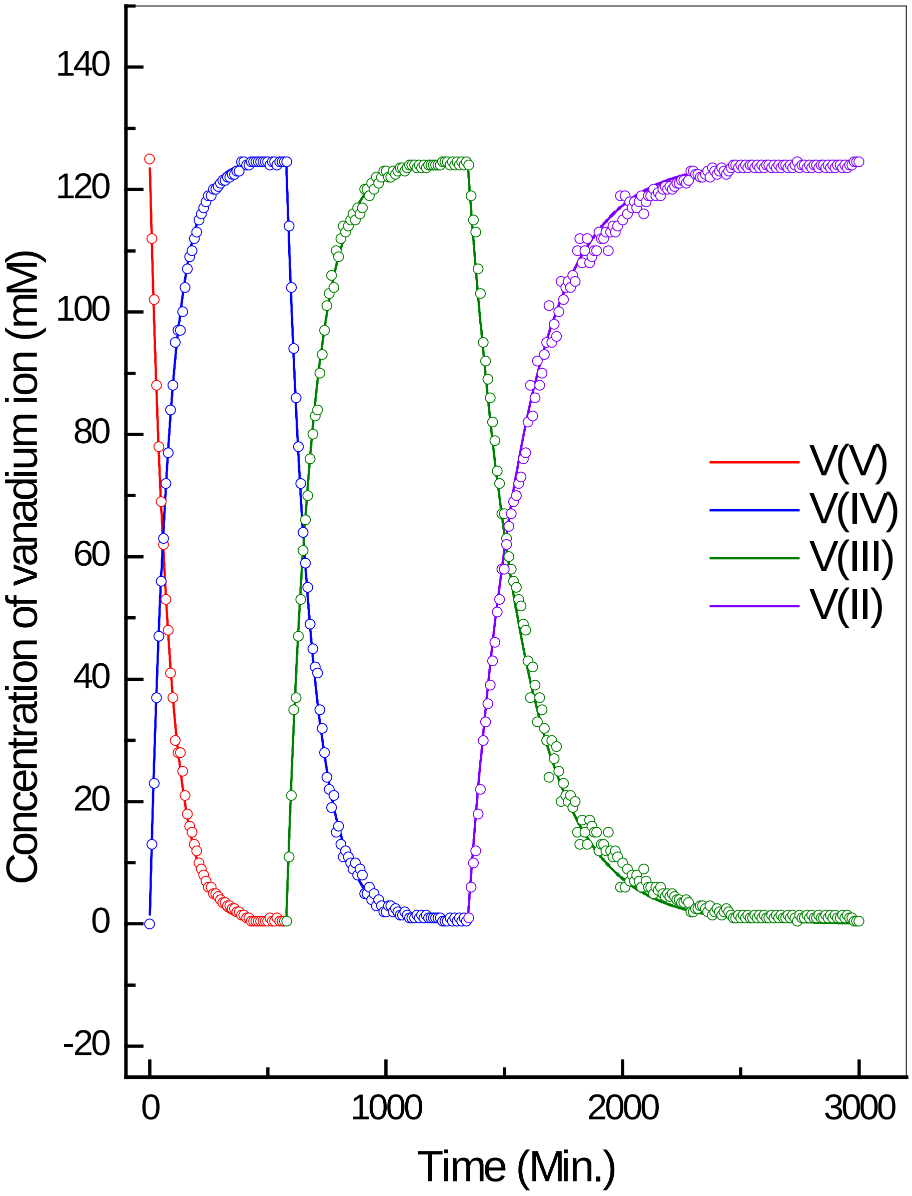

Fig 4.4: UV-visible spectra of V(II) and V(III) formate

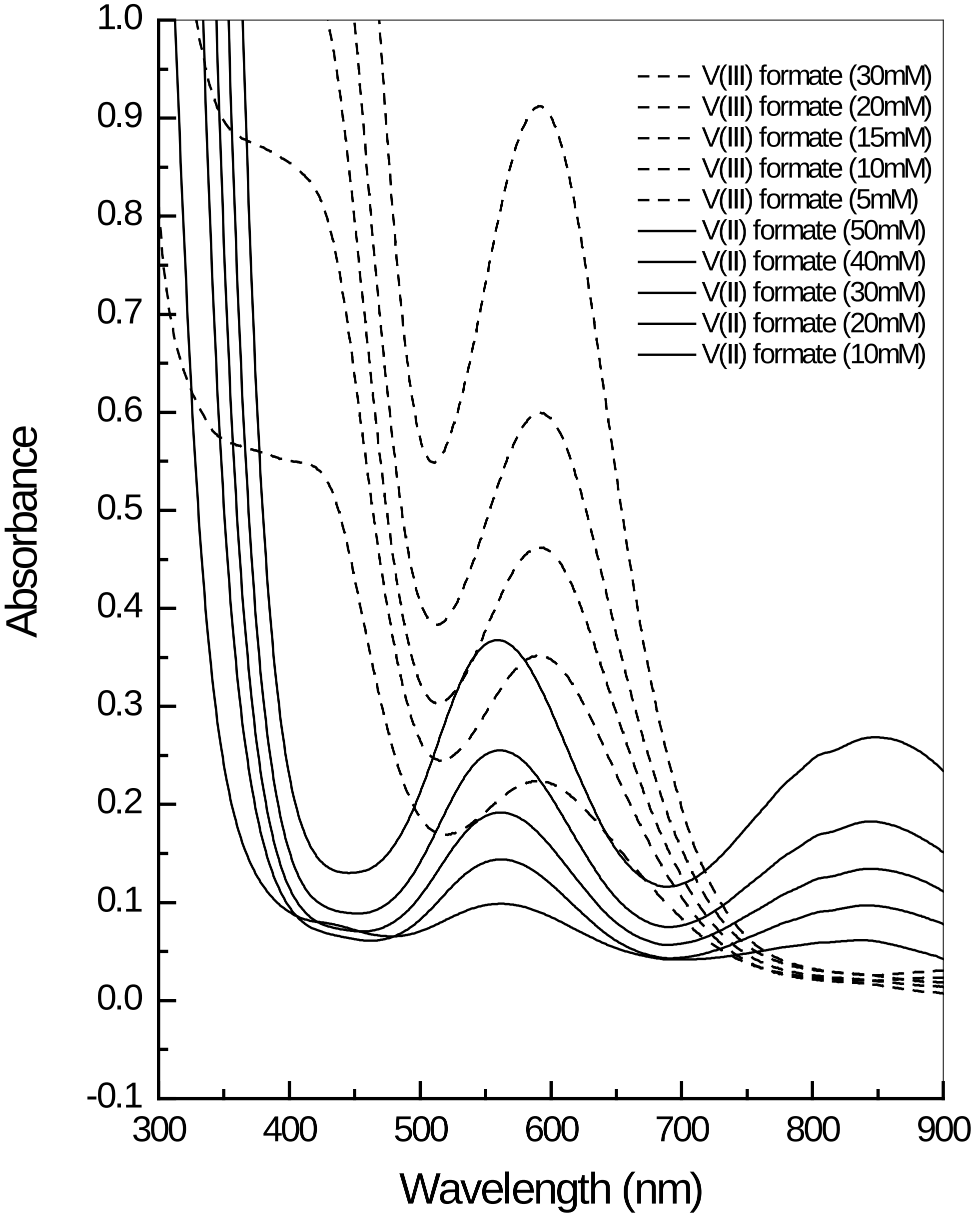

However, the peak positions for the two species are severely interfering at the peak of 562 nm for V(II) and the absorbance for the peak at 843 nm is too low. Thus, the determination of V(II) and V(III) as formate is not suitable for this concentration range. The spectral behaviour of V(II)and V(III) in thiocyanate medium is shown in **Fig 4.6**. The spectra was obtained in a high acidic medium wherein vanadium aliquot was added to the conc. HCl solution followed by KSCN addition to eliminate any possibility of hydroxylation of V(III). Well separated peaks for V(II) and V(III) were obtained with V(II) SCN having a maxima at 724 nm while V(III) SCN having a maxima at 595 nm. A good linear behaviour was obtained for the two peaks as shown in **Fig 4.5** for V(II) SCN at 595 nm and 724 nm respectively and at 595 nm and 724 nm for V(III) SCN respectively. The results of the analysis of known mixtures of V(II) and V(III) are given in **Table 4.3**. The requirement of maintaining an acidic condition leads to slight error in the determination of V(II) by this method as V(II) is partly oxidized in the high acidic medium.

Table 4.3: Results of analysis of V(II)-V(III) mixture (triplicate analysis)

Mixture Taken V(II) + V(III) (mM)	V(II) analysed (mM)	V(III) analysed (mM)
5 + 5	4.43 ± 0.59	5.51 ± 0.58
10 + 10	9.17 ± 1.04	10.14 ± 1.09
5 + 10	4.05 ± 1.49	10.61 ± 0.81
10 + 5	9.35 ± 1.02	5.43 ± 0.92

Fig 4.5: Calibration plots of various V(II) and V(III) species

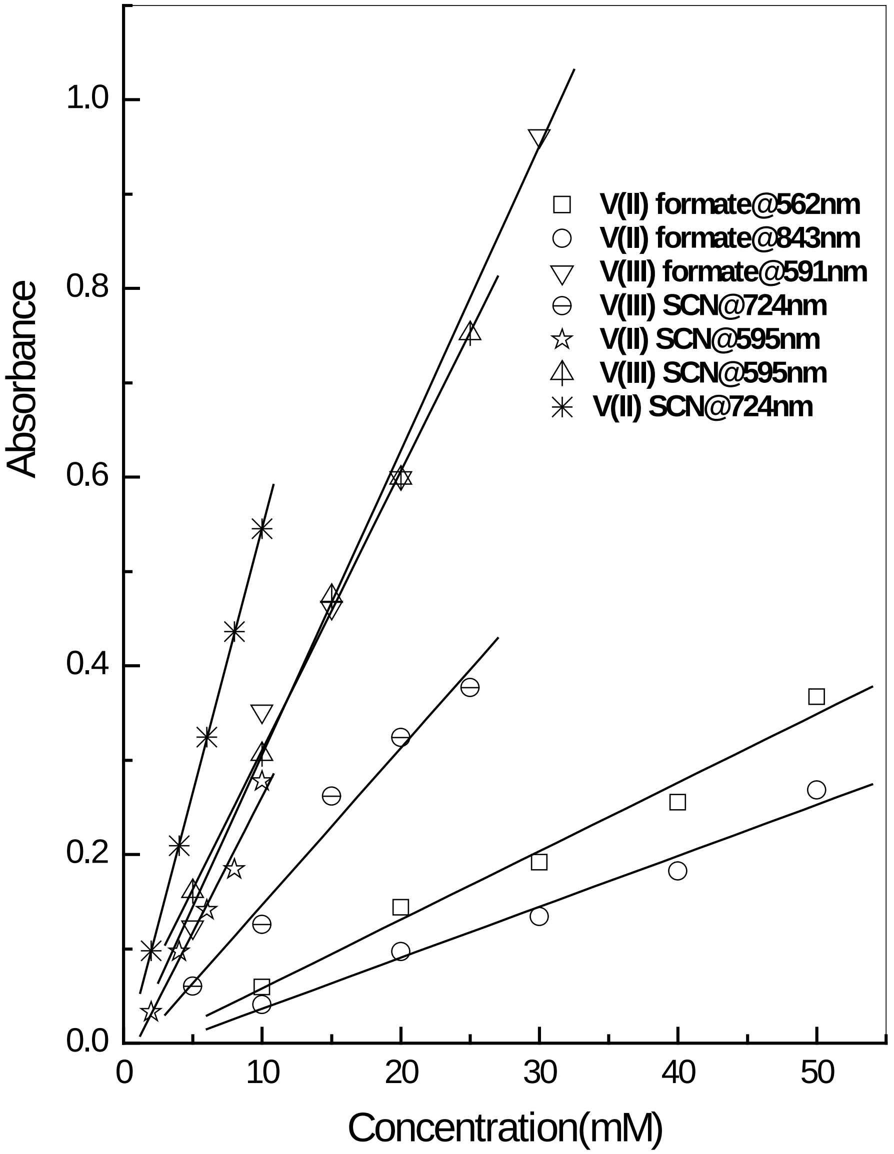

Fig 4.6: UV-visible spectra of V(II) and V(III) thiocynate

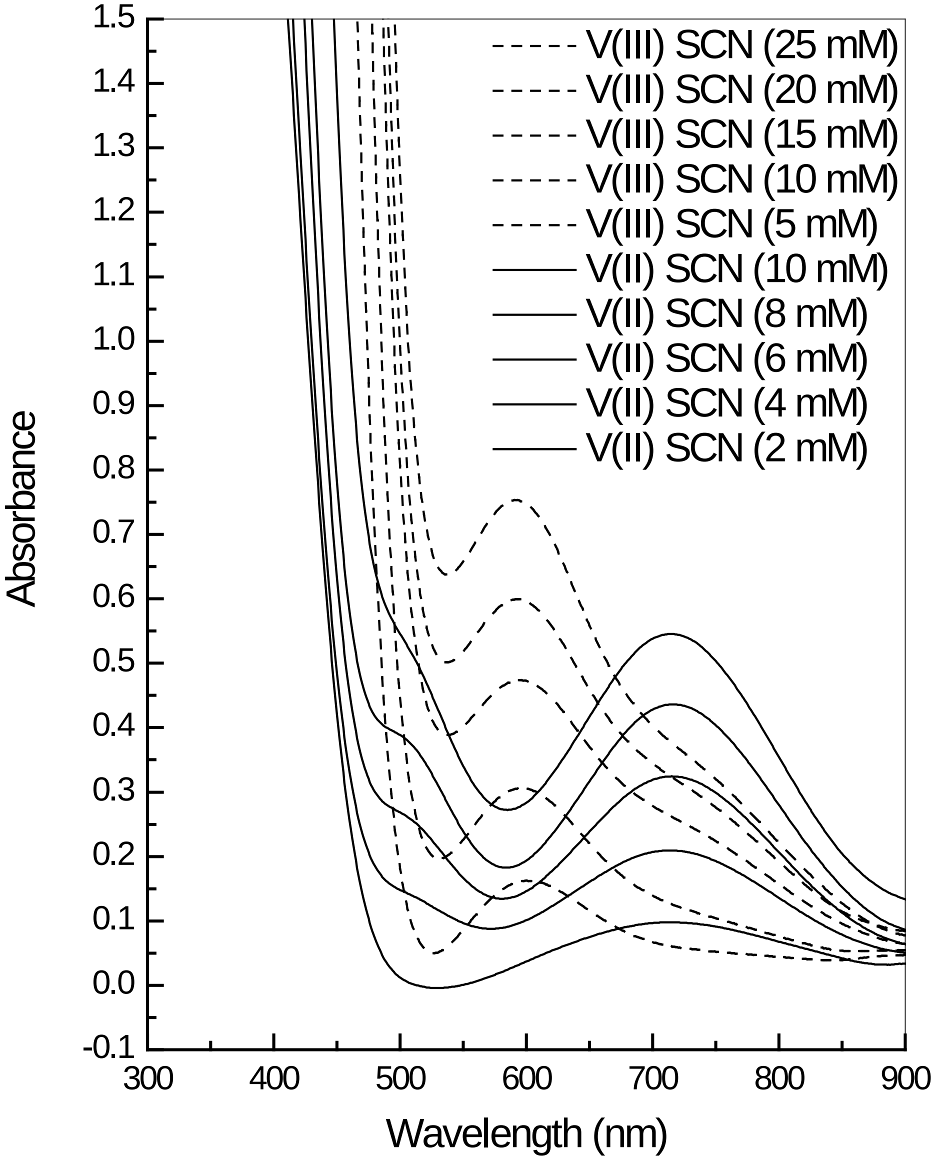

Summary

The on line monitoring methodology for electrolytic synthesis of low oxidation state of vanadium by solution potential monitoring with AC impressed probe has been developed. A simple and rapid redox speciation methodology for aqueous vanadium ions solutions of all possible oxidation states has been developed. It is an indirect spectrophotometric method based on the redox interaction of ferrous with V(V) and the subsequent analysis of the ferric sulfosalicylic acid complex. A direct spectrophotometric method for evaluating V(III)/V(II) mixture based on analyzing the thiocyanate complex has also been studied.

4.4 References

[1] E. L. Martin and K. E. Bentley, *Anal. Chem.*, 34 (1962) 354.

[2] C. J. Wood, *Progress in Nuclear Energy*, 23 (1990) 35.

[3] M. J. C. Taylor and J. F. van Staden, *Analyst*, 119 (1994) 1263.

[4] C. Agarwal, M. K. Deb, R. K. Mishra, *Analytical Letters*, 23 (1990) 2063.

[5] S. A. Abbasi, *Analytical Letters*, 9 (1976) 113.

[6] M. R. Shishehbore and R. Jokar, *Anal. Methods*, 3 (2011) 2815.

[7] W. R. King, and C. S. Garner, *J. Phys. Chem.*, 58 (1954) 29.

[8] C. L. Rulfs, J. J. Lagowski, and R. E. Bahor, *Anal. Chem.*, 28 (1956) 84.

[9] H. Willard and P. Young, *Ind. Eng. Chem.*, 6 (1934) 48.

[10] K. Ogawa and N. Tobe, *Bull. Chem. Soc. Japan*, 39 (1996) 223.

[11] D. G. Karamanev, L. N. Nikolov, V. Mamatarkova, *Minerals Engineering*, 15 (2002) 341.

[12] V. S. Tripathi, J. Manjanna, G. Venkateswaran, B. K. Gokhale and V. Balaji, *Ind. Eng. Chem. Res.*, 43 (2004) 5989.

[13] A. J. Bard and L. R. Faulkner, *Electrochemical Methods Fundamentals and Applications: Second Edition*, John Wiley & Sons, Inc., 2001, pp 445.

CHAPTER-5

Chromate Sorption over Magnetite in Presence of Gamma Irradiation

5.1 Introduction

Aqueous chromate removal on various iron oxides has been evaluated in several studies [1, 2]. Chromate has been in use as a corrosion inhibitor for various applications where iron based alloys are used [3]. In the shutdown cooling heat exchanger (closed system) in reactor systems such as BWRs, chromate is still in use as the corrosion inhibitor. Under certain operational conditions this chromate can come into primary coolant recirculation circuit and can interact with the magnetite bearing surface of the structural materials. Here, the presence of ionizing radiation will be an important parameter to be accounted for the interaction of chromate with magnetite. Structural modification of the oxide surface of the recirculation system due to concomitant presence of chromate and irradiation is of immense importance. Presence of chromium bearing outer oxide surface has various important implications. One of the important implications of the chromium bearing oxide surface is modification in the chemical formulation to be employed for decontamination of the recirculation system. The effect of radiation on the dissolution formulations has been studied by several authors [4, 5] but the effect of irradiation on oxide modification in concomitant presence of a particular chemical species which can alter the nature of the required dissolution formulation has not been reported so far. Immobilization of carcinogenic chromate using ferrous containing substrates has been evaluated by several authors [6-8]. Magnetite is one of the feasible substrates reported for the purpose. However, concomitant presence of irradiation has not been investigated so far. Although effect of γ-irradiation on solids have been studied extensively [9-12], the effect of irradiation on this heterogeneous chemical interaction has not yet been reported. Chromate interaction with magnetite in the presence of gamma irradiation has been studied and compared with the corresponding isothermal interaction.

5.2 Experimental

Magnetite was prepared through the hydrothermal route by heating $Fe(OH)_2$ under nitrogen atmosphere at 600 ^{o}C [13, 14]. Magnetite was equilibrated with potassium dichromate solutions at different temperatures viz. 40, 60 and 80 ^{o}C, at a given surface area to volume ratio and also irradiated at different absorbed doses in the range of 20 - 1000 kGy using a ^{60}Co source. For isothermal experiments at different temperatures, 50 ml of 2 mM chromate solution was equilibrated with 1.0 g of magnetite whereas for gamma irradiation studies, 25 ml of 2.0 mM chromate solution was equilibrated with 0.5 g of magnetite at each dose. Kinetics of chromate reduction was followed for the equilibration experiments at different temperatures. Irradiation experiments were also carried out in the presence of nitrous oxide. At the end of the equilibration experiments the oxides were recovered and were characterized by XRD and XPS. For XPS analysis, the dried powder samples were pressed on Indium foil and were loaded in the fast entry chamber, and shifted to the analysis chamber after half an hour. The drying process is natural and as these materials are very stable in ambient atmosphere, no change is expected. Excitation source was non-monochromatic Al k_α with energy 1486.6 eV. The analyzer resolution is 0.4 eV at 20 eV pass energy. The residual chromate was estimated spectrophotometrically by using the standard s-diphenylcarbazide method.

5.3 Results and discussion

5.3.1 Solution evaluation for isothermal interaction

Chromate sorption behaviour on magnetite at various temperatures is shown in **Fig 5.1(A)**. The kinetics of chromate sorption has been explained using the Lagergren's pseudo first order kinetic model [15]. The integrated first order rate expression of Lagergren is:

$$\log_{10}(q_e - q_t) = \log_{10} q_e - \frac{kt}{2.303} \qquad (5.1)$$

Where, q_e is the amount sorbed at equilibrium (mg/g), q_t is the amount sorbed at time t (min) and k is the first order sorption rate constant (min^{-1}). A good fitting to the Lagergren's pseudo first order kinetic model for the experimental data was obtained as shown in **Fig 5.1(B)**. This indicates that the chromate sorption rate on magnetite depends on the available sorption capacity of magnetite. The increase in the rate constant with temperature followed Arrhenious behaviour. However, the sorption of chromate on magnetite followed a saturation behaviour. At higher concentrations of chromate (**Fig-5.1B**), the sorption was not complete although there was a considerable amount of ferrous ions still remaining in the oxide. This suggests that only the surface sites of magnetite have participated in the chromate removal.

Fig 5.1: (A) Chromate removal on magnetite with varying temperature (50 ml of 2 mM chromate solution equilibrated with 1.0 g of magnetite) (B) Lagergren's pseudo first order kinetic model fitting for sorption of 50 ml of 10 mM chromate on 1 g of magnetite

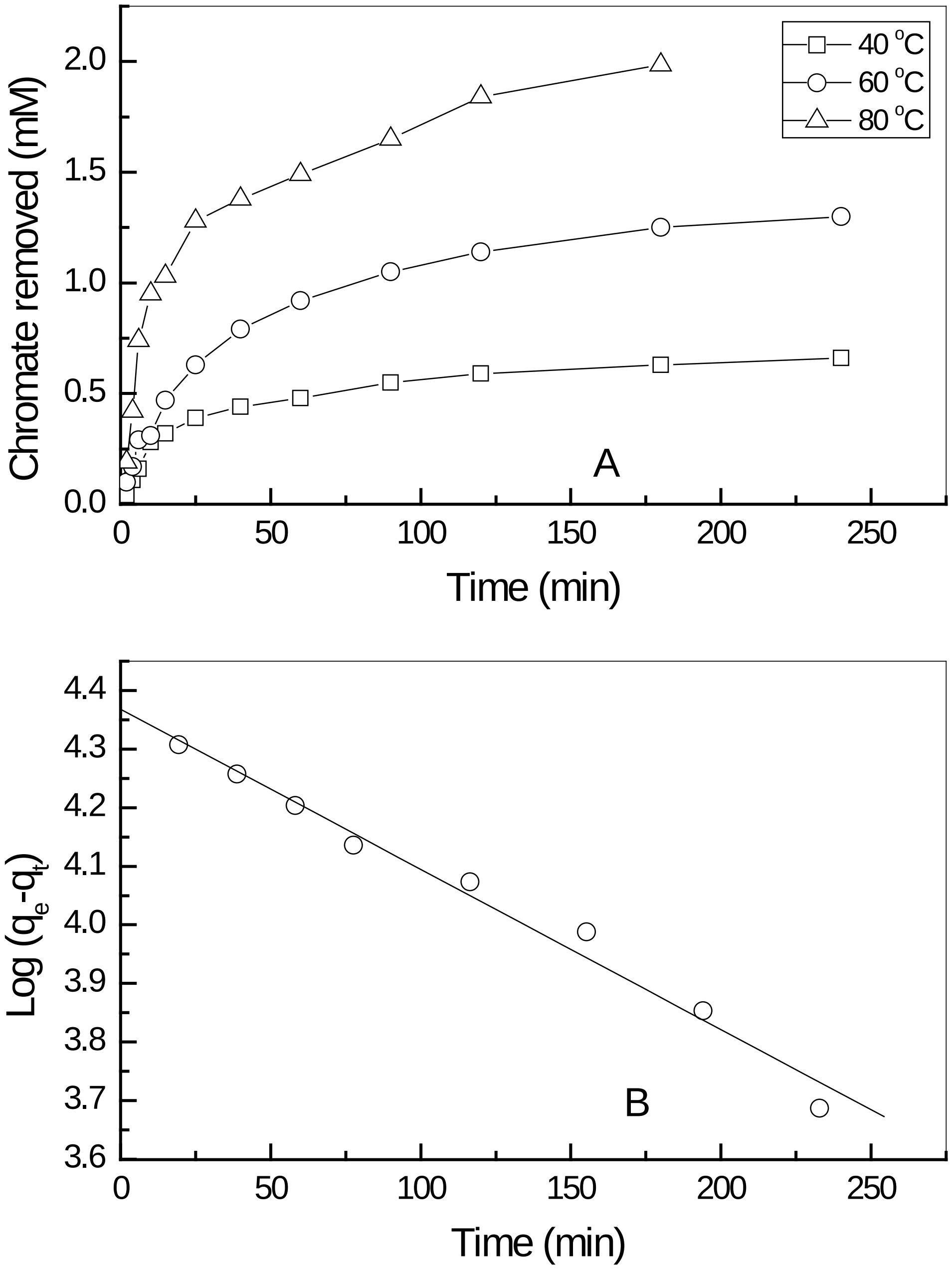

5.3.2 Oxide evaluation for isothermal interaction

There is insignificant difference in the XRD patterns of the magnetite samples before and after equilibration with chromate solution as shown in **Fig 5.2** (A and B). However, there is a slight shift in the peak positions towards the maghemite XRD pattern. The photoelectron peaks Cr $2p_{3/2}$ and Fe $2p_{3/2}$ were analysed from the XPS spectra obtained with the magnetite equilibrated with chromate solutions. Cr $2p_{3/2}$ spectra obtained for the different temperature equilibrated magnetite is shown in **Fig 5.3**. Cr $2p_{3/2}$ photoelectron peak was analyzed to find the chemical state of Cr adsorbed on the surface of magnetite at different temperature. In **Table 5.1** the binding energy and the peak widths of Cr $2p_{3/2}$ peaks at different temperature of the solution are shown. The binding energy was seen within a range of 576.6 – 576.8 eV, which indicates the presence of Cr^{3+} state on magnetite. The spin – orbit splitting of Cr $2p_{3/2}$ and Cr $2p_{1/2}$ peaks was measured to be 9.9 eV unlike the case of 9.3 eV for Cr^{6+} state. This further confirms the chemical state of Cr as Cr^{3+}. The Cr $2p_{3/2}$ peak was fitted to Gaussian- Lorenzian peak fitting equation according to the guideline of fitting [16]. A good fitting was observed for Cr^{3+} ion bonded within an octahedral field as shown in **Fig 5.4** which matches well with the literature data [17]. This suggests that the Cr ions on the surface of the magnetite are residing in a lattice of Cr_2O_3 wherein cations are bonded within an octahedral field. Fe $2p_{3/2}$ photoelectron peaks are analyzed to find the role of Fe in magnetite for the chemical interaction. In **Fig 5.5** and **Table 5.1**, Fe $2p_{3/2}$ spectra from samples treated with chromate at different temperatures are shown. From the binding energy of Fe $2p_{3/2}$ it appears that the Fe was also in 3+ state on the magnetite particles. This shows that there was a redox

Fig 5.2: XRD pattern of (A) pure magnetite, (B) magnetite treated with chromate at 60 ^{o}C and (C) magnetite treated with chromate at 350 KGy gamma dose.

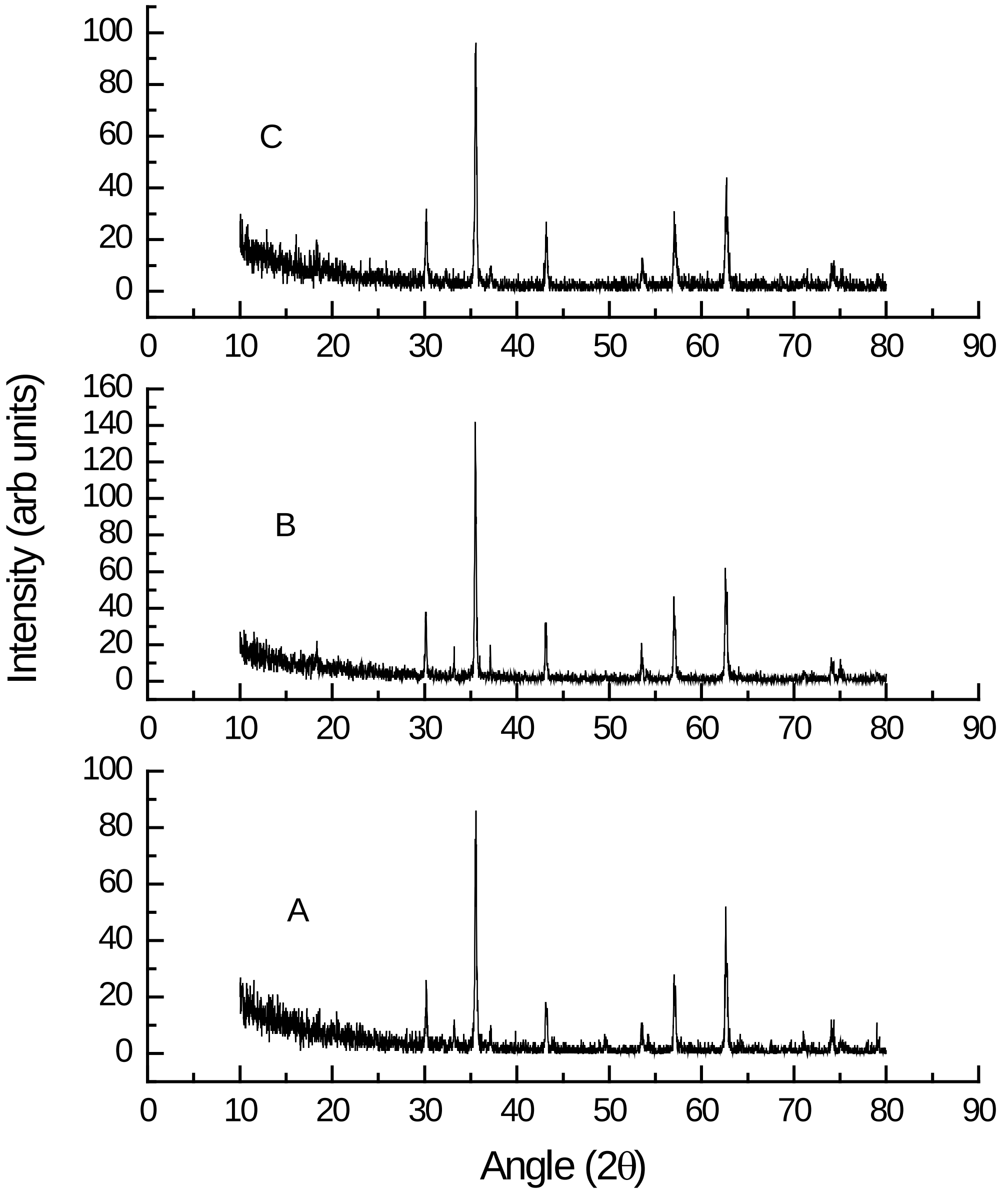

Fig 5.3: Cr 2p$_{3/2}$ photoelectron peak from the magnetite samples treated with chromate at different temperatures.

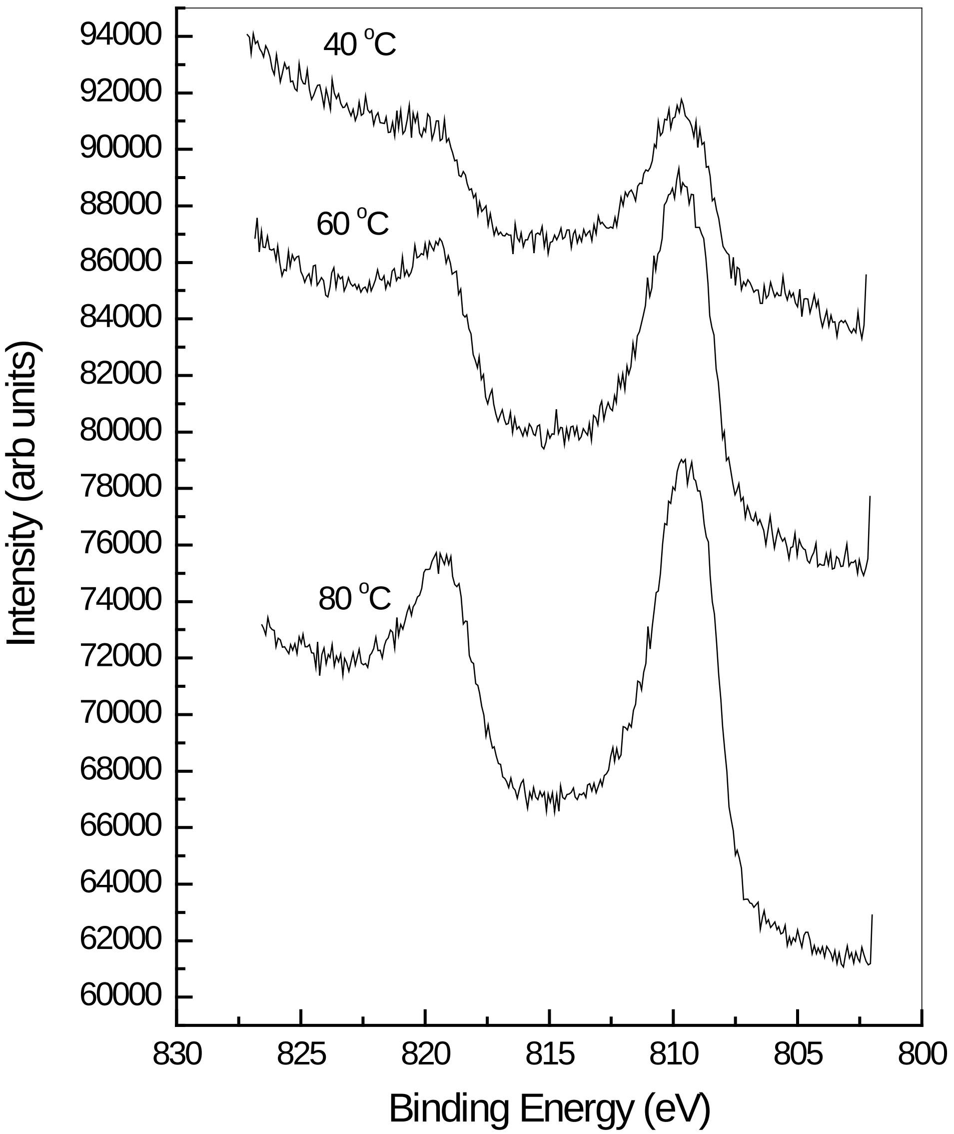

Table 5.1: Cr $2p_{3/2}$ and Fe $2p_{3/2}$ binding energy values obtained from magnetite equilibrated with chromate solution at different temperature

Sample **Fe_3O_4 + Chromate**	**B.E. Cr $2p_{3/2}$ (FWHM) eV**	**B.E. Fe$2p_{3/2}$ (FWHM) eV**
T= 40 °C	576.8 (2.7)	711.0 (3.9)
T=60 °C	576.8 (2.8)	710.9 (3.9)
T=80 °C	576.6 (2.8)	710.8 (3.9)

Fig 5.4: Deconvolution of Cr $2p_{3/2}$ peak to show that Cr resides in a lattice similar to Cr_2O_3

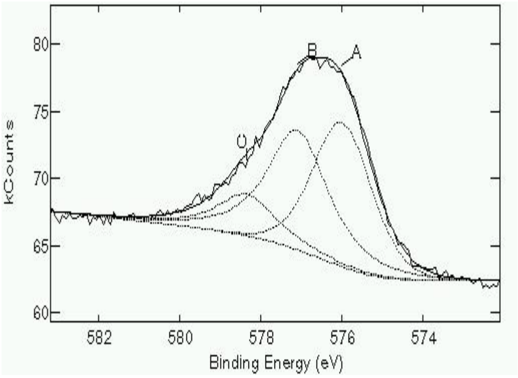

Fig 5.5: Fe 2p photoelectron peak from the magnetite samples treated with chromate at different temperature

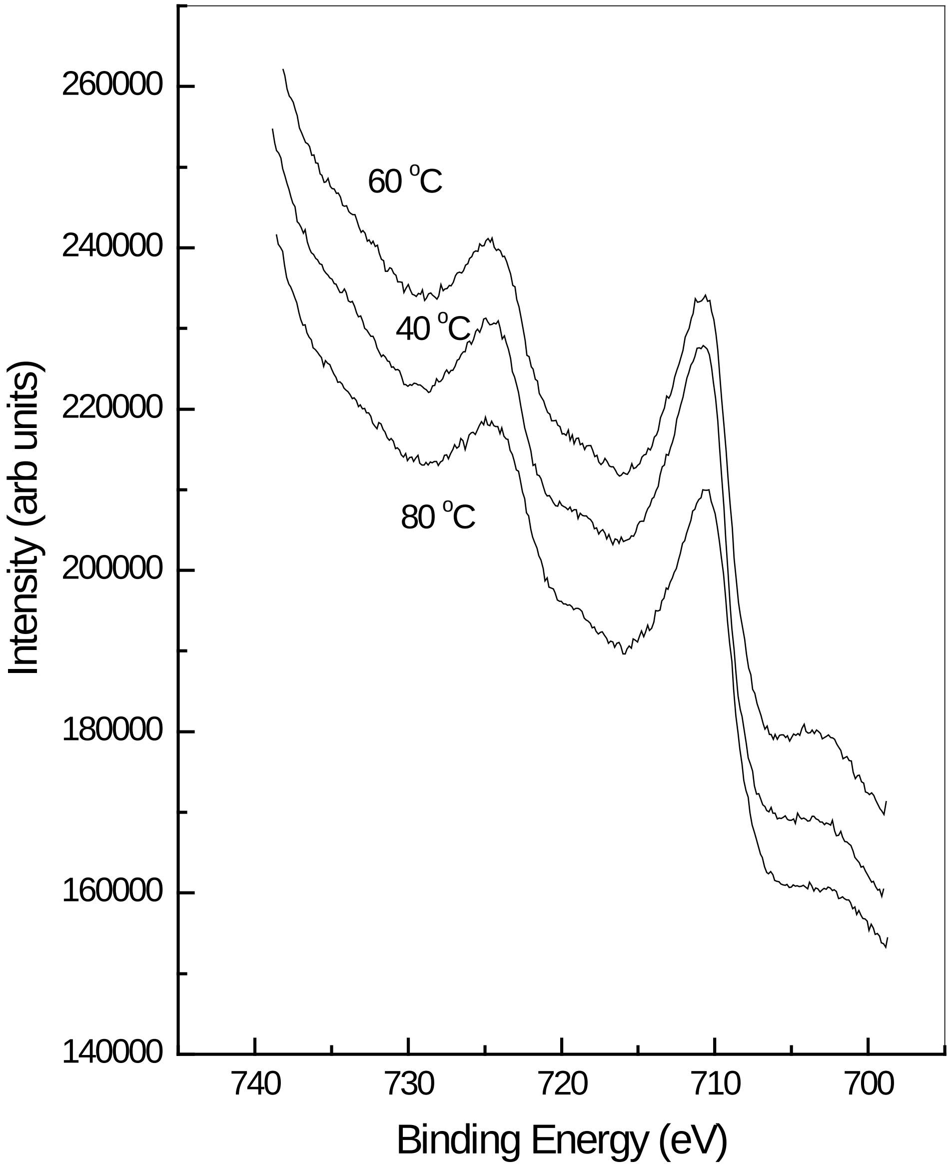

interaction of chromate ions in solution with Fe^{2+} ions in magnetite. Generally Fe $2p_{3/2}$ in magnetite does not show any satellite peak. But in the present case, a weak satellite peak appeared at around 8 eV above the main Fe $2p_{3/2}$ peak, which confirmed the dominance of Fe^{3+} in the treated magnetite powder. The principle Cr $2p_{3/2}$ peak has binding energies and line structure very similar to published XPS spectra for Cr_2O_3 [17]. It is observed that the pH of the chromate solution increased upon equilibration with magnetite. Also, the saturation behaviour of chromate sorption on magnetite has been attributed to the formation of passive maghemite layer on the surface of magnetite thereby stopping the further interaction of chromate with the ferrous ion [2]. Taking into account all the above facts, the interaction of chromate with magnetite can be represented as:

$$6Fe_3O_4 + K_2Cr_2O_7 + 2H^+ \rightarrow 9\ \gamma\text{-}Fe_2O_3 + Cr_2O_3 + H_2O + 2K^+ \qquad (5.2)$$

5.3.3 Solution evaluation of gamma irradiated chromate-magnetite system

The chromate solution was also equilibrated with magnetite under gamma irradiation at various doses. The chromate reduction with dose received is given in **Fig 5.6**(A). The chromate reduction under irradiation was again fitted to a Lagergren's pseudo first order kinetic model with respect to the dose received. The good fitting obtained with the experimental data is shown in **Fig. 5.6**(B). Thus, the rate of chromate reduction on magnetite appears to increase linearly with dose. The rate constant obtained by this fitting is 0.0047 kGy^{-1} whereas that for isothermal treatment at 80 ^oC is 0.0041 min^{-1}. Thus, the chromate reduced per kiloGray of gamma irradiation received is comparable to the chromate reduced per minute in isothermal equilibration at 80 ^oC. In another set of experiments, chromate solution was irradiated at 200 kGy with varying amounts of

Fig 5.6: (A) Chromate sorption on magnetite under gamma irradiation (25 ml of 2.0 mM chromate solution was equilibrated with 0.5 g of magnetite at each dose). (B) Lagergren's pseudo first order kinetic model fitting for chromate reduction with respect to dose.

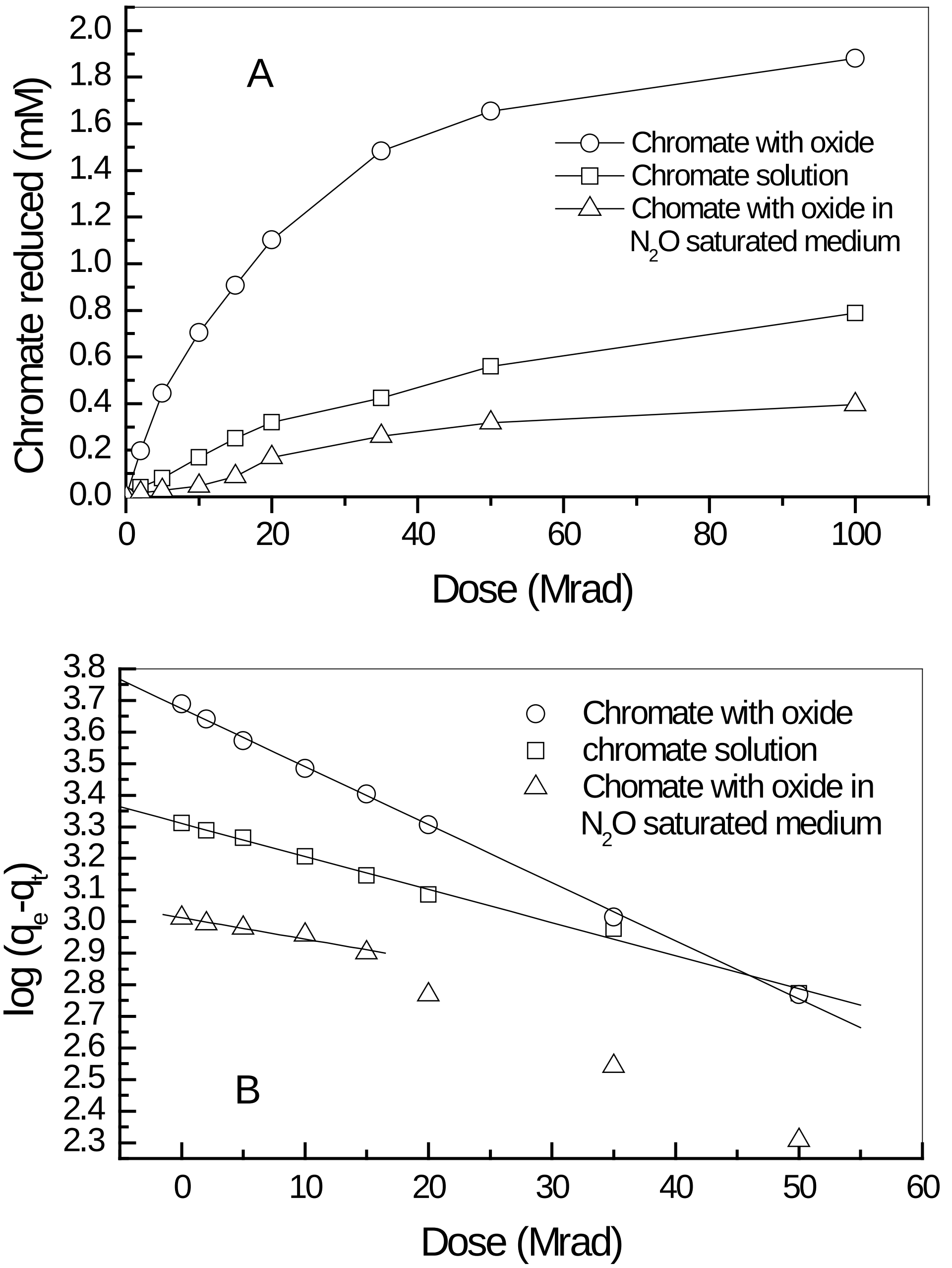

magnetite as described in **Table-5.2**. The chromate reduction increased with the increasing amount of magnetite. Amount of chromate reduced normalized to the amount of magnetite taken has shown a decreasing trend with the increasing amount of magnetite. This suggests that the chromate reduction on magnetite is a surface phenomenon in the presence of irradiation.

Table 5.2: Sorption of 25 ml of 2 mM chromate on varying magnetite amount at 200 kGy dose

Amount of Magnetite (g)	**Chromate sorbed (mM)**	**Chromate sorbed per gram of magnetite (mmol/g)**
0.25	0.59	0.015
0.5	1.08	0.027
1.0	1.27	0.032

Chromate reduction on magnetite in the presence of irradiation was also studied with N_2O saturated medium. In this oxidizing medium, the thermal effect of irradiation as well as effect of the time of exposure could be evaluated. It was observed that the amount of chromate reduced in the N_2O saturated medium in the presence of magnetite was less than the chromate reduced by the same dose in the absence of magnetite. Also, for gamma irradiation experiments, the sum of the concentrations of chromate reduced in the absence of magnetite and the chromate reduced in the presence of both magnetite and N_2O under similar experimental conditions is less than that for chromate and magnetite mixture.

Fig 5.7: (A) Lagergren's pseudo first order kinetic model fitting for chromate reduction on magnetite with respect to varying dose rates. (B) Variation in the rate constants obtained with varying dose rates

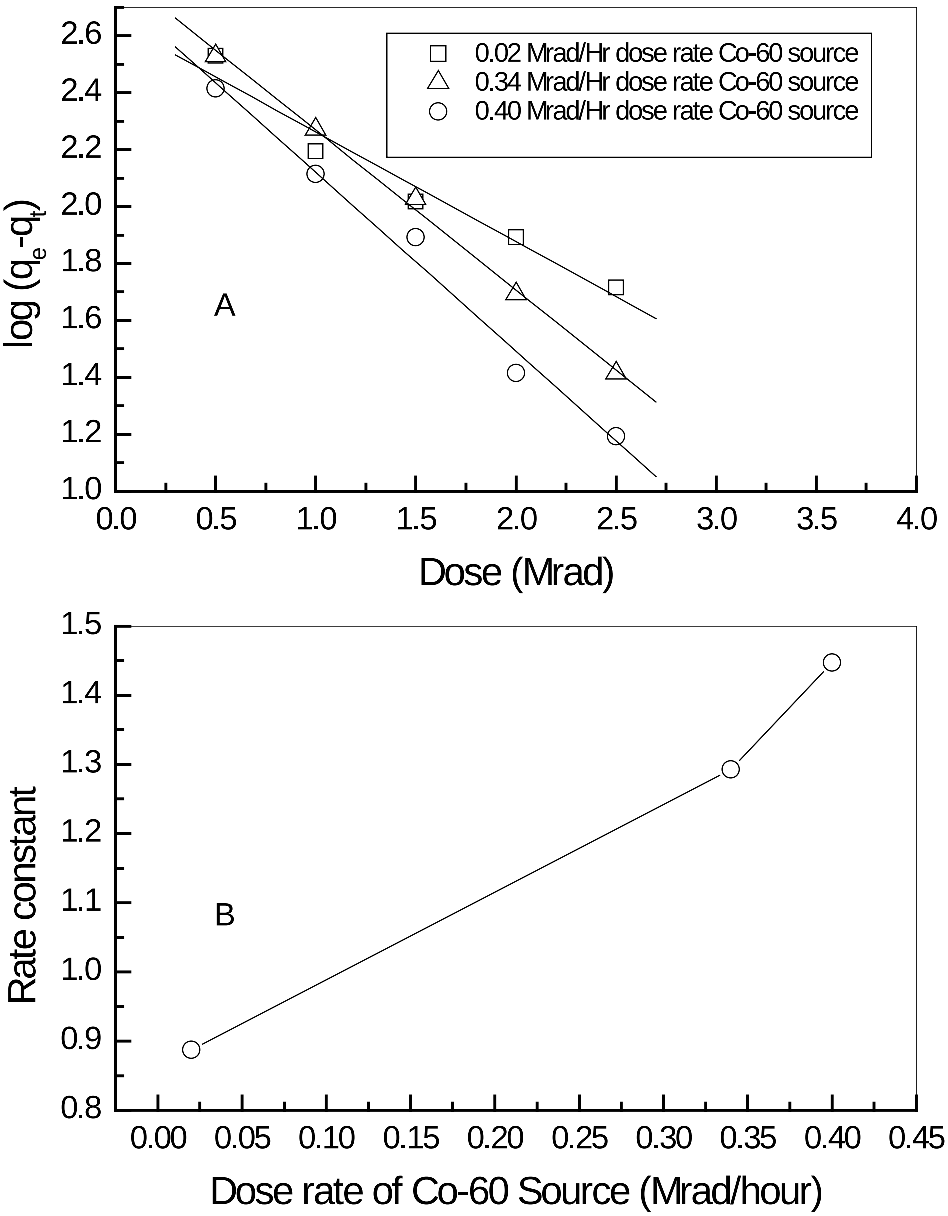

Thus, the cumulative effect of irradiation in the absence of magnetite and irradiation in oxidizing condition on chromate reduction is less than that in presence of magnetite in neutral aqueous environment. This indicates that the gamma irradiation has an effect on both chromate and magnetite surface. The effect of irradiation on the oxide surface can be attributed to formation of additional nucleation centers [18] which will enhance the heterogeneous redox interaction. Chromate reduction on the magnetite surface was also studied using different Co-60 gamma sources having different dose rates. The chromate-magnetite systems were exposed to same overall accumulated doses in all the gamma sources. The pseudo first order fitting of the experimental data is shown in **Fig 5.7**(A). The values of the rate constants obtained by the fitting of the experimental data to the Lagergren's pseudo first order kinetic model have shown direct dependence on the dose rates of the source as shown in **Fig 5.7**(B). The rate constants increased with the increase in the dose rate of the source. This shows that the chromate reduction on magnetite directly depends upon the water radiolysis. At higher dose rates, the concentration of the radiolytic products is more and hence a higher rate constant value is obtained indicating a faster reduction process.

5.3.4 Oxide evaluation of gamma irradiated chromate-magnetite system

Fig 5.8 and **Table 5.3** show the Cr $2p_{3/2}$ photoelectron peak and their binding energy under different radiation dose of chromate treatment with magnetite. Chromium was found to increase with the radiation dose as shown in **Fig 5.8**. The binding energy of Cr $2p_{3/2}$ showed the presence of Cr^{3+} on magnetite after the treatment. In the irradiated case,

Fig 5.8: Cr 2p photoelectron peak from the magnetite samples treated with chromate at different radiation doses

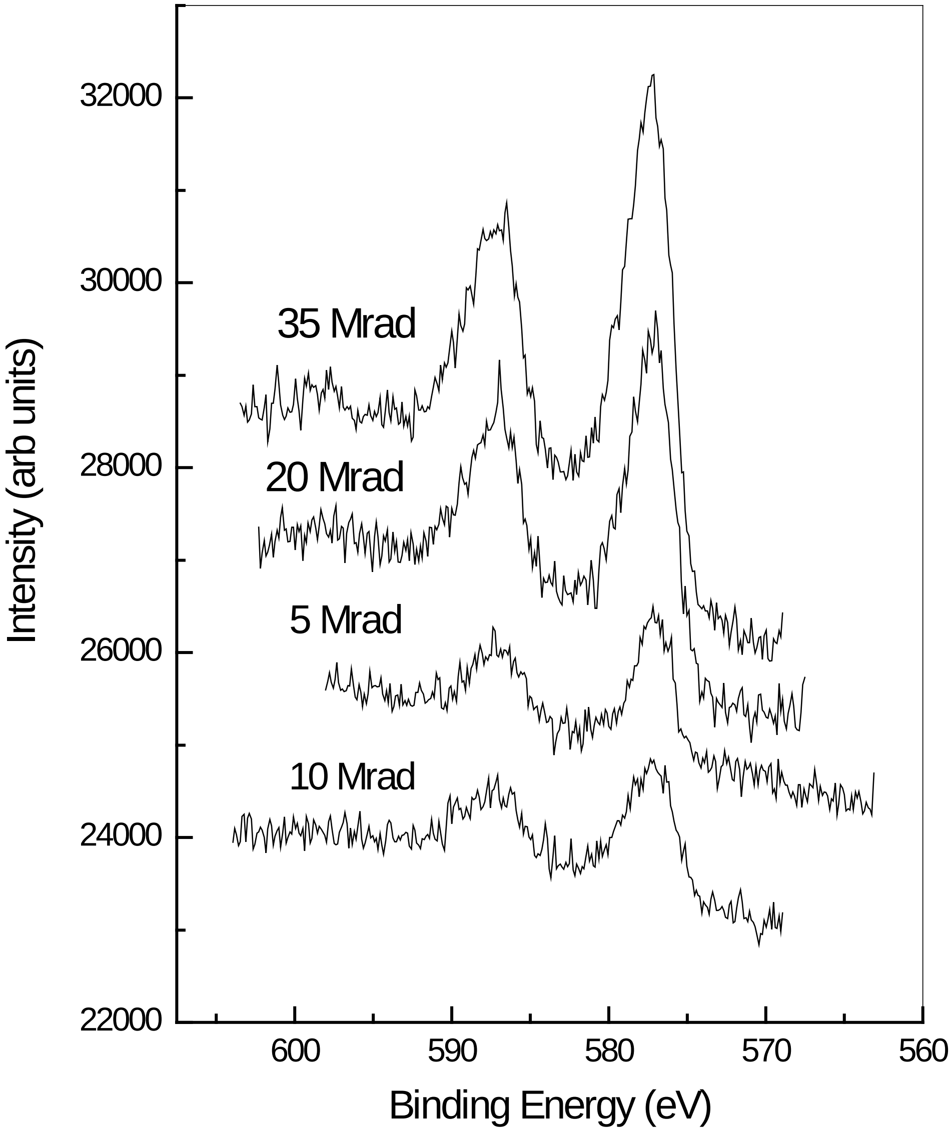

Table 5.3: Cr $2p_{3/2}$ and Fe $2p_{3/2}$ binding energy values obtained from magnetite in chromate solution exposed at different gamma doses

Fe_3O_4 + chromate at	Cr$2p_{3/2}$ (FWHM) eV	Fe$2p_{3/2}$ (FWHM) eV
50 kGy	577.2 (2.6)	711.2 (3.9)
100 kGy	577.4 (3.3)	711.3 (4.3)
200 kGy	577.2 (3.1)	713.2 (5.5)
350 kGy	577.5 (3.3)	711.3 (4.4)

Cr $2p_{3/2}$ peak binding energy and peak width is higher that the non-irradiated case. It appears that Cr in the irradiated sample is present as different Cr^{3+} bearing species. Though the Cr 2p peaks are broad, the peak center appears to be very sharp unlike the case of Cr_2O_3. The peak position indicates a majority of Cr-OH type species residing on the surface of the magnetite. Similarly Fe 2p peak also showed higher binding energy and broader peak unlike the previous case as shown in **Fig 5.9**. In general the Fe $2p_{3/2}$ peak is the most intense peak and used widely for data processing and conclusions. But in the present case as the satellites of Fe $2p_{3/2}$ appeared superimposed on the huge back ground of Fe $2p_{1/2}$ peak, we observed that satellite peak analysis Fe $2p_{1/2}$ peak is more reliable and less complicated compared to Fe $2p_{3/2}$. Anyway, the chemical information obtained from Fe $2p_{1/2}$ or Fe $2p_{3/2}$ is exactly same. The spectral characteristics indicate that the chemical interaction between chromate and the magnetite under gamma irradiation is different from that in the absence of gamma irradiation.

Fig 5.9: Fe 2p photoelectron peak from the magnetite samples treated with chromate at different radiation doses

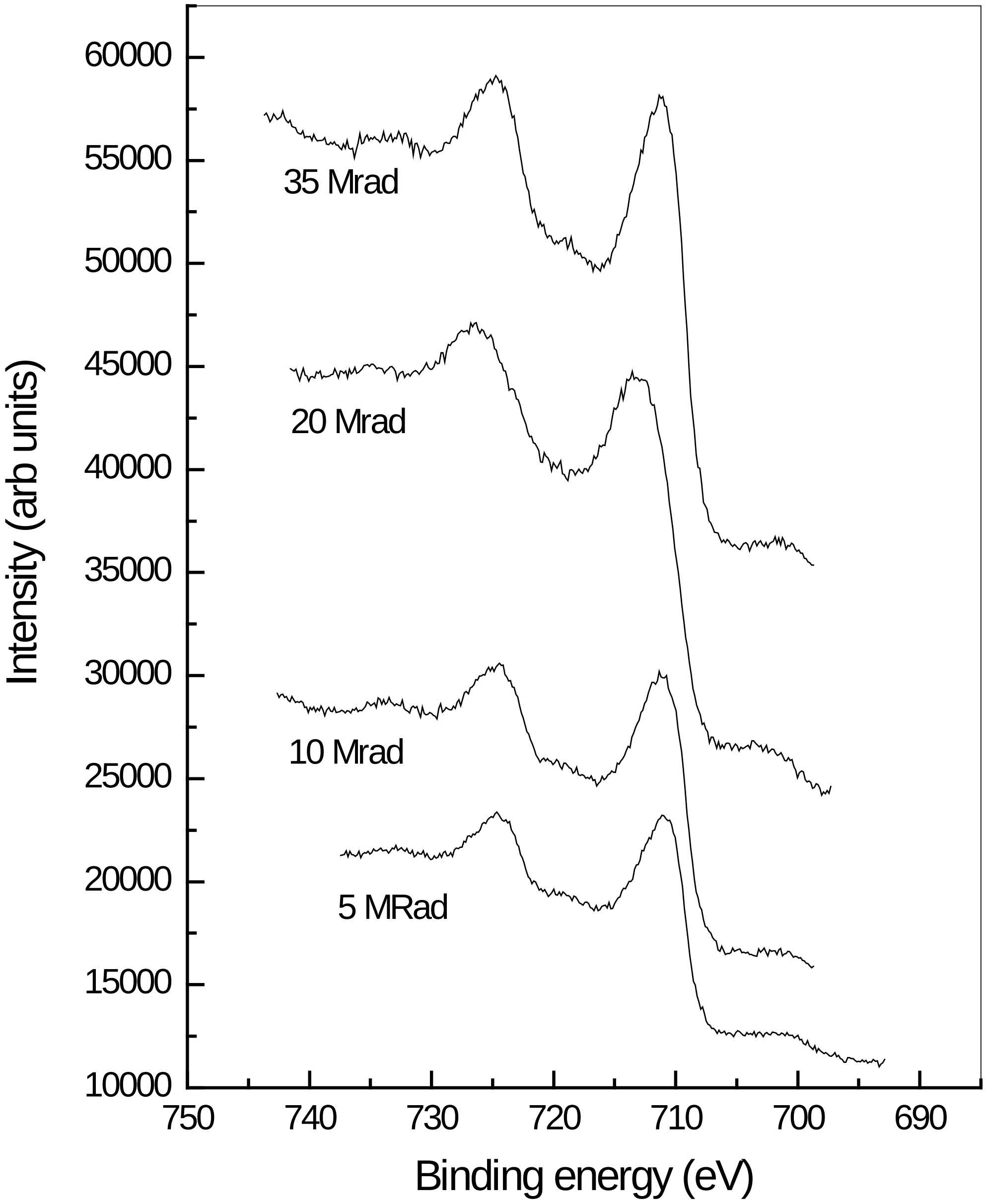

Fig 5.10: O1s photoelectron spectra for magnetite equilibrated with chromate under different conditions

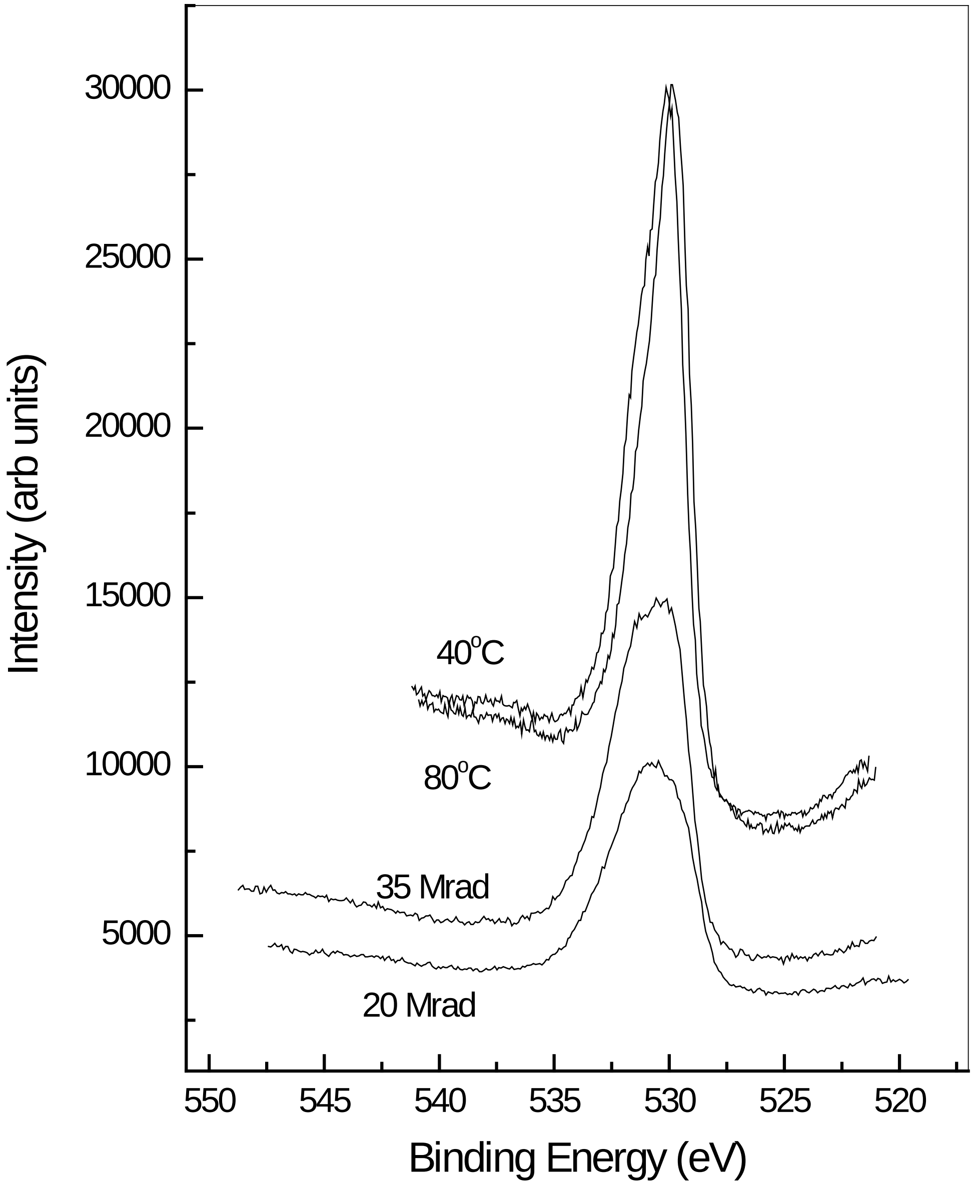

The satellite peak for the magnetite treated with chromate under gamma irradiation is not very prominent. O 1s peaks was compared for the magnetite samples equilibrated with chromate with temperature with the one obtained from the magnetite samples equilibrated with chromate solution at different doses, as shown in **Fig 5.10**. It is seen that the O1s peak in case of non irradiated case is sharp and comparable with peak shape of O1s showed by standard magnetite [19, 20]. But in the irradiated case the O1s peak is broader and indicated the presence of some –OH group in the sample (peak at around 531.5 eV). Peak fitting of Cr 2p, Fe 2p and O1s photoelectron peaks under magnetite irradiated at 350 kGy is shown in **Fig 5.11**. A summary of the results obtained by the fitting is given in **Table 5.4**.

Table 5.4: Results from deconvolution of Cr $2p_{3/2}$, Fe 2p and O 1s photoelectron peaks from magnetite after exposure in chromate with irradiation to 350 kGy dose

Fe 2p $_{1/2}$		**Cr 2p**		**O1s**	
b.e (eV)	**Remarks**	**b.e (eV)**	**Remarks**	**b.e (eV)**	**Remarks**
733.3	Sat Fe^{3+}	577.8 (85%)	CrOOH	531.7 (68%)	-OH
729.5	Sat Fe^{2+}				
725.6	Fe^{3+} (FeOOH)	576.9 (15%)	Cr_2O_3	530.1 (32%)	-O-
723.9	Fe^{3+} and Fe^{2+}				
			Trace of Cr^{+6}		

This suggests that Cr^{3+} on the surface of magnetite was present in two different compounds, CrOOH and Cr_2O_3. Similarly the presence of FeOOH was also found after fitting the Fe $2p_{3/2}$ spectrum. The O1s spectrum showed that majority of O1s signal

Fig 5.11: (A) Cr $2p_{3/2}$, (B) Fe 2p and (C) O 1s photopeak deconvolution from Magnetite after exposure in Chromate with irradiation 350 KGy

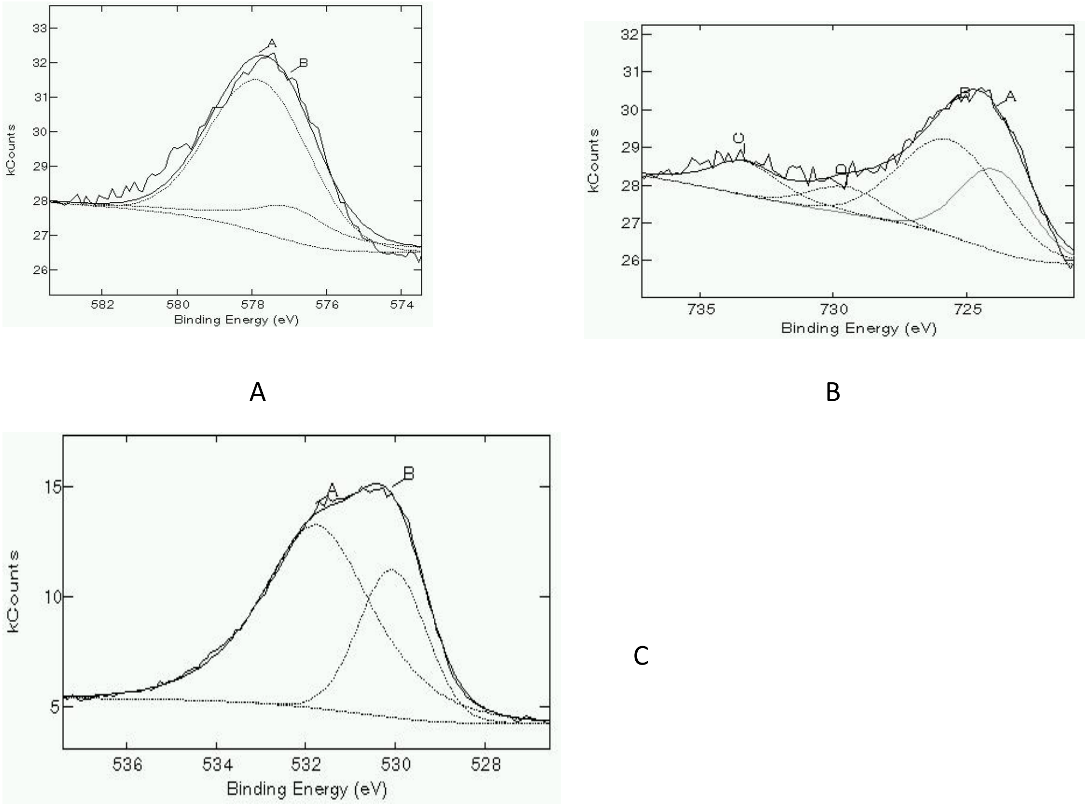

A

B

C

comes from the –OH type species on the surface, which can be attributed to the presence of FeOOH and CrOOH. Thus, the redox interaction in the presence of γ-irradiation seems to proceed through several different pathways. Prominent presence of hydroxyl group indicates the important role of reducing radicals on the heterogeneous redox interaction. The effect of Co-60 γ irradiation on chromate reduction on magnetite can be attributed to the combined action of the reducing radiolytic species generated during the process in solution and the action of radiation on the surface. The initial pH of the mixtures in all the experiments was around 4.65. The primary reducing radical in this pH range is aqueous electron and hydrogen radical whose G value remains constant upto the pH of around 10 in pure water [21]. Also, the molecular product yield at higher pHs are low and hence the reducing radicals can directly act on the chromate.

Summary

Chromate reduction on magnetite in presence of γ irradiation has followed a Lagergren's pseudo first order kinetic model with respect to the applied dose. The extent of chromate reduction with increasing magnetite amount has indicated that the process is a surface phenomenon. Also, the effect of radiolytic species on both the chromate solution and the magnetite surface could be established by studying the N_2O saturated solution of chromate and studying chromate reduction on magnetite using different γ sources. XPS data has shown a difference in the surface composition of magnetite equilibrated with chromate due to the effect of irradiation and it corroborates the solution analysis results.

5.4 References

[1] H. Abdel-Samad, and P. R. Watson, *App. Surf. Sci*., 108 (1997) 371.

[2] M. L. Peterson, A. F. White, G. E. Brown and G. A. Parks, *Environ. Sci. Technol.*, 31 (1997) 1573.

[3] E. McCafferty, M. D. Bernett and J. S. Murday, *Corrosion Science*, 28 (1988) 559.

[4] R. M. Sellers, *Radiat. Phys. Chem.*, 21 (1983) 295.

[5] S. J. Keny, A. G. Kumbhar, G. Venkateswaran and K. Kishore, *Radiat. Phys. Chem.*, 72 (2005) 475.

[6] J. M. Zachara, D. C. Girvin, R. L Schmidt and C. T. Resch, *Environ. Sci. Technol.*, 21 (1987) 589.

[7] R. M. Powell, R. W. Puls, S. K. Hightower and D. A. Sabatini, *Environ.Sci. Technol.*, 29 (1995) 1913.

[8] S. E. Fendorf and G. Li, *Environ. Sci. Technol.* **1996,** *30*, 1614-1617.

[9] N. Fujita and C. Matsura, *Radiat. Phys. Chem.*, 43 (1994) 205.

[10] S. Wang and H. Xin, *Radiat. Phys. Chem.*, 56 (1999) 567.

[11] A. B. El-Bediwi, M. Saada, A. A. El-Fallal and S. El-Khaligy, *Radiation Effects and Defects in Solids*, 166 (2011) 223.

[12] M. dos Santos Afonso and C. Di Risio, *Radiat. Phys. Chem.*, 58 (2000) 261.

[13] G. Visalakshi, G. Venkateswaran, S. K. Kulashreshtha and P. N. Moorthy, *Mater. Res. Bull.*, 28 (1993) 829.

[14] E. Matijevic, *Ann. Rev. Mater. Sci.*, 15 (1985) 483.

[15] E. Demirbas, M. Kobya, E. Senturk and T. Ozkan, *Water SA*, 30 (2004) 533.

[16] A. R. Pratt, D. W. Blowes and C. J. Ptacek, *Environ. Sci. Technol.*, 31 (1997) 2492.

[17] I. Grohmann, E. Kemnitz, A. Lippitz and W. E. S. Unger, *Surface Interface Analysis*, 23 (1995) 887.

[18] R. M. Mahfouz, S. M. Al-Shehri, M. A. S. Monshi and N. M. Abd El-Salam, *Radiation Effects and Defects in Solids*, 157 (2002) 515.

[19] X. Wei-Xing, W. Lu-Chun, W. Rui and F. Xian-Cai, *J. Colloid Interface Sci.*, 179 (1996) 350.

[20] K. Wandelt, *Surf. Sci. Rep.*, 2 (1982) 1.

[21] J. W. T. Spinks and R. J. Woods, *An Introduction to Radiation Chemistry*, third ed.; John Wiley: New York, 1990, pp 255-263.

CHAPTER-6

Water Chemistry Control by Weak Base Anion Exchanger

6.1 Introduction

Soluble burnable poison in the moderator has been selected for reactivity control during startup and shutdown (secondary shutdown system) of the 540 MWe pressurized heavy water reactors (PHWRs) in India. Gadolinium as gadolinium nitrate is added into the heavy water moderator system for this purpose. This is accomplished by adding the secondary shutdown system (SDS) inventory which is a concentrated acidic $Gd(NO_3)_3$ solution to the moderator system. The pH range of operation for the moderator system is specified to be 5.0-5.5 as long as gadolinium is present and the conductivity in $\mu S\ cm^{-1}$ has to obey an approximate empirical relationship $\kappa = \{4\ [Gd] + 2\}$, where κ is conductivity in $\mu S\ cm^{-1}$, [Gd] is the concentration of gadolinium in $mg\ kg^{-1}$, the constant 4 carries $\mu S\ kg\ cm^{-1}\ mg^{-1}$ and the constant 2 carries $\mu S\ cm^{-1}$ unit. The upper limit for pH is restricted to avoid any precipitation of gadolinium in the system [1-4] and the lower limit is fixed to maintain the material compatibility of the different structural materials of the composite moderator system [5, 6]. Colloidal hydroxide/hydrous oxide/oxide formation has been reported for rare earths in the pH range of 4.5 to 6.0 at relatively much higher concentrations by forced hydrolysis [7]. Reactor operation or criticality depends on the Gd concentration in the moderator. The concentration of gadolinium before first approach to criticality was held at 2 $mg\ kg^{-1}$, and after ~140 efficient full power days it was kept at 0.7 $mg\ kg^{-1}$ at the time of startup while as a secondary shutdown tool gadolinium is used at 15 mg kg^{-1} concentration in the moderator system. Removal of gadolinium from moderator system involves a mixed bed of strong acid cation exchanger (SAC) and weak base anion exchanger (WBA). Weak base anion exchanger is used to avoid any precipitation of gadolinium as $Gd(OH)_3$ due to removal of nitrate prior to Gd^{3+} removal on SAC. This is possible when strong base anion exchanger is used in place weak base anion exchanger. The use of WBA also facilitates selective removal of gadolinium over boron. Boron is present as a conjugate base of a weakly acidic species in aqueous medium. This cannot be removed on weak base anion exchanger. Thus, from a mixture of boric acid and gadolinium nitrate, nitrate ion will be selectively removed on weak base anion exchanger column. Boric acid was used during the first approach to criticality for fine adjustments of reactivity (reactivity change brought about for unit change in its concentration is less for boron as compared to gadolinium) since it has a lower neutron absorption cross section (~780 barns for natural boron) as compared to gadolinium (~ 48 000 barns for natural gadolinium). During the removal of gadolinium through such a column, in the initial stages the pH at the outlet of the column went above 5.5 and remained above 5.5 for about one half life of recirculation (~ 6 hours) through the column. However, the bulk moderator system pH remained within the specified limit throughout the run. Feasibility of maintaining the pH of the ion exchange column outlet within the specified limits of the bulk moderator system by the leach out of nitric acid from the weak base resin of the column has been studied. The leach out characteristics of nitric acid from weak base resin as a function of nitric acid loading and initial inlet concentration at a particular flow rate is evaluated. Based on the evaluation of leaching from the nitric acid loaded weak base anion exchanger, a column configuration is suggested for maintaining the column outlet pH within the specified limits during the Gd^{3+} removal from the moderator system.

6.2 Experimental

Macroporous weak base anion exchanger (Auchtel duolite ARA 9369 WBA with macroporous polystyrene matrix, tertiary amine functional group and total exchange capacity of 1.4 meq ml^{-1}) resin was used for studying the nitric acid leachout characteristics in both once through and recirculation modes. Nano pure water (specific resistance: 18.2 MΩ-cm) was used for all the experiments. Once through mode elution studies involved passing nano pure water through different nitric acid loaded weak base anion exchanger (NLWBA) mixtures with fresh weak base anion exchanger columns and also eluting nitric acid solutions at various pHs through different nitric acid loaded weak base anion exchanger mixtures with fresh weak base anion exchanger columns. In the recirculation mode experiments, nano pure water was recirculated through different nitric acid loaded weak base anion exchanger mixtures with fresh WBA and also an equivalent amount of nitric acid in solution was recirculated through a fresh weak base anion exchanger column. In all these experiments, 10 l solution was passed through 10 ml of the resin (column diameter was 1.5 cm while the average resin bead diameter was around 0.05 cm and hence wall effects were negligible) at a flow velocity of 170 cm min^{-1} which simulates the flow velocity in the moderator purification circuit in the Indian 540 MWe PHWRs.

In another set of experiments, $Gd(NO_3)_3$ removal from TAPP 3&4 moderator system was simulated. The moderator inventory is 2,66,363 liters of heavy water while the ion exchange columns have a volume of 200 liters. In the laboratory studies, 60 liters of 4 and 15 mg kg^{-1} solution of $Gd(NO_3)_3$ at pH 5 was circulated through 80 ml resin column. The column consisted of 16 ml strong acid cation exchanger (Auchtel duolite ARC 9351 in H^+ form with macroporous polystyrene matrix, sulfonic acid functional group and exchange capacity of 1.8 meq ml^{-1}) topped mixed bed of 8 ml strong acid cation exchanger and 48 ml weak base anion exchanger as such and in another experiment, a similar column with a bottom packing of 8 mL of 5 % NLWBA mixture with fresh weak base anion exchanger. Thus, the ratio of total solution to total resin volume in the experimental condition was almost half of that in the reactor. For removal of 15 mg kg^{-1} gadolinium, the amount of weak base anion exchanger taken was resulting in about 20 % loading upon complete removal of gadolinium from the system while the amount of strong acid cation exchanger taken was for about 40 % loading upon complete removal of gadolinium. Strong acid acid exchanger topping was provided for sequential removal of Gd^{3+} on top strong acid cation exchanger followed by removal of resulting HNO_3 on the mixed bed to avoid any possibility of precipitation of gadolinium due to initial removal of nitric acid and hence increase in pH.

pH and conductivity were measured at regular intervals of time in all experiments using PHAN pH meter from Lab India with a resolution of 0.01 pH units and CON 1500 conductivity meter from Eutech Instruments with four probe electrode and resolution of 0.001 µS cm^{-1}. In nitric acid elution experiments, concentration of nitric acid was determined from the pH values. Gd was measured spectrophotometrically by Arsenazo(III) method at 650 nm [8].

6.3 Results and Discussion

6.3.1 Leachout behaviour of WBA column

Leaching characteristics of nitric acid from various nitric acid loaded weak base anion exchanger mixtures with fresh weak base anion exchanger have been analyzed for the once-through column experiments. Sorption behaviour of strong acids on weak base resin has been studied in details in earlier works [9, 10]. Bhandari et al. [9] observed significant reversibility even at high hydrochloric or nitric acid concentrations and they proposed a model accounting for sorption equilibria and dynamics by considering an electrical double layer at the pore walls. In the present work, we have used a simple empirical approach to evaluate the nitric acid sorption-desorption behaviour on weak base resin under given experimental conditions. This approach is sufficient to serve our purpose of calculating the required amount of nitric acid loaded weak base anion exchanger mixture with fresh weak base anion exchanger to be used as a bottom layer of the column to achieve the desired pH at the outlet during Gd^{3+} removal with the given flow velocity and the ratio of resin volume to amount of Gd^{3+} to be removed.

Nitric acid leaching from nitric acid loaded weak base anion exchanger on eluting pure water at a fixed flow velocity is assumed to depend only on the amount of nitric acid sorbed on the nitric acid loaded weak base anion exchanger. This implies that upon eluting pure water through a nitric acid loaded weak base anion exchanger mixed with fresh weak base anion exchanger column, the column outlet nitric acid concentration or conductivity would vary as a first order decrease with respect to time. Therefore, plot of the outlet conductivity against time for weak base anion exchanger columns loaded with nitric acid loaded weak base anion exchanger mixed with fresh weak base anion exchanger to different extents is fitted to a first order decrease according to the equation:

$$x = x_o \exp(-\lambda t) \tag{6.1}$$

where x is the conductivity of the column outlet solution in μS/cm, x_o is the conductivity equivalent of the total nitric acid loaded on the column, λ is the leaching constant in min^{-1} and t is time in minutes.

Levenberg-Marquardt algorithm is used for fitting and parameter evaluation through 'origin' software. For lesser loading of the column, a good fitting is obtained as indicated by the low chi square values. Also, the leaching constant obtained by the fitting is almost similar upto 50 % nitric acid loaded weak base anion exchanger mixture with fresh weak base anion exchanger. Here, x_o is an experimentally known parameter but we have not fixed it during the fitting. This approach was taken to maintain uniformity in the procedure followed for single mode of leaching and multiple mode of leaching which is discussed later. The fitting of column outlet conductivity to the first order decrease is not satisfactory for experiments of higher loading of the resin. The leachout behaviour is then visualized as a sum of several simultaneous leaching modes with each of the mode following a first order decrease. This will lead to a leaching behaviour where the total nitric acid leachout is the sum of leachout from sites with varying strength of nitric acid retention. The column outlet conductivity upon elution of pure water through the nitric acid loaded weak base anion exchanger column can then be represented as:

$$x = x' + x'' + ... = x_o^{'} \exp(-\lambda' t) + x_o^{''} \exp(-\lambda'' t) + ... \qquad (6.2)$$

where x is the conductivity of the column outlet solution, x’, x” … are the conductivity contribution from each individual mode with $x_o^{'}$, $x_o^{''}$ … being the initial conductivity from the respective modes and λ’, λ” … being the leaching constants of the respective modes. The distribution of nitric acid in various modes will depend upon the structure of the resin beads and upon the distribution of the functional groups in the resin bead. The parameters obtained by fitting the experimental data to equation 6.2 are given in **Table-6.1**.

The elution of pure water through a five percent nitric acid loaded column has given a similar chi square value upon fitting the column outlet conductivity data to single, two or three modes of leaching. However, the fitting to two, three or four modes of leaching has given one mode of leaching with a negative leaching constant. A negative leaching constant can be visualized as a representation of pickup instead of leaching. Since the column is loaded only to an extent of five percent, the leached out nitric acid may again be picked up by the remaining ion exchange sites. The negative leaching constants in all modes are very small and the initial conductivity for that particular mode is also very small. This indicates the marginal pickup of the released nitric acid by this mode of action of the column.

Table 6.1: Parameters obtained by fitting various modes of leaching to the outlet conductivity of once through elution with high purity water through WBA resin columns loaded with NLWBA mixed with fresh WBA to different extents.

Type of leaching	Parameters obtained	5% NLWBA	10 % NLWBA	20 % NLWBA	50 % NLWBA	100 % NLWBA
Single mode	Chi square	0.003	0.002	0.064	1.391	56.404
	$x_o^{'}$	2.91± 0.05	4.29± 0.04	6.84± 0.23	21.20± 1.07	81.65± 8.86
	λ’	0.009± 0.001	0.011± 0.001	0.011± 0.001	0.011± 0.002	0.033± 0.006
Two modes	Chi square	0.003	0.001	0.0003	0.010	1.344
	$x_o^{'}$	0.26± 2.71	0.02± 0.11	6.13± 0.04	17.64± 0.25	44.75± 4.12
	λ’	-0.023± 0.140	-0.066± 0.102	0.008± 0.001	0.005± 0.001	0.011± 0.003
	$x_o^{''}$	2.75± 0.03	4.36± 0.07	4.87± 0.61	18.66± 2.05	122.18± 16.73
	λ”	0.017± 0.033	0.014± 0.003	0.318± 0.030	0.270± 0.028	0.236± 0.039
Three modes	Chi square	0.005	0.002	0.001	0.015	0.558
	$x_o^{'}$	0.86± --	0.60± --	0.53± --	17.88± 0.74	1.32± 8.63
	λ’	-0.008± --	-0.012± --	0.318± --	0.006± 0.002	-0.055± 0.124
	$x_o^{''}$	1.07± --	1.23± --	6.13± 0.11	3.4×10^{-7}± --	62.92± 10.97
	λ”	0.024± --	0.018± --	0.008± 0.001	-0.328± 1.900	0.032± 0.033
	$x_o^{'''}$	1.09± --	2.56± --	4.34± --	19.60± 4.01	206.68± 186.12
	λ’’’	0.023± --	0.019± --	0.318± --	0.288± 0.062	0.4254± 0.261
Four modes	Chi square	--	--	--	--	--
	$x_o^{'}$	0.69± --	3.8×10^{-9}± --	0.70± --	2.52± --	5.20×10^{-9}± --
	λ’	-0.010± --	-0.487± --	0.008± --	0.005± --	0.167± --
	$x_o^{''}$	0.78± --	0.05± --	0.14± --	2.5×10^{-9}± --	27.70± --
	λ”	0.022± --	0.002± --	0.318± --	-0.452± --	0.067± --
	$x_o^{'''}$	0.82± --	1.15± --	5.44± --	15.35± --	32.99± --
	λ’’’	0.022± --	0.002± --	0.008± --	0.006± --	0.005± --
	$x_o^{''''}$	0.73± --	3.15± --	4.73± --	19.58± --	166.49± --
	λ’’’’	0.022± --	0.017± --	0.318± --	0.287± --	0.355± --

Similar results are obtained with the column having ten percent nitric acid loading. Chi square values obtained from the fitting to single mode of leaching for both cases are comparable and very small. Also, the leaching constant for single mode of leaching for these two cases is comparable. Thus for all practical purposes, the leaching behaviour of ten or five percent nitric acid loaded columns can be assumed to follow single mode of leaching following a first order release of nitric acid at a given flow rate.

The chi square value obtained by fitting the outlet conductivity data of elution of pure water through the twenty percent nitric acid loaded weak base anion exchanger column to single mode of leaching was higher by two order of magnitudes when compared to that for two or three modes of leaching. Fitting to two or three modes of leaching indicates that the major amount of nitric acid is held at the ion exchange sites of the column with a smaller leaching rate constant. Fitting to a single mode of leaching behaviour has given a similar leaching rate constant as that obtained for five or ten percent nitric acid loaded weak base anion exchanger columns though the chi square value for single mode of leaching fitting has increased by an order of magnitude. The leaching behaviour for twenty percent nitric acid loaded weak base anion exchanger column should be assumed to follow more than one mode of leaching based on the respective chi square values obtained.

Fifty and hundred percent nitric acid loaded weak base anion exchanger columns outlet conductivity data gave a very poor fitting to single mode of leaching. Fittings for multiple modes of leaching to these data have given better results. Parameters obtained by fittings for multiple modes of leaching show that major contribution to conductivity came from the mode with a higher leaching rate constant. This indicates that the major amount of nitric acid is held by relatively weaker interaction at higher loading of the column.

Thus, a single mode of leaching can be used to explain leaching behaviour at lower nitric acid loadings. At higher loadings multiple mode of leaching is better to explain the leachout behavior.

In another set of experiments, inlet solution of nitric acid at several pHs was passed through a nitric acid loaded weak base anion exchanger column in a once through mode at the same flow rate. Here, there is a loading of the column at a constant rate accompanied by the leaching of nitric acid. The rate of change of nitric acid amount or the solution conductivity equivalent of nitric acid on the column can be expressed as:

$$\frac{dx_r}{dt} = at - \lambda_l(x_r + at) \qquad (6.3)$$

where x_r is the solution conductivity equivalent of nitric acid sorbed by the weak base anion exchanger column, λ_l is the leaching constant, 'a' is the solution conductivity equivalent added per unit time and t is the time. The integrated form of this expression with the limits of $x_r = x_r^o$ at t = 0 is:

$$x_r = a(1-\lambda_l)[\frac{t}{\lambda_l} - \frac{1}{\lambda_l^2}] + \exp(-\lambda_l t)[x_r^o + \frac{a(1-\lambda_l)}{\lambda_l^2}] \qquad (6.4)$$

The nitric acid leached out is linearly dependent on the nitric acid sorbed on the weak base anion exchanger column. Thus, the conductivity of the nitric acid leached out from the column can be represented as:

$$x_s = b\{a(1-\lambda_l)[\frac{t}{\lambda_l} - \frac{1}{\lambda_l^2}] + \exp(-\lambda_l t)[x_r^o + \frac{a(1-\lambda_l)}{\lambda_l^2}]\} \qquad (6.5)$$

where x_s is the solution conductivity and 'b' is the fraction of the sorbed nitric acid coming into the solution. The parameters obtained by fitting the experimental data to the equation (6.5) are given in **Table 6.2**.

Table 6.2: Parameters obtained by fitting the experimental outlet conductivity data of elution of varying inlet pH solutions through different columns loaded with nitric acid loaded weak base anion exchanger mixed with fresh WBA to different extents in a once through mode.

Parameters obtained	20% NLWBA with I/L pH:4.0	20% NLWBA with I/L pH:4.5	5% NLWBA with I/L pH:4.5	5% NLWBA with I/L pH:4.7
Chi square	0.069	0.003	0.001	0.001
b	0.004±0.007	0.016±0.004	0.006±0.001	0.005±0.001
a (fixed)	0.455	0.1664	0.1678	0.1612
λ_l	0.013±0.004	0.0141±0.003	0.0136±0.002	0.018±0.002
x_r^o	107.63±3.60	98.60±1.30	22.53±0.90	24.70±0.87

Here, the value of 'a', the solution conductivity equivalent added to the column per unit time was fixed as the calculated one based on the inlet solution conductivity, total inlet solution volume and the flow rate. The values of leaching constant obtained by this fitting are comparable to that for the once through leaching cases. However, there is a slight increase in the leaching rate constant with the increase in the pH of the inlet for any particular column configuration. This again indicates that leaching of nitric acid from weak base anion exchanger column is a combined effect of concentration or mass action and electrostatic repulsion.

Leaching behavior is also evaluated in recirculation mode of column operation. In recirculation mode of operation there is a simultaneous leachout and pickup of nitric acid on the weak base anion exchanger column. A model based on instantaneous quantitative removal of nitric acid by the weak base anion exchanger column and nitric acid loading dependent leachout at a constant flow rate from the column has been developed and used to explain the weak base anion exchanger column behavior. A single mode of leachout has been assumed to simplify the problem. The rate of conductivity variation in the recirculation system can then be expressed as:

$$\frac{dx_s}{dt} = \lambda_l x_r - \lambda_p x_s \qquad (6.6)$$

where λ_p is the pickup constant and other parameters are same as defined earlier. For a closed recirculation system the total conductivity is constant.

$$x_o = x_r + x_s \qquad (6.7)$$

where x_o is the solution conductivity for the entire nitric acid in solution. Combining this and the above expression and integrating gives the general solution:

$$x_s \exp\{(\lambda_l + \lambda_p)t\} = x_o\left(\frac{\lambda_l}{\lambda_l + \lambda_p}\right)\exp\{(\lambda_l + \lambda_p)t\} + c \qquad (6.8)$$

where c is the integration constant. Particular solutions for the above expression are obtained for two limiting cases. In one case, the entire nitric acid solution conductivity equivalent is considered to be initially sorbed on the weak base anion exchanger resin. Then, the boundary condition is: at t = 0, $x_s = 0$. Using this we get

$$x_s = x_o\left(\frac{\lambda_l}{\lambda_l + \lambda_p}\right)[1 - \exp\{-(\lambda_l + \lambda_p)t\}] \qquad (6.9)$$

In another case the entire nitric acid is considered to be initially present in the solution. Here, the boundary condition is: at t=0, $x_s=x_o$. This gives the expression

$$x_s = \left(\frac{x_o}{\lambda_l + \lambda_p}\right)[\lambda_l + \lambda_p \exp\{-(\lambda_l + \lambda_p)t\}] \qquad (6.10)$$

Equations (6.9) and (6.10) are used for fitting the experimental data obtained under identical conditions. Two different kinds of recirculation experiments were carried out. In one, pure water was circulated through the nitric acid loaded columns of different nitric acid loadings while in the other, different nitric acid concentrations were passed through the fresh weak base resin. The parameters obtained by fitting the above equations to the experimental data are given in **Tables 6.3** and **6.4**.

Table 6.3: Parameters obtained by fitting the experimental bulk conductivity data of recirculation of initially pure water through columns loaded with nitric acid loaded weak base anion exchanger mixed with fresh weak base anion exchanger to different extents.

Parameters evaluated	5% NLWBA	10% NLWBA	20% NLWBA	50% NLWBA	100% NLWBA
Chi square	0.027	0.033	0.030	1.424	10.728
λ_l	0.010 ±0.010	0.011 ±0.006	0.011 ±0.003	0.011 ±0.019	0.034 ±0.005
λ_p	0.026	0.026	0.026	0.026	0.026
x_o	24.97 ±0.34	50.61 ±0.43	106.19 ±1.87	266.22 ±8.38	542.80 ±8.69

Table 6.4: Parameters obtained by fitting the experimental bulk conductivity data of recirculation of different concentrations of nitric acid solution through fresh weak base anion exchange columns.

Parameters evaluated	Nitric acid concentration equivalent to 5% NLWBA	Nitric acid concentration equivalent to 10% NLWBA	Nitric acid concentration equivalent to 20% NLWBA	Nitric acid concentration equivalent to 50% NLWBA	Nitric acid concentration equivalent to 100% NLWBA
Chi square	0.032	0.219	2.141	57.252	211.800
λ_l	0.002±0.000	0.001±0.000	0.001±0.000	0.002±0.000	0.003±0.001
λ_p	0.026	0.026	0.026	0.026	0.026
x_o	27.93 ±0.02	49.90 ±0.47	102.85 ±1.32	268.22±6.32	535.35±10.94

The results of recirculation of pure water through various nitric acid loaded weak base anion exchangers were similar to that obtained for once through elution of pure water through same nitric acid loaded weak base anion exchangers in terms of leaching constants. The relatively poor fitting at higher loadings or at higher concentrations of nitric acid in solution are similar to that for once through experiments and can be explained by the same reasoning. However, the leaching constants obtained upon recirculation of nitric acid solutions through fresh weak base anion exchangers were an order of magnitude lower than that for the recirculation of pure water through equivalent amount of nitric acid containing nitric acid loaded weak base anion exchanger. For the column loaded with nitric acid the pure water entering the column will be in contact with the nitric acid loaded resin, whereas in the case of nitric acid solution recirculation through a fresh weak base anion exchanger, the nitric acid loaded resin part will be in contact with the solution having high concentration of nitric acid for most of the time. Thus leaching of nitric acid depends on both the amount of nitric acid sorbed on the weak base anion exchanger column and on the nitric acid concentration in solution. Thus the equilibrium effect becomes very important in the recirculation case. Equilibrium constants were determined for these experiments. The equilibrium constant for sorption of nitric acid on weak base anion exchanger can be represented by the process [11]

$$HNO_3 + P\text{–}NR_2 \leftrightarrow P\text{–}R_2NH^{+}\text{–}NO_3^{-} \qquad (6.11)$$

where P is the polymeric matrix of the weak base anion exchanger and R is the alkyl group attached to the nitrogen is given by the expression

$K_{eq} = {q_{HNO_3}} \big/ {q_{WBA} \times [HNO_3]}$, where K_{eq} is the equilibrium constant (l $mmol^{-1}$), q_{HNO3} is the capacity of nitric acid on weak base anion exchanger (meq/ml) and q_{WBA} is the remaining capacity of the weak base anion exchanger and $[HNO_3]$ is the nitric acid concentration in solution (mM) under equilibrium conditions.

The recirculation of pure water through various nitric acid loaded columns has been evaluated by fitting the experimental values of solution nitric acid concentration to equation (6.9) and thus determining the total nitric acid amount. The total nitric acid amount for each case was then taken from the weighted average of the values obtained from all cases. The equilibrium constants for the 5 %, 10 %, 20 %, 50 % and 100 % weak nitric acid loaded base anion exchanger mixtures with fresh weak base anion exchanger thus determined were 5.8, 7.2, 10.5, 9.2 and 8.7 respectively. For lower loadings a large number of unused weak base anion exchanger capacity is there although small concentration of nitric acid is still remaining there in solution. At very high loading the remaining concentration of nitric acid in solution is high and this again decreases the equilibrium constant. The equilibrium constants evaluated for the experiments where nitric acid concentration equivalent to 5 %, 10 %, 20 %, 50 % and 100 % loading were recirculated through fresh resin were 9.1, 13.5, 20.3, 6.5 and 6.2 respectively. Ideally the equilibrium constant should be same for all concentrations but the experimental values have a variation. This again indicates there is a varying pickup behaviour of weak base anion exchanger with changing concentration of nitric acid. The high equilibrium constant value for 20 % nitric acid loaded weak base anion exchanger mixture with fresh weak base anion exchanger can be correlated with the lesser leaching constant obtained for the same experiment.

Thus, an empirical quantitative estimation of nitric acid leachout from weak base anion exchanger column under given experimental conditions could be achieved. A single mode of leaching could satisfactorily explain the nitric acid pickup behaviour for upto 20 % loading or for 20 % nitric acid loaded weak base anion exchanger mixture with fresh weak base anion exchanger. The efficient removal of nitric acid on weak base anion exchanger is possible if the percentage loading is kept in the range of around 20 %.

6.3.2 Removal of gadolinium from solution

Gadolinium as $Gd(NO_3)_3$ solution is used for reactivity control in moderator at two concentrations of 2 mg kg^{-1} and 15 mg kg^{-1} in the 540 MWe PHWRs (Tarapur Atomic Power Station Units 3 and 4). 2 mg kg^{-1} gadolinium is used for first approach to criticality or startup after a Xe-135 poisoned shutdown while 15 mg kg^{-1} gadolinium is used for shutdown purposes. During the presence of gadolinium in solution, the pH of the moderator system is specified to remain between 5.0 to 5.5. Precipitation of gadolinium at higher pHs as hydroxide, carbonates, silicates etc. and structural material integrity concerns at lower pHs is the basis for this limit of pH. Removal of gadolinium from solution is carried out by using a combination of strong acid cation exchanger and weak base anion exchanger resins. Weak base anion exchanger resin has to be used since gadolinium is also used along with boron for fine control of reactivity insertion. Weak base anion exchanger is used so that boron is not removed and since it cannot remove nitrate as long as the counter ion is Gd^{3+}. On weak base anion exchanger, nitrate can be removed as nitric acid only as shown by equation (6.11). In the laboratory experiment for removal of 15 mg kg^{-1} gadolinium, the amount of weak base anion exchanger taken was resulting in about 20 % loading upon complete removal of gadolinium from the system while the amount of strong acid cation exchanger taken was for about 40 % loading upon complete removal of gadolinium. The column configuration used was a strong acid cation exchanger topped mixed bed of strong acid cation exchanger and weak base anion exchanger. The ratio of strong acid cation exchanger to weak base anion exchanger in the column was 1:2 in terms of volume and the distribution of strong acid cation exchanger was again 1:2 in terms of volume in the mixed bed layer and the top layer respectively. strong acid cation exchanger topping was provided for sequential removal of Gd^{3+} on top strong acid cation exchanger and of HNO_3 on the mixed bed to avoid any possibility of precipitation of gadolinium due to initial removal of nitrate. The hardware limitations of the plant require at the maximum the use of only two columns for 15 mg kg^{-1} gadolinium removal from the moderator system with each one taking half of the total ionic load. In our experiments we have reduced the solution volume to resin volume ratio to half of that of the system and removed the whole ionic load corresponding to 15 mg kg^{-1} [Gd] on one

Fig 6.1: pH variation during (A) removal of 4 mg kg^{-1} Gd and (B) removal of 15 mg kg^{-1} Gd with a SAC topped mixed bed

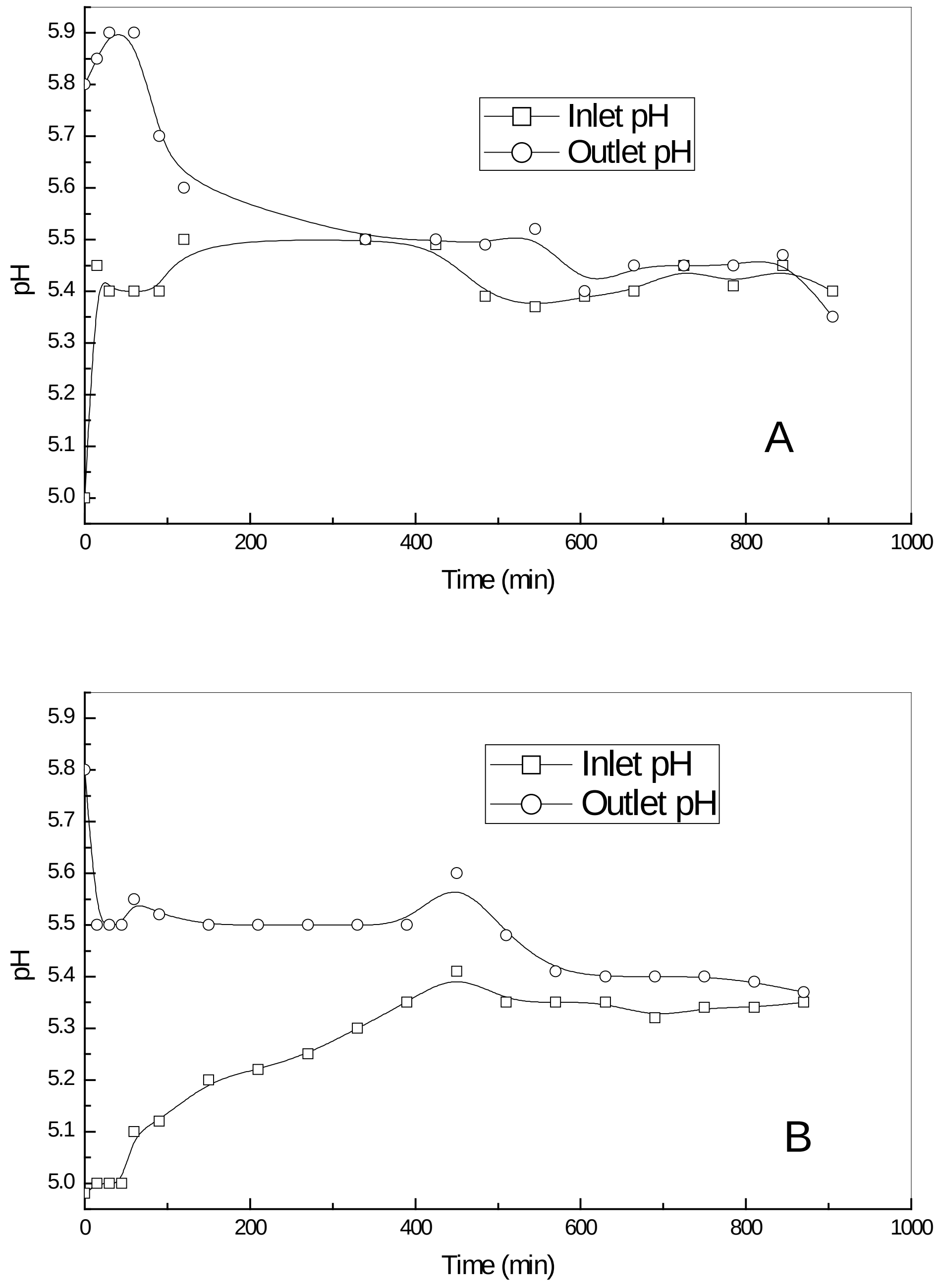

Fig 6.2: Conductivity variation during (A) removal of 4 mg kg^{-1} Gd and (B) removal of 15 mg kg^{-1} Gd with a SAC topped mixed bed

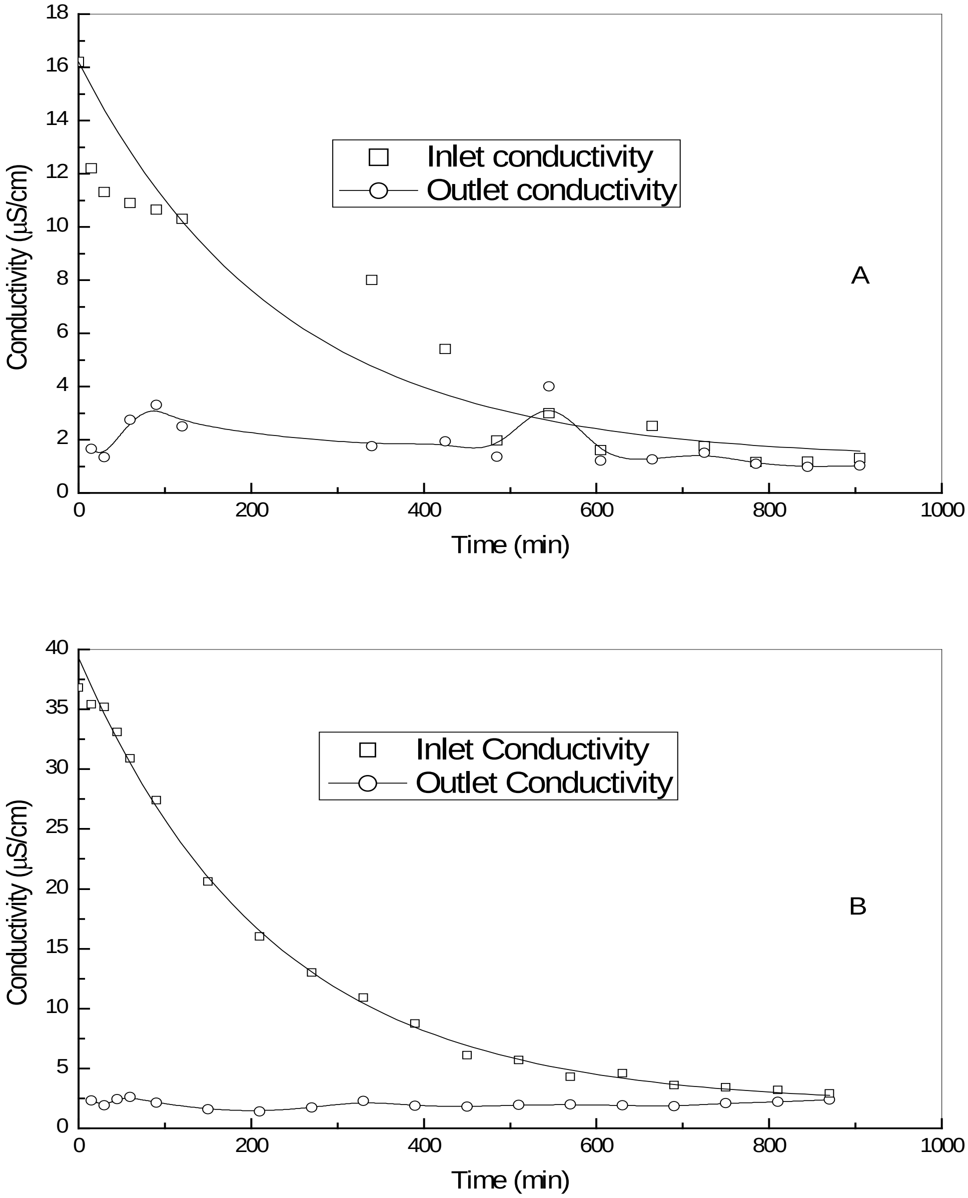

Fig 6.3: Gadolinium concentration variation during (A) removal of 4 mg kg^{-1} Gd and (B) removal of 15 mg kg^{-1} Gd with a SAC topped mixed bed

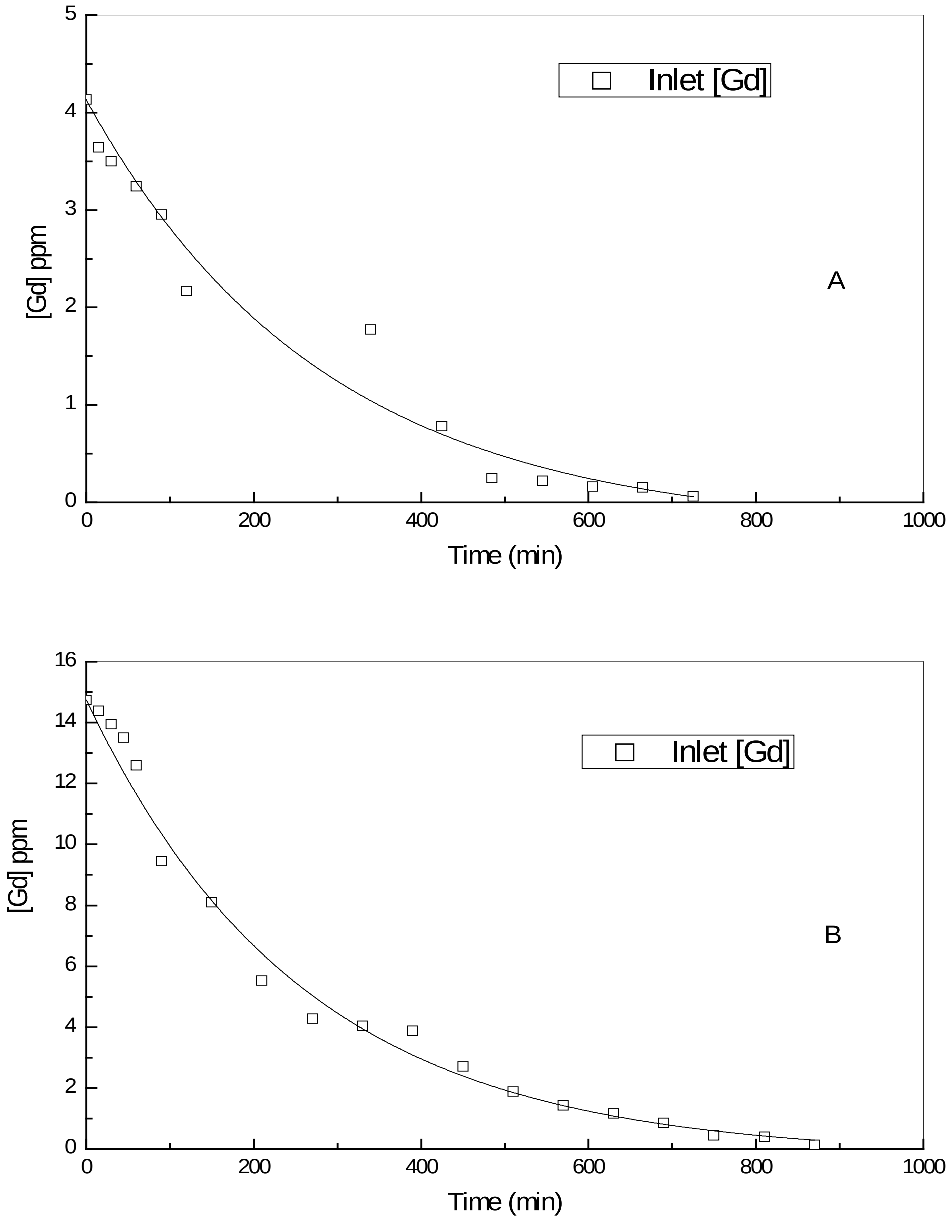

column so that the ionic loading of one column in the system could be simulated. Same composition of ion exchanger was used for removing 4 mg kg^{-1} gadolinium from the solution as well in lab experiments so as to simulate 2 mg kg^{-1} gadolinium removal from the system using one column. Here the concentration of gadolinium was doubled to obtain the same percentage ionic loading on the column as that in the system for half the solution volume used. The behavior of pH, conductivity and concentration of gadolinium in solution during the removal of 4 mg kg^{-1} and 15 mg kg^{-1} gadolinium are shown in **Figures 6.1, 6.2** and **6.3**. The outlet pH for both experiments are higher than 5.5 for about initial one half life as shown in **Fig 6.1**.

Although there is no gadolinium in solution at the column outlet, mixing of this higher pH water with system water may result in localized increase in pH and thus there is a chance of gadolinium precipitation in that region. The system conductivity (inlet) behaviour was fitted to equation (6.10). The leaching constants for both experiments obtained by fitting are similar to the one obtained for pure nitric acid recirculation for 20 % loading of the weak base anion exchanger. The system gadolinium concentration was also fitted to equation (6.10). The leaching constant obtained for both experiments were negative indicating that there is no leachout of gadolinium from the column leading to the quantitative removal of gadolinium on the column. Thus, the leaching constant obtained by fitting the system conductivity behaviour to the equation accounting for simultaneous pickup and leachout is due to the nitric acid leachout from the weak base anion exchanger of the column. This also explains the pH behaviour of the column outlet for both cases. The initial high pH of the outlet is due to almost quantitative ionic removal on the column. But with the ionic loading of the column, the nitric acid from weak base anion exchanger starts leaching out. This leads to the decrease in pH of the outlet at later period of gadolinium removal.

The above column configuration was compared with a mixed bed column of strong acid cation exchanger and weak base anion exchanger (1:1 capacity wise). Same amount of strong acid cation exchanger and weak base anion exchanger resins were used to prepare the mixed bed column. The behavior of system conductivity variation and gadolinium removal were similar but the variation in pH during gadolinium removal was lying in a wider range as shown in **Fig 6.4**.

Also the outlet pH at later stages is lying at lower values as compared to the technical specifications. Weak base anion exchanger can remove nitrate as nitric acid only and not as $Gd(NO_3)_3$. Thus in the mixed bed nitrate will be removed over a comparatively wider band of the column as compared to the strong acid cation exchanger topped mixed bed where gadolinium will be initially removed on strong acid cation exchanger. This will result in nitric acid leaching at a relatively early stage in case of mixed bed and also a higher leach out at later stage of gadolinium removal on the mixed bed. Thus to obtain a narrow band of outlet pH during gadolinium removal the strong acid cation exchanger topped bed is better as compared to the pure mixed bed. Further in the mixed bed configuration, any strong base functional group in the weak base anion exchanger (usually specified at less than 3 %) can cause gadolinium precipitation especially if the $Gd(NO_3)_3$ solution contacts the anion resin first. This is a possibility as homogeneous mixing cannot be practically ensured.

Fig 6.4: Variation of pH during 15 mg kg^{-1} Gd removal using a mixed bed of SAC and WBA

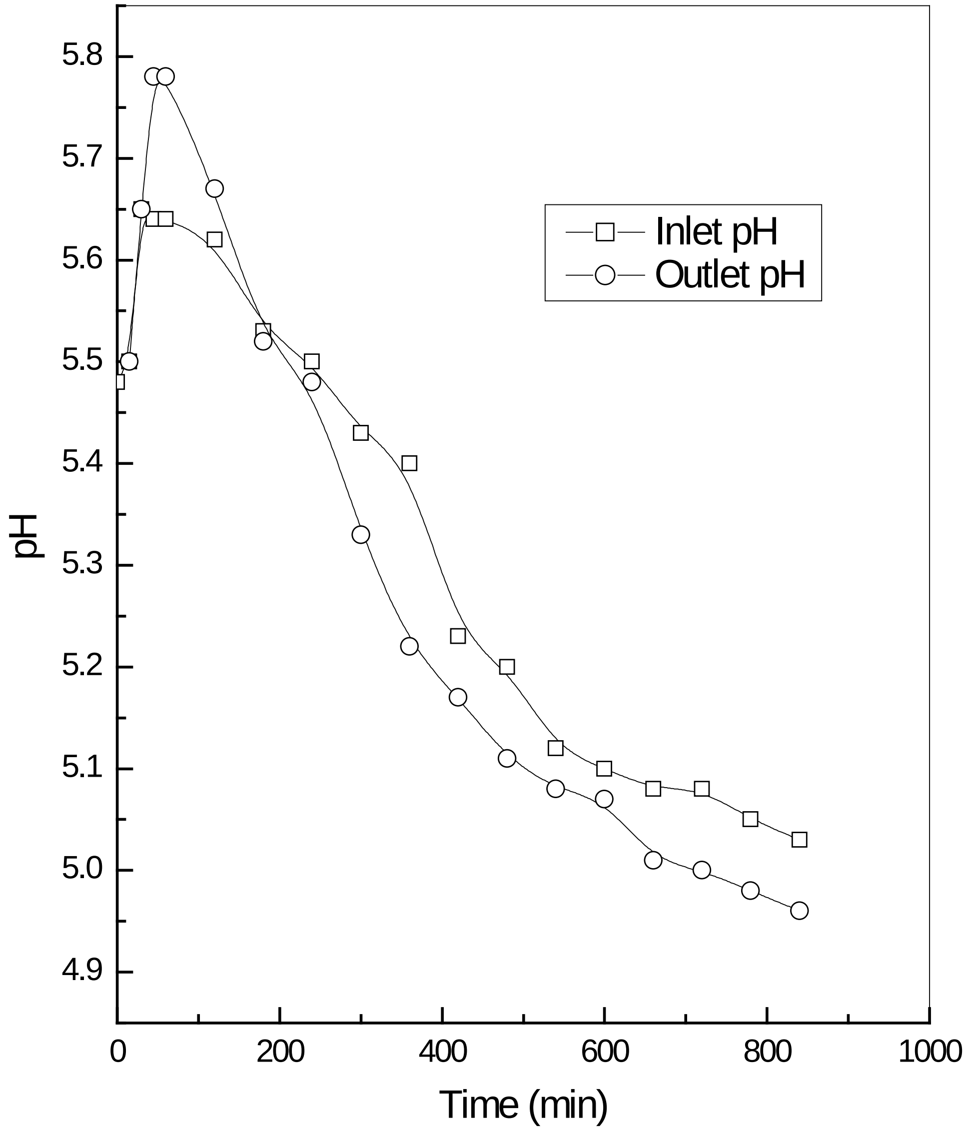

The leachout behaviour of nitric acid from nitric acid loaded weak base anion exchanger has been used to obtain the ion exchange column outlet pH within the specified limits from the beginning of gadolinium removal. For the given flow velocity through the column and volume of the weak base anion exchanger resin in the column, the percentage loading of nitric acid required to maintain the outlet pH within the specified limits for first few half lives could be determined. The amount and percentage loading of nitric acid loaded weak base anion exchanger of the column was selected on the basis of above results. 5 % nitric acid loaded weak base anion exchanger was arrived at as the bottom layer for the said column configuration and flow velocity to keep the outlet pH in the specified limits during the initial stages of gadolinium removal.

The behavior of pH, conductivity and concentration of gadolinium in solution during the removal of 4 mg kg^{-1} and 15 mg kg^{-1} gadolinium using a column with 5 % nitric acid loaded weak base anion exchanger under same condition as the earlier mentioned column are shown in **Fig 6.5, 6.6** and **6.7**.

The outlet pH for both 4 mg kg^{-1} and 15 mg kg^{-1} gadolinium has remained well within the technical specifications throughout the gadolinium removal as shown in **Fig 6.5**. The system conductivity and gadolinium concentration variation during the use of this column have shown a similar behavior as obtained by the use of the previous column indicating same efficiency of this column for gadolinium removal. Thus, the later column configuration provides a methodology for maintaining an iso pH regime during the gadolinium removal.

Fig 6.5: pH variation during (A) removal of 4 mg kg^{-1} Gd and (B) removal of 15 mg kg^{-1} Gd with a SAC topped mixed bed followed by a 5% NLWBA

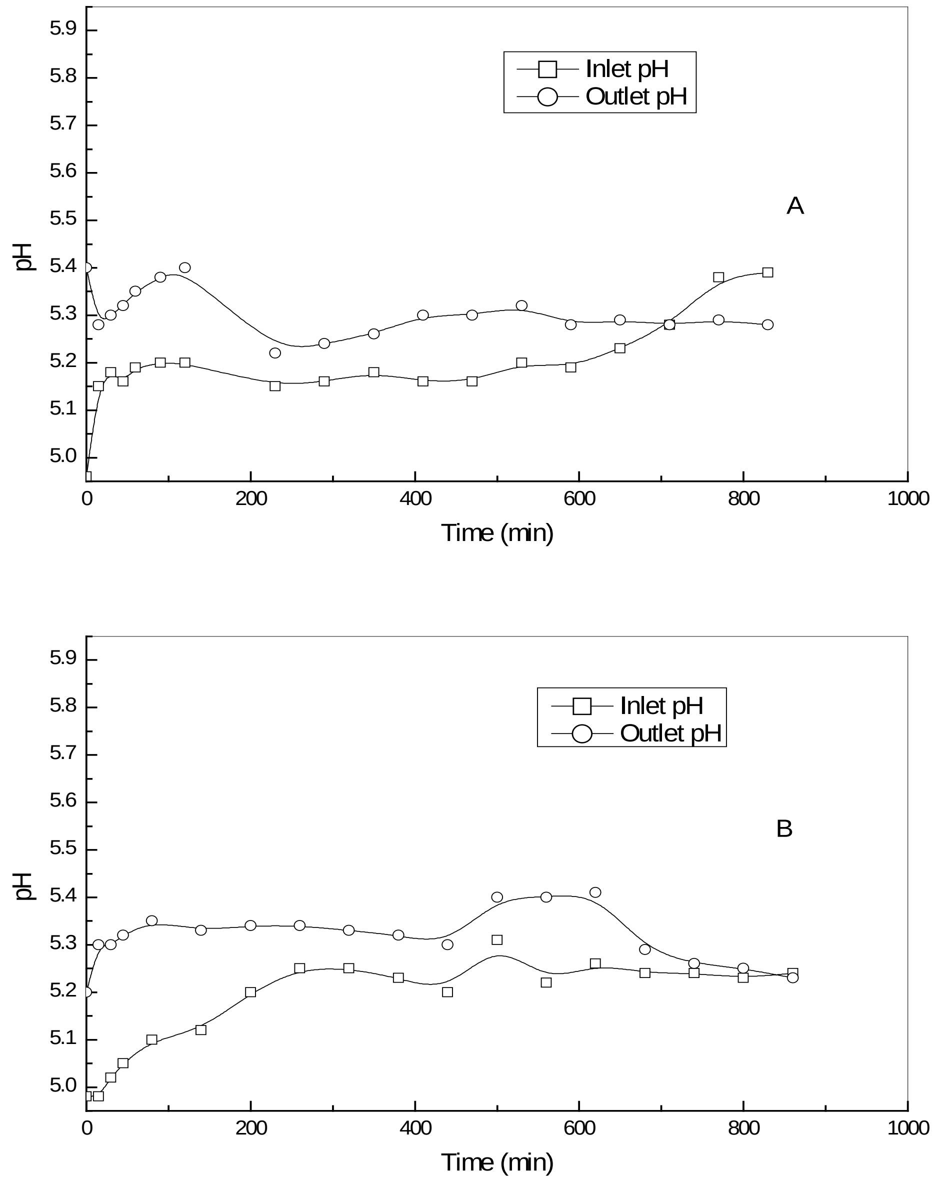

Fig 6.6: Conductivity variation during (A) removal of 4 mg kg^{-1} Gd and (B) removal of 15 mg kg^{-1} Gd with a SAC topped mixed bed followed by a 5% NLWBA

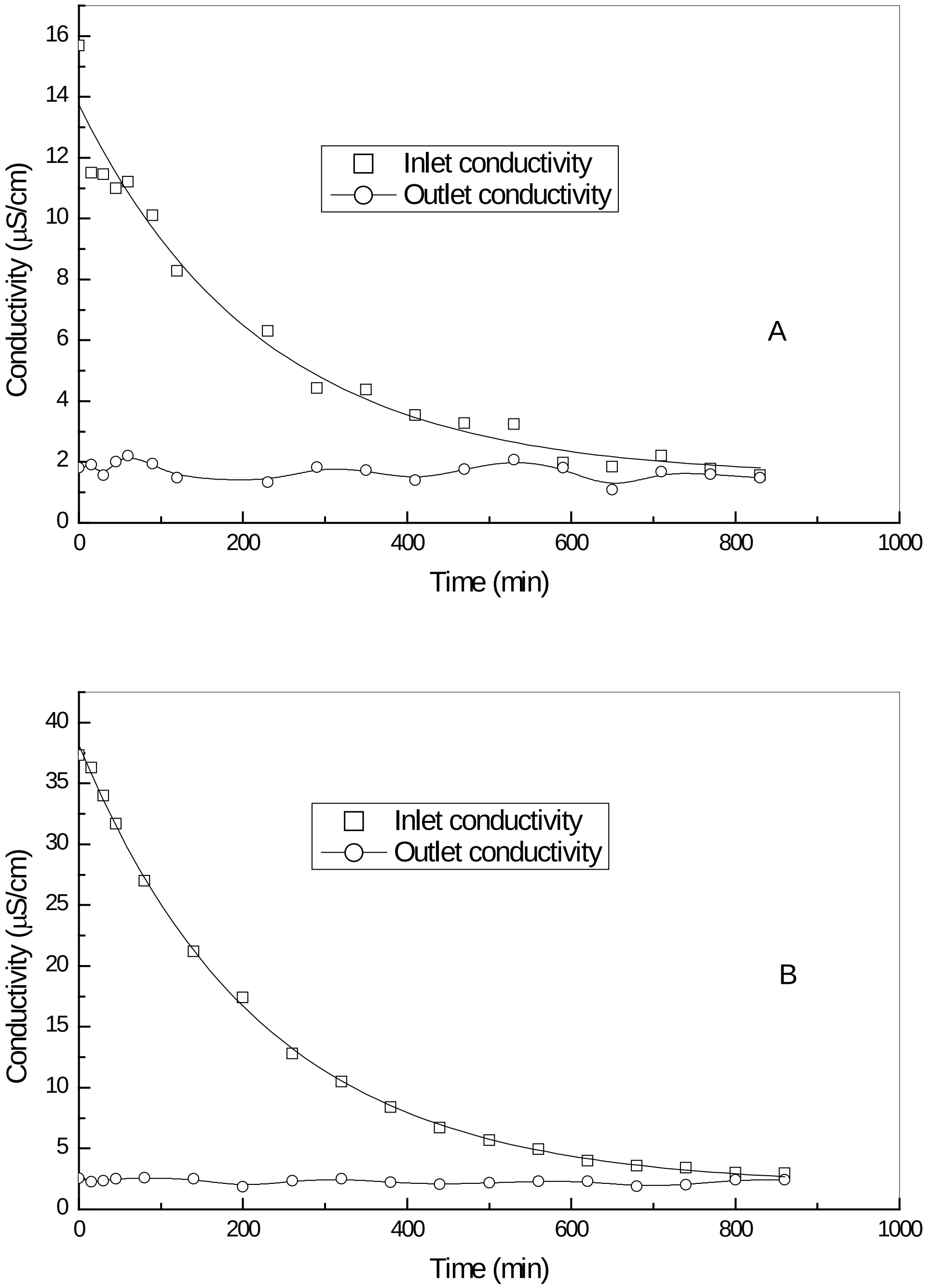

Fig 6.7: Gadolinium concentration variation during (A) removal of 4 mg kg^{-1} Gd and (B) removal of 15 mg kg^{-1} Gd with a SAC topped mixed bed followed by a 5% NLWBA

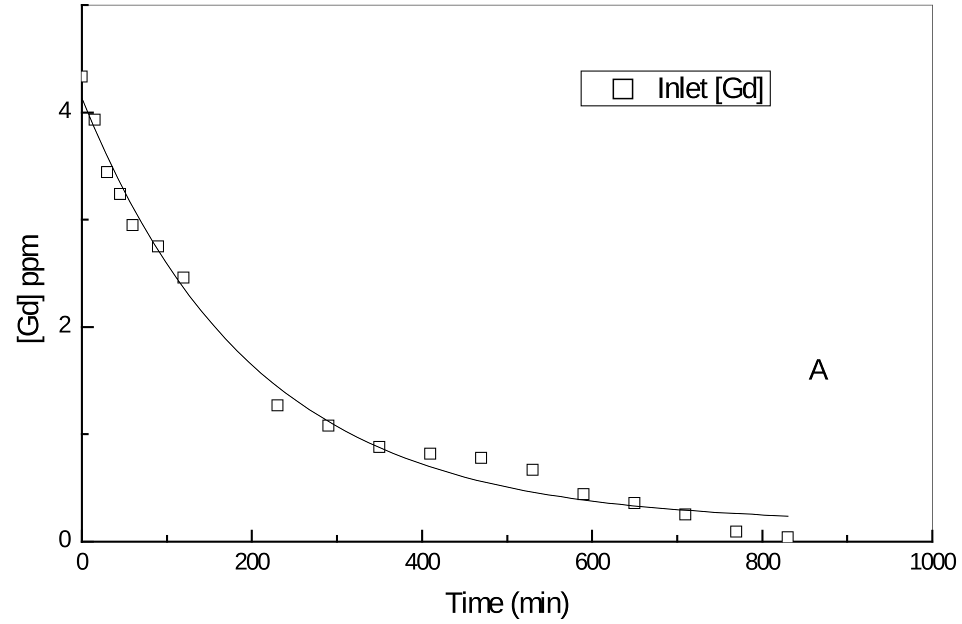

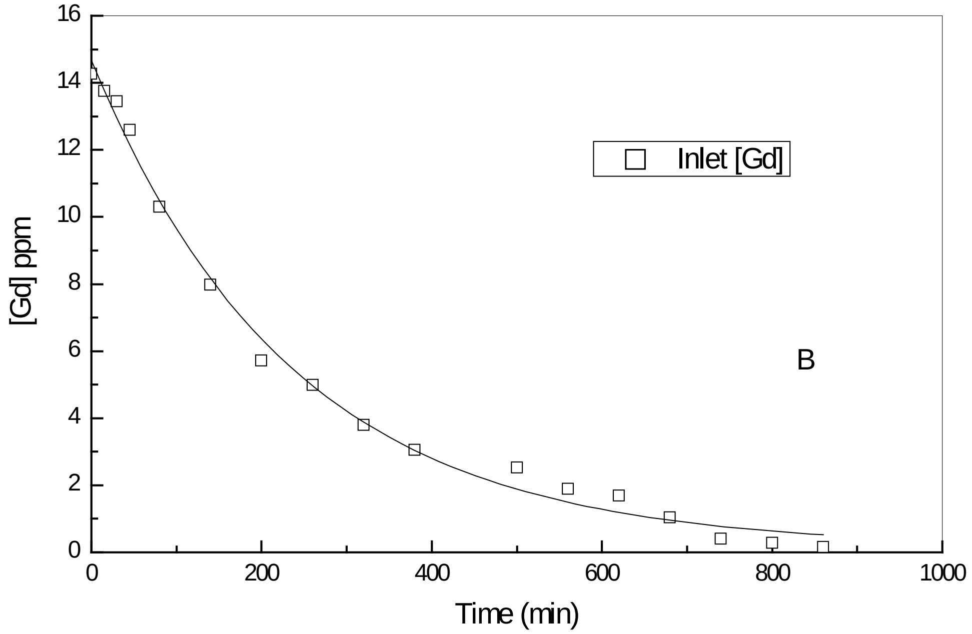

Summary

Elution of nano pure water through various nitric acid loaded weak base anion exchangers (NLWBAs) has shown that there is a leachout of nitric acid from the nitric acid loaded weak base anion exchanger. The fitting of the experimental data to the first order decrease of the leaching rate has shown a good agreement upto 20% initial loading of the weak base anion exchanger (WBA). At higher loadings the leaching follows multiple mode behavior. Elution of different pH nitric acids through nitric acid loaded weak base resins has shown that the leachout of nitric acid from weak base resin is a combined effect of mass action and electrostatic repulsion. Recirculation of nitric acid solution through weak base anion exchanger and nano pure water through nitric acid loaded weak base anion exchangers has shown that the leaching of nitric acid is governed by the equilibrium effect.

$Gd(NO_3)_3$ removal using a strong acid cation exchanger topped mixed bed of strong acid cation (SAC) and weak base anion exchanger column led to high column outlet pHs during initial stages of the run. Strong acid cation exchanger topped mixed bed of strong acid cation exchanger and weak base anion exchanger has given better result for gadolinium removal as compared to a similar composition mixed bed under identical conditions in terms of the pH profile. Use of a 5 % nitric acid loaded weak base anion exchanger under the given flow velocity and the given available resin capacity has led to efficient removal of gadolinium while adhering to the technical specification of pH to remain between 5.0-5.5.

6.4 References:

[1] T. Moeller and N. Fogel, *J. Am. Chem. Soc.*, 73 (1951) 4481.

[2] D. Barber and D. H. Lister, *Proceedings series of water chemistry and corrosion problems in nuclear power plants*, IAEA, Vienna, Switzerland. Nov. 22-26 (1982). pp. 149-161.

[3] R. Gilbert, L. Lepine, M. Laurin, L. Ouellet and R. Gauthier, *Can. J. Chem. Eng*., 63 (1985) 978.

[4] P. Sasikumar, K. Shivakamy, A. L. Rufus, V. K. Mittal, S. Bera, S. Velmurugan, S. V. Narasimhan, *Power plant chemistry*, 9 (2007) 34.

[5] G. T. Chandler and M.H. Anderson, WSRC-MS-91-502 (1991).

[6] M. G. Fontana, *Corrosion engineering third edition*, McGraw-Hill book company, 1987.

[**7**] E. Matijevic, United States Patent 5015452 (1991).

[8] S. C. Dash, R. S. Sharma, S. Dutta and G. Venkateswaran, *BARC Newsletter*, 272 (2006) 9.

[9] V. M. Bhandari, V. A. Juvekar and S. R. Patwardhan, *Ind. Eng. Chem. Res*., 31 (1992) 1060.

[10] M. O. Simonnot, and S. Ouvrard, *Chem. Eng. Sci.*, 60 (2005) 1849.

[11] V. M. Bhandari, T. Yonemoto and V. A. Juvekar, *Chem. Eng. Sci.*, 55 (2000) 6197.

CHAPTER-7

Conclusions

Synthesis of vanadium in low oxidation state for its application in decontamination of nuclear power plants has been studied. The required compound could be prepared in both aqueous solution as well as in the solid form. Aqueous vanadyl ions were found to have higher solubility than that of vanadate ions in formic acid media. The pronounced effect of deprotonation on the higher oxidation state of vanadium results in this behavior. The conductivity evaluation could clearly indicate the maximum instantaneous solubility limit for vanadate ions in formic acid medium. The instantaneous solubility behavior of vanadyl in formic acid medium is complicated by its the tendency of redissolution.

Studies on electrochemical evaluation of carbon based electrode and stainless steel electrodes for selection of better cathode material for aqueous vanadium reduction have shown that carbon based electrodes are more suited for the application. The evaluation of Tafel plots indicated that a significant part of current is lost in hydrogen evolution by formic acid reduction on stainless steel electrodes while the acid blocks the active sites on carbon electrode resulting in reduction of current density. Thus, a higher current efficiency is obtained for vanadium reduction on carbon based cathode.

Controlled current electrolysis of 350 mM aqueous vandyl formate has resulted in precipitation of an ionic V(III) compound. The compound readily dissolves in pure water but subsequently precipitates out as polymer depending upon concentration and ageing duration. Controlled current electrolysis of vanadate and vanadyl formate solutions with concentrations below 125 mM results in formation of aqueous solution of vanadous formate.

Chemical reduction of 350 mM vanadyl formate using Zn amalgam has resulted in precipitation of a vanadous compound. The product has been found to contain traces of zinc as per the elemental analysis. The chemical formulae of the vanadium compounds precipitated out by exceeding their solubility limits in the different oxidation states viz. V(V), V(IV), V(III) and V(II) were determined by a combination of chemical analysis, spectroscopic techniques, thermogravimetry and XRD. The formulae of the synthesized compounds were found to be V_2O_5, $VO(HCOO)_2 \cdot H_2O$, $V(OH)(HCOO)_2$ and $V(HCOO)_2 \cdot 2H_2O$ respectively.

In-situ monitoring of the electrolytic synthesis of vanadous formate based on continuous solution potential monitoring with a redox electrode impressed with a high frequency alternating voltage to overcome polarization of the electrode has been developed.

A simple, rapid and sensitive indirect spectrophotometric method has been developed for redox speciation of aqueous vanadium formate solution. Addition of known excess vanadate could convert all contiguous redox couples of vanadium formate into V(V)/V(IV) mixture. V(V) in solution is evaluated by adding Fe(II) and estimating the Fe(III) formed by the spectrophotometric determination of its sulfosalicylic acid complex.

Direct spectrophotometric determination of aqueous V(III)/V(II) formate solution could be achieved by adding thiocyanate as complexing agent. V(II) absorption peaks undergo a blue shift in the thiocyanate media and thereby giving well resolved peaks for the two aqueous vanadium redox species.

Chromate reduction on magnetite in the presence of γ irradiation follows a Lagergren’s pseudo first order kinetic model with respect to the applied dose. The extent of chromate reduction with increasing magnetite amount indicates that the process is a surface phenomenon.

XPS data has shown a difference in the surface composition of magnetite equilibrated with chromate due to the effect of irradiation as compared to that of isothermal equilibration. Thus, the additional pathways of chromate sorption on magnetite in the presence of gamma irradiation could be ascertained.

Elution of nano pure water through various nitric acid loaded weak base anion exchangers (NLWBAs) has shown that there is a leach out of nitric acid from the NLWBA. The fitting of the experimental data to the first order decrease of the leaching rate has shown a good agreement upto 20% initial loading of the weak base anion exchanger (WBA). At higher loadings the leaching follows multiple mode behavior.

Recirculation of nitric acid solution through WBA and nano pure water through NLWBAs has shown that the leaching of nitric acid is governed by the equilibrium effect.

Gadolinium nitrate removal using a strong acid cation (SAC) topped mixed bed of SAC and WBA column led to high column outlet pHs during initial stages of the run.

SAC topped mixed bed of SAC and WBA has given better result for gadolinium removal as compared to a similar composition mixed bed under identical conditions in terms of the pH profile.

Use of a 5% NLWBA under the given flow velocity and the given available resin capacity was found to accomplish efficient removal of Gd while adhering to the technical specification of pH to remain between 5.0-5.5.

Future scope of work

The synthesis methodology for the V(II) formate requires further modifications to improve the yield. At present there is a significant loss of the compound which remains stuck on the surface of the zinc amalgam. Alternate routes of preparation like using the V(III) compound synthesized in this study for the electrolytic preparation in a suitable medium should also be studied. The redissolution methodology for this compound also requires further investigation to avoid any oxidation during dissolution.

The effect of gamma irradiation on other similar chemical species like permanganate which are applied in the primary heat transport system for specific purpose should also be investigated.

The water chemistry control by using ion exchange resins with suitable selectivity coefficient for the other chemicals used in the sytem should also be investigated. The chemicals of interest are lithium hydroxide, zinc acetate, monoethanolamine among others.